An Investigation of Dynamically Measured Elastic/Mechanical

Properties for Consolidated Rocks and Unconsolidated Porous

Media Including Natural Petroleum Reservoir Sands

by

Susan M.T. Howarth

A thesis submitted to the Faculty and the Board of Trustees of the Colorado School of Mines in partial fulfillment of the requirements for the degree of Doctor of Philosophy (Petroleum Engineering).
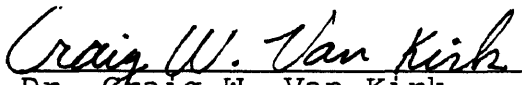
Golden, CO

Date _November 23 1987_

Signed: _____
         Susan M.T. Howarth

Approved: _____
          Dr. _____
          Thesis Advisor

Golden, CO
Date _Nov. 23, 1987_

_____
Dr. Craig W. Van Kirk
Head, Department of
Petroleum Engineering

ABSTRACT

Elastic/mechanical rock properties, such as Young's modulus, Poisson's ratio and bulk modulus (the inverse of bulk compressibility) are used in reservoir engineering calculations. This research focused on bulk compressibility of both consolidated rock and unconsolidated sands. Values of bulk compressibility are necessary for: 1) calculating reservoir compaction and surface subsidence, 2) predicting oil and gas recovery, 3) designing well completions, 4) implementing proper sand flow control measures and 5) instituting enhanced oil recovery (EOR) processes. Using incorrect bulk compressibility values can result in poor engineering and unplanned capital expenditures.

Bulk compressibility can be measured using static or dynamic methods. Statically measured bulk compressibility is the volumetric deformation caused by applied pressure. Dynamically measured bulk compressibility is calculated from wave velocity measurements through rock. For an isotropic, homogeneous, and elastic material, such as steel, the static and dynamic compressibility values are the same. Reservoir rocks and unconsolidated sands are neither homogeneous nor isotropic and the values of bulk compressibility measured from the two methods differ; static compressibility can be more than twice the value of dynamic compressibility. Static

values of bulk compressibility better represent how the reservoir rock deforms as fluid is withdrawn than does dynamic bulk compressibility.

The objective of this research was to make dynamic measurements under hydrostatic pressure up to 5000 psig and calculate the bulk compressibility for both consolidated rocks and unconsolidated samples which included actual reservoir sands, frac sand, and glass beads. The unconsolidated samples were analyzed to determine if there were relationships between grain shape (angularity), grain size, or mean grain diameter and wave velocities and bulk compressibility. Additional work was performed which resulted in better understanding of core preparation procedures.

Three theoretical models were employed in the analysis of results. The porosity of the samples was calculated from wave velocities using the Wyllie time-average equation. The other two models from Gassmann (1951) and Biot (1956), which predict static bulk compressibility from dynamic wave measurements, were compared.

Microscopic analysis on unconsolidated samples indicated that grains were not crushed or cracked during core preparation or testing. Consolidated Berea sandstone properties were shown to be sensitive to some core

preparation procedures. Air permeability was dramatically increased with small temperature increases during drying, and liquid permeability was extremely sensitive to the saturating fluid composition.

No definite trend between wave velocity and grain size or angularity was determined. Dynamic bulk compressibility of actual reservoir samples samples was comparable to that of the artificial samples having the same mean grain diameter. Bulk compressibility values predicted using the Gassmann (1951) model were comparable to those predicted using the Biot (1956) model for frac sand with grain sizes smaller than 20/40 mesh.

Dedicated
to
the Memory of

my Godfather,

Peter McDonald
August 9, 1986

and

my Grandmother,

Rose Anne McDonald
June 19, 1987

"The woods are lovely, dark and deep.
But I have promises to keep
And miles to go before I sleep,
And miles to go before I sleep."

- Robert Frost

TABLE OF CONTENTS

T-3280

LIST OF FIGURES

Appendix B-Dynamic bulk compressibility versus
pressure for all cores:

LIST OF TABLES

ACKNOWLEDGEMENTS

1. INTRODUCTION

Accurate in-situ measurements of porosity, permeability, and formation compressibility are essential for reservoir engineering calculations including material balance prediction of water drive performance and enhanced oil recovery (EOR) pressure maintenance performance. Additionally, understanding the mechanisms and effects of formation compressibility is necessary for calculating surface subsidence, for designing well completions, and for measuring in-situ stress to determine appropriate sand production control.

Early work with consolidated and unconsolidated sand was concerned with measuring static properties from recovered cores. These static properties were measured by applying pressure, either hydrostatic, biaxial or uniaxial, and measuring the deformation of the core to determine elastic moduli and compaction. More recently, it was discovered that dynamic rock properties, those calculated using acoustic wave velocities, could be determined from acoustic well logs. These shear and longitudinal wave velocities can be used to calculate dynamic elastic moduli and compressibility. For homogeneous, isotropic elastic materials, such as steel, the static and dynamic moduli are the same. But, for reservoir

rocks which are heterogeneous and anisotropic, the moduli measured using the two techniques differ.

Using acoustic, also known as sonic, logs to provide dynamic moduli from acoustic wave velocities has many advantages: 1) the wave velocities are measured in-situ during routine logging operations; 2) a continuous wave form is recorded for the entire interval logged; 3) no additional rig time is required for coring operations; and 4) the moduli are well and reservoir specific so no averaged or correlated data are required for subsequent calculations. The one major problem with this method is that it is not always possible to measure reliable shear (s-wave) velocities with current logging tools because shear waves do not travel through fluid. Sometimes shear waves can be seen on a longitudinal (p-wave) profile in consolidated rock. (Although the literature suggests that reliable p-wave measurements can be made through unconsolidated sands, this research showed that reliable p-waves cannot be measured at pressures below 2000 psig.)

The static elastic moduli and rock compressibility are the values used in most reservoir engineering calculations, such as material balance, surface subsidence and well completion design work. A consolidated core from the reservoir can be cleaned, dried, resaturated and mounted in a

test cell. Axial and radial strain measurements can be made at varying pressures to simulate reservoir conditions and measurement can be repeated. Problems arise, however, with unconsolidated sand. In order to closely simulate reservoir conditions, it is desirable to have an undisturbed sand sample with in-situ grain orientation, porosity, and permeability. This is virtually impossible with unconsolidated sand; cores must be reconstructed from loose sand prior to testing, which brings greater uncertainty into testing procedures and subsequent analysis.

Because in-situ measured dynamic rock properties are easier and less costly to obtain than laboratory measured static properties, those needed for reservoir depletion studies, correlations are needed to relate the necessary static and dynamic rock properties. Numerous authors working with consolidated cores have found some correlations and work continues to completely solve the problems. The work with unconsolidated cores is not as advanced and, in fact, very little has been published on the subject.

The ultimate long term goal of the Acoustic Velocity Sand Control Project is to determine if correlations exist for relating static and dynamic moduli for unconsolidated sand and to further define unconsolidated sand properties. The immediate goal of this research was to design the

appropriate testing procedure for unconsolidated sand, to
make fundamental measurements of dynamic elastic moduli, to
determine which rock properties are the most critical for
future work, and to determine the direction of future work
with unconsolidated sand. It should be pointed out that the
term elastic (by definition) applies to materials that are
isotropic and homogeneous, such as steel. Elastic moduli
including Young's modulus, Poisson's ratio, bulk modulus, and
Lame's coefficients are also, by definition, applicable to
elastic materials. Throughout the literature these misnomers
are used to describe rock properties which may be elastic
only over small stress ranges.

Dynamic properties were measured for 22 samples; five
consolidated rock cores including two previously tested by
Montmayeur (1985), two glass bead packs, six frac sand packs,
and nine natural reservoir sand packs. Dynamic measurements
were made on the cores in this experiment under hydrostatic
pressure up to 5000 psig. Montmayeur (1985) made both
dynamic and static measurements on frac sand samples under
hydrostatic pressure up to 5000 psig for similarly prepared
frac sand packs. Using Biot's model he was able to predict
static bulk compressibility from dynamic measurements at high
pressure. A goal of this project was to compare the dynamic
measurements between Montmayeur's (1985) consolidated and

unconsolidated samples and those of this experiment based on grain size analysis. Additionally, Gassmann's model was used on Montmayeur's (1985) frac sand dynamic data to predict static bulk compressibility from dynamic measurements and the results from the Gassmann (1951) and Biot (1956) models were compared.

2. LITERATURE REVIEW

2.1. Rock Properties

Rock properties such as in-situ stresses, porosity, permeability and compressibility are used by reservoir engineers in material balance and volumetric calculations for estimating reserves and maximizing production. Rock compaction is important during the design and implementation of well completions and in the problems associated with sand control and surface subsidence. Researchers have spent considerable amounts of time trying to derive correlations between rock properties to help quantify their interrelationships, thus reducing the costly additional rig time and laboratory analysis associated with gathering core data.

2.1.1. Porosity and Permeability

Porosity is perhaps one of the easiest rock properties to measure. It can be measured in-situ with acoustic, density, or neutron logs or in the laboratory on recovered core samples or drill cuttings. Likewise, permeability can

be measured in-situ during pressure transient well testing or in the laboratory. The laboratory-measured values of permeability can differ from the in-situ-measured values because of the different pressure testing conditions.

While the higher reservoir temperatures have little or no effect on permeability and porosity measured in the laboratory and in-situ, the effect of higher reservoir pressures on permeability can be significant. Carpenter and Spencer (1940) showed that the change in porosity with pressure for their sample rocks under hydrostatic pressure up to 8000 psig was small. Wilhelmi and Somerton (1967) showed that the reduction in porosity under triaxial loading conditions was approximately 5 to 8 percent of the original unstressed porosity value.

Fatt and Davis (1952) studied the reduction in permeability with overburden pressure. They measured the permeability of eight sandstone cores at zero overburden pressure and under hydrostatic pressures up to 15,000 psi to simulate higher overburden pressures. They found that the permeability of the rocks decreased most significantly in the zero to 3000 psi range, equivalent to approximately 5000 feet of overburden. At 3000 psi the permeabilities decreased to 59 to 89 percent of their zero overburden pressure values.

Fatt (1953) also studied the effect of overburden pressure on effective and relative permeability of a gas-oil system and the reduction in pore volume with overburden pressure on four sandstone cores. His pore volume and effective permeability measurements were made under hydrostatic pressures of zero to 5000 psi and relative permeabilities were measured at zero and 3000 psi hydrostatic pressure and zero pore pressure. Gas saturation was measured at the overburden pressure. Lower effective gas permeabilities result if gas saturation is measured at surface (zero overburden pressure) conditions before high pressure is applied. As overburden pressure increases, the pore volume gas saturation decreases because capillary effects hold the oil, the wetting-phase fluid, in the pores. He measured relative gas permeability as gas saturation increased and as it decreased, but used the values of relative gas permeability as gas saturation increased in his analysis. Results showed that gas relative permeability on the four cores did not change under the 3000 psig hydrostatic pressure and that laboratory relative permeability data can be used if the effective permeability is corrected for pressure.

Wyble (1958) studied the effects of confining pressure with atmospheric pore pressure on Weir, Kirkwood and Bradford

sandstone core samples. He found that over the zero to 5000 psig pressure range for confining pressure, porosity decreased less than 10 percent while electrical conductivity decreased 20-30 percent. Klinkenberg permeability decreased asymptotically 50-65 percent at 5000 psig. He attributed the asymptotic decline limit of 3500-4500 psi to being the maximum pressure the formation was under during geologic burial.

McLatchie et al. (1957) also studied the effects of high overburden pressure on permeability of shaley sands. Measurements of oil permeability were made at zero overburden pressure and with increasing hydrostatic pressure up to 5000 psi and decreasing hydrostatic pressure from 5000 psi down to zero. Their data showed that the lower the zero overburden pressure permeability was, the greater the reduction in permeability would be at a given overburden pressure. This trend opposed that of other researchers whose work generally showed that the reduction in permeability with overburden pressure increases with zero overburden pressure permeability. McLatchie et al. (1957) attribute the discrepancy to the use of shalier sands than the other researchers used.

McLatchie et al. (1957) also compared the zero overburden pressure permeability of their rock samples prior to pressure

testing to the zero overburden pressure permeability after
pressurizing the rock up to 3000 psi. Their results
indicated a small, 4 percent, reduction in permeability for
high permeability rocks but found a larger, up to 60 percent,
reduction in permeability for shaley cores. After a year,
however, some of their cores regained their initial zero
overburden pressure permeability, illustrating the inherent
memory of rocks and their elastic behavior. Similar results
are noted by Van der Knaap (1960).

2.1.2. Compressibility

Compressibility is an often overlooked rock property
that is important in reservoir engineering calculations and
is the focus of this work. The available equipment was used
to test unconsolidated sands under hydrostatic test
conditions, the condition under which bulk compressibility is
defined.

It is interesting to note that before 1940 research on
compressibility was performed almost exclusively on
unconsolidated samples (Botset and Reed 1935). Since then,
most of the recent research on compressibility has been
concerned with consolidated rocks but the focus is changing
to encompass the study of unconsolidated sand

compressibility, also. Because the published literature on unconsolidated sand compressibility is sparse, this review will chronicle the development of work on consolidated rock compressibility and the work with unconsolidated sand as they have progressed. It is expected that, although research on unconsolidated sands has lagged that of consolidated rocks, work with unconsolidated sands will parallel that of the consolidated rocks.

Rock compressibility is an important factor in petroleum reservoir calculations. While the effect of rock compressibility is negligible in material balance calculations for saturated reservoirs it can significantly affect reservoir engineering calculations for geopressured gas reservoirs, heavy oil reservoirs, undersaturated reservoirs and for predicting water drive performance. As an example, if the rock compressibility is equal to half the oil compressibility of an undersaturated oil reservoir, the omission of rock compressibility would result in a 50 percent overestimation of oil in place. Similarly, Harville and Hawkins (1967) show that in geopressured gas reservoirs, rock compressibilities are higher than normal and neglecting rock compressibility could also result in a significant overestimation of gas in place using traditional P/Z graph techniques.

The early work with rock effective compressibility
consisted of measuring static properties on recovered cores.
Carpenter and Spencer (1940) were among the first to
investigate the compressibility of consolidated oil-bearing
sedimentary rocks to determine its relationship to surface
subsidence. Those early researchers considered sand
compressibility to be a negligible factor as a production
mechanism for unconsolidated sands and concluded that it
would be even a less important factor for consolidated
formations (Botset and Reed 1935; Carpenter and Spencer
1940). Carpenter and Spencer (1940) calculated the
compressibility by measuring the amount of pore fluid
expelled during their test in which the pore fluid pressure
is held constant at atmospheric pressure while the external
hydrostatic pressure was increased. This method does not
model reservoir conditions during production, however,
wherein the pore fluid pressure declines over time.

Static properties, measurements of core deformation to
determine elastic moduli and compressibility, are taken as
pressure, either hydrostatic, triaxial or uniaxial, is
applied to the core. Effective rock compressibility is the
result of two simultaneous effects occurring as reservoir
pressure declines during production: 1) the net load on the
rock increases as reservoir fluids become less effective in

opposing overburden weight, and compaction of the rock
structure results causing a decrease in pore volume; and 2)
the individual rock grains expand into the pore space as
reservoir fluid pressure declines.

Hall (1953) investigated the compressibility of
consolidated rocks under hydrostatic pressure and presented
correlations of effective rock compressibility and porosity.
This widely misused correlation was based upon a very limited
data base, 12 samples. The formation compaction and
effective compressibility correlations were for consolidated
sandstone and limestone reservoirs and showed that both
compressibility and compaction decreased with increasing
porosity.

McLatchie et al. (1957) studied the effective
compressibility of reservoir rock and its relationship to
permeability. Their initial results showed that effective
compressibility could not be directly correlated with
porosity and that the amount of shale in the rock and other
factors might have to be accounted for.

Hall's (1953) work was further disputed by Newman
(1973), who published a more thorough paper relating pore
volume compressibility of consolidated, friable, and
unconsolidated rock to porosity. His data base, 265 samples,
was considerably larger than Hall's (1953), and he studied

effects of temperature, cycling and time. His results for consolidated cores were in poor agreement with Hall's (1953), but he found the same general trend of decreasing compressibility with increasing porosity. Newman (1973) noted that unconsolidated samples showed the opposite trend, increasing compressibility with increasing porosity (Figure 2.1.1). In fact, if Hall's (1953) correlation is used incorrectly for unconsolidated sand, the pore volume compressibility could be off by a factor of 20. Further, Newman (1973) noted that unconsolidated sand showed "significant inelastic behavior (permanent volume reduction with pressurization, resulting from internal grain failure)". He concluded that for unconsolidated samples, "pore-volume compressibility is not merely porosity dependent; other stress parameters need to be investigated". It should be noted that Newman's analysis was based upon data compiled for various rocks tested under different conditions and stress states.

While Newman and the others were measuring the static properties of rocks, others were discovering uses for acoustic log and wave velocity data to describe elastic and mechanical properties of reservoir rocks. Using the acoustic log data, they were in fact finding the sand's dynamic properties. Stein (1976) correlated his "cementation index"
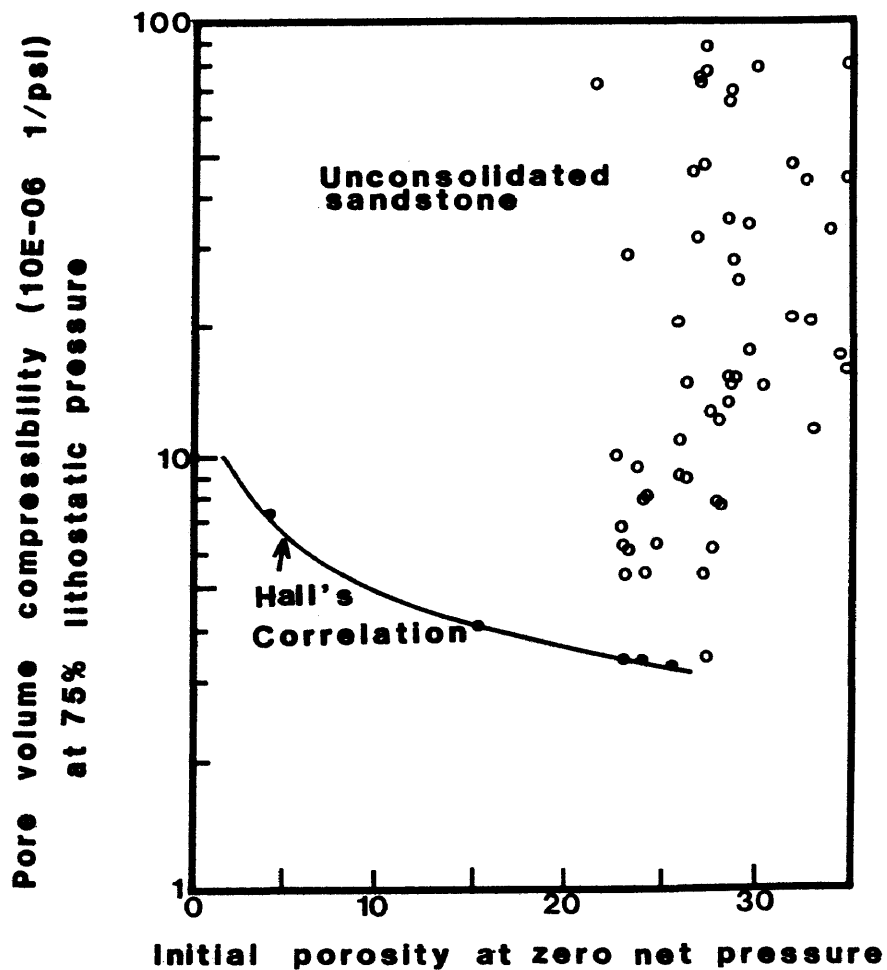
Figure 2.1.1. Pore-volume compressibility at 75 percent
lithostatic pressure versus initial
sample porosity for unconsolidated
sandstones. [After Newman (1973)]

to critical flow rate for sand production. This work was based on plots of shear modulus (G), derived from acoustic log data, versus depth. Kohlhaas (1980) and others used wave pulse profiles from logs to calculate shear (s-wave) and longitudinal (p-wave) velocities. These plots were then used to identify stress-sensitive sand intervals so that proper sand control measures could be taken. This work was well-specific but the need was recognized for correlating dynamically derived rock properties with those from static tests in the laboratory.

Because static properties are considered to be more characteristic of the reservoir conditions for depletion studies than are dynamic properties, as shown in Table 2.1.1 from Montmayeur and Graves (1986), the static moduli and compressibility are used for reservoir engineering calculations and should be used for hydraulic fracturing calculations (Lin and Heuze 1986). Because dynamic measurements are easier to take and less costly than static, correlations are needed between dynamic and static moduli.

At this point, it is obvious that static and dynamic rock properties need to be discussed separately. First, though, the literature on the different rock property models will be reviewed, and the two methods of measuring

Table 2.1.1.
Typical Testing Characteristics for One Set of Data
[Montmayeur and Graves (1986)]

Test Parameter	Static Test (Load induced parameter)	Dynamic Test (Wave induced parameter)
Loading rate (psi/sec)	10 to 70	$2.5 \cdot 10^6$
Stress Magnitude (psig)	5000	50
Strain (in/in)	$3 \cdot 10^{-3}$	$10 \cdot 10^{-6}$

rock properties and current research concerned with correlating between static and dynamic rock properties will be discussed.

2.2. Elastic-Mechanical Properties

2.2.1. Definition of Elastic Properties

Elastic properties are defined for isotropic, homogeneous, solid materials like steel. Further, it is assumed that the material acts reversibly along the linear stress-strain curve. While not all materials are linearly elastic by definition they do behave linearly over certain stress ranges. The elastic properties will be defined in terms of the right hand system of rectangular coordinates as outlined by Jaeger and Cook (1971).

The stress components at a point under the previously described system can be described by the stress tensor, Equation (2-1), where σ is the normal stress and τ is the shear stress.

$$
\begin{bmatrix}
\sigma_x & \tau_{xy} & \tau_{xz} \\
\tau_{yx} & \sigma_y & \tau_{yz} \\
\tau_{zx} & \tau_{zy} & \sigma_z
\end{bmatrix}
= \text{Stress tensor} \qquad (2\text{-}1)
$$

For porous fluid filled media, assuming that the bulk
material is continuous, the stress tensor is divided into two
parts; a hydrostatic part that accounts for changes in volume
(Equation 2-2) and a deviatoric part that accounts for
changes in the shape of the rock (Equation 2-3); both defined
in terms of $\bar{\sigma}$, also known as the octahedral normal stress
(Van der Knapp 1959; Jaeger and Cook 1971).

$$
\text{Hydrostatic} =
\begin{bmatrix}
\bar{\sigma} & 0 & 0 \\
0 & \bar{\sigma} & 0 \\
0 & 0 & \bar{\sigma}
\end{bmatrix}
\qquad (2\text{-}2)
$$

$$
\text{Deviatoric} =
\begin{bmatrix}
\sigma_x - \bar{\sigma} & \tau_{xy} & \tau_{xz} \\
\tau_{yx} & \sigma_y - \bar{\sigma} & \tau_{yz} \\
\tau_{zx} & \tau_{zy} & \sigma_z - \bar{\sigma}
\end{bmatrix}
\qquad (2\text{-}3)
$$

where $\bar{\sigma} = \frac{1}{3}(\sigma_x + \sigma_y + \sigma_z)$

Using Lame's coefficients, λ and G (the shear modulus),
the following Equations, 2-4 a-c, express the linear
relationship between the stress and strain components. Note
that $(\lambda + 2G)$ relates the stress and strain in one direction
while λ relates them for the two perpendicular directions
(Jaeger and Cook 1971).

$$\sigma_x = (\lambda + 2G)\ \varepsilon_x + \lambda\varepsilon_y + \lambda\varepsilon_z \qquad (2\text{-}4a)$$

$$\sigma_y = \lambda\varepsilon_x + (\lambda + 2G)\ \varepsilon_y + \lambda\varepsilon_z \qquad (2\text{-}4b)$$

$$\sigma_z = \lambda\varepsilon_x + \lambda\varepsilon_y + (\lambda + 2G)\ \varepsilon_z \qquad (2\text{-}4c)$$

Further definition of elastic parameters depends upon
the imposed stress state. Sawabini (1972) identifies the
official classification and alternatives used in the
literature (Figure 2.2.1).

Two elastic properties, Young's modulus, E, and
Poisson's ratio, ν, are defined for a system under uniaxial
stress, $\sigma_z = \sigma_y = 0$. Young's modulus is the ratio of
longitudinal stress to longitudinal strain and Poisson's
ratio is the ratio of lateral strain (expansion) to
longitudinal strain (compaction). Substituting the stress
conditions of zero lateral stress into Equations 2-4(a-c),
Equations 2-5 and 2-6 follow.
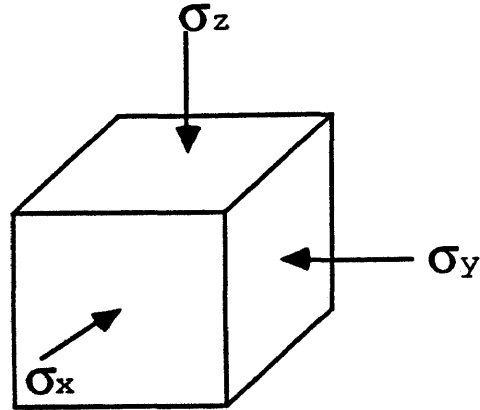
STRESS STATE	SAWABINI (1972) CLASSIFICATION	CLASSIFICATION FOR THIS STUDY
$\sigma x = \sigma y = \sigma z$	HYROSTATIC	HYROSTATIC
$\sigma x \neq \sigma y \neq \sigma z$	POLYAXIAL	POLYAXIAL
$\sigma x = \sigma y \neq \sigma z$	TRIAXIAL	TRIAXIAL
$\sigma x = \sigma y = o$ (constrained)	UNIAXIAL	UNIAXIAL
$\sigma x = \sigma y, \sigma z = o$ (constrained)	BIAXIAL	—

Figure 2.2.1. Stress classification. [After Sawabini
               et al. (1972).]

$$E = \frac{\sigma_z}{\varepsilon_z} = \frac{G(3\lambda + 2G)}{(\lambda + G)} \tag{2-5}$$

$$v = \frac{-\varepsilon_y}{\varepsilon_z} = \frac{-\varepsilon_x}{\varepsilon_z} = \frac{\lambda}{2(\lambda + G)} \tag{2-6}$$

When the sample is stressed hydrostatically, $\sigma_x = \sigma_y = \sigma_z = P$, the resulting deformation is volumetric. The bulk modulus, K_b, is defined in terms of the applied hydrostatic pressure, P, and the volumetric strain, Δ, Equation 2-7 (Jaeger and Cook 1971).

$$K_b = \frac{P}{\Delta} \tag{2-7}$$

where:

$$\Delta = \varepsilon_x + \varepsilon_y + \varepsilon_z$$

When the equal stresses are substituted into equations 2-4 a-c and added, the bulk modulus is expressed in terms of Lame's constant parameters (Equation 2-8). Petroleum engineers are more familiar with the reciprocal of bulk modulus which is the bulk compressibility, C_b, (see Equation 2-9).

$$K_b = 1 + \frac{2}{3}G \tag{2-8}$$

$$C_b = \frac{1}{K_b} = \frac{3}{3\lambda + 2G} \tag{2-9}$$

The five elastic properties (λ, G, E, v, K_b) have been expressed in terms of each other and only two properties are needed to define the other three properties, Table 2.2.2.

2.2.2. Effective Stress

Elastic/mechanical rock properties are directly related to their stress state as discussed in the previous section. Various authors have suggested relationships to define the appropriate stress state of rocks.

Terzaghi (1943) introduced the concept of effective stress in fluid saturated porous media. He defined effective stress, σ_e, as the difference between the normal stress, σ_n, and the neutral stress, σ_w, also called the pore water pressure (Equation 2-1).

$$\sigma_e = \sigma_n - \sigma_w \qquad (2\text{-}1a)$$

or

$$\sigma_e = P_c - P_p \qquad (2\text{-}1b)$$

where:

P_c = Confining pressure

P_p = Pore fluid pressure

Table 2.2.2.
Rock Property Interrelationships
[After Montmayeur (1985)]

CALCULATED PROPERTIES	KNOWN PROPERTIES		
	E, ν	λ, G	K_b, G
G	$\dfrac{E}{2(1 + \nu)}$	—	—
λ	$\dfrac{\nu E}{(1 + \nu)(1 - 2\nu)}$	—	$K_b - \left(\dfrac{2}{3}\right) G$
E	—	$\dfrac{G(3\lambda + 2G)}{(\lambda + G)}$	$\dfrac{9GK_b}{G + 3K_b}$
ν	—	$\dfrac{\lambda}{2(\lambda + G)}$	$\dfrac{\left(\dfrac{3}{2}\right) K_b - G}{G + 3K_b}$
K_b	$\dfrac{E}{3(1 - 2\nu)}$	$\lambda + \left(\dfrac{2}{3}\right) G$	—

He defined it as the effective stress because, "it represents that part of the total stress which produces measurable effects such as compaction or an increase of the shearing resistance" (Terzaghi 1943). This definition applies to fully saturated porous media but other authors suggested stress relationships for both fully and partially saturated samples.

In 1955 Brandt introduced a theory to "explain the influence of pressure, porosity, and liquid saturation through a porous granular medium." In determining the effective pressure for an aggregate of spherical particles, Brandt states that the liquid (pore pressure) should be subtracted from the external confining pressure and explains that this is true due to the exposure of the entire spherical grain to the pore fluid, Equation 2-2a, below.

$$P_e = P_c - P_p \qquad\qquad (2-2a)$$

where:

P_e = Effective pressure

P_c = Confining pressure

P_p = Pore fluid pressure

However, because the grain cement material prohibits the entire irregularly shaped grain in a consolidated sandstone

from being exposed to the pore fluid, Brandt (1955) suggests that Equation 2-1a be modified to Equation 2-2b, below. Brandt (1955) concludes that α, a proportionality constant, should be 1.0 if internal pore pressure, P_P, is less than half of the confining external pressure, P_c. He calculated values from experimental work of 0.86 to 0.88 with an average value for saturated sandstone of 0.87.

$$P_e = P_c - \alpha P_P \qquad\qquad (2-2b)$$

Fatt (1957) calculated pore volume compressibilities as a function of net overburden pressure for his samples. He defined his net overburden pressure to be the same as Brandt's (1955) for effective pressure, Equation 2-2b. Noting that Brandt used $\alpha = 0.85$ to "take into account that the internal fluid pressure does not wholly react against the external pressure." Citing that this factor is structure dependent and thus not constant for all rocks, Fatt(1957) states that α varies from 0.75 to 1.00 for his samples with an average value of 0.85.

Dobrynin (1962) studied the effects of overburden pressure on sandstone using constant pore pressures of atmospheric pressure and 1800 psi while raising external pressure from zero to 20,000 psi. He compared the results

using Brandt's (1955) $\alpha = 0.85$ and found there was
"practically no difference."

While the foregoing definitions of effective pressure
were based primarily on empirical data, Nur and Byerlee
(1971) presented an "exact effective stress law for elastic
deformation of a rock with fluids." They present a
theoretically sound derivation for α for which α is defined
to give the effective pressure for bulk volumetric strain,
Equation 2-2c. This expression for α was proposed at first
by Geertsma (1957) but his derivation was questioned, Nur and
Byerlee (1971).

$$\alpha = 1 - (K/K_S) \tag{2-2c}$$

where:

K = Bulk modulus of dry aggregate (frame)

K_S = Intrinsic bulk moduli of solid (grain)

Garg and Nur (1973) contended that the Nur-Byerlee
(1971) effective stress law is valid only for linearly
elastic porous rocks and that it underestimated pore pressure
effects. They point out that two effective stress laws may
be necessary; one to describe the failure surface and another
to describe stress-strain relationships. The results found
by Brandt (1955), Fatt (1957), and others that α is close to

one are due to the compressibility of the solid grains being
small compared to the compressibility of the dry aggregate.
This derivation assumes the rock is linearly elastic and that
all of the pores are interconnected and the fluid contained
in them is at equilibrium.

Robin (1973) compares the effective pressure law for
bulk volumetric strain (which defines α as in Equation 2-2c)
to a derivation for α (Equation 2-2d) where the variation of
the pore volumes is considered.

$$\alpha = 1 - \left(\frac{\phi K}{K_S - K} \right) \qquad (2\text{-}2d)$$

where:

ϕ = Porosity

K = Bulk modulus of dry aggregate

K_S = Intrinsic bulk modulus of solid

Again, when $K \ll K_S$, the relationship reduces to the
effective pressure law of Equation 2-2a. Robin (1973) used
Nur and Byerlee's (1971) value for porosity and both moduli,
K and K_S, and calculated two values for α, using equations 2-
2c and 2-2d of 0.64 and 0.97, respectively. From this he
concludes that there is no single effective pressure law.
Robin (1973) further concludes that unless it has a simple

form, the concept of effective pressure is not very useful;
when a property is not a linear function of pressure,
effective pressure is not a simple analytical expression.

Christensen and Wang (1985) investigated the relative
importance of pore and confining pressure of Berea sandstone
dynamic elastic properties. They found that the changes in
wave velocities through Berea sandstone samples caused by
change in confining pressure were not canceled by changing
the pore pressure and equal amount. Specifically, bulk
compressibility changes caused by changing the external
confining pressure are undercompensated for by equal changes
in pore pressure (case 1) and Poisson's ratio and shear wave
velocity are over compensated for under the same conditions
(case 2). The authors refer to Equation 2-2e which explains
this phenomena with regard to the definition of effective
pressure.

$$\alpha = 1 - \left[\frac{\left(\dfrac{\partial Q}{\partial P_P}\right)_{P'_d}}{\left(\dfrac{\partial Q}{\partial P_d}\right)_{P'_P}}\right] \qquad (2\text{-}2e)$$

where:

    Q = A physical quantity

    P_d = Confining pressure minus pore pressure

The authors found that for case 1, values of α were less than one and for case 2, values of α were greater that one. The authors attribute this to the presence of highly compressible clays in the Berea sandstone samples.

2.2.3. Compressibility

The isothermal compressibility of a porous rock and its individual components, the pore space and matrix material (grains), must be defined for a specific stress system. Generally, the bulk rock compressibility and the rock matrix compressibility are defined in Equation 2-3a and 2-3b (Geertsma 1957; van der Knaap 1959; Chierici et al. 1967).

Bulk rock: $\quad C_b = \dfrac{-1}{V_b}\left(\dfrac{dV_b}{d\bar{\sigma}}\right)_{P_p}$ $\qquad\qquad$ (2-3a)

Rock matrix: $\quad C_g = \dfrac{-1}{V_g}\left(\dfrac{dV_g}{dP_p}\right)_{\bar{\sigma}\, -\, P_p}$ $\qquad\qquad$ (2-3b)

where:

Pp = Internal pore fluid pressure

$\bar{\sigma}$ = External mean stress

V_b = Bulk volume

V_g = Rock matrix (grain) volume

The compressibility of the pore volume with pressure has been defined in two ways, and it is important to distinguish between them and know which one is being used. Carpenter and Spencer (1940) measured the compressibility of their rocks by keeping the pore fluid pressure constant at atmospheric pressure and increasing the external hydrostatic pressure. The change in pore volume was calculated from the volume of fluid expelled, and the compressibility, C_f, was calculated using Equation 2-4.

$$C_f = - \frac{1}{V_p} \left(\frac{dV_p}{d\bar{\sigma}} \right)_{P_p} \qquad (2\text{-}4)$$

Hall (1953) refers to the compressibility measurement, C_f, made by Carpenter and Spencer (1940) as formation compaction. Hall (1953) calculated the pore volume compressibility, C_p, on his rocks by measuring the change in pore volume, V_p, with the fluid extrusion method. The

external hydrostatic pressure was held constant at 3000 psi
while the internal pore fluid pressure was decreased from
1500 psi in 100-200 psi increments. Equation 2-5 defines
this pore compressibility at the stress conditions which Hall
(1953) called "effective reservoir rock" compressibility.
Hall (1953) attributed the difference between C_f and C_p to the
rock expansion caused by the expansion of the rock grains
with pressure decrease.

$$C_p = - \frac{1}{V_p} \left(\frac{\partial V_p}{\partial P_p} \right)_{\bar{\sigma}} \qquad (2\text{-}5)$$

Van der Knaap (1959) defines the bulk volume
compressibility, C_b, to be the "change in bulk volume per
unit change in effective hydrostatic tension on the frame
$(\sigma - \bar{\sigma})$, the pore fluid tension (σ) remaining constant"
(Equation 2-6a). This reduces to Equation 2-6b with the
constant pore fluid pressure state.

$$C_b = - \frac{1}{V_b} \left(\frac{\partial V_b}{\partial (\sigma - \bar{\sigma})} \right)_{\bar{\sigma}} \qquad (2\text{-}6a)$$

$$C_b = \frac{1}{V_b} \left(\frac{\partial V_b}{\partial \bar{\sigma}} \right)_{\sigma} \qquad (2\text{-}6b)$$

Similarly, he defines pore compressibility, C_p, as "the
fractional change in pore volume per unit of change in
effective hydrostatic tension $(\sigma - \bar{\sigma})$, the pore fluid
tension (σ) remaining constant" (Equation 2-7a). Again, this
equation is reduced to Equation 2-7b with the constant pore
fluid pressure state.

$$C_p = -\frac{1}{V_p}\left(\frac{\partial V_p}{\partial(\sigma - \bar{\sigma})}\right)_{\bar{\sigma}} \qquad (2\text{-}7a)$$

$$C_p = \frac{1}{V_p}\left(\frac{\partial V_p}{\partial\bar{\sigma}}\right)_{\bar{\sigma}} \qquad (2\text{-}7b)$$

Van der Knaap (1960) presents data showing that the
relative volume change in both rock bulk and pore
compressibility are linear if pore pressure is varied at the
same magnitude and rate as the external pressure. However,
nonlinear relationships result if the change in pore or rock
volume is measured only as a function of the external stress.
This paper is an excellent reference for compressibility
measurements on porous rocks.

Marek (1973) presented two correlations for predicting
the pore compressibility, C_p, for consolidated sandstones
Equation 2-8a and, for limestones, 2-8b. This work is based
on van der Knaap's (1960) and provides the plots of

$$\left(1 - \frac{d\bar{\sigma}}{d\sigma}\right)$$

versus pressure for sandstone and limestone reservoir rock.

Sandstones: $Cp = \dfrac{877}{(\sigma - \bar{\sigma})^{0.7}} \left(1 - \dfrac{d\bar{\sigma}}{d\sigma}\right) \cdot 10^6 \ psi^{-1}$ (2-8a)

Limestones: $Cp = \dfrac{36.36}{(\sigma - \bar{\sigma})^{0.58}} \left(1 - \dfrac{d\bar{\sigma}}{d\sigma}\right) \cdot 10^6 \ psi^{-1}$ (2-8b)

where:

$$\left(\sigma - \bar{\sigma}\right) = (P_{ob} - P_i) + \left(1 - \frac{d\bar{\sigma}}{d\sigma}\right)(P_i - P)$$

P_{ob} = Overburden pressure (psi)

P_i = Initial pore fluid pressure (psi)

σ = Pore fluid pressure (psi)

$\bar{\sigma}$ = Effective mean stress (psi)

P = Pore fluid pressure after production (psi)

Marek (1973) also provides useful values for rock matrix compressibility, C_g, for consolidated sandstones (Equation 2-

9a) and limestones (Equation 2-9b) which were originally

measured by van der Knaap (1960).

Sandstones: $C_g = 0.186 \cdot (10^{-6})$ psi^{-1} (2-9a)

Limestones: $C_g = 0.096 \cdot (10^{-6})$ psi^{-1} (2-9b)

The effective pore compressibility can be calculated by

subtracting C_g from C_p (van der Knaap 1960; Marek 1973).

It becomes obvious that the current usage of isothermal

compressibility of the bulk rock, the pore volume, or the

matrix material must be well defined. For this research, all

measurements were made with constant internal atmospheric

pore pressure, P_p, with varying external hydrostatic stress,

$\bar{\sigma}$, for both the unconsolidated cores and for the consolidated

rock samples (Equation 2-10a and 2-10b). Rock matrix

material compressibility is as defined by Geertsma (1957),

van der Knaap (1959), Chierici et al. (1967), and Equation 2-

10c.

Pore Compressibility: $C_p = -\dfrac{1}{V_p}\left(\dfrac{\partial V_p}{\partial \bar{\sigma}}\right)_{P_p}$ (2-10a)

Rock Bulk Compressibility: $C_b = -\dfrac{1}{V_b}\left(\dfrac{\partial V_p}{\partial \bar{\sigma}}\right)_{P_p}$ (2-10b)

Rock matrix (grain)

Compressibility:
$$C_g = - \frac{1}{V_g} \left(\frac{\partial V_g}{\partial \bar{\sigma}} \right)_{P_p} \qquad (2\text{-}10c)$$

where: V_p = Pore volume

V_b = Bulk volume of rock

V_g = Matrix material (grain) volume

$\bar{\sigma}$ = External mean stress, $(\sigma_x + \sigma_y + \sigma_z)/3$

P_p = Internal pore fluid pressure

2.2.4. Predicting Formation Compaction from Laboratory Hydrostatic Compressibility Test Data

Uniaxial compaction, axial stress imposed on a confined test sample, best models reservoir compaction conditions during depletion. The net effective stress increases as the pore fluid pressure declines and the formation compacts as the rock grains expand. Almost all of the compaction is in the vertical direction because the rock surrounding the formation prohibits lateral strain. This is especially true for reservoirs in which the areal dimension greatly exceeds the reservoir thickness. Most laboratory tests are performed under hydrostatic or triaxial stress conditions and researchers are working on methods to use hydrostatic and these data to predict reservoir compaction.

From elastic theory, uniaxial compaction, U_z, the relative change in the thickness of the reservoir, is related to the reduction in pore fluid pressure, ΔP, and the uniaxial compaction coefficient, C_m, with Equation 2-11 (Geertsma 1966; Teeuw 1971). This equation was derived for linear elastic behavior and must be generalized for appropriate application to the analysis of porous media.

Linear: $Uz = C_m\Delta P$ (2-11)

where:

$$C_m = \frac{1}{3}\left(\frac{1 + v}{1 - v}\right)(1-\beta)\ C_b$$

v = Poisson's ratio

C_b = Bulk compressibility

$\beta = C_{ma}/C_b$

C_{ma} = Rock matrix compressibility

Scorer and Miller (1974) present an application of Geertsma's (1966) linear formula, Equation 2-12, that was used to predict surface subsidence as a result of formation compaction at Long Beach, California. (Further discussion of the application in surface subsidence prediction is found in Section 2.7.1.)

Linear: $U_z(0,0) = -2(1-v)\ C_m \cdot h \cdot \Delta P \left\{1 - \dfrac{C}{\sqrt{1 + C^2}}\right\}$ (2-12)

where: $U_z(0,0)$ = Subsidence at the center of the disc-
                     shaped reservoir

           $C = d/r$

           d = Depth of reservoir

           r = Radius of reservoir

           C_m = Uniaxial compaction coefficient = $\dfrac{1}{V_b}\left[\dfrac{\delta V_p}{\delta p}\right]$

           h = Thickness of the reservoir

The uniaxial compaction coefficient can be determined
using three testing methods: 1) the oedometer test cell in
which a sample is subject to axial compaction wherein the
cell prohibits lateral deformation; 2) a triaxial cell test
in which the sample is subject to axial compaction and
lateral deformation is prevented through application of the
corrected radial stress; and 3) a combination of hydrostatic
testing and estimation of Poisson's ratio to calculate the
uniaxial compaction coefficient. Teeuw (1971) investigated
the three methods for consolidated rock samples to determine
which provided the best compaction data for predicting
in-situ reservoir compaction. His work showed that the
oedometer was not a good method to use on consolidated
samples because incorrect placement of the core in the cell
could lead to "uncontrollable" crushing of the sample. Work
by Roberts and de Souza (1958) on unconsolidated sand in an

oedometer cell showed crushing of sand grains at pressures as
low as 4500 psi.

The stress-strain relationship is generally nonlinear
for porous media and the nonlinear relationship between
hydrostatic normal stress, σ_e, and uniaxial compaction, U_z, is
expressed in Equation 2-13. In this equation, a and n are
empirically derived constants and it is assumed that
Poisson's ratio is constant and the atmospheric pore pressure
is also constant.

$$\text{Nonlinear:} \qquad U_z = \frac{1}{3}\left(\frac{1+\nu}{1-\nu}\right) a\ \sigma_e^{\,n} \qquad\qquad (2\text{-}13)$$

For triaxial tests Poisson's ratio can be related to the
axial, σ_a, and lateral, σ_l, stresses with the following
expression (Equation 2-14). Again, n is the empirically
derived constant which is the same value as for Equation 2-13.

$$\frac{\sigma_a}{\sigma_l} = \left(\frac{n}{1-n}\right)^{\frac{1}{n}} \qquad\qquad (2\text{-}14)$$

For consolidated sand samples, Teeuw (1971) concluded
that to best measure the uniaxial compaction the
investigation should: 1) make hydrostatic compaction
measurements on samples, and 2) measure the uniaxial

compaction with the triaxial cell equipment to measure

Poisson's ratio. From these data the uniaxial compaction can

be calculated with Equations 2-13 and 2-14, above.

Most recently, Andersen and Jones (1985) and Andersen

(1985) investigated the relationship between hydrostatically

measured compressibility and uniaxial-strain pore volume

compressibility using nonlinear theory noting that the

hydrostatic compressibility can be twice as large as uniaxial

compressibility. Their experiments showed that the power-law

model could be used to related uniaxial and hydrostatic

strain and that uniaxial strain, ε_z, could be predicted from

hydrostatic strain data with Equation 2-15. They also

present a mean stress approximation to account for non-

linearity which also uses the power law exponent, n.

Nonlinear: $\varepsilon_z = \alpha Ah \ (\sigma_z{}^n - \sigma_0{}^n)$ (2-15)

where:

A,h,n = Empirical constants from hydrostatic data

$\alpha = 0.74$

σ_0 = stress at initial condition

Their results showed that for consolidated samples their

power law model technique was very successful in predicting

uniaxial compaction from hydrostatic test data as compared to

actual uniaxial data. For friable sandstone, however, their
method tends to under predict the magnitude of uniaxial
compaction from hydrostatic data.

2.3. Static Tests

Static tests of rock properties refers to those methods
in which rock sample cores are subject to external stress
under uniaxial, biaxial, triaxial or hydrostatic conditions.
The deformation of the sample under the imposed stress
conditions is measured and the appropriate rock elastic
properties can then be determined. Because the elastic
properties, E, v, λ, G, and K_b are defined under specific test
conditions not all of these parameters can be determined from
each of the aforementioned stress testing conditions.
Computational methods are available to translate hydrostatic
and triaxial data to uniaxial in some cases.

2.3.1. Static measurement apparatus

There are three types of pressure cells generally used for measuring rock static properties; the oedometer, the triaxial or biaxial cell, and the hydrostatic cell. In most cases the triaxial cell is capable of performing hydrostatic tests also.

The oedometer is simply a thick walled cell fitted with a piston on top and a fluid release valve near the bottom. It is designed for measuring the uniaxial (z-direction) compaction with zero lateral deformation, also known as a constrained uniaxial test system. The oedometer has long been used in soils testing and for determining reservoir and soil compaction.

The triaxial cell allows the axial (z-direction) stress to be varied independently from the radial or confining stress (x- and y-directions). In a triaxial cell special cases of uniaxial confined stress tests, also performed with an oedometer, can be performed by adjusting the confining stress to prohibit lateral deformation. Using the triaxial cell for the constrained uniaxial test is better than an oedometer for consolidated rocks (Teeuw 1971). The triaxial cell can also be used to perform uniaxial unconfined stress tests in which the rock sample is stressed in the axial

direction with zero confining stress to permit lateral
deformation. Both Young's modulus and Poisson's ratio are
defined under uniaxial unconfined stress conditions. The
triaxial cell can be used to perform hydrostatic tests for
which the axial and confining stresses are equal. Of course,
the triaxial cell can also be used to test rock samples under
varying conditions of axial and confining stress.

The hydrostatic test cell exerts equal stress on all
sides of the sample. Bulk modulus, the reciprocal of bulk
compressibility, is defined for conditions of hydrostatic
stress.

2.3.2. Effects of temperature

Researchers have investigated how different temperatures
effect rock properties because reservoir temperatures are
much higher than typical laboratory temperatures. Carpenter
and Spencer (1940) performed most of their compressibility
tests at 91°F but for two Woodbine sandstone samples, tests
were run at a higher temperature, 146°F. Results for one
core showed that compressibility at 91°F was greater than at
146°F but for the other core the compressibility was lower at
91°F than at 146°F and they concluded that there was no

apparent relationship between temperature and compressibility at pressures below 8000 psi.

Von Gonten and Choudhary (1969) studied the effects of temperatures as high as 400°F on the pore volume compressibility of reservoir rock. They noted an average of 21 percent increase in pore volume compressibility at 400°F compared to room temperature. The pore volume compressibility was 55 percent higher at 400°F than at 75°F for one sample.

Newman (1973) performed most of his compressibility measurements at 74°F but did perform some at temperatures between 130°F and 275°F. His results were inconclusive but he recommended, based on the work of Von Gonten and Choudhary (1969), that measurements of compressibility should be made at reservoir temperature.

Morita et al. (1985) measured rock deformation, permeability, electrical resistivity, compressional and shear wave velocities, change in pore volume and deformation on Berea sandstone for varying stress load paths at temperatures between 70°F and 380°F. They found that temperature effects were similar to effects caused by pore pressure changes; both distort the rock uniformly. However, because high temperatures decrease the rock grain rigidity, temperature caused greater changes in rock properties. Their results

showed that stress-strain curve hysteresis was reduced after temperature cycles and strain was reduced because of temperature induced rock expansion. Results were inconclusive as to whether or not higher temperatures contributed to increased permeability because of the difficulty associated with estimating the change in the fluid viscosity with temperature.

In their uniaxial compaction tests for modeling non-linear reservoir compaction, de Waal and Smits (1985) did not find significant differences in compaction at 20°C (68°F) and 90°C (194°F). Aktan and Farouq Ali (1975) performed tests to determine the effects of cyclic and in-situ heating on absolute permeability, elastic rock properties and electrical resistivities of Berea, Boise, California and Tennessee sandstones. The greatest damage to the rock structure is caused during the first heating cycle. Effects from subsequent heat cycling were negligible. The electrical resistivity on the four sandstones decreased with increased heating temperatures and the permeability of the Berea and Boise samples increased with higher temperatures.

2.3.3. Effects of load cycling

Because elastic theory is applied to model the behavior of porous media under imposed stress conditions, it would be particularly advantageous if rocks did indeed exhibit elastic behavior. However, this is not generally the case. Not only is their behavior inelastic, but significant hysteresis also occurs during stress loading and unloading cycles. Researchers have found that the degree of elasticity and compressibility in rock behavior is a function of the number of times a rock sample is subject to stress loading cycles, the magnitude of stress imposed, and the stress rate. There is no general agreement as to which is the "best" way to stress the sample, at what rate, and how many times so that its behavior during laboratory tests most closely models reservoir behavior.

Fatt (1957) wrapped his fluid filled cores in copper jackets and subjected them to an external hydrostatic pressure of 10,000 psi for several hours to form the jacket tightly around the core sample. The pressure was released during which time he assumed they were recovering their initial pore volume, and compressibility test runs were performed. Fatt (1957) found that for his unconsolidated

sand samples, he had to apply 15 cycles of external pressure
to 2000 psi to remove hysteresis effect.

Newman (1973) did some interesting work with
unconsolidated sand and samples by comparing the effects of
hydrostatic loading on two sets of unconsolidated sand
samples. One set consisted of carefully handled cores
recovered in rubber sleeve core barrels and frozen on site
and were kept frozen until testing to help preserve grain
arrangement. The other set was from the same core but was
purposely disturbed to rearrange the grains. He found that,
although the rearranged sample showed higher initial
compressibility than the undisturbed sample, cycling the
disturbed sample returned it to in-situ grain packing
conditions and that cycling caused significant internal
failures (Newman 1973). During his compressibility tests for
unconsolidated sands, the cores used were those of the first
set, carefully handled and frozen prior to testing. His
results showed that during the compressibility test
pressurization cycles, the cores exhibited inelastic behavior
with permanent reduction in volume which resulted, at least
in part, from internal grain failure. His compressibility
tests on both consolidated and unconsolidated samples were
obtained during the first stress cycle.

Teeuw (1971), in hydrostatic laboratory tests to predict formation compaction, found that it was not until after the first hydrostatic cycle that his core samples exhibited elastic behavior. De Waal and Smits (1985), who also modeled reservoir compaction, use the first cycle uniaxial compressibility in their model. Their work also showed that initial compressibility was a function of the rate of stress imposed; high stress rates resulted in low initial compressibility and low stress rates resulted in high initial compressibility for both consolidated and unconsolidated samples.

Mattax and Clothier (1974) investigated uncertainties associated with core analysis of friable and unconsolidated sands. Included among the areas of core analysis they researched was the question of whether or not unconsolidated sand cores can be recovered without disturbance and the question of whether or not first cycle compaction is meaningful. They found that, in regard to the significance of first cycle compaction data, their cores exhibited very large first cycle compaction. Previously this phenomena was attributed to grain crushing but their test did not show this. They define a dual component compaction system; an instantly recoverable purely elastic strain component and a slowly recoverable time dependent visco-elastic strain

component. They have strong evidence that first cycle
compaction is "a realistic reservoir phenomenon" but the lab
measured value is too high due, in part, to laboratory
procedure induced systematic error. They suggest that the
first cycle compressibility values are usable when multiplied
by $\frac{2}{3}$ to take the systematic error into account. They found
that the hysteresis loop does not close during the first
cycle but in the second and third cycles hysteresis was
nearly eliminated and sample compaction was almost
reversible.

Botset and Reed (1935) performed constrained uniaxial
compaction test on 30/40 mesh saturated sand in an oedometer
apparatus. They applied a 1000 psi load to the sample and
let it come to equilibrium, for a period of approximately two
hours, before increasing the pressure by another 500 psi,.
This was repeated until the uniaxial pressure was 3025 psi at
which time the pressure was held constant for 18 hours. This
cycle was repeated 6 more times. Their results showed that
porosity was reduced from 41.2 to 36.6 percent and that 8
percent of the sand grains were crushed. They attributed the
continued decrease in porosity with each cycle and the
hysteresis to the grain crushing.

Roberts and de Souza (1958) ran uniaxial constrained
compressibility tests on well and poorly-sorted Ottawa sand

samples; some dry, some saturated. They found that at high
pressure the sands were more compressible than at lower
pressures. They attributed this to the shifting and rolling
of sand grains at low pressures and the shattering and
crushing of grains at higher pressures. The pressure at
which the dry sand sample grains began to shatter was lower
for the uniform grain size samples, 4000 psi, than it was for
the well-sorted samples, 7500 psi, showing that the initial
pressure for grain failure breakdown is a function of the
initial sample porosity.

2.3.4. Effects of time

Researchers have observed a "creep" or time-lag effect
in rock samples under stress (Roberts and de Souza 1958;
Brighanti 1972; Newman 1973; Montmayeur 1985; Dunn 1986).
Newman (1973) noted that during his compressibility tests,
most significant volume changes occurred during the first few
minutes of stress application and that 30 minute pressure
increments were usually sufficient for stress equilibrium
from a practical standpoint. He observed that "the true
stress equilibrium cannot be obtained in the laboratory in

any practical time" (Newman 1973) but did not investigate time effects further.

Roberts and de Souza (1958) observed, during compressibility tests on both uniform sand samples and graded samples, that at low pressures, the sands are fairly incompressible and the compression is the result of elastic grain compression and grain crushing at contact points. They found that once the intergranular stress meets or exceeds the critical stress, time lag becomes more important: "At pressures above the critical pressure the time lag is due to a continuing process: there is a gradual build-up of stress on individual grains resulting in shattering, a redistribution of stress occurs followed by a stress build-up and shattering of other grains." Further, their work showed that at low pressure the time lag is due to a continuing process of grain rearrangement which is dependent on the sample density.

Montmayeur (1985) found that for unconsolidated samples, the elastic rock properties were a function of time. Dunn (1986) also reported a time lag creep effect with his rock testing.

Mattax and Clothier (1974) reported that the large first cycle compaction was not readily attributable to grain crushing. They also found that a rock will return to its

initial unloaded state after a period of time following a
load-unload stress cycle and they define a dual-component
system for rock compaction. These components are 1) an
instantaneously recoverable purely elastic strain and 2) a
slowly recoverable time dependent viscoelastic component.

De Waal and Smits (1985) noted time-effects in their
uniaxial compressibility tests. Results showed that the
initial compressibility is lower for high stress rates and
that the initial compressibility is higher for low stress
rates.

2.3.5. Effects of stress

Rock properties are significantly effected by the
induced stress. Wilhelmi and Somerton (1967) measured pore
and static elastic rock properties of sandstone under
triaxial stress conditions. Their tests were on Boise,
Bandera and Berea sandstones at several confining pressures
and axial stress to 80 percent of their failure stress. They
found that permeability and porosity reductions were greater
for rock under hydrostatic stress conditions than they were
under triaxial stress conditions. Porosity reduction under
triaxial loading was small, 5-8 percent of the original

unstressed value, but permeability reduction was much higher under triaxial loading, 10-20 percent for Berea and Bandera samples and 65 percent for the Boise samples. Most of the reduction occurred in porosity and permeability during the hydrostatic loading cycle prior to the triaxial test. Using strain gauges to calculate elastic moduli under triaxial stress, they found that shear and Young' moduli increased with confining pressure but, although Poisson's ratio increased with axial stress, it showed no consistent change with confining pressure.

Van der Knaap (1959) notes that to accurately describe volume changes in porous rocks, the bulk and pore volumes must be known functions of pore fluid and hydrostatic pressure because the relationships describing volume changes are nonlinear. While linear approximations of this relationship can be made for small incremental stresses and strains, van der Knaap presents data showing the effects of large incremental changes in stress.

Dobrynin (1962) shows that pore pressure determines physical property changes in sandstone rocks under overburden pressure. Further, the maximum pore compressibility and net overburden pressure can be used to calculate the pore compressibility, and net overburden pressure can be used to calculate the pore compressibility of sandstones for

pressures up to 20,000 psi. He presents a relationship, shown in Equation 2-16, relating bulk compressibility to pressure.

$$C_b = \left[\phi \, \frac{C_P^{max}}{\log \left(\frac{P_{max}}{P_{min}} \right)} \, \log \frac{P_{max}}{P} \right] + (1 - \phi) C_r \qquad (2-16)$$

where:

C_b = Bulk compressibility

ϕ = Porosity

P = Effective pressure for α = 0.85

P_{max} = Empirically between 25,000 and 30,000 psi

P_{min} = Empirically between 0 and 300 psi

C_P^{max} = Maximum pore compressibility

C_r = Rock matrix compressibility

Gray et al. (1963) studied the effect of stress on the permeability of Berea, Boise and Grubb sandstone cores. They showed that the permeability anisotropy of their samples was a function of overburden pressure and that for cylindrical samples subjected to mechanical stress the reduction in permeability with pressure is a function of the radial stress divided by the axial stress ratio. Their results also show that the reduction in permeability under hydrostatic (uniform) stress is greater than the reduction in permeability under nonuniform (triaxial) stress and that laboratory measurements of permeability reduction under

hydrostatic stress will be greater than the in-situ
permeability reduction.

Kumar (1976) reports that increases in Poisson's ratio
with pressure are usually small but that in certain cases it
can be significant. If Poisson's ratio is used to calculate
other rock properties such as Young's modulus or bulk
compressibility, it is necessary to have an accurate
measurement of Poisson's ratio.

2.3.6. Effects of saturation

Although the effects of saturation on dynamic rock
properties has been extensively researched (see section
2.4.6. of this study), the effect of pore fluid on static
elastic properties is small. Because of the relative ease of
measuring rock properties on dry core samples compared to
fluid saturated samples many laboratory measurements are made
on dry samples and the results are then applied to fully or
partially saturated reservoir formations. Mann and Fatt
(1960) investigated the effects of pore fluids on elastic
properties of Berea, Boise, and Bandera sandstone. Their
results showed that bulk compressibility increased by 10 to
30 percent, Young's modulus decreased by 8 to 20 percent and

Poisson's ratio for Berea and Boise samples change a small amount when saturated with an aqueous solution. The Bandera sample showed a 100 percent increase in Poisson's ratio with saturation which was due to its high clay content.

2.4. Dynamic Rock Properties

2.4.1. General Discussion

Laboratory dynamic rock properties are derived from longitudinal, also known as p- or compressional, and shear, also known as s- or transverse, wave velocities using pulse techniques: a transducer generates the waves which travel through the rock and are received by another transducer. In the field, when a compressional wave is triggered downward into the earth, as in seismic exploration work, the p-wave energy travels straight downward. As it reaches the different subsurface interfaces, it vibrates and sends out new p-waves in all directions: the compressional energy acts like a hammer blow as it hits the interface and causes vibrations. When the p-wave encounters an angled interface, the sideward component of the wave induces s-waves (Coffen 1986).

Compressional waves comprise alternating compressions and decompressions. The rock particles vibrate backward and forward as the wave travels and the direction of p-wave propagation is in the same direction as the particle direction of motion. Compressional waves are alternating oscillations of the medium they travel through so they travel slower through gas than they do through rock. Velocity of p-waves is also a function of both the density and compressibility of the pore fluid.

In contrast, as a shear wave travels, the particles vibrate from side to side and are refracted and reflected like any other wave. S-waves do not travel through fluid as do p-waves and the velocity of s-waves is a function of the pore fluid density. Instead, shear waves travel through rock bypassing the pores and are only slightly affected by the pore fluid in the rock. Shear waves travel slower than compressional waves and the ratio of p-wave to s-wave velocity can be used to identify formation lithology, see section 2.4.3.

The fact that longitudinal waves will travel through rock and fluid whereas shear waves will only travel through rock does not cause problems in the laboratory, but does when measuring velocities in the well bore. As shown in Figure

2.4.1, the p-wave is generated at point A by a transducer. When the p-wave reaches the well bore fluid-casing interfaces at point B, an s-wave is generated from the p-wave. Both waves travel through the formation to point C, the casing-well bore interface. The p-waves arrive first at point C because they have a greater velocity in the formation rock and fluid and the s-waves only travel through the rock. The p-wave continues through the well bore fluid to the receiving transducer, point D, and the p-wave velocity is recorded there. The s-waves, however, cannot continue traveling to the receiver because the s-wave cannot travel through the wellbore fluid. Sidewall wireline logging tools are being developed to alleviate this problem: if the acoustic tool is held against the well bore casing, both the shear and compressional waves should reach the receiver. Figure 2.4.1 is only a schematic drawn to show the wave paths and it does not imply that s-waves travel farther out into the formation.

To further complicate matters, s-wave velocities are affected by the degree of grain-to-grain contact in the sand. As a result, the less compacted the sand, the greater the wave attenuation. This dampening and weakening of waves, affected by other factors including fluid density, distribution and saturation and microfractures also occurs to a lesser degree for p-waves.
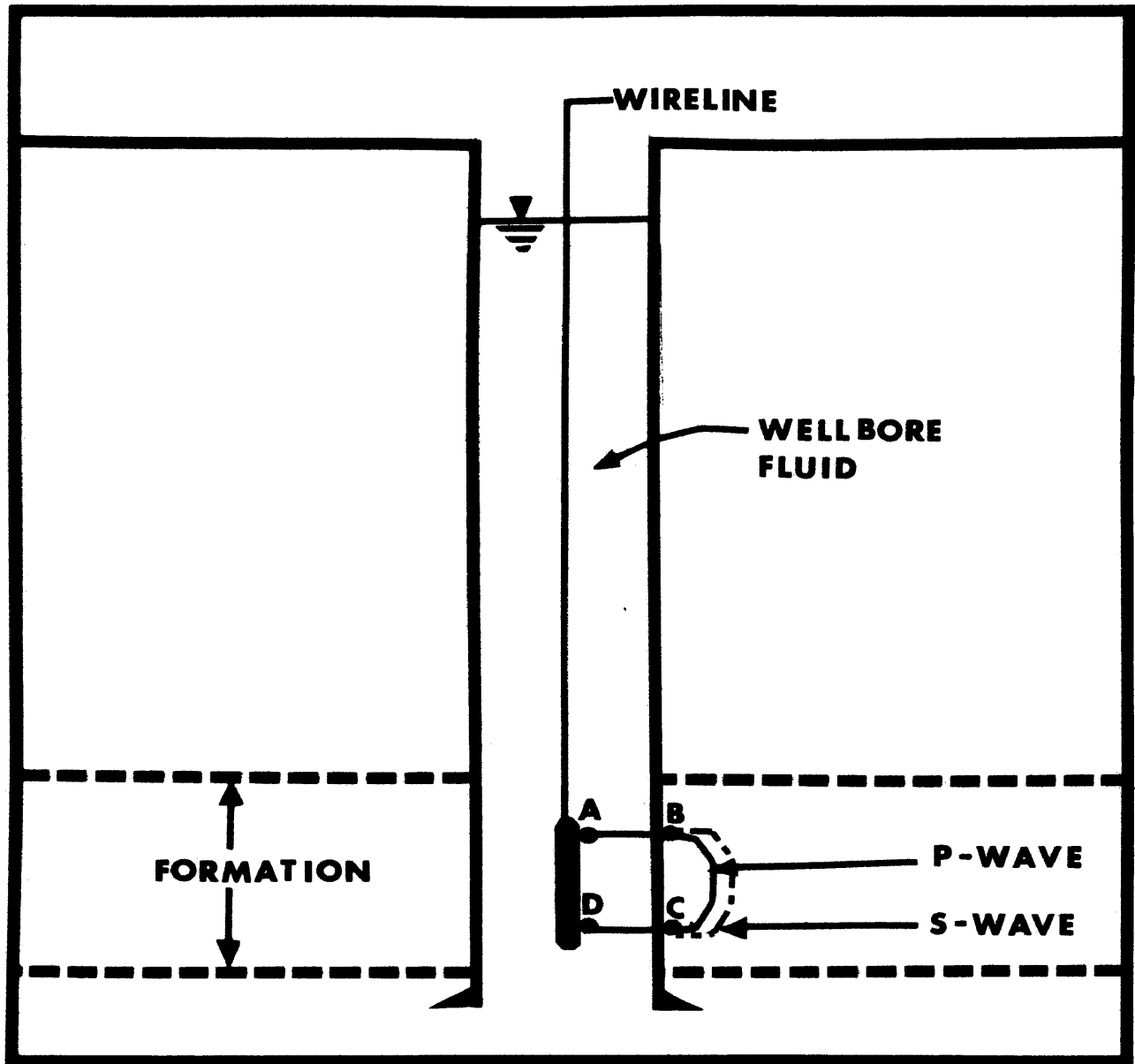
Figure 2.4.1.   P- and s-wave paths from wave generation
               to wave receiver.

Shear wave attenuation is one of the major factors and
sources of problems in unconsolidated sand research. When
laboratory test pressures are high, grain-to-grain contact is
very good and both p- and s-waves can be detected. At lower
pressures, the contacts are not as good and the shear waves
are severely attenuated. This becomes a problem for
unconsolidated sands which are typically found in low
pressure reservoirs. Also, as an unconsolidated sand is
stressed at constant pressure, the individual grains realign
themselves and the wave velocity changes as the grain-to-
grain contact geometry changes. This results in the time
related "creep" effect noted by Montmayeur (1985) and Dunn
(1986).

2.4.2. Elastic rock properties from dynamic measurements

The velocities of the shear wave (V_s) and the
longitudinal wave (V_p) can be used to calculate elastic rock
properties. The velocity of the longitudinal wave is related
to the bulk density, ρ_b and (λ + 2G) by Equation 2-17a.
(λ+2G) is also refered to as the combined modulus.
Similarly, the shear wave velocity is related to the shear
modulus, G, and the bulk density with Equation 2-17b.

$$V_P = \frac{1}{\Delta t_P} = \sqrt{\frac{\lambda + 2G}{\rho_b}} \qquad (2\text{-}17\text{a})$$

$$V_S = \frac{1}{\Delta t_S} = \sqrt{\frac{G}{\rho_b}} \qquad (2\text{-}17\text{b})$$

where:

Δt_P = Longitudinal wave travel time

Δt_S = Shear wave travel time

All of the five dynamic (annotated with subscript "D")
elastic constants can be determined from the measurements of
bulk density and shear and longitudinal wave travel times as
outlined below. Rearrangement of Equations 2-17a and b gives
Equations 2-18a and b, with appropriate units.

Shear Modulus: $G_D = 1.34 \cdot 10^{10} \dfrac{\rho_b}{\Delta t_S^2}$ (2-18a)

$(\lambda + 2G)_D = 1.34 \cdot 10^{10} \dfrac{\rho_b}{\Delta t_P^2}$ (2-18b)

for: G_D and $(\lambda + 2G)_D$ in psi

ρ_b in gm/cc

Δt_P in μsec/ft

Δt_S in μsec/ft

Substitution of 2-18a into 2-18b results in an equation for λ (Equation 2-18c).

Lame's Coefficient: $\lambda_D = 1.34 \cdot 10^{10} \, \rho_b \left(\dfrac{1}{\Delta t_P{}^2} - \dfrac{2}{\Delta t_S{}^2} \right)$ (2-18c)

Having now defined two elastic constants, the other three can be calculated using Equations 2-18d, e, and f.

Poisson's Ratio: $\quad \nu_D = \dfrac{\lambda}{2(\lambda + G)} = \dfrac{0.5 - \left(\dfrac{\Delta t_P}{\Delta t_S}\right)^2}{1.0 - \left(\dfrac{\Delta t_P}{\Delta t_S}\right)^2}$ (2-18d)

Young's Modulus: $\quad E_D = \dfrac{G(3\lambda + 2G)}{\lambda + G}$ (2-18e)

Bulk Modulus: $\quad K_D = \lambda + \left(\dfrac{2}{3}\right) G$ (2-18f)

Researchers have found that the shear and longitudinal wave velocities are affected by pressure, temperature, different pore fluids, fluid saturation, porosity, and lithology, which accordingly will affect the elastic dynamic rock properties. The effect of each of these parameters on shear and longitudinal wave velocities will be discussed.

2.4.3. Effects of lithology

Acoustic wave velocities and the ratio of longitudinal to shear wave velocity are a function of rock lithology. Measurements of wave velocity have been made through hard rocks (Keller 1981) and typical petroleum reservoir rocks including sandstone, limestone and dolomite (Pickett 1963; Domenico 1984). Attempts have been made to identify formation porosity and lithology from wireline log measurements of longitudinal and shear waves. Frost and Fertl (1982) devised an unconventional approach for determining s-wave velocity from a combination of measured p-wave velocity and nonacoustic well log data.

Keller (1981) measured acoustic, mechanical and electrical properties on an assortment of low porosity rocks including schist, gneiss, metarhyolite, and granite. He observed a "pronounced correlation" between compression strength and density, dielectric constant and acoustic wave travel times. However, he suggests using caution when "inferring rock conditions from geophysical measurements" because a large percentage of his data contradicted his observed correlations.

Domenico (1984) studied Pickett's (1963) laboratory

measured values of shear and longitudinal wave velocities

through dolomite, limestone, and sandstone and the laboratory

measured porosity for the limestone and sandstone samples

under differential pressure from 500 to 6000 psi. He found

that the range of p-wave velocity to s-wave velocity ratios

for the ninety percentile data grouping were as follows:

V_p/V_s	Lithology
1.58 - 1.75	Sandstone
1.78 - 1.84	Dolomite
1.84 - 1.98	Limestone

Domenico (1984) attributes the ratio differences to the

differences in s-wave velocities for the samples because the

p-wave velocities and the densities of the sandstone,

dolomite and limestone are very close. Using the Wyllie

(1956, 1958) time average equation (see section 2.4.6 of this

study), Equation 2-19a, and Pickett's (1963) wave velocity-

porosity equation, Equation 2-19b, Domenico (1984) determined

A and B, constants for a given rock type.

$$\frac{1}{V_P} = \frac{\phi}{V_W} + \frac{(1 - \phi)}{V_m} \qquad\qquad (2\text{-}19a)$$

where:

V_P = P-wave velocity

V_W = Velocity through fluid

V_m = Rock matrix velocity

ϕ = Porosity

$$\frac{1}{V} = A + B\phi \tag{2-19b}$$

where:

V = P- or s-wave velocity

A,B = Constants

Domenico explains that A is a function of the matrix velocity and B is a function of the differential pressure, consolidation, and pore geometry. He shows that Equations 2-19a and 2-19b are equal when $A = \frac{1}{V_m}$ and $B = \left(\frac{1}{V_W}\right) - \left(\frac{1}{V_m}\right)$. His analysis shows that for sandstones the s-wave velocity is more sensitive to porosity than the p-wave velocity and the difference in p- and s-wave velocity appears to be a good porosity indicator for sandstone but probably not for limestone.

Hicks and Berry (1955) observed that acoustic velocity is a function of the sand-shale content of the formation. They noted that the acoustic velocity can be used to help

identify the shaliness of a formation; shale layers have a
lower velocity than do sand layers with shaley-sand layers
having intermediate velocities. They note that some
exceptions to this trend can be found in young, shallow
formations.

Frost and Fertl (1982) present a method for estimating
the shear wave travel time from a combination of longitudinal
wave travel time, $(\Delta t_P)_{log}$, from acoustic logs and non-
acoustic well log data. Using Pickett's (1963) experimental
data for shear and longitudinal wave travel times for
sandstone, dolomite, and limestone together with a
relationship they developed for shear wave divided by
longitudinal wave travel times, $\dfrac{\Delta t_S}{\Delta t_P}$, with porosity, Frost and
Fertl (1982) developed another relationship, Equation 2-20
below, from which shear wave travel time can be estimated,
$(\Delta t_S)_e$.

$$(\Delta t_S)_e = \left(\frac{\Delta t_S}{\Delta t_P}\right) \cdot (\Delta t_P)_{log} \qquad\qquad (2-20)$$

The authors use a "back-door" approach to derive the $\left(\dfrac{\Delta t_S}{\Delta t_P}\right)$
relationship for anisotropic shales and shaley sands using
Poisson's ratio and contend that the estimated shear wave

travel times are reasonably accurate for sand-shale
sequences.

Wilkens et al. studied the effects of clays on the
compressional wave velocity and porosity on 20 dry sandstone
samples with varying clay content at 0.5 kbar (7300 psi).
They measured the compressional wave velocity through the
samples and compared them to the velocity modeled using
aspect ratios determined from observed pore geometry from
scanning electron microscope (SEM) thin sections. The aspect
ratio is the ratio of microcrack length to width. They found
that the modeled and measured wave velocities agreed to
within 10 percent, that the presence of clays in the pores
acts to reduce the porosity but not the pore space, and thus
clay rich sandstone samples at a specified porosity have
larger pore space and a correspondingly lower velocity. They
compared the sample SEM porosity and measured compressional
wave velocity to the porosity calculated from the Wyllie time
average equation using the compressional wave velocity and
found that the SEM measured porosity values were consistently
lower than those predicted by the Wyllie time average
equation and attribute this to the presence of clays in the
pore space.

The authors also compared porosity values measured using
an air pycnometer and those observed using the SEM and found

that "the actual void volume within microporosity zones is approximately 50 percent." Finally, they conclude that "when considering two dry samples of equal porosity, one containing clay and one with no pore space filling, the lower velocity of the clay rich samples is not the result of some clay effect on the frame moduli, but rather reflects that the clay rich sample actually has a larger pore space volume than the clean sample."

Tosaya and Nur (1982) investigated diagenesis and clay effects on longitudinal wave velocity through sandstone and shale samples. They measured the p-wave velocities on the water or brine saturated cores, all 18 of which were not perpendicular to the bedding plane, under independently controlled pore confining pressures of 5900 psi and 12000 psi, respectively. Using x-ray diffraction, thin-section microscopy and elemental analysis, they were able to obtain the clay contents for each sample. Combining their experimental data with that of DeMartini et al. (1976), Tosaya and Nur (1982) developed an empirical relationship, Equation 2-21, which relates p-wave velocity, V_P, to porosity and the volume fraction of clay, C, that is only considered valid under the previously defined stress conditions, for porosity from 4 to 20 percent and for a maximum 72 percent clay content.

$$V_P = -2.4C - 8.6 \, \phi + 5.8 \qquad\qquad (2-21)$$

The authors indicate that the p-wave velocity is a stronger function of porosity than clay content by a factor of nearly 4. Further, the equation is considered to be independent of the clay mineral chemical composition and location of clay, whether it be inside the open pore space or between the rock mineral grains.

Kowalski (1975) used acoustic and density well logs to obtain formation strength parameters using a refined method to estimate shear wave travel time. He found that his values of Poisson's ratio, shear, bulk, and Young's moduli correlated well with the lithology but was unable at the time to compare the dynamic results to static test values. He notes that shear modulus, G, and the formation lithology are closely related and variations in shear modulus "appear to reflect variations in the grain size present in the lithology."

Minear (1982) studied three clay models and their estimates of clay and shale effects on shear and longitudinal wave velocity. The three models investigated were the laminated shale model in which shaley layers alternate with clean sandstone layers, the structural shale model in which

the grain matrix material is made up of quartz and shale
grains, and the dispersed clay model in which the clay is
considered to be contained in the pore fluid or lining the
pore surfaces. He found that for shale fractions less than
30 percent, the effects of clay on shear and longitudinal
wave travel time are about the same and increase by almost
the same amount. In the dispersed clay model the clay only
effects the pore fluid elastic constants and its effect on
wave travel time is a function of the clay density. There is
a negligible effect on shear and longitudinal wave travel
time if clay density is similar to marine clay (1.40 gm/cc).
If clay density is near that of sandstone (2.65 gm/cc) it
will affect shear wave travel time in the same manner as the
other two clay models. The effect on longitudinal wave
travel time is on the order of one third of the magnitude of
the two other models.

2.4.4. Effects of pressure

Numerous authors have investigated stress effects on
acoustic wave velocities. Studies have shown that wave
velocities are functions of both the external overburden
stress and pore fluid pressure. Increasing pore fluid
pressure causes wave velocities to decrease, and increasing

external stress causes wave velocities to increase (Timur 1977). Jones and Nur (1983) note the increase in shear wave velocity and decrease in attenuation with increasing pressure. Further discussion of the dependence of p- and s-wave velocity with effective pressure is found in Section 2.2.2. of this report.

Wyllie et al. (1956; 1958) studied pressure effects on wave velocity through porous media including synthetic sphere packs and natural sedimentary rock cores. They found that as the applied uniaxial pressure on consolidated cores was increased, the longitudinal wave velocity also increased until it reached a maximum limiting velocity which did not change with further increase in pressure. For unconsolidated samples, however, a limiting velocity was not reached because the samples collapsed and grain crushing occurred under a lower pressure than that required for a limiting velocity to be reached. They also found that when the hydrostatic pressure within the pores is the same as the external hydrostatic pressure, and both are increased at the same rate, the initial velocity increase is fast, then it slowly increases at a nearly linear rate. For rock samples with only a small difference between the hydrostatic internal pore pressure and the external hydrostatic pressure, the variation of velocity with pressure repeats the aforementioned process.

When the difference between the internal and external
pressure is high, the initial rapid velocity increase was not
observed.

Wyllie et al. (1958) explain the effects of pressure on
wave velocity through dry, partially, and fully saturated
samples assuming that the rock material contains many cracks
which can be closed if the external stress is sufficiently
greater than the internal pore pressure. However, if the
pore fluid pressure is the same as the external pressure
these cracks will remain open. Because the rock grain
material is relatively homogeneous at high differential
pressure, the difference between the internal pore and
external pressures, there is little energy loss as the wave
travels through the rock. The authors contend that the
relative air and liquid saturations are not important at high
differential pressures because the wave velocity is so much
greater through rock matrix material as compared to either
fluid phase. When the differential pressure is lower,
however, the cracks are not closed and the wave signal
traveling through the rock matrix material loses energy while
the wave signal traveling through the fluid becomes more
important. Both of these factors result in a lower value for
wave velocity at lower differential pressures. Also at lower
differential pressures, the relative air and liquid

saturations become important because air acts to increase the
wave signal reflection coefficient passing from the matrix
material to the fluid phase and the velocity decreases. When
the fluid pressure is raised the gas goes into solution, the
volume of gas decreases and the wave velocity subsequently
increases. The authors conclude that large differential
pressures should be applied to rock samples in order to
obtain good data.

Gardner et al. (1964) studied the effects of both
pressure and fluid saturation on elastic wave velocity and
attenuation through sandstones and unconsolidated samples of
glass spheres and quartz sand. They cite that, assuming the
grain packing of their consolidated samples was sufficiently
uniform to ensure equal contact forces at all contact points,
the elastic moduli will be proportional to the cube root of
the applied pressure. They found that their measured elastic
moduli are proportional to the square root of the applied
pressures for pressures under 5000 psi and attribute the
discrepancy to the unequal contact force for samples at
applied pressures under 5000 psi. They noted a relationship
between hysteresis and pressure; the elastic moduli tend to
be smaller for increasing pressure loads than for decreasing
pressure loads. For their dry unconsolidated samples they
note that the moduli are proportional to the square root of

pressure for pressures less than 1000 psi but for applied
pressures between 1000 and 5000 psi the moduli gradually
approach a cube root of pressure proportionality at 5000 psi.
They noted hysteresis effects for the dry unconsolidated
samples; the first and second pressure load and unload cycles
are noncoincident but after repeated application of load
cycles a repeatable curve was obtained. They made their
measurements after stabilizing the unconsolidated sample pack
by twice cycling from 50 to 500 psi and found that hysteresis
effects were greater for glass spheres had less repeatable
results than did the quartz sand. Poisson's ratio, which was
found not to be dependent on porosity or pressure, was shown
to be 0.1 and 0.25 for the quartz sand and glass bead packs,
respectively.

Hicks and Berry (1956) discuss the effect of pressure on
acoustic velocity and note that the velocity is proportional
to the difference between the external confining pressure and
the internal pore pressure, not on the magnitude of either
pressure. They conclude that an abnormally high pressured
reservoir, having normal confining pressure but elevated pore
pressure, will have an abnormally low acoustic velocity
because the pressure difference will be abnormally low.
Similarly, a reservoir with abnormally low pore pressure and

high confining pressure will have a high acoustic velocity because of the high pressure difference.

Montmayeur (1985) found that dynamically measured Young's modulus was proportional to mean stress to the $\frac{1}{7.9}$ power for consolidated rocks and to the $\frac{1}{2.3}$ power for his saturated unconsolidated frac sand packs. Brandt (1956) states "the theory indicates that the speed of sound is proportional to the $\frac{1}{6}$ power of the pressure." He presents a plot of Nasu's (1940) data which shows the speed of sound from experimental data to be proportional to pressure to the $\frac{1}{2}$ to $\frac{1}{7}$ power which covers the $\frac{1}{6}$ power range Brandt (1956) quoted from the theory.

Jones and Nur (1983) studied the velocity and attenuation of seismic shear wave velocity through Berea cores at elevated temperatures and pressure. They measured the wave velocity at different pore and confining pressures in the following manner: the pore pressure was held constant at 5 bars (0.75 psi) and the confining external pressure was raised incrementally to 205 bars (3000 psi) then, while holding the confining pressure constant at 205 bars, the pore fluid pressure was raised from 5 to 205 bars. The authors concluded that because higher velocities occurred at high pore pressures than at low pore pressure "the confining pressure (P_c) is somewhat more efficient in increasing

velocity than pore pressure (P_P) is in decreasing it." Using
the definition for effective pressure, P_e, as that in
Equation 2-2b, they found that $\alpha = 0.97$ fit their data (Jones
and Nur 1983).

2.4.5. Effects of fluids and saturation

Longitudinal wave velocity is a function of the density
and the compressibility of the pore fluid whereas the shear
wave velocity is also a function of the fluid density but not
the compressibility, White and Sengbush (1986). Knowing the
compositions and relative saturations of the pore fluids and
how they affect shear and longitudinal wave velocities is
important. Additionally, the determination of elastic
constants requires both the wave travel times and the bulk
density, which is also a function of the pore fluid
composition and saturation. A wealth of information exists
in the literature about the effects of saturation and
saturating fluid composition on dynamic elastic rock
properties.

Wyllie et al. (1956) measured the longitudinal wave
velocities through their cores after drying them in an oven
and when they were saturated with distilled water. They
found that the wave velocity through the dry samples was less

than the velocity through the water saturated sandstone samples and that the limiting velocity was less for the dry samples. They also investigated the partial saturation, water and air, effects on wave velocity through sandstone samples. The results showed that velocity decreased as water saturation declined from 100 to 70 percent, the velocity from 10 to 70 percent was constant and below 10 percent water saturation, the velocity changes were erratic (Wyllie et al. 1956). The testing conditions were at atmospheric pressure and the authors contend that these results may not apply to rocks under pressure. The authors measured the velocity of a Berea sandstone sample dry, 95 percent water saturated and 100 percent water saturated under increasing hydrostatic pressure. While the velocity through the 100 percent water saturated core was relatively constant with increasing pressure, the dry and partially saturated sample showed increasing wave velocity with pressure which reached a limiting velocity at high (approximately 6000 psi) pressures. The velocity through the partially (95 percent) saturated sample was, at all pressures, higher than through the dry sample. Wyllie et al. (1956) attribute this phenomenon to the application of different pressures to the water phase. For example, in the fully saturated sample the rock matrix material is under relatively low pressure as compared to the

water so the velocity is correspondingly low for fully saturated sample than for the dry or partially saturated sample.

Hicks and Berry (1956) studied how fluid pressure, fluid compressibility, porosity and pressure on the rock skeleton affect acoustic velocity in porous media. The authors used Gassmann's (1951) theoretical solution for sound velocity in a hexagonal packing of spherical grains with liquid filled pore space, White and Sengbush's (1953) theoretical solution for sound velocity in a cubical packing of spherical grains with liquid filled pore space and Brandt's (1955) theoretical formulation of sound velocity through randomly packed, non-spherical particles with varying porosity to evaluate the effects of changing various parameters. The authors substituted equal values for the variables into each of the three equations and qualitatively compared the results of the three solutions.

In regard to fluid compressibility, their results from all three solutions show that acoustic velocity decreases with increasing saturating fluid compressibility, all else constant. The velocity decreases 15 to 20 percent as the saturating fluid changes from water to oil (Hicks and Berry 1956).

Gardner et al. (1964) showed that while the addition of water to a dry sample will decrease the elastic moduli measured the application of simulated overburden pressure will reduce the magnitude of the decrease. Their explanation is that water weakens the rock framework but the applied pressure strengthens the framework.

Aktan and Farouq Ali (1975) found during their tests on the effects of cyclic and in-situ heating of cores that their saturated Berea samples had higher values of Young' modulus than their dry samples. The decrease in Young's modulus with each heating and cooling cycle was greater for the saturated than for the dry cores in all cases, Berea, Boise, California and Tennessee samples. Poisson's ratio measured from wave velocities during the in-situ heating test decreased for all the saturated and dry samples except for the Tennessee sandstone which showed an increase in Poisson's ratio for both dry and saturated samples.

Elliott and Wiley (1975) studied the partial saturation, air and brine, effects on compressional wave velocity through unconsolidated Ottawa sand packs for five water saturations, 0, 9, 45, 85 and 100 percent. Net confining pressures were varied from zero to 10,000 psi. Their works showed that the compressional wave velocity is strongly dependent on the water saturation at high, greater than 85 percent, and low,

less than 9 percent, water saturations. At intermediate water saturations, the velocity and water saturation are independent. They also showed that wave velocity is greatest at 100 percent water saturation and lowest for partial saturations and dry sand, zero water saturation, showed compressional wave velocity to be greater than the intermediate saturation velocity but not as great as for 100 percent water saturation.

The authors were unable to measure the effect of water-gas distribution on the longitudinal wave velocity but propose that higher velocities would result from uneven water distribution than from more even distributions. They explain this with the results showing that both dry and fully water saturated samples have greater longitudinal wave velocities than do partially saturated samples. Their work also shows that for greater the differential pressure, the low-gas saturation effects decrease. In summary, Elliott and Wiley (1975) show that small gas saturation will produce the same effects on longitudinal velocity through unconsolidated sand packs as high gas saturations.

Domenico (1974) notes that acoustic velocity in a sand reservoir will decrease as bulk density increases, but increases as the fluid compressibility decreases: the increase in bulk density and the decrease in fluid

compressibility both occur as water saturation increases.
Further, in an oil sand, the decreasing fluid compressibility
effect of increasing velocity overshadows the increasing bulk
density effect of decreasing velocity. For a gas sand, the
effects are opposite; the decrease in velocity caused by
increasing bulk density is the dominant factor for water
saturations less than 80 percent.

Gregory (1976) investigated the influence of fluid
saturation on the shear and longitudinal wave velocities,
densities, and elastic moduli of sedimentary rock samples
under confining pressures from zero to 10,000 psi and pore
pressures near atmospheric pressure. Water saturations were
varied from zero to 100 percent. The results indicate that
fluid compressibility and density, fluid-cement intergranular
acoustic coupling, and fluid-solid chemical interactions near
grain contacts are primary factors that influence fluid
saturation effects (Gregory 1976). Further, the results show
that the lowest p-wave velocities are found in reservoir
sands containing gas. The presence of gas reduces the
dynamic elastic rock moduli and decreasing pressure enhances
this effect. Except for Poisson's ratio, elastic moduli
decrease with increasing porosity.

With regard to work done by others, Gregory found some
interesting contradictions and confirmations. His work

showed that fluid saturation effects on velocity are not
always controlled by the compressibility of the pore fluid,
which contradicts some work by Hicks and Berry (1956). In
support of Biot (1956), Gregory's (1976) work showed that the
s-wave velocity of dry rocks does exceed the fully liquid
saturated s-wave velocity through the same rock at high
confining pressure (greater than 9000 psi) for all
porosities. Derivation for Biot's (1956) theory at pressures
below 9000 psi for low porosity rocks is explained by Biot's
assumption that microcracks are negligible which presumably
does not hold at low confining pressures which are
insufficient to close microcracks.

Domenico (1976) presents results of his laboratory
measurements of shear and longitudinal wave velocity through
unconsolidated Ottawa sand packs for various brine
saturations at 1500 psig confining pressure. He was able to
determine the uniformity of the brine distribution by using
sodium iodide as the brine salt and x-raying the sample.
Results showed that the uniformity of brine distribution was
a function of the brine saturation; the low the brine
saturation, the lower the degree of liquid distribution
uniformity. Wave velocity measurement results showed p-wave
velocity to be almost constant from zero to 85 percent water
saturation and above 85 percent, the velocity increased

appreciably to a maximum value at 100 percent water saturation. Shear wave velocity decreased linearly with increasing water saturation.

Using Geertsma's (1961) derivation of Biot's p-wave velocity through porous media for infinite frequency, Domenico (1976) compared his results to those calculated from Geertsma's equation and found discrepancies at high brine saturations. Attributing the differences between measured and calculated results to the variation of gas and brine distribution in different sized pores. Domenico (1976) also experimented with spherical glass beads to ensure a more uniform pore size distribution. Results from tests with the glass bead tests indicate that the discrepancy between measured and calculated values of p-wave velocity were indeed due to the saturation-pore size relationship. The differences between Domenico's (1976) and Elliott and Wiley's (1975) results can likewise be due to different saturation distributions.

Nur et al. (1979) measures shear and compressional wave velocities and attenuation for clay-bearing sandstone samples at varying temperatures, 20°C, 145°C and varying pores pressures from 0 to 7 bars (0 to 100 psi) with constant external confining pressure of 300 bars (4400 psi). During the 20°C tests the water within the samples was single phase

water throughout the decreasing then increasing pore fluid pressure cycle. During the 145°C test the pore fluid started out as water at high pore pressure but changed to steam at pore pressures below 4 bars (59 psi), the water-vapor transition for 145°C.

Results from wave velocity measurements show that for the low temperature test, 19°C, there was negligible change in shear and compressional wave velocity over the pore pressure range. For the high temperature test, however, there were interesting changes in both shear and longitudinal wave velocity and, correspondingly, in Poisson's ratio: 1) the p-wave velocity reaches a minimum value at approximately 4 bar pore pressure, the water-steam transition for 145°C, but the p-wave velocity did not show a similar response, 2) when the rock is filled with steam, at pressures less than 4 bar, the p-wave velocity is lower than it is for the water saturated rock but the s-wave velocity is higher than it is for the water saturated rock, 3) the $\frac{V_p}{V_s}$ ratio and Poisson's ratio decrease as the pore pressure decreases and the pore fluid goes from water to steam, and 4) the shear and compressional waves have higher amplitudes when the pore fluid is steam than when it is water, Nur et al. (1979). The authors suggest an explanation for the p-wave velocity minimum observed near the steam-water transition. They

contend that it "may be due to the combined effect of increasing density, as more and more steam transforms into water, and the low fluid bulk modulus which remains low as long as any steam is present."

Tosaya et al. (1984) measured shear and longitudinal wave velocities through unconsolidated tar and heavy oil sand samples at varying temperatures, pressures, and brine-oil saturations to assess the application of seismic imaging for mapping EOR thermal fronts. Results show that the presence of gas or steam is easily detected in sands with high brine/oil ratios. For sands with brine to oil ratios of 0.5 or less the steam is not as easily detected but results indicate that wave velocity and attenuation are very sensitive to the higher temperature of the steam heated oil. Tosaya et al. (1984) attribute the dependence of p-wave velocity and temperature to the increase in oil viscosity with increased temperature.

Bacri and Salin (1986) investigated the acoustic velocity through oil and brine saturated sandstone for both drainage and imbibition processes. They found that although the fully saturated (either oil or brine) samples had similar acoustic velocities, the velocities decline appreciably during both the drainage and imbibition processes. The

authors explains the imbibition results quantitatively and the drainage results using Gassmann's and Biot's theories.

Coyner and Cheng (1984) measured the shear and longitudinal wave velocities through dry and saturated Berea sandstone samples in an apparatus designed for independent variation of pore and hydrostatic confining pressures. They were able to isolate the chemically induced effects of the saturating fluid from the physical effects induced by the saturating fluid in the pore space on the wave velocities by using benzene as their saturating fluid because it is nonreactive with both sandstone silicate material and carbonate matrix material. Their results showed that the dry and benzene saturated Berea had nearly the same s-wave velocity at low pressure, less than 4500 psi, the saturated sample had a higher shear wave velocity than the dry sample. For all pressures the elastic moduli measured for the saturated samples were higher than for the dry samples when the differential pressure was increased, both the dry and saturated samples showed an increase in the shear and longitudinal wave velocities. The longitudinal wave velocities were consistently higher for the saturated samples compared to the dry samples. The authors used this data to test various theoretical predictive models. They found that a technique developed by Cheng and Toksoz (1979) was able to

predict the pressure dependent porosity change to within 0.1
percent of the observed porosity change for their pressure
range 0 to 14,500 psi.

2.4.6. Effects of porosity

In 1956, Wyllie et al. studied the effects of porosity
on longitudinal wave velocity through glass sphere
aggregates. They introduced the "Wyllie time-average
equation", Equation 2-22, which relates the inverse of the
average system wave velocity to the sum of inverse velocity
through the pore and matrix rock material.

$$\frac{1}{V_{average}} = \frac{\phi}{V_{pore}} + \frac{1-\phi}{V_{grain}} \qquad (2-22)$$

The authors measured the wave velocities through nine
aggregate glass bead packs and compared the measured to
calculated, from the time average equation, values. They
consistently found the time average calculated results to be
higher than the observed wave velocity atmospheric pressure.
At higher pressures where a limiting p-wave velocity could be
reached they found that the measured limiting p-wave velocity
did agree well with the calculated time average velocity.

Hicks and Berry (1956) observed that acoustic velocity decreases with increasing porosity. Using Brandt's (1955) equation for acoustic velocity through randomly packed, non-spherical particles with varying porosity they predicted this phenomenon. Hicks and Berry (1955) also compared their laboratory velocity measurements of acoustic velocity through consolidated sandstone cores at 6000 psi differential pressure with porosities from 3 to 30 percent, and found that their results agreed well with the Wyllie time average equation. They concluded that for the range of their sample porosities the velocity of sound decreases up to 60 percent with increasing porosity. Further, in studying the effects of saturating fluid compressibility on acoustic velocity, they found that the velocity variations with fluid compressibility are more pronounced in high porosity formations and these effects of fluid compressibility diminish with decreasing porosity.

Geertsma and Smit (1960) discuss Wyllie's time-average equation for the wave velocity through a fluid saturated rock. They cite dangers in using the time average equation because it is "based on the dubious assumption that the porous medium can be replaced by a series of alternating solid and liquid layers, which the wave front passes perpendicular to the interfaces between both phases." They

feel that because the equation is used so frequently it is surrounded with "an aura of scientific truth" although the relationship neglects the pressure dependent rock bulk deformation properties. They present theory which shows the wave velocity dependence on elastic properties of the rock bulk material and its two components, rock matrix material and the pore fluids. They suggest that future research study the effects of porosity, grain matrix and cement composition and grain size distribution on bulk rock compressibility.

Elliott and Wiley (1975) investigated the effects of air-water saturation on the longitudinal velocities of unconsolidated sands. They found that the Wyllie time average equation was not appropriately applicable to determining the longitudinal wave velocity in partially saturated (air-water) unconsolidated sands. They found that Wyllie's equation, intended for estimating water-saturated sandstone porosity, ignores the sensitivity of wave velocity to net confining pressure and cannot adequately distinguish between gas and liquid acoustic effects, Elliott and Wiley (1975).

Graves (1982) found a linear relationship between Lame's constant, λ, and porosity, ϕ, for consolidated rocks under different triaxial pressure conditions, Equations 2-23 and 2-24.

$$\lambda = -18.87\phi + 5.26 \qquad\qquad (2-23)$$

where:

Axial pressure = 5000 psig

Confining pressure = 1000 psig

Pore pressure = 0 psig

$$\lambda = -18.21\phi + 4.92 \qquad\qquad (2-24)$$

where:

Axial pressure = 4000 psig

Confining pressure = 2000 psig

Pore pressure = 0 psig

She also found a relationship between dynamic $(\lambda + 2G)^{0.5}$, dynamic Poisson's ratio, and porosity for her consolidated sandstone core samples.

2.4.7. Effects of temperature

Longitudinal and shear wave velocities are affected by increased temperatures, albeit to a lesser degree than the effects of pressure, porosity and lithology (Timur 1977).

Accordingly, the dynamic elastic constants calculated from wave velocities are also affected.

Aktan and Faroug Ali (1975) investigated the effect of cyclic and in-situ heating on elastic constants of Berea, Boise, California and Tennessee sandstones. The heating and cooling cycles were made by placing the cores in steel core holders that were heated to 550°F at 200 psig. The p- and s-wave velocities were measured while the cores were subjected to triaxial pressure loads of zero to 5000 psig axial pressure in 1000 psig increments while keeping the radial confining pressure at 60 percent of the axial pressure load. They measured the in-situ wave velocities at 300°F by heating the core inside the triaxial cell and simultaneously measuring the shear and longitudinal wave velocities. The wave velocities decreased for the cores under both heating tests although the reduction in velocity was more pronounced for the cyclic heated test cores. Accordingly, Young's modulus, bulk moduli and Poisson's ratio all decreased after the cyclic heating tests and during the in-situ tests. The authors attributed the reduction in wave velocity to the formation of microcracks during the heating and cooling cycles.

Morita et al. (1985) also found a decrease in both p- and s-wave velocity while cycling temperatures from 70°F to

370°F as well as significant reduction in the wave amplitudes. They noted significant hysteresis in wave velocities during the first heating cycle due to permanent compaction.

Timur (1977) investigated the effects of temperature on sandstone and carbonate samples by measuring compressional and shear waves velocities at restored overburden and pore fluid pressure for temperatures up to 200°C (392°F). Most work previous to his, were concerned with measuring velocities at constant temperature as functions of pressure. Timur (1977) found that the decrease in both shear and longitudinal wave velocities decreased linearly with increasing temperature over the temperature range investigated (20°C - 180°C) for both brine saturated sandstone and limestone samples at different pore fluid and confining pressures. For each 100°C increase in temperature, the average decrease in shear and longitudinal wave velocities for a 100°C increase in temperature were 0.9 and 1.7 percent, respectively. He noted that the rock with the highest decrease in both s- and p-wave velocities, 2.5 percent for each, was also the sample with the highest porosity, the Boise sandstone.

Jones and Nur (1985) studied the effect of elevated temperature and pressure on both the velocity and attenuating

shear wave. Their results from experiments on Berea samples shows that there is a strong decrease in shear wave velocity with temperature for all pressure investigated. Similarly, the wave attenuation decreases with increasing temperature. The authors do not think that thermal relaxation is a significant loss mechanism for the system investigated. The thermal relaxation mechanism models losses caused the irreversible heat flow in a heterogeneous material induced by strain waves and predicts significant increases in wave attenuation with temperature for a water saturated rock.

Shumway (1958) investigated the effects of temperature on compressional wave velocity for water saturated unconsolidated sediments. He found that the velocity increases with increasing temperature as it does for a water sample alone. The author attributes this similarity to the dominance of water compressibility in the compressibility behavior of a water-sediment system: the compressional wave velocity through a water-sediment mixture is a function of porosity and the density and compressibility of both the water and the sediment particles.

2.4.8. Effects of microcracks

Microcracks, also known as microfractures, have been studied extensively over the last fifteen years to determine how they affect various physical properties of rocks including shear and longitudinal wave velocities, bulk rock compressibility, and elastic mechanical properties. Their effect on the measurement of wave velocities have been noted by Wyllie et al. (1956, 1958). Walsh (1965a, b, c) has studied their effects on elastic mechanical properties. Montmayeur (1985) applied Walsh's theory to correct and correlate static and dynamic values of bulk compressibility using microcrack porosity.

Microcracks are defined as three dimensional rock openings for which one dimension is significantly greater than at least one of the other two (Simmons and Richter 1976; Kranz 1983), and the length is on the order of 100 μm or less. These authors further define microcracks based on whether they occur within a rock grain, (intragranular or intracrystalline), along the boundary between the grains (grain boundary cracks), across a grain boundary and into a grain (intergranular or intercrystalline), or across the grain from boundary to boundary (transgranular). Both thermal and mechanical stress can induce and cause growth of

microcracks when the local strength is exceeded. Kranz
(1983) notes that hydrostatic pressure stabilizes cracks and
inhibits growth.

Wyllie et al. (1956, 1958) observed that as the
differential pressure (external confining pressure minus
internal pore pressure) increases, microcracks close and as
they close the longitudinal wave velocity increases. This
phenomena continues until a pressure is reached at which all
the microcracks close, and a limiting wave velocity is
attained. Further increases in differential pressure will
not cause any increase in wave velocity.

Walsh (1956a) contends that the presence of microcracks
offers an explanation, albeit quantitative, for the pressure
induced initial changes in elastic moduli. He studied the
effects of microcracks on rock compressibility, Walsh
(1965a), on elastic uniaxial rock compression, Walsh (1965b),
and on Poisson's ratio, Walsh (1965c). In his uniaxial
compression studies, from which Young's modulus and Poisson's
ratio are measured, Walsh (1965b,c) found that the stress-
strain relationship was non-linear at low pressures but at
high pressures became more linear, and he observed hysteresis
effects. He found that both Young's modulus and Poisson's
ratio depend on the state of the microcracks; whether they
are open, as they are at low stress, or whether they are

closed, as they are at high stress. For Young's modulus he
found (Walsh 1965b) that as uniaxial pressure was applied the
microcracks close and the resulting value of Young's modulus
increases from a value below that of an uncracked sample. He
also observed hysteresis in the stress-strain curve during a
load-unload cycle. For Poisson's ratio he found that at low
stress it is less than the intrinsic value and at higher
stresses, as the microcracks close, it is greater than the
intrinsic value.

Walsh attributes these observations of change in
Poisson's ratio and Young's modulus and stress-strain
hysteresis effects to the frictional sliding of one crack
face over another as the microcrack closes with increased
stress during a load-unload cycle. Walsh (1965b) suggests
using the value of Young's modulus calculated from the
initial stress-strain slope on the unloading cycle because
"cracks which have undergone sliding do not immediately slide
in the other sense when the load is reduced."

In his studies of rock bulk compressibility, Walsh
(1965a), derived relationships for compressibility based on
pore and microcrack geometry. He found that the "effect upon
compressibility of a certain concentration of narrow cracks
equals the effect of the same number of spherical pores with
a diameter roughly two-thirds that of the cracks."

Montmayeur and Graves (1986) combined Biot's theory with microcrack analysis by Walsh (1979) to define or correlation between static and Biot corrected dynamic measured bulk compressibility, Equation 2-25a below.

$$\frac{\left(1 - \frac{C_{bdc}}{C_{bs}}\right)}{3.2\left(\frac{C_{bdc}}{C_{bs}}\right) - 1} = 2140\,(\phi_m) \qquad\qquad (2\text{-}25a)$$

where:

C_{bdc} = Dynamic bulk compressibility corrected with
   Biot's theory (psi^{-1})

C_{bs} = Static bulk compressibility (psi-1)

ϕ_m = Microcrack porosity

He found a correlation between the corrected (Biot theory) bulk compressibility of high stress to bulk compressibility at in-situ stress, again taking the microcrack porosity into account, Equation (2-25b) (Montmayeur and Graves 1986).

$$\frac{C_{bdc1}}{C_{bdc}} = -0.54 + 0.083\,\log(\phi_m) \qquad\qquad (2\text{-}25b)$$

where:

C_{bdc1} = Dynamic bulk compressibility corrected with

Biot's theory at stress greater than 400 psig (psi-1).

2.4.9. Dynamic measurements

Laboratory measurements of shear and longitudinal velocities through consolidated rocks to determine dynamic properties is almost a routine laboratory procedure and a wealth of information has been published regarding those measurements. Similar measurements on unconsolidated samples are relatively scarce. While researchers have measured wave velocities though glass bead and frac sand packs, wave velocity measurements through actual unconsolidated reservoir samples have not been found in the literature. This section presents published information on consolidated rocks and unconsolidated sands.

2.4.9.1. Consolidated Rocks

In his Master's Thesis, King presented shear wave velocity measurements through dry rock samples under hydrostatic pressure to 800 psig using ultrasonic waves. He found that at higher pressures, there was "an almost linear dependence on some power of applied pressure", but felt his

upper pressure limits were in insufficient for conclusive results. King reported shear wave velocities of 175 μsec/ft and 161 and μsec/ft for Berea samples at 200 and 800 psig, respectively. He noted that shear wave velocities were slightly reduced for samples which were inadvertently saturated during the test runs.

In a later study King (1969), realizing advantages of measuring shear and longitudinal wave velocities concurrently through dry rock samples, was able to measure both the wave velocities and the the axial and lateral strains on Boise and Berea sandstone cores under hydrostatic pressure to 6000 psig. King reported the shear and longitudinal wave velocities, corrected for change in core length, for his Boise and Berea cores. The shear wave velocity changed from 182 μsec/ft at 500 psig to 121 μsec/ft at 5000 psig. Similarly, the longitudinal wave velocity decreased from 114 μsec/ft to 80 μsec/ft as hydrostatic pressure increased from 500 psig to 5000 psig. King also calculated and compared Young's modulus and Poisson's ratio using both static and dynamic values and found that the dynamic values were higher than the static values but that the values approached each other as hydrostatic pressure increased.

Gregory (1962) measured shear wave velocities of sedimentary rock samples under pressure and presents wave

velocity data from Wyllie, Gardner, and Gregory (1962).
Among this is data for dry Berea which shows that increasing
pressure from 500 psig to 5000 psig results in a decrease in
p-wave wave velocity from 119 to 83 microsecond per foot and
a decrease in shear wave velocity from 175 to 140
microseconds per foot.

Jones and Nur (1983) measured the shear wave velocity
and attenuation on Berea sandstone with 21% porosity for
samples with varying confining and pore pressures up to 2900
psig. For effective pressure, hydrostatic confining pressure
minus pore pressure, at 22°C, shear wave velocities decreased
from approximately 182 to 152 microseconds per foot under a
500 to 2900 psig hydrostatic pressure increase.

Timur (1977) measured the shear longitudinal wave
velocities through Berea and Boise sandstone as function of
temperature at simulated reservoir conditions. Finding that
longitudinal and shear wave velocities decrease by less than
two percent for a 100°C temperature increase they reported
the wave velocities for various effective (overburden minus
pore pressure) pressures. For the Berea sample with 17.11
percent porosity, compressional wave velocity decreased from
74 to 69 microseconds per foot for an effective pressure
increase from 1130 psig to 11,300 psig while shear wave

velocity decreased from 130 to 117 microseconds per foot over the pressure increase.

Coyner and Cheng (1984) measured shear and longitudinal wave velocities on sedimentary and igneous benzene saturated rocks. Benzene was chosen because it is nonreactive with silicate materials and carbonates. The author felt that with benzene they were able to independently study physical effects on velocity of pore spaces and pore fluid. Data was taken for both dry and saturated Berea sandstone with 18 percent porosity at confining hydrostatic pressures between 3500 and 7250 psig. Result showed that shear wave velocities were very close for the dry and benzene saturated rock but for the longitudinal wave velocities the saturated velocities were higher that for the dry rock. Results showed that p-wave velocity decreased from approximately 92 to 74 microseconds per foot when confining pressure was increased from 500 to 5000 psig. Similarly, the p- wave velocities decreased for 152 to 117 with an increased in hydrostatic pressure from 500 to 5000 psig.

Data presented by Graves (1982) and Montmayeur (1985) on shear and compressional wave velocities through their Berea samples was comparable to the data previously cited. Under hydrostatic loading for brine saturated Berea cores, Graves (1982) reported decreased in p- and s- waves travel time of

89 to 77 microseconds per foot and 148 to 125 microseconds

per foot, respectively, for pressure increased from 500 to

5000 psig. Montmayeur's (1985) reported values were

comparable.

2.4.9.2. Unconsolidated porous media

Measurements of wave velocities through unconsolidated

porous media can be categorized into one of two areas:

marine sediments and frac sand/glass bead packs. The work

with marine sediments is not directly applicable to the

determination of unconsolidated sand reservoir

compressibility measurements because they are at low

pressures and are much younger formations in terms of

compaction and geologic age. The work with spherical glass

beads and frac sands was the precursor to work with actual

reservoir samples.

Hamilton et al. (1970), made in-situ measurements of

sand density and compressional and Stoneley wave velocities

and attenuation for sea-floor sediments. The shear wave

velocities were then calculated from the Stoneley wave

velocities. The authors concluded that for the small wave-

induced stresses, that "either Hookean-elastic or

viscoelastic equations can be used to compute

compressional-wave and shear-wave velocities and other
constants". They also concluded that this study showed the
marine sediments were capable of transmitting shear waves.
They reported longitudinal and shear wave velocities of 169
to 209 microseconds per foot and 1547 to 3464 microseconds
per foot, respectively.

In a later study, Hamilton compiled shear wave velocity
data for soft sediments representing marine sands. The
measurements were made in-situ in natural saturated sediments
at depths of 2100 feet. A relationship between shear wave
velocity and depth was developed, Equation 2-26a, which
compares well with correlation developed at Shell Development
Company, Equation 2-26b. These Shell correlation result from
wave velocity measurements made on course and fine quartz
sand varying pressures. The depth-wave velocity correlation
was then derived from the pressure-velocity relationship
(Hamilton et al. 1976).

$$V_S = 128 \ D^{0.28} \qquad\qquad\qquad 2\text{-}26a$$

$$V_S = 120 \ D^{0.28} \qquad\qquad\qquad 2\text{-}26b$$

where:

V_S = Shear wave velocity (m/sec)

D = Depth in sand body (m)

The study indicates that shear wave velocity is proportional to pressure to the 1/3 to 1/6 power, reaching the 1/6 power at very high pressure. Hamilton (1978) summarizes relationships between p-wave velocity and depth for four types of marine sediments.

In a later paper, Hamilton (1977) presents relationships between compressional wave velocity and density for submarine rocks and sediments. Further he finds that density and wave velocity values can be used, within certain limitation, to identify subsurface rock types and mineral species. Hamilton (1977) used in-situ and laboratory data to develop an empirical density - compressional wave velocity relationship for various lithologies. Hamilton presents the Gardner et al. (1974) and Ludwig, Nafe, and Drake (1970) relationships which are considered to be "good generalization of velocity - density relations in the sea floor". The Gardner et al. (1974) relation, Equation 2-27, was derived from a combination of in-situ well logs and laboratory measurements performed on recovered cores from oil wells.

$$\rho = 0.23 \ V_p^{0.25} \qquad\qquad (2-27)$$

where:

ρ = Density (gm/cc)

V_p = Compressional wave velocity (ft/sec)

Stoll (1977) presents a mathematical model which describes wave propagation though fluid saturated particulate powers media. This model is based upon two energy mechanisms; the first one occurs at the skeletal grain contacts and the other results from the relative notion of the pore fluid and the sediment frame described by the Biot model. Stoll's (1977) model predicts both wave velocity and attenuation based on strength and rock properties including porosity, permeability and grain size.

Various researchers have measured shear and longitudinal wave velocities through unconsolidated particle packs of glass beads and frac sand. No reported measurements of wave velocities through recovered cores from actual petroleum reservoirs have been found in the literature. Measurements through marine sediments were reported in Hamilton (1971), but these were at low pressure, atypical of petroleum reservoirs. Shirley and Hampton (1978) measured shear wave velocities through kaolinite clay laboratory sediments as part of the development of shear wave measurement transducers

for laboratory sediments. Kowallis, et al. (1984) measured shear and longitudinal velocities through poorly consolidated sandstones at low pressure and found the wave velocities were intermediate between values for well consolidated sandstones and loose sand.

Domenico (1977) investigated the elastic properties of unconsolidated sand packs, consisting of 1)glass beads and 2) natural fine Ottawa sand that were gas saturated and water saturated. He reported similar results between the glass bead and natural sand packs. Brine saturated Ottawa sand showed increasing p-wave velocity from 6300 ft/sec to 7000 ft/sec as differential pressure was increased for ·500 to 5000 psi. Similarly, s-wave velocity increased from 2000 ft/sec to 3200 ft/sec for the same pressure increase. Domenico reported that shear wave measurements were unreliable at low (less than 100 psi) differential pressures. Similar measurements over the same pressure range for brine saturated glass bead packs showed increasing p-wave velocities of 6500 ft/sec to 7100 ft/sec and 2000 ft/sec to 2800 ft/sec, respectively.

2.5. Modeling Rock Properties with Dynamic Measurements

There are three widely used models which relate acoustic wave velocity to rock properties; Wyllie's time-average equation, Gassmann's model and Biot's model. Wyllie's time average model relates p-wave velocity to porosity. Both Gasmann's and Biot's models relate p-wave velocity to static bulk compressibility. These models will be discussed briefly in this section. Their application to the dynamic data in this study will be discussed in Chapter 6.3 of this report.

2.5.1. Wyllie's time-average model

Wyllie et al. (1953) developed the widely used and widely misused time-average equation which relates the p-wave velocity from acoustic logs to formation porosity. This model was presented in linear form as either Equation 2-28 or 2-29.

$$t_p = t_f \, \phi + t_{ma} \, (1-\phi) \qquad\qquad (2-28)$$

where:

t_p = Acoustic log p-wave travel time

t_f = p-wave travel time through pore fluid

t_{ma} = p-wave travel time through matrix material

ϕ = Porosity

$$t_p = A + B\phi \qquad\qquad (2-29)$$

where: A, B = Empirical constants for local conditions

Wyllie's equation is appropriately applicable to determining porosity from acoustic log measurements in well compacted, well cemented formations. Further, the effective stress in the formation must be high enough so that the terminal velocity is reached, usually greater than 4000 psi, and the pore fluid travel time be close to the value for water, 190 microseconds per foot. The model tends to underestimate porosity for carbonates, especially those with secondary or vugular porosity and overestimates formation porosity for less compacted formations. There are corrections available for determining the formation porosity when the formation conditions do not meet the afore-mentioned specifications. The reader is directed to well logging literature, especially Hilchie (1978) and Jorden and Campbell (1986), for the appropriate corrections.

2.5.2. Gassmann model

In 1951 Gassmann presented a model to describe "the elastic behavior of porous media under small stress

variations". Such stress could be induced by "sound waves as well as shear vibrations". Gassmann (1951) defined the porous media as a "polyphase" system made up of a single porous solid or loose grain framework whose pores were either gas or liquid filled. This framework (matrix) was defined to behave elastically and be homogeneous and isotropic on both macroscopic and microscopic levels and the pore fluid was defined to be isotropic. The material comprising the framework (grains) is both homogeneous and isotropic.

Gassmann defined two systems for his model; open and closed. The open system assumes a differentially elastic framework for which the pores are open to the "outside" so that pore fluid can flow outward under differential pressure. In the open system pore fluid fiction and inertial resistance can be neglected if the stress is changed very slowly. The open system defines the framework (matrix) elastic properties. The closed system assumes that stress variations are sufficiently small so that there is no flow of the pore fluid in relation to the grains, but rather, they move in tandem.

Gassmann relates the bulk modulus, K, of the closed system (consisting of framework and pore fluid) to the bulk moduli of the solid grain material, K_g, the framework matrix material, K_{ma}, and the pore fluid, K_f, with Equation 2-30.

$$K = \frac{K_g(K_{ma} + Q)}{K_g + Q} \qquad (2\text{-}30)$$

where:

$$Q = \frac{K_f(K_g - K_{ma})}{\phi(K_g - K_f)}$$

Equation 2-30 can be rearranged into the form of equation 2-31 which shows that the dynamic bulk modulus, K_d, of a fluid saturated rock is the sum of the frame bulk modulus (K_{ma}) and a fluid term.

$$K_d = K_{ma} + \left[\frac{\left(1 - \dfrac{K_{ma}}{K_g}\right)^2}{\left(\dfrac{\phi}{K_f}\right) + \left(\dfrac{(1-\phi)}{K_g}\right) - \left(\dfrac{K_{ma}}{K_g^2}\right)} \right] \qquad (2\text{-}31)$$

The velocity of a longitudinal wave, V_p, traveling through the fluid saturated porous rock is given by Equation 2-32.

$$(2\text{-}32)$$

$$V_p = \left(\frac{M}{\rho}\right)^{0.5}$$

where: $M = K + \dfrac{4}{3} G$

G = Shear modulus

White and Sengbush (1987) discuss the Gassmann model and
explain that for low frequencies, the p-wave has a long
length and "the relative displacement between fluid and
skeleton (frame) is small compared to the skeleton
displacement itself, because of fluid viscosity". White's
(1965) formulation of the Gassmann model is presented in
Jorden and Campbell (1986), Equation 2-33, relates the p-wave
travel time through a fluid saturated rock, V_p, to its static
bulk modulus, K_s.

$$V_p{}^2 = \left\{ \frac{1}{\rho_b} \left[K_S + \frac{\left(1-\frac{K_g}{K_{ma}}\right)^2}{\left(\frac{\phi}{K_f} + \frac{(1-\phi)}{K_{ma}} - \frac{K_g}{K_{ma}{}^2}\right)} \right] \right\} \qquad (2\text{-}33)$$

It should be noted that the Gassmann model as originally
formulated did not specifically relate static and dynamic
bulk moduli. Recently, however researchers including Towle
(1978) and Graves (1982) have suggested using this White
modified form of Gassmann's equation to relate static and
dynamic bulk moduli. These static/dynamic formulations of
Gassmann's model require the subtle assumption that the
static bulk modulus is equal to Gassmann's skeletal framework
(matrix) bulk modulus. When Gassmann discusses measuring the

bulk modulus of the framework (matrix) he suggests using the open system model. In Gassmann (1951), the definition for framework (matrix) bulk moduli is the same as the definition of static bulk modulus, the inverse of bulk compressibility.

2.5.3. Biot model

Most of the assumptions of the Biot model (1941, 1954, 1956, 1962) are the same as those for the Gassmann model; the model was derived for fluid saturated elastic porous media, it accounts for the grain matrix frame and pore fluid deformation during wave propagation, and it assumes that the largest grain size diameter is much smaller than the propagating wave length. It differs from the Gassmann model in that it allows for relative motion between the viscous pore fluid and the rock grain matrix material and the fluid movement through the pores is Darcian flow. The Biot model accounts for high frequency wave propagation. For low frequency wave propagation, less than 20 KHz, the Biot model reduces to the Gassmann model equation, Equation 2-33.

Biot's model derives a set of coupled differential equations using equations of state, equations of motion and a continuity equation from which two predictions are made. The first one is that there are actually two different

compressional waves that propagate through a porous media. One wave is a plane body wave which propagates through homogeneous elastic media of finite length whose amplitude is decreased by energy loss across boundaries from energy radiation and transmission as well as scattering. (This wave is the one of practical interest.) The second wave which quickly attenuates "has propagation characteristics of a diffusion or heat conduction phenomenon" (Jorden and Campbell 1986). The second prediction is that a single shear wave exists whose velocity and attenuation are also defined by the set of coupled differential equations. The Biot model includes parameters which account for the pore geometry, a mass coupling coefficient, and a structure term which is related to tortuousity.

An applicable form of Biot's equation to acoustic logging was derived by Geertsma and Smit (1961) and presented in Jorden and Campbell (1986). This derivation relates p- and s-wave velocity to rock bulk (static) compressibility including frequency, viscosity, and mass coupling variables, Equation 2-34.

$$V_p^2 = \left[\frac{M^4 + N^4 \left(\frac{Wc}{W}\right)^2}{M^2 + N^2 \left(\frac{Wc}{W}\right)^2} \right] \qquad (2\text{-}34)$$

where: $M^2 = (P \cdot Q) + R$

$$P = \cfrac{1}{\rho_b\left(1-\cfrac{P_f\phi}{\rho_{bk}}\right)}$$

$$Q = \left[\cfrac{\left(\cfrac{\rho_b\phi}{kP_f}\right)+\left(1-\cfrac{C_{ma}}{C_r}\right)\left(1-\cfrac{C_{ma}}{C_r}-\cfrac{2\phi}{k}\right)}{C_{ma}(1-\phi)+C_f\phi-\left(\cfrac{C^2_{ma}}{C_r}\right)}\right]$$

$$R = \cfrac{1}{C_b} + \cfrac{4}{3}G$$

$$N^2 = \left(\cfrac{1}{\rho_b}\left[\cfrac{\left(1-\cfrac{C_{ma}}{C_r}\right)^2}{C_{ma}(1-\phi)+C_f\phi+\left(\cfrac{C^2_{ma}}{C_r}\right)}\right]\right) + R$$

$$W_C = \cfrac{\mu}{k\rho_b}\left[\cfrac{\rho_b^2}{\rho_b(\rho_fk/\phi)-\rho_f^2}\right]$$

where:

G = Shear modulus

μ = Pore fluid viscosity

W = Angular velocity

k = Mass coupling factor

C_f = fluid compressibility

C_{ma} = Rock matrix compressibility

C_r = Rock grain compressibility.

Montmayeur (1985) studies the Biot model extensively in regard to the relative importance of the different variables including pore fluid saturation, mass coupling coefficient, frequency, and energy loss mechanisms. Montmayeur (1985) found, for an ideal case in which the static rock properties were those of a clean sandstone and fluid properties were those of a typical reservoir fluid, the following: 1) That "a small change in this range (water saturation) can have a drastic effect on computed rock properties", 2) that for fully water saturated rocks, dynamic properties were not a function of the mass coupling factor, 3) the static compressibility is greater the dynamic, and 4) that dynamic properties such as Young's modulus and Poisson's increase sharply between 96 and 100% water saturation. As far as energy loss mechanisms were concerned, Montmayeur notes the work of Johnston, et al. (1979) who showed that, for low pressure and ultrasonic wave frequencies the primary energy loss was due to microcracks, friction, Biot fluid flow, and scattering. Further, he notes that as pressure is increased, the fluid flow "dominates with all other effects decreasing due to the closure of microcracks" (Montmayeur 1985). Montmayeur only investigated high, ultrasonic frequency

effects.   Appendix C contains a reproduction of Montmayeur's
formulation for the Biot model.

2.6.   Comparison of Static and Dynamic Properties

Ide (1936) was the first to try to develop correlations
between static and dynamic rock properties. His dynamic
tests were performed after the static tests on various rock
samples including granite, olivine diabase, norite, slate,
quartzitic sandstone, gneiss, dolomite and marble at
atmospheric pressure to test the validity of applying
elastic-wave propagation theories to describe rock behavior
under stress conditions. He measured the modulus of rigidity
and Poisson's ratio using dynamic methods on the rock
samples. For Poisson's ratio and Young's modulus, he found
that statically determined values were smaller than
dynamically determined values and static values of modulus of
rigidity are larger than dynamically determined values. He
notes that the discrepancies between static and dynamic
values might decrease if the values were measured at
reservoir pressures. He attributes these differences to
rocks being insufficiently homogeneous and isotropic for the
elastic theories to be valid in describing their behavior.

Sutherland (1962) also tested a series of rocks first under static then under dynamic conditions in order to examine the significance of their differences. He found that, for his samples, dynamic Young's modulus was greater than static by 4 to 25 percent except for two samples. He suggests that discrepancies found between Young's modulus calculated from total stress divided by total strain and Young's modulus calculated from incremental stress divided by incremental strain might be due to the closing of cracks, cavities and pores. After they are closed, the stress-strain relationship should be linear. He contends that the value of Young's modulus calculated from incremental stress and strain is closer to the true value of Young's modulus. Sutherland (1962) found that the differences between his static and dynamic Poisson's ratio was as high as 364% with static values consistently higher than dynamic. His dynamic modulus of rigidity was 12-29% higher than his static values.

Sutherland (1962) agrees with Ide (1936) that dynamic measurements are insensitive to the presence of cracks and pores in the rock. Sutherland (1962) also concludes that the order of magnitude of difference between static and dynamic values for a rock type is the same as the deviations between different specimens of the same rock type in a series of static tests and that static/dynamic moduli differences could

be a function of laboratory procedure. This was disputed by

both R.H. Merrill and W.G. Fischer in a discussion of

Sutherland's (1962) paper [see Sutherland (1962)] who stated

that the differences were a function of rock properties, not

laboratory technique.

Gregory (1962) was among the first to measure dynamic

properties under varying stress conditions and compare them

to static values. He also investigated the relationship

between dynamic and static elastic constants of both dry and

liquid-saturated sedimentary rocks. He found that, in

agreement with Ide (1936), dynamic elastic constants are

higher than static elastic constants for sedimentary rocks.

Further, he concluded that elastic constants attain limiting

values at moderate frame pressure and that dynamic elastic

constants increase with the presence of liquid pore saturants

while static elastic constants decrease with liquid pore

saturates present at increased frame pressure. At low frame

pressure, both static and dynamic elastic constants decrease

with the presence of pore fluid. Gregory (1962) also found

that Poisson's ratio remains constant for water saturated

sedimentary rocks under compression in the zero to 30 percent

porosity range. Further, he investigated hysteresis effects

under small stress cycles and supports using the tangent

method over the secant method for calculating Young's
modulus.

Walsh (1965b) suggests that his model for a rock with
microcracks can be used to explain why the values of Young's
modulus measured statically are less than those measured
dynamically even for tests in which both dynamic and static
measurements are taken at the same stress level. He explains
that while the static value is the average slope of the
stress-strain curve at an arbitrary point at a specified
stress, the dynamic value is the average slope of the stress-
strain loop produced from the superposition of the wave
induced small alternating stresses on the already statically
stress system.

Tuman and Alm (early 1960's) measured both static and
dynamic moduli simultaneously by transmitting a supersonic
pulse through sandstone cores under static test with varying
pore pressure. They did not use a separate shear wave
crystal but used the shear wave generated by the p-wave in
this analysis. Tuman and Alm found that the magnitude of
dynamic Young's modulus increased as effective stress
increased along the direction of wave propagation but static
Young's modulus decreased with increasing effective stress.
Both dynamic Young's modulus and shear modulus were greater
than their static counterparts but static Poisson's ratio was

larger than dynamic Poisson's ratio. They observed that p-wave velocity is a function of effective stress only in the direction of wave propagation.

Simmons and Brace (1965) compared static and dynamic compressibility measurement of rocks, fused quartz, and steel. They found that for very high pressures (45,000 to 135,000 psi) dynamic and static measured compressibility were within a few percent. However, at atmospheric pressure static compressibility was always greater than dynamic compressibility by as much as several hundred percent. They attributed the discrepancy to the effects of cracks on the two measurements. They agreed with Ide (1936) and Sutherland (1962) that the velocity of pulse wave propagation is less likely to be affected by cracks in rock cores than is the strain of the whole sample under static stress; the strain gauge measured static stress is over the length of the sample and therefore sees the high initial stress that can be associated with microcrack closure whereas at a few megacycle frequency the elastic energy pulse could bypass cracks and a large portion of the wave energy would pass through as if no cracks were present.

Dvorak (1970) compared the values of Young's modulus from static and dynamic (seismic) measurements. Observing that dynamic Young's modulus is higher than static Young's

modulus by as much as a factor of 3, he offered several

explanations that could account for the differences.

1) <u>Time effects</u>: Dynamic measurements take only

   microseconds with fast unloading. Static tests have

   loads induced for hours and deformation stabilization

   with time occurs. In compact rock, the time

   difference between stress application and strain

   reactions is not negligible under static tests.

2) <u>Stress magnitude</u>: Static loads during tests are 2 to

   3 orders of magnitude higher than dynamic loads and

   associated non-linearity will affect the results.

3) <u>Temperature effects</u>: Slow static tests are isothermic

   causing increased deformation as compared to

   adiabatic character of dynamic tests wherein short

   time alternative stresses are not compensated

   thermally.

4) <u>Fluid Saturation</u>: A decrease in static Young's

   modulus and an increase in dynamic Young's modulus

   are caused by the presence of moisture in rock

   masses.

5) <u>Cracks and void space</u>: The higher the void ratio, the
   smaller the associated values of both static and
   dynamic Young's modulus. The difference is highly
   affected by open cracks and the ability of elastic
   waves to pass by without a decrease in velocity.
   Under static tests with cyclic loading the
   associated deformations are much greater.

King (1969) measured static and dynamic elastic moduli
simultaneously and his apparatus was designed to include
broad band transducers so that acoustic wave attenuation
would be observed. His results compared favorably with other
researchers; dynamic elastic moduli for dry isotropic or
transversely isotropic sandstone are greater than
concurrently measured static elastic moduli, the ratio of
dynamic to static elastic moduli decrease with increasing
hydrostatic stress. This difference is, once again,
explained by the presence of microcracks within the rocks.
Similar work by Howarth (1984) showed comparable results with
equipment measuring static and dynamic Young's modulus
simultaneously on dry sandstone rocks.

Cheng and Johnston (1981) studied in depth the effects
of microcracks on the difference between static (K_s) and

dynamic (K_d) measured values of bulk moduli on several dry

rock samples including sandstone, tuff, granite, shale and

limestone at pressures from zero to 15,000 psi during the

first loading cycle. Their work supports the idea that there

is a strong correlation between the ratio of K_s/K_d and the

presence of microcracks in rocks: K_s/K_d for sandstone ranges

from 0.5 at atmospheric pressure to almost unity at 30,000

psi. K_s/K_d for rocks exhibiting elastic behavior under static

loading was shown to be inversely proportional to microcrack

porosity. For rocks with low microcracks density, K_s/K_d

remained constant with pressure at 0.7. Their limestone

samples showed time dependent behavior associated with pore

collapse and K_s/K_d approached 0.1 at high pressure and during

the unloading cycle, this ratio became lower at low pressures

than valves calculated during the loading cycle due to

microcracks initiated during pore collapse.

Graves (1982) simultaneously measured static and dynamic

elastic rock properties on 31 consolidated rock samples. She

developed a method to calculate all dynamic elastic rock

properties using log measured values of p-wave travel time,

bulk density and porosity. Further, she found that Poisson's

ratio showed no consistent trend with increasing effective

stress, that static and dynamic Young's modulus were higher

for lower porosity cores and the difference in static and

dynamic moduli increased with decreasing porosity. She found a linear relationship between dynamic λ and porosity for non-carbonate rocks independent of stress state and one between dynamic Poisson's ratio, λ + 2G, and porosity for sandstone rocks. With regard to effective stress definition, she noted that Tresca's criterion did not define biaxial loading stress state, that mean effective stress as defined for hydrostatic loading does not describe biaxial loading conditions, and that the traditional hydrostatic definition of effective stress more closely describes a biaxial stress state. She used a modified version of Gassmann's equation to relate dynamic and static bulk moduli for porous (greater than 6.5%) non-carbonates. Her other conclusions were in line with previously published work.

Morita et al. (1984) conducted experiments on Berea sandstone to simultaneously measure porosity, p- and s-wave velocity and radial and axial values of strain, permeability, and formation factor under triaxial, uniaxial, and hydrostatic loading and varying temperatures (70°-380°F) conditions to study rock property changes during reservoir compaction. Their results showed that 1) formation factor, porosity, and permeability were more directly related to strains rather than stress, 2) five different phases appeared in rock properties - initial non-linear phase caused by pore

opening and closing, a linear phase, a plastic non-linear phase caused by microcrack growth, and a volume change of the rock matrix by pore fluid pressure and temperature phase, 3) coefficients of rock property equations could be determined using their loading cycles, 4) their semianalytical rock property equations were accurate and did not require many data points, and 5) their rock property equations predict rock properties during reservoir compactions. They concluded that rock properties are independent of pore pressure provided that effective stress was kept constant. They also found that temperature, which uniformly distorts rock, caused more rock property change than pore pressure because temperature decreases rock grain rigidity.

Lin (1985) measured ultrasonic wave velocities through Mesa Verde sandstone and shales in six directions simultaneously as functions of confining pressure to 100,000 psi at room temperature. He calculated dynamic elastic moduli from the wave velocities and compared them to their previously measured static values (Lin 1985). His results showed that the sandstones were transversely isotropic and that, as previous research has shown, dynamic moduli were greater than static moduli but that dynamic Poisson's ratios are smaller than static. He also compared the laboratory measured values of p-wave velocities to in-situ measured

values from acoustic logs. This analysis showed that
although the laboratory measured p-wave velocities were
faster than the in-situ measured velocities, they were
compatible. He attributed the difference to the testing
condition differences; laboratory samples are usually
homogeneous, small and intact whereas in-situ the region
between wave source and reception may contain cracks and
joints.

In a more recent paper (Lin and Heuze 1986), the authors
compared in-situ dynamic moduli to static and dynamic
laboratory moduli directly. They used the laboratory data
from Lin (1985) on dry samples and sonic and density logs for
the in-situ gas and water saturated calculated moduli. Their
shear wave velocities were estimated from Schlumberger
Variable Density record of the sonic logs but they suggest
that more current sonic logs are able to measure the p- and
s-wave velocities directly. The authors found disagreements
among the static laboratory, dynamic laboratory and dynamic
in-situ elastic moduli which they attribute to different
testing conditions, saturations, and laboratory to reservoir
sealing effects. Another point they overlooked is that their
test were all made at different times during the rock's
stress history. The authors agree that for hydraulic
fracturing calculations (to simulate this quasi-static

process involving high stress and low strain) the most

relevant measurement of elastic moduli would be from static

in-situ testing.

Myung and Helander (1972) measured the elastic moduli

using the pulse technique for 15 cores under simulated

formation pressure (triaxial testing) in the laboratory and

compared them to elastic moduli determined from the 3-D

velocity log in the field. The triaxial pressure was

adjusted to the overburden pressure at the depth the core was

taken. They found a very good correlation using a least

square fit between the shear and compressional wave

velocities for the same rock, Equation 2-35, 2-36, below.

Shear Velocity: $\quad V_{3-D} = 0.99\ V_{lab} + 367$ $\qquad$ (2-35)

Compressional Velocity: $\quad V_{3-D} = 0.97\ V_{lab} + 674$ $\qquad$ (2-36)

The authors calculated Young's modulus, shear modulus, bulk

modulus and Poisson's ratio from their laboratory dynamic

tests, in-situ wave velocities and compared them to

previously measured (Geyer and Myung 1970) static values.

Results show that the correlation of laboratory static values

to in-situ dynamic values are not as good as that between

laboratory and in-situ dynamic, as would be expected.

Most recently, Montmayeur (1985) and Montmayeur and
Graves (1985) made basic simultaneous measurements of
acoustic p- and s-wave velocities, radial axial strains and
pore volume changes for cores under varying biaxial and
hydrostatic stresses. Although all of the previously
published and discussed work relating or comparing static and
dynamic elastic moduli were for measurements on metal rods,
hard rocks and consolidated sandstone rocks, Montmayeur
(1985) and Montmayeur and Graves (1985) also made
measurements on unconsolidated frac sand cores. From their
tests they concluded that rock elastic properties are
controlled by stress conditions which are a function of the
maximum stress applied to the rock; for hydrostatic tests
this is the mean stress and for biaxial tests this is the
differential stress. Further they found that rock elastic
properties are a function of the number of pressure cycles
applied to the rock and of the applied stress system.
Concluding that dynamic and static properties should be
measured at the same time in the rock's stress history, they
found that elastic properties of unconsolidated sand are a
strong function of pressure cycle size or time. Above a mean
pressure of 4000 psi all microcracks closed and the rocks
behaved as if uncracked. Montmayeur (1985) suggested using
Wyllie's equation for calculating porosity at hydrostatic or

differential above 4000 psi. Also, above 4000 psi he found
that Biot's theory could be used to correct dynamic to static
elastic properties but below 4000 psi, both Biot's and
Walsh's theories should be applied to correlate dynamic to
static rock properties. He also found that, at high
pressures dynamic Young's modulus was less than static and
that this might be used to the testing procedure and timing
of measurement.

In a subsequent paper, Montmayeur and Graves (1986)
presented their correlations relating static and dynamic rock
properties citing microcracks as the key to the dynamic-
static relationships. For unconsolidated sands and
consolidated rocks not containing microcracks, Biot's theory
sufficiently relates dynamic and static properties. For
rocks with open microcracks, usually at pressure below 4000
psi, both Biot's and Walsh's theories are required to relate
dynamic to static properties. For this model, three rock
properties are required; microcrack porosity (ϕ_m),
dimensionless bulk compressibility (r_{cso}) when no stresses are
applied, and dimensionless bulk compressibility (r_{csi}) when
all internal stresses are relieved. A general correlation
relating the ratio of corrected dynamic to static bulk
compressibility with microcrack porosity was presented in
Equation 2-37a (Montmayeur and Graves 1986). For cores under

hydrostatic testing a correlation between the ratio of
dynamic corrected bulk compressibility at high stress (C_{bdc1})
to the one at in-situ stress (C_{bdc}) with microcrack porosity
(ϕ_m) was also presented (2-37b) but this correlation was not
found to hold for all biaxial data. They also correlated the
ratio of static (E_s) to corrected dynamic Young's modulus
(E_{dc}) for biaxial testing of sandstone cores on stabilized
cycles to external stress (P), (2-37c). Montmayeur contends
that for ideal materials without a history of exposure to
high pressure or temperature, such as sintered glass beads or
marine sediments, Biot's theory explains the dynamic to
static relationship.

$$\frac{1 - \dfrac{C_{bdc}}{C_{bs}}}{\left(3.2 \dfrac{C_{bdc}}{C_{bs}} - 1\right)} = 2140 \ (\phi_m) \qquad\qquad (2\text{-}37a)$$

where:

C_{bdc} = Dynamic bulk compressibility corrected with Biot's
relations (psi^{-1})

C_{bs} = Static bulk compressibility (psi^{-1})

(ϕ_m) = Microcrack porosity

$$\frac{C_{bdc1}}{C_{bdc}} = -0.54 + 0.083 \log (\phi_m) \qquad\qquad (2\text{-}37b)$$

where:

C_{bdc1} = Dynamic bulk compressibility corrected with

Biot's relations at high stress (greater than

4000 psig) (psi^{-1})

$$\frac{E_s}{E_{dc}} = 0.81 + 2.0 \cdot 10^{-4} P \qquad\qquad (2-37c)$$

where:

E_s = Static Young's modulus (psi)

E_{dc} = Corrected dynamic Young's modulus (psi)

In summary, work to relate static and dynamic elastic
moduli in the past fifty years has progressed with the
technology required to measure the properties. Most of the
work has been done on consolidated rocks with recent
attention directed at relating the difference in static and
dynamic moduli to microcrack density and closure.
Recognizing that to derive correlation between static and
dynamic measurement, both strongly dependent on the stress
state of the rock, it is best to measure them simultaneously.

Researchers, except for Montmayeur and Graves (1985) and
(1986), have found that dynamic Young's modulus is greater
than static Young's modulus. There is no general trend yet
established relating static and dynamic Poisson's ratio.

Work by Gassmann (1951), Biot (1956), and Walsh (1979) has been used to correlate static and dynamic rock properties.

Prior to 1936 most work with rock properties was on unconsolidated samples. Coming full circle, attention is also being directed at relating static and dynamic properties of unconsolidated rocks. Work with unconsolidated sand in this area has been restricted by the severe attenuation of shear waves through unconsolidated samples, especially at low pressures. More recently it has been shown that Biot's theory applies to correlate static and dynamic bulk compressibility for ideal media previously unexposed to high pressure and/or temperature. Work in this study with ideal media (glass beads), quasi-ideal (Ottawa frac sand), and real sand (recovered reservoir unconsolidated sand) should shed more light on this application of Biot's work and the possible application of Gassmann's work.

2.7. Applications

Research work continues in the area of relating elastic mechanical properties of unconsolidated sand and consolidated rocks. Wire line log information will provide information on fracture detection in consolidated intervals, sand production and reservoir compaction and subsidence. With this

information, reservoir and production engineers will be
better able to design effective sand control and reservoir
stimulation procedure programs and predict and plan for
reservoir compaction and surface subsidence. Because
fracture detection is concerned with consolidated formations
and this work focuses on unconsolidated sand properties, only
compaction and subsidence and sand control will be discussed
in this section.

2.7.1. Reservoir compaction and surface subsidence

The physical mechanisms of formation compaction during
deposition and later during production depletion are both
affected by pressure, overburden, time, and lithology.

Maxwell (1960) performed over two hundred experiments on
quartz sand and natural sandstone under pressure and
temperature conditions similar to reservoir conditions to
study compaction and cementation. He found that although the
two processes occur independently of each other, each is
facilitated by the flowing of alkaline saline water. While
compaction was also facilitated by the combination of high
temperature distilled water, cementation was not effected.
Cementation was found to occur within the first 24 hours of a
test and if saline water is present the degree of cementation

was found to be directly related to temperature; increasing degrees of cementation with increasing temperature. During formation burial many variables affect compaction and cementation. Maxwell (1960) lists them in order of importance: 1) overburden weight, 2) internal fluid pressure, 3) temperature, 4) time, and 5) lithology (including mineralogy, grain size distribution, and sorting), 6) pore fluid composition and 7) pore fluid movement.

When a petroleum reservoir or aquifer compacts by rearrangement of reservoir sands and plastic flow of the soft intergrain material as reservoir pressure decreases during fluid depletion, the surface above the depletion interval may subside. The magnitudes of reservoir compaction and surface subsidence are not equal and they do not occur simultaneously. Surface subsidence often causes costly problems, especially when it occurs unexpectedly in or near large metropolitan areas such as Venice, Italy, Houston, Texas and Long Beach, California. Surface subsidence is also a problem when its magnitude exceeds expectations and the means of reanalyzing and rectifying the situation cost millions of dollars, as it is at Ekofisk in the North Sea. Understanding and investigating the mechanisms involved during compaction and subsidence will lead to the development of reliable predictive models.

Surface subsidence typically occurs above aquifers and petroleum reservoirs with the following characteristics: 1) high porosity, 2) thick producing interval (in the hundreds of feet), 3) large surface area extent, 4) shallow depth (less than 5000 feet), and 5) large pressure decline during depletion (McCabe 1986). The only way to control reservoir compaction and surface subsidence is through pressure maintenance operations with the injection of water or gas. The magnitude of sand and rock compressibility during compaction (pressure decline) and expansion (pressure increase are different: it takes a larger pressure change to return a reservoir to pre-compaction thickness than the pressure change required for compaction. Problems arise when the pressure increase necessary to pump the reservoir back up exceed the fracture pressure of the formation and unwanted fractures and formation damage occur. However, Allen (1966) notes that in the Wilmington Field the formation did not fracture even when the water injection pressure exceeded the overburden pressure. With steady increase of injection rate, the permeability at the wellbore increased up to 10 percent which was attributed to recovery of compaction induced permeability loss as the effective stress was lowered with increasing pore pressure.

Two infamous urban surface subsidence problems are
Houston, Texas and Long Beach, California. The city of
Houston has subsided $1\frac{1}{2}$ to 8 feet in the past 70 years. This
subsidence was caused primarily by aquifer compaction as the
ground water level declined and to a lesser degree, by small
local petroleum reservoirs during depletion, Holzer and
Bluntzer (1984). The ground level of Long Beach, California
dropped up to 29 feet at a rate of 1 to 2 feet per year
during the depletion of the underlying Wilmington Oil Field.
Efforts to stop or reduce reservoir compaction and surface
subsidence with water injection pressure maintenance were
successful with immediate results. Although subsidence has
ceased, the reservoir has rebounded only a fraction of its
total subsidence: in 9 years (from 1958 to 1964) the
reservoir rebounded 8 to 9 inches with associated surface
rebound 40-50 percent of the reservoir rebound at a rate of $\frac{1}{4}$
feet per year, Allen (1967).

Perhaps the most notable recently publicized subsidence
problem is that in the North Sea Ekofisk Field. Although the
reservoir compacted 3-5 meters (9-15 feet) in the center of
the field, after commencing production in 1970, the
subsidence was not noticed until 1984. Although engineers
planned for some subsidence, the actual magnitude exceeded
expectations. The field has a large areal extent, thick

producing interval and large pressure decline during
depletion but it is not typical of most compacting
reservoirs: Ekofisk consists of 2 naturally fractured
(hairline) chalk formations about 10,000 feet deep.
Researchers have not noticed any signs of effective
permeability reduction as the reservoir compacted. The area
of subsidence on the sea floor closely resembles the
underlying reservoir in size and shape. The center has
subsided approximately 40-45 cm per year at a constant rate
since 1979 but the prediction of future subsidence rate is
difficult. Computer modeling is inexact because of
limitations imposed by geophysical and well log information
of the overlying rock and accurate measurements of early
phases of compaction and subsidence are not available for
history matching (McCabe 1986; Barton et al. 1986). Pressure
maintenance operations through water and gas injection have
begun but computer modeling accuracy is as yet undetermined
(McCabe 1986). As in the Wilmington Field compaction, the
seabed subsidence is 65 to 85 percent of the Ekofisk
reservoir compaction (Wiborg and Jewhurst 1986).

Understanding compaction and expansion mechanisms will
help engineers develop methods to more accurately predict
reservoir and overburden compaction that result in surface
subsidence which will reduce costly miscalculations. In the

late 1960's Allen (1967) and Geertsma (1966) began modeling

compaction and subsidence. Allen (1967) describes a

technique using a collar locater log to measure the

shortening of casing joints and determine the magnitude of

compaction. Scorer and Miller (1974) note Geertsma's (1966)

linear formula, Equation 2-38, which was used to closely

approximate the surface subsidence at Long Beach.

$$U_z (0,0) = -2(1-\nu) \; C_m \cdot h \cdot \Delta P \left\{ 1 - \frac{C}{\sqrt{1 + C^2}} \right\} \qquad (2\text{-}38)$$

where:

   $U_z(0,0)$ = Subsidence at the center of the disc-shaped reservoir

   ΔP = Change in pressure

   $C = \dfrac{d}{r}$

   d = Depth of the reservoir

   r = Radius of the reservoir

   C_m = Uniaxial compaction coefficient = $\dfrac{1}{V_b} \left[\dfrac{\delta V_p}{\delta P} \right]$

   h = Thickness of the reservoir

More recently, de Waal and Smits (1985) have developed a

loading rate dependent model to predict reservoir compaction

and surface subsidence. Their model uses laboratory

measurements to describe compaction with a single normalized

non-linear compaction curve. Further understanding and

accurate predictions may come from the development of ways to monitor and model compaction on in-situ with wireline logs.

2.7.2. Sand control

The flow of unconsolidated and friable sand has been a costly problem in the oil and gas industry for decades. Sand production wears out oilfield equipment prematurely, causes sand bridging in surface flow lines, casing and tubing, thus causing expensive time consuming workovers. The shallow tertiary formations, especially those of the Miocene Epoch, throughout the world are the location of many sand flow problems although no general relationship between depth and occurrence of sand flow problems has been established (Rogers 1971a; Suman et al. 1983). Sand flow appears to be rate-sensitive and because the maximum sand-free flow rate can be uneconomically low, producers are often compelled to flow at higher rates and accept the problems associated with sand flow (Rogers 1971a).

2.7.2.1. Predicting sand flow problems

It is best to be able to predict sand flow problems so that sand control methods can be implemented prior to expensive workovers and equipment replacement, and sand

control measures should be implemented prior to the onset of any sand flow problem. Stuivenwold and Mast (1980) discuss the merits of a tool developed by Shell research to accurately detect sand production in multi-phase flow wells, gas wells and single-phase liquid wells. They consider this tool to be more sensitive than the acoustic sand detector and it helps locate the sand producing interval.

According to Tixier et al. (1973) and Rodgers (1971a) sand flow is a function of many forces acting on the sand including flow rate pore fluid pressure depletion, near perforation pressure gradient, fluid induced scrubbing action on the sand, and interfacial tension between sand grains and pore fluids. Two factors are important in determining whether or not the sand is able to overcome these forces: 1) the formation's in-situ strength and 2) the ability of the sand to form stable arches around perforations, Tixier et al. (1973).

A method for relating sand flow to acoustic longitudinal wave velocity, bulk density, and sand shaliness and elastic constants was presented by Tixier, Loveless, and Anderson (1973). Because these measurements are made with wireline logging tools they reflect the in-situ formation strength. Using the dynamic elastic constants definitions and the Anderson, et al. (1972) relationship between shaliness and

Poisson's ratio, Tixier et al. (1973) showed that although shear modulus, G, and bulk compressibility, C_b, are fairly insensitive to Poisson's ratio and their ratio, $\frac{G}{C_b}$, is insensitive to shaliness, they are affected by porosity and thus compressional wave travel time.

Tixier, Loveless and Anderson (1973) note that, "So far, we have no cases where sanding has occurred in oil or gas sands with $\frac{G}{C_b}$ greater than $0.8 \cdot 10^{12}$ psi^2." They also state that when $\frac{G}{C_b}$ is less than or equal to $0.7 \cdot 10^{12}$ psi^2 sand control has been necessary for tertiary Gulf Coast sands. They also indicate that formations in which shear modulus, G, is greater than $0.6 \cdot 10^6$ psi with either oil or gas production, sand flow should not be a problem. The authors had yet to establish a relationship between water production rates and the dynamic elastic moduli. Details of their calculation methods and pertinent assumptions can be found in SPE 4532.

There are three general sand flow management methods in practice: 1) production at flow rates below the maximum sand-free flow rate with natural sand arching, 2) mechanical sand control using gravel packs, screens, and slotted liners, and 3) synthetic sand consolidation using chemicals. Each of these methods will be discussed individually.

2.7.2.2. Sand arching

Numerous researchers including Terzaghi (1945), Hall and
Harrisberger (1970), and Stein and Hilchie (1972)
investigated the mechanical process of natural sand arch
formation across a hole, and more specifically, across
wellbore perforations. Their work has shown that the
formation and stability of natural sand arches across
wellbore perforations is dependent upon a number of factors
such as formation permeability, interfacial tension, pore
fluid saturations, sand grain type and geometry, fluid
pressure, in-situ stress state, and production flow rates.

Hall and Harrisberger (1970) postulated after their
"trap-door" experiments that because loosely packed sand
failed to arch there are two conditions required for sand
arch stability. "1) dilatency and 2) cohesiveness or some
other restraint on the surface grains." Dilatency is defined
by the authors as an increase in matrix volume and porosity
caused by rolling and sliding of grains over one another.
Cohesion is caused by grain cementation and by capillary
forces. They also noted that arching was a function of flow
rate across the arch at low stress but remained stable
independent of flow rate at high stress.

Tippie and Kohlhaas (1973) investigated the effects of
flow rate on unconsolidated sand arch stability using a
physical sand pack well completion model. Their experiments
showed that arch size is a function of the production rate;
as the rate increases so does the size of the arch. They
noted that sand failure could occur if production rates were
not started at low rates and slowly increased, that arch
growth is dependent on production rate and the size of the
initial arch, that fines migration could contribute to arch
failure. They observed two distinguishable arch failure
mechanisms: 1) an ongoing failure in which small quantities
of sand are produced over long time periods and 2) a massive
failure in which a lot of sand is produced in a short time.

Cleary, Melvan and Kohlhaas (1979) investigated fluid
property and confining stress effects on arch stability for
unconsolidated sands. They observed that "an arch which
forms around a perforation orients itself so that its minimum
cross-sectional area faces the direction of maximum stress."
Using two pore fluid systems, water-kerosene and water-
mineral spirits, they noted that cohesion (interfacial
tension) and viscous effects are important in the formation
and restructuring of sand arches.

Stein and Hilchie (1972) presented a method to estimate
the maximum sand-free production rate from friable sandstones

using the natural sand arching mechanism. In order to make this estimate, three things are necessary: 1) formation strength (dynamic shear modulus) from well logs, 2) a formulation of the stabilization mechanism for the friable sandstone face, and 3) the application of the strength and stability mechanism considerations to the well performance (Stein and Hilchie 1972). In practice, the required data are the dynamic shear modulus estimated from acoustic velocity logs and at least one production test for a well in the same area to estimate the critical pressure drawdowns for other wells in the area. The production test, consisting of a series of increasing production rates, is used to determine the flow rates for which there is no sand flow and the flow rate for high, unstoppable sand flow. This data is related back to the well in question in the same area as the test well to estimate the maximum sand-free flow rate. This method assumes "that the ratio between total reservoir pressure drawdown and the pressure gradient at the face of individual sand arches was the same for all wells" (Stein et al. 1974).

Stein, Odeh and Jones (1974) presented a more specific method for estimating maximum sand-free production rates than Stein and Hilchie (1972) which eliminated their broad assumption. The new method requires knowledge or reasonable

estimation of formation permeability, dynamic shear modulus
and pore fluid properties.

2.7.2.3. Mechanical sand control

Mechanical sand control methods use screens, gravel
packs, or slotted lines to control the flow of sand from the
formation. Of the three general sand control methods, gravel
packing is considered to be the most reliable. The use of
any of these mechanical methods requires information about
the formation sand grain size distribution which is easily
found by performing a sieve analysis on recovered sand
samples. This knowledge about grain size distribution is
necessary to correctly choose the screen opening size, the
gravel size for gravel packing and the slot opening size for
sloted liners. Other information about the formation, gravel
material, and slot an screen configuration are important for
installing a reliable mechanical sand retention device
(Suman, Ellis and Snyder 1983).

The literature is filled with information on choosing
the best mechanical device or combination of devices, gravel
packs in conjunction with slotted liners for example, for the
sand control problem at hand. Detailed discussion regarding
any of the aforementioned mechanical sand-retention methods

is beyond the scope of this work. A good starting place for information to help design good mechanical sand control is Suman et al. (1983).

The one relationship that exists between this work and mechanical sand control is that the compressibility of frac sand and glass beads in both 20/40 and 60/80 mesh are investigated. Because these grain sizes are typical of many grand pack sand sizes the information obtained in this study should help toward gaining knowledge about the compaction and compressibility of the gravel pack material under stress conditions.

2.7.2.4. Chemical consolidation of sand

Rogers (1971c) discusses synthetic sand consolidation using organic chemical resins. The process involves injecting the liquid resin into the formation where it subsequently hardens. Rogers (1971c) and Rike (1966) cite six characteristics of a good sand consolidation resin: 1) suitably low viscosity to permit pumping into the formation while maintaining favorable polymerization, 2) strong resin, 3) long shelf life, 4) good adhesion to sand grains with chemical bonds, 5) resistant to well bore and reservoir fluids when hardened, and 6) short time span for hardening.

Synthetic sand consolidation is classified by the process involved; phase separation or overflush. According to Rogers (1971c) and Rike (1966) a good consolidation process has the following characteristics: 1) the resin should arrive at well site prepared for injection to minimize on-site preparation, 2) the chosen process should be applicable to open the expected temperature range, 3) the chosen process should work for formations with different mineral contents, 4) the resin should not harden prematurely before being placed in the formation, and 5) the decrease in formation permeability should be minimized.

Suman, Ellis, and Snyder (1983) list favorable reservoir characteristics that could reduce synthetic consolidation costs and result in a less expensive sand control method than gravel packing. A good candidate zone would have the following: high reservoir pressure, limited tendency to produce sand, no previous production of sand, high sand quality, thin (less than 10 feet thick) zone, and good vertical permeability, Suman et al. (1983). The authors provide a comprehensive list of available chemical sand consolidation systems which includes application details. In addition they provide an excellent discussion of synthetic chemical consolidation.

Rike (1966) reviews the use of a phenolic resin, developed by Humble Oil and Refining Company, to consolidate oil sand in south Louisiana in 545 jobs. He found that process was shown to be successful in both the laboratory and in the field and that unsuccessful treatments could usually be corrected with subsequent retreatment. The success of the process could be improved by paying particular attention to perforation and by using clean fluids.

Davies and Meijs (1980) of Shell research present a discussion of a synthetic sand consolidation technique using "Silicalock". This method showed favorable results in field testing; reduction in sand production with minimal loss in productivity. Their process involves injecting a stream of vaporized liquid silicon tetrachloride in nitrogen gas into the formation. Consolidation occurs as the injected chemicals react with the connate water to form silica cement. The advantages of this process are that the treatment is through tubing so no rig is required and only gas is injected so the chances of productivity reduction are minimized, the on-site chemistry is simplified and chemical placement problems are reduced.

In summary, there are many different ways to control the flow of sand out of the formation; mechanical processes, chemical processes and natural processes. Each one has its

particular merits and accompanying disadvantages. Although
detailed descriptions about the sand control are beyond the
scope of this study there are some areas of overlap between
this work and information which can help in sand flow
prediction and sand control design. Information about
unconsolidated sand compressibility for grain sizes
appropriate for gravel packing will help researchers
understand stress effects on gravel packs in-situ, in-situ
formation strength characteristics from well logs (wave
travel times) can help indicate the potential for sand
control problems so appropriate measures can be taken.

3.   EXPERIMENTAL APPARATUS: DESCRIPTION AND CALIBRATION

3.1.   History and Development

Krug (1977) designed the original equipment used in the
Acoustic Velocity Sand Control Project in the Petroleum
Engineering Department at the Colorado School of Mines. His
triaxial pressure cell allowed the independent variation of
axial stress, confining stress, and pore fluid pressure. The
cell was constructed from 5.5 inch O.D. steel pipe with 0.5
inch wall thickness, designed for 15,000 psi. He used the
cell to measure bulk compressibility, porosity, resistivity,
permeability and dynamic elastic properties of rock samples.
He measured the change in porosity with a fluid extrusion
measurement system and the longitudinal strain with strain
transducers. Colorado School of Mines Thesis number T-1964
contains details of his equipment description and work.

Graves (1982) modified the existing triaxial cell to
improve consolidated rock measurements of pore volume change,
shear and longitudinal wave velocities, and radial and axial
strains. She also used the fluid extrusion system for
measuring change in pore volume, noting that results were
unreliable. The radial and axial strains were measured with
strain gauges mounted on the cores, a time consuming method

that was not advised for future research. Shear and
longitudinal wave travel times were measured using the pulse
technique.

Montmayeur (1985) added further modifications to the
triaxial cell to facilitate improved measurements on
consolidated rock and unconsolidated sand. Special problems
with unconsolidated sands precluded the use of strain gauges
to measure radial and axial strains and shear wave
attenuation problems made it necessary to upgrade the wave
propagation travel time measurement system. He did not
modify the basic cell design, however. Details of his
triaxial cell assembly and calibration can be found in
Colorado School of Mines Thesis T-3099.

3.2. Triaxial Cell Design

The basic triaxial cell (Figure 3.2.a) was not modified
for this work. Axial pressure is still applied with a piston
(A) in the top cap and the confining fluid, hydraulic oil,
enters the cell at the bottom and exits through a line in the
top cap. Two suspending rods (C) support the core holders.
The p- and s-wave crystal heads (B) are discussed in sections
3.4 and 3.5 of this chapter. All electrical connections are
made through the top cap.
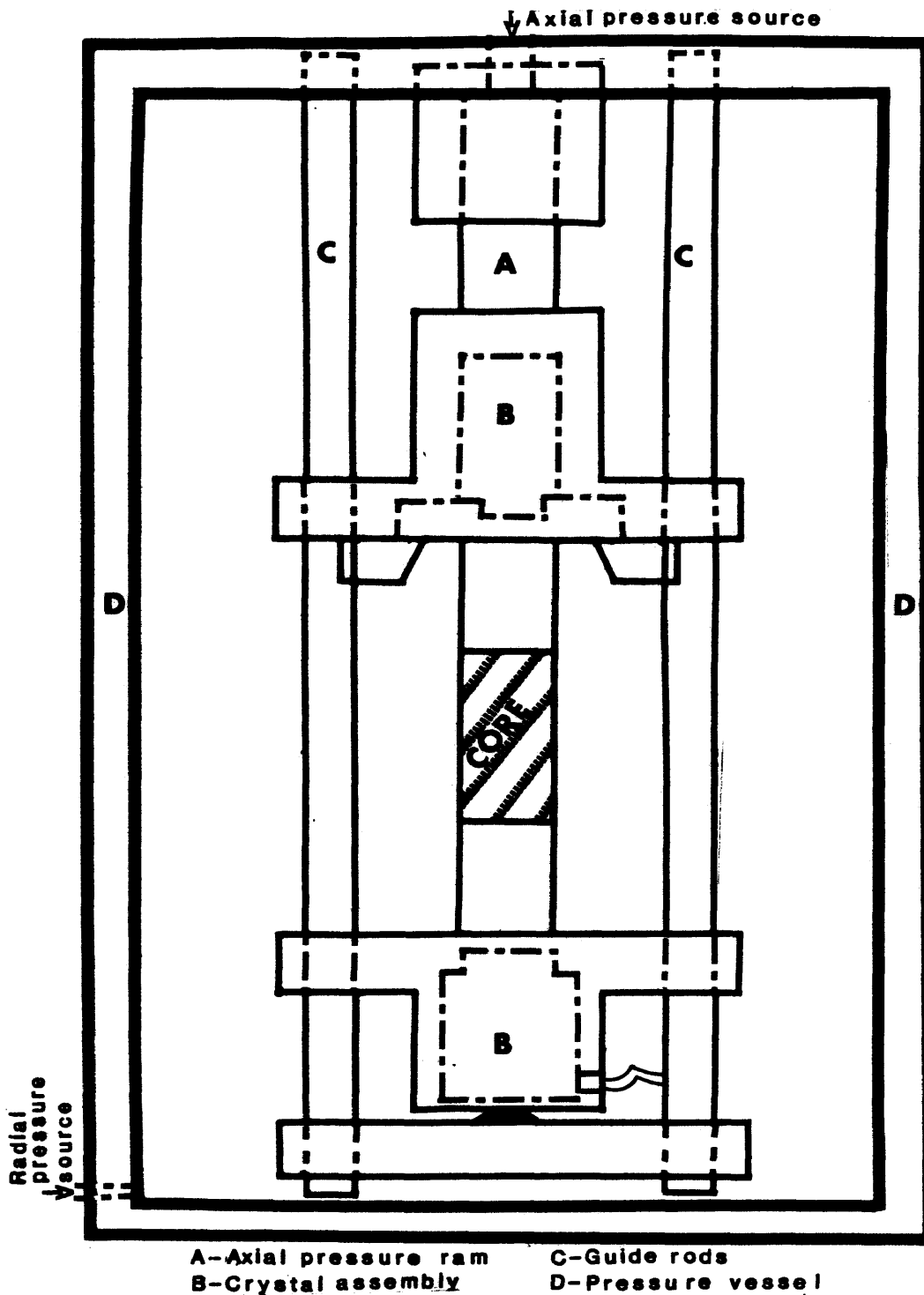
Figure 3.2.a.   Triaxial cell.

Both the axial pressure piston (A) and the bottom core holder support are rounded. This allows the top and bottom core holders to rotate slightly so that good contact between the top and bottom core and head faces can be achieved.

Although the cell is currently designed to withstand 10,000 psig pressure, it was only used up to 5000 psig axial pressure and 5000 psig confining pressure. Confinement pressure cannot be greater than the axial pressure with this design. Figure 3.2.b is a schematic diagram of the cell pressure system. The cell pressure system was redesigned to include a set of pumps whose pressure rate could be controlled. The ENERPAC pump used previously is not easy to control and Montmayeur (1985) recommended that an alternate pump system be added. Details of the pore and confining fluid systems are found in sections 3.6 and 3.7.

3.3.   Core Mounting Assembly

A complete discussion of core preparation methods for the consolidated and unconsolidated samples is presented in Chapter 4. In summary, consolidated cores were cut approximately 1.5 inches long by 0.75 inches in diameter. Unconsolidated core packs were molded to the same dimensions by saturating the sand sample in brine solution and quick
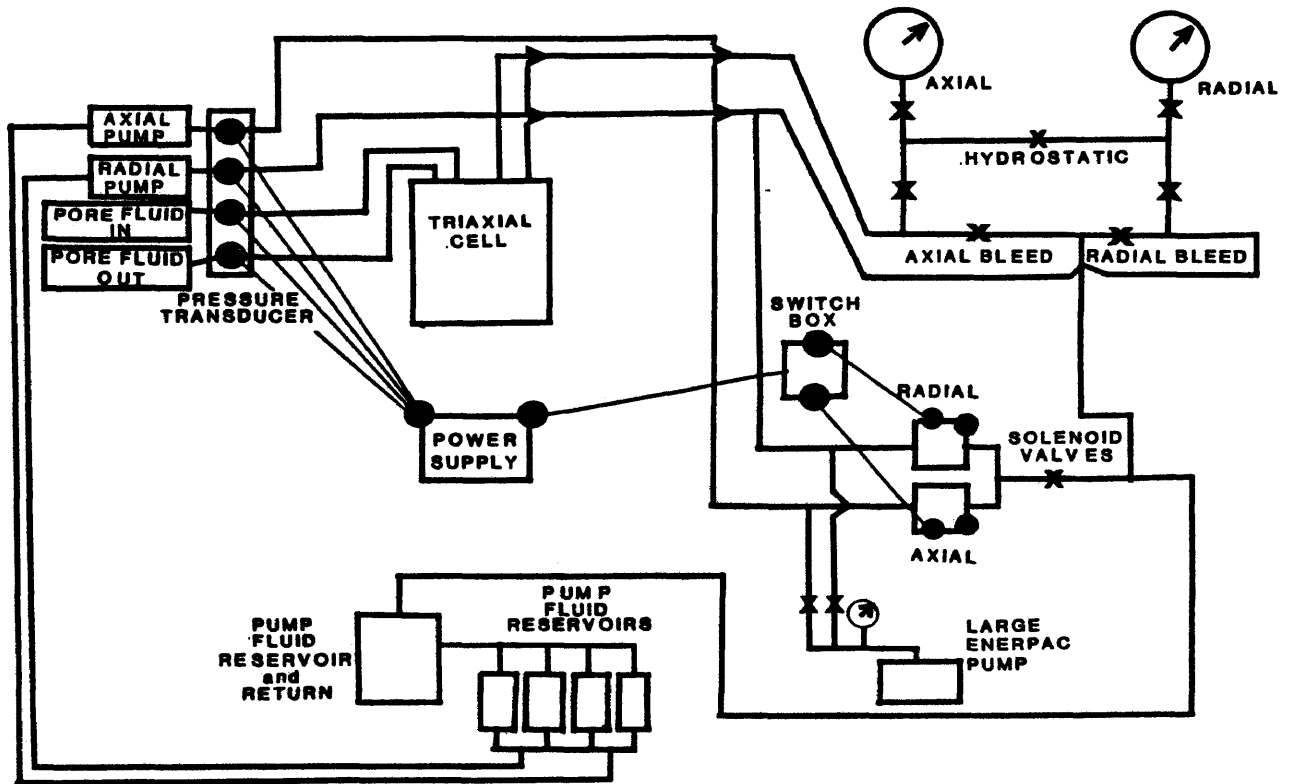
Figure 3.2.b. Cell pressure system.

freezing in liquid nitrogen. The object was to keep the unconsolidated core packs frozen until they could be mounted in the cell and stressed to 500 psig.

The brine saturated consolidated rock and frozen unconsolidated sand cores were mounted in the same way (Figure 3.3.) but the assembly of the core and sleeve holder was different. For the consolidated cores, a 400 mesh screen (A) was placed at each end of the core to prevent fines or loose grains from migrating into and clogging the pore fluid system. Heat shrink tubing of 0.75 inch diameter was applied to the core assembly, extending approximately 0.75 inches over each end of the core to provide an overlapping seal over the heads (C).

For the unconsolidated packs, the heat shrink tubing could not be directly applied because the heat needed to shrink the tube around the core would melt the sample prematurely. The assembly of the unconsolidated sand packs was as follows:

A. Two 2.5 inch long pieces of 0.75 inch diameter heat shrink tubing were seperately shrunk around a 0.75 inch diameter metal rod. One piece was used for freezing the core and the other was used for mounting the core in the cell.
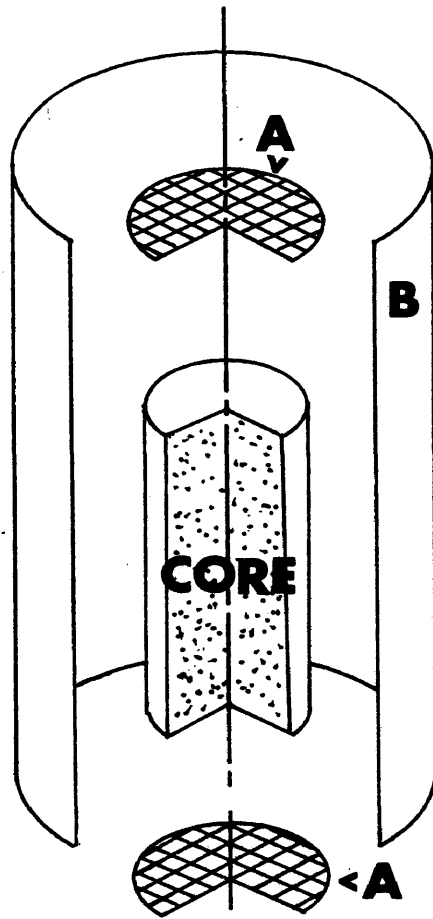
A-400 MESH SCREEN
B-HEAT SHRINK TUBING

Figure 3.3. Core mounting assembly.
[After Montmayeur (1985)]

B. One end of a piece of the pre-shrunk heat shrink
   tubing was plugged with a 0.75 inch steel plug and
   inserted into the steel core mold apparatus (see
   Montmayeur 1985). Sand and brine were added to form a
   core approximately 1.5 inches long. The weight of the
   sand added was measured. Another 0.75 inch steel
   plug was inserted in the top end and the core was
   removed from the mold and frozen by immersing if in
   liquid nitrogen for 2 minutes.

C. After removal from the liquid nitrogen the core was
   cut out of the frozen heat shrink tube and its
   diameter, length and weight were measured.

D. The core was quickly inserted into the second piece
   of pre-shrunk heat shrink tubing and mounted in the
   test cell as described in Section 3.3 of this study.

For the larger grain size (20/40) packs two layers of
heat shrink tube were necessary because the large angular
grains would perforate a single layer of heat shrink tubing.

For the last cores tested, Reservoir Samples 4-A, 7-A,
3-A, 5-A, 5-B, 6-A, 2-B and the glass bead packs, a technique
was developed that allowed the same heat shrink tube to be
used during both freezing and testing. A layer of Saran Wrap
was inserted between the steel plugs (see Step B) and the
core/heat-shrink tubing. This allowed the plugs to be more

easily removed from the ends of the core. There had been
problems separating the frozen core and steel plugs. Also
sand grain particles remained imbedded in the heat shrink
tube after freezing.

The core was mounted in the cell. After tightening the
core longitudinally into the apparatus to ensure good contact
between the core and heads, the hose clamps around the heads
were tightened. A 0.5 inch long piece of 0.75 inch I.D. by
1.0 inch O.D. Tygon tubing was placed between the core heat
shrink extension and the hose clamp to help ensure a good
seal and prevent the hose clamp from cutting the heat shrink
tubing.

3.4. Static Measurement System

Static measurements were not made on cores in this
study. Comparisons of static and dynamic measurements were
made between data obtained by Montmayeur (1985) and that of
this study. Details of his static measurement system and
calibration can be found in his dissertation, T-3099 at the
Colorado School of Mines.

3.5. Dynamic Measurement System

3.5.1. Description

The wave pulse technique used by Graves (1982) and Montmayeur (1985) was also used in this study to measure the shear and longitudinal wave travel times through the core samples. The external wave propagation and measurement system was unchanged since Montmayeur (1985) but the internal p- and s-wave crystal head design was changed.

Figure 3.5.1.a is a schematic diagram of the external wave generation and measurement system. The square pulses are triggered by a Hewlett-Packard 214-A pulse generator. The pulse amplitude was adjusted for each core to ensure superior wave measurements. The elapsed time between pulses was adjusted to remove interference between subsequent wave trains. A Nicolet 204-A digital oscilloscope received the wave signals at a 50ns sample rate and sent them to the Omnigraph 100 X-Y plotter so that they could be recorded to ensure consistency in choosing wave travel times. Figure 3.5.1.b shows the details of the heads containing the p- and s-wave piezoelectric crystals which generate and receive the waves. This head was designed and built by Preston Graves. The bottom and top stainless steel heads are
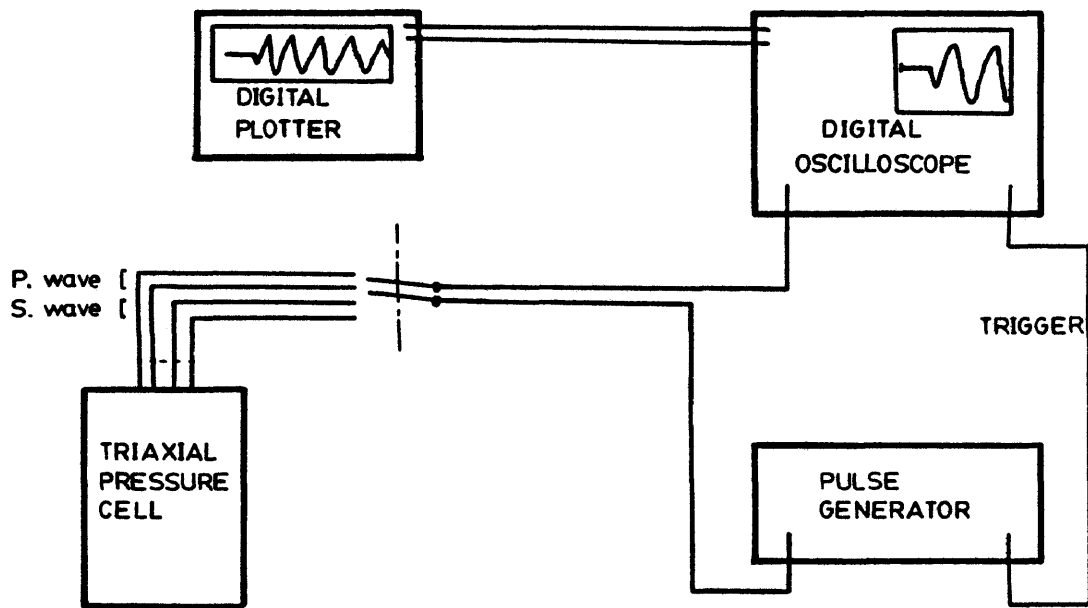
Figure 3.5.1.a.   External wave measurement system.
[After Montmayeur (1985)]
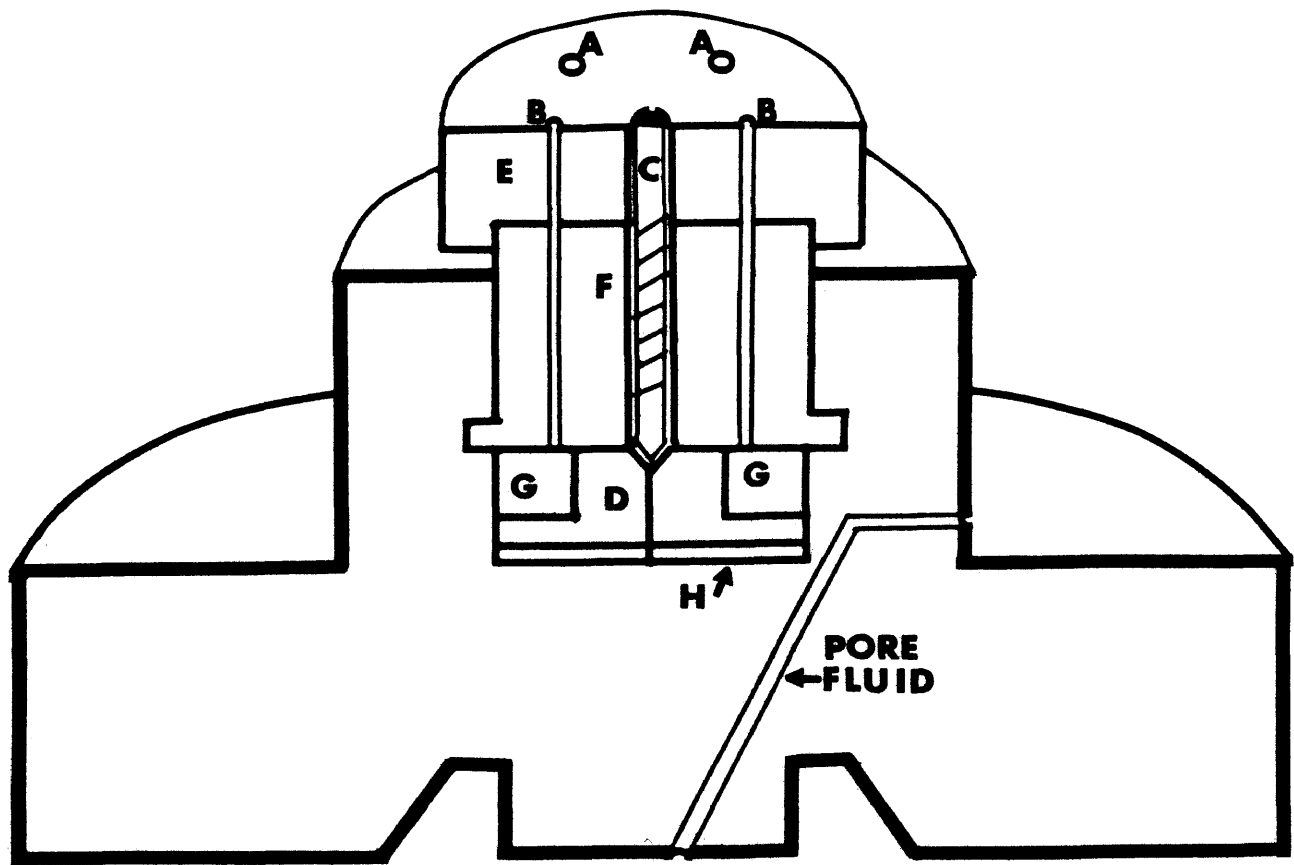
PIEZOELECTRIC
CRYSTAL HEAD DETAIL

A—Screw terminal holes   E—Nylon sleeve

B—Wire pass through holes   F—Steel sleeve

C—Screw   G—Shear wave crystals

D—Nylon spool   H—Compressional wave
                                 crystals

Figure 3.5.1.b. Piezoelectric crystal head design detail.

identical, both are isolated from pore and confining fluids and are maintained at atmosphere pressure. The lead titanate zirconate crystals are a broad band width source and are well suited for the ultrasonic measurements. Both the longitudinal and shear crystals have a 750 KHz resonant frequency. The heads are grounded for the wave travel time measurements as they were for Montmayeur (1985) so that there would not be interference between the two waves.

The p-wave crystals resemble a thin circular wafer cut in half (H) that sit at the base of a cylindrical cut in the stainless steel head. On top of the p-wave crystals lies a piece of nylon that resembles the bottom of a spool; it is also cut in half (D). Surrounding the spool are the s-wave crystals (G). They resemble a hollow cylinder, also cut in half. Atop the s-wave crystal and nylon spool is a steel sleeve (F). Two holes (B) are drilled into the sleeve through which fine wire can be connected to the crystals. A screw is centered in the sleeve (C) which, when tightened, separates the nylon spool and pushes the s-wave crystals to the walls to contact the steel head. Another nylon sleeve (E) lies on top of the steel one. It also contains the wire pass-through holes and form holes (A) for screw terminals to connect the crystals to in- and out-going electronics.

It should be noted that the crystal head was redesigned

to facilitate better wave measurements for unconsolidated samples. Typically the pore fluid passes vertically down through the center of the crystals. Fluid flowing through the crystals might effect the wave propagation. Because shear and longitudinal waves are attenuated in unconsolidated samples, every effort was made to improve wave transmission to the core sample. With this in mind, the pore fluid hole was drilled as shown on Figure 3.5.1.b, rather than vertically down through the crystals.

For this study, although both the top and bottom heads can be used as either source or receiver, the top head is used as the source with the bottom head as receiver. In addition, in the bottom head both halves of the s-wave crystals are coupled to improve wave resolution.

3.5.2. Calibration

The longitudinal and shear wave travel time calibrations were not dependent on confining or axial pressure within the pressure limits of this experiment. The calibrations were made to determine the wave travel times through the stainless steel heads on each end of the core.

Figure 3.5.2.a shows the calibration curves for the longitudinal and shear wave travel times. The system was

DYNAMIC SYSTEM CALIBRATION
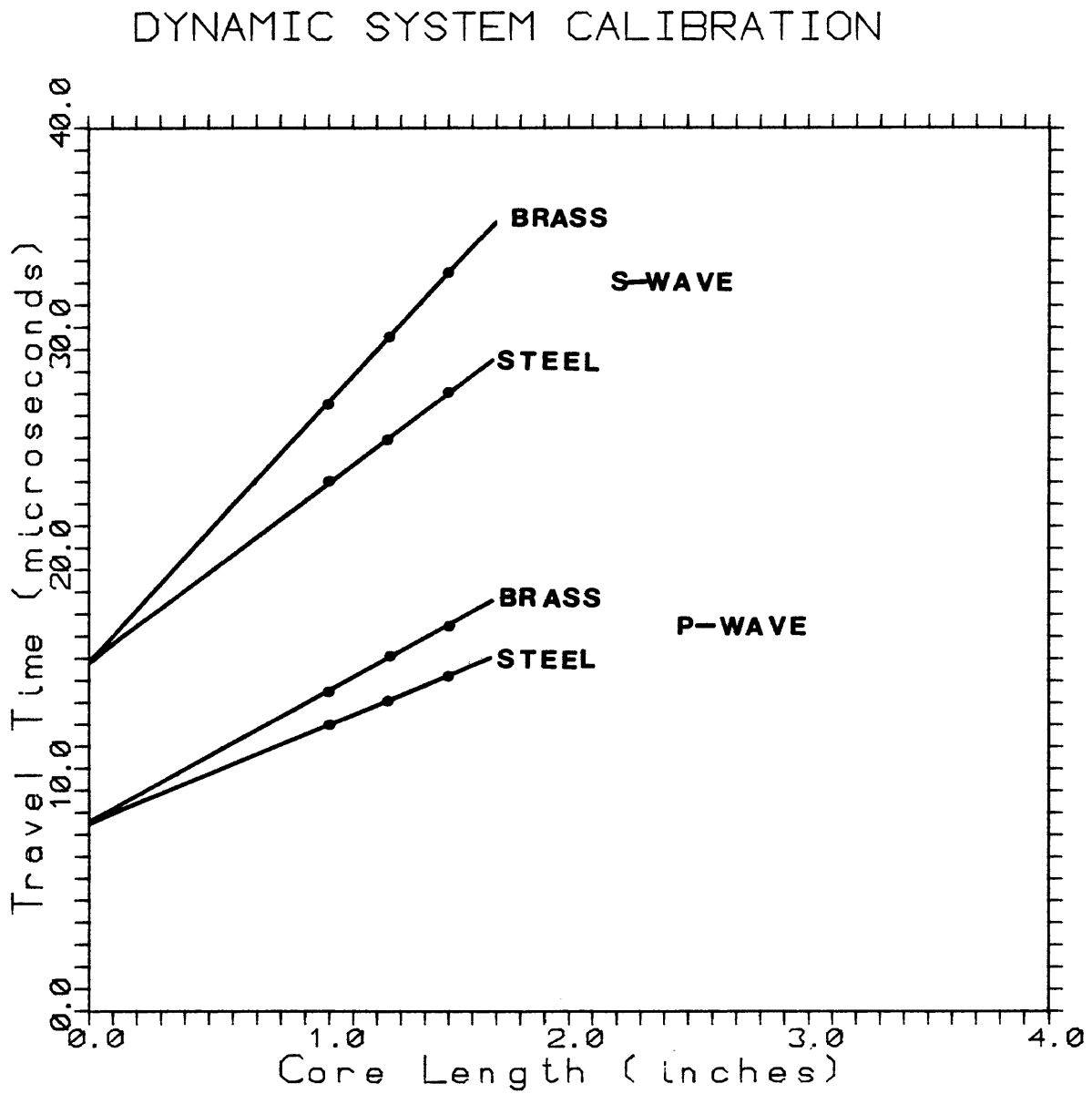
Figure 3.5.2.a.   Dynamic system calibration curves.

calibrated by inserting 0.75 inch diameter metal (stainless steel and brass) rods of different lengths into the core holder and passing p- and s-waves through them with 5000 psig axial pressure applied to ensure good coupling. Shear and longitudinal wave travel times were then chosen for each rod of each metal used and plotted versus core (rod) length. A least squares best fit line was drawn through the points for both p- and s-waves for each metal and extrapolated to zero core length (Figure 3.5.2.a). The travel time at zero core length is then the travel time through the heads. When no core was in place, the travel times through the heads were measured by passing waves through the top and bottom heads in contact with each other. Results were the same as those using the core length extrapolation method described. The steel and brass core travel times were measured independently by Dr. Guy Towle (Table 3.5.2) and his results were compared to those of this study, as well as those by Krug (1972), Graves (1982) and Montmayeur (1985).

The calibration times through the heads are as follows:

p-wave : 8.661 μsec

s-wave : 15.840 μsec

Using these corrections, Young's modulus and Poisson's

Table 3.5.2.

Comparison of Measured Brass and Steel Elastic Properties

Property	Measured by	Brass	Stainless Steel
V_p(ft/sec)	Howarth (author)	14048	18944
	G. Towle	13900	19300
	Montmayeur (1985)	13810	—
	Krug (1977)	—	18423
	Graves (1982)	—	18607
V_s(ft/sec)	Howarth (author)	7082	10216
	G. Towle	8070	10200
	Montmayeur (1985)	6950	—
	Krug (1977)	—	10074
	Graves (1982)	—	10027
$E(10^6\text{psi})$	Howarth (author)	15.1	30.0
	Published*	15.0	28.4
	Graves (1982)	14.8	27.7
	Montmayeur (1985)	14.0	28.0
ν	Howarth (author)	0.330	0.293
	Published*	0.340	0.290
	Graves (1982)	0.329	0.296
	Montmayeur	0.327	0.297

* Higdon et al.(1976)

ratio were calculated for the brass and steel rods and compared to their known elastic properties using Equations 2-18 (a-f). These are presented in Table 3.5.2.

Figure 3.5.2.b is an example of longitudinal and shear wave trains through a steel rod. The lower train is the longitudinal wave and the upper train is the shear wave.

3.6. Pore Fluid System

The pore fluid system used by Montmayeur (1985) was unchanged (Figure 3.6) except for the removal of the fluid extrusion pore volume measurement system. Montmayeur (1985) found that this system was unreliable and that results were not repeatable. It was removed until a suitable system could be designed and implemented for future work. The Ruska proportioning pump system pumps the mineral oil drive fluid which in turn circulates the brine pore fluid through the core.
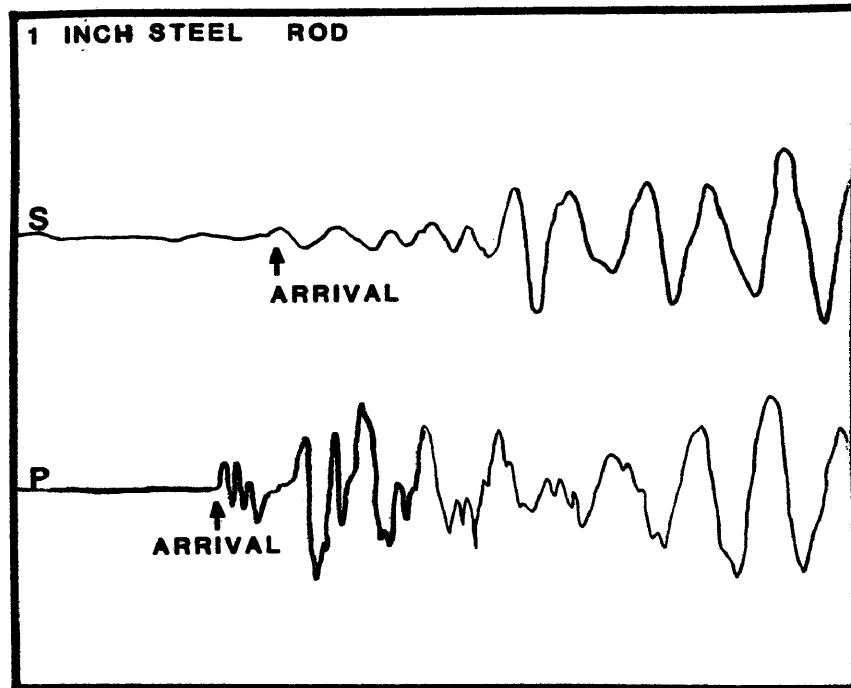
Figure 3.5.2.b.   Shear and longitudinal wave train examples
                  through a steel rod.
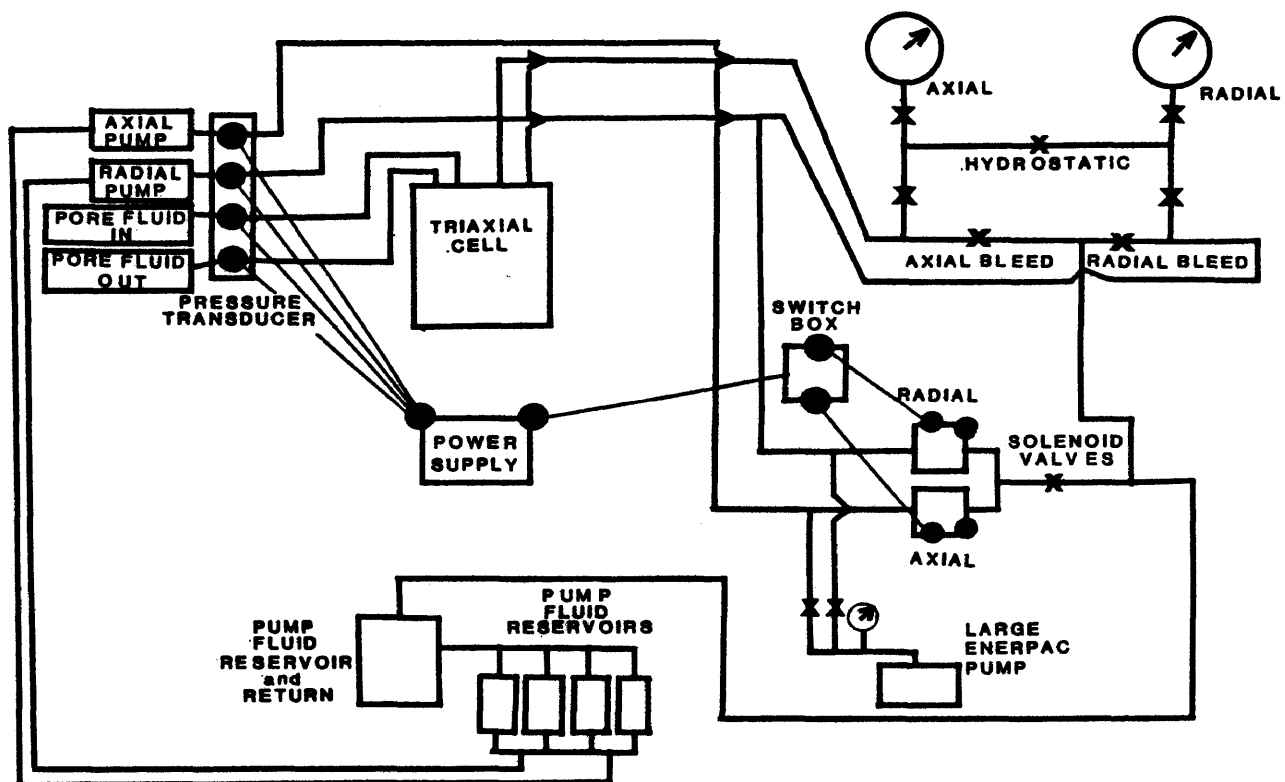
Figure 3.6. Pore fluid system. [After Montmayeur (1985)]

4. CORE PREPARATION

Dynamic tests were run on both consolidated and unconsolidated cores. Consolidated rocks were tested to become familiar with the testing apparatus, to calibrate the equipment, and to add to the consolidated rock data base. Dynamic measurements were made on glass bead packs, frac sand packs and natural reservoir sand packs. As part of the research, comparisons were made between Montmayeur's (1985) frac sand data on which both static and dynamic measurements were taken, and those of this study. It was necessary, therefore, to prepare the unconsolidated cores in the same manner as Montmayeur (1985). Similarly, the dynamic measurements through the consolidated cores were compared to Montmayeur's (1985) and so the consolidated cores had to be similarly prepared for testing. Because of the inherent physical differences between consolidated and unconsolidated rocks, preparation of core samples was different. Details of the two core preparation procedures follow. Appendix D contains the core nomenclature code for all samples.

4.1. Consolidated Rock Cores

Five of Montmayeur's (1985) consolidated cores and ten Berea sandstone cores were prepared for testing. The Berea cores, donated by Marathon Oil Company, were cut, ends trimmed parallel, cleaned, dried, measured for porosity and air permeability, saturated with brine or kerosene and measured for liquid permeability. Of the five cores used by Montmayeur, STB2, STB5, STD2, K5C2, and STB1, one (K5C2) broke during the liquid permeability test. Of the ten Berea cores, HCB3 and HCB4 did not survive the liquid permeability test. Of the prepared cores, six were used for the hydrostatic test dynamic measurements (STD2, STB5, HCB5, HCB6, HCB11, AND HCB13). Only HCB6 broke during the test procedure.

It was desirable to follow Montmayeur's method for consolidated core preparation as closely as possible in order to add to his data base and to have comparable results. Montmayeur's cores were found in vials, some dry, some partially soaking in 50,000 ppm NaCl brine solution. The cores were encrusted with dried salt and the ends of some were still coated with epoxy glue from his testing preparation. The cores were in this condition for over 18 months before attempts were made to clean them.

The first attempt to clean the cores was to scrape off the salt and epoxy, trim the ends parallel and clean them in a Soxhlet extractor with toluene. The cores were removed from the Soxhlet, dried in an oven at 600°F for four hours as Montmayeur did. Subsequent porosity measurements showed extreme reduction of pore space most likely due to precipitation of salt within the pores. At this point the decision was made to try to clean the salt out of the cores with an osmotic process.

The second attempt to clean Montmayeur's cores was more successful. They were weighed and placed in lower salinity, 5000 ppm NaCl brine solution to remove the precipitated salt. Every two days, the salt solution was changed and the cores were reweighed until the weight change from the previous measurement was negligible. Total soaking time was ten days. Assuming that as much salt as possible had been removed from the cores, these five cores were cleaned and tested in the same manner as the ten Berea cores. Grain density calculations agreed within 1.7 percent to those calculated by Montmayeur.

The ten Berea cores were cut with a diamond drill to approximately 0.75 inch diameter by 1.5 inches long. The ends were trimmed parallel and the length and diameter of each core was measured with a caliper eight times. The eight

length measurements were to ±0.005 in as were the eight

diameter measurements. The arithmetic mean of these

measurements was used as the average diameter and length for

each core. The cores were cleaned in the Soxhlet toluene

extractor for 24 hours to remove residual hydrocarbons.

After removal from the extractor the cores were dried in a

130°F oven for 24 hours then taken out and reweighed. They

were not dried in a 600°F oven as Montmayeur did because the

high temperature causes thermal microcracks to form within

the rock (Kranz 1985).

Grain volume measurements were made using the Beckman

pycnometer and bulk volume measurements were made using a

Ruska porosimeter. From these measurements the grain

density, ρ_g, and effective porosity, ϕ, of each core were

calculated using Equations 4-1 and 4-2.

$$\rho_g = \frac{W_d}{V_g} \quad \text{(gm/cc)} \tag{4-1}$$

$$\phi = \frac{V_b - V_g}{V_b} \tag{4-2}$$

where:

W_d = Core weight, dry (gm)

V_g = Grain volume (cc)

V_b = Bulk volume (cc)

The air permeability of each core was measured using a wet test meter and Ruska gas permeameters. The core lithologies, weights, dimensions, densities, porosities, and air permeabilities are summarized in Table 4.1.a. A comparison of measured rock properties with Montmayeur's is presented in Table 4.1.b which shows that his calculated porosity values were higher than those of this study. Jones (1972) correlation was used to calculate the Klinkenberg corrected permeability using Equations 4-3 and 4-4.

$$K_a = K_l(1+b/P) \tag{4-3}$$

$$b = 6.9 \ K_l^{-0.36} \tag{4-4}$$

where:

K_l = Liquid permeability (md)

K_a = Air permeability (md)

b = Klinkenberg correction factor (psi)

P = Average pressure (psi)

All five of Montmayeur's cores and six of the Berea cores, HCB1, HCB2, HCB4, HCB5, HCB6, and HCB7 were saturated with 50,000 ppm NaCl brine solution at 2000 psig. All eleven cores were placed in a saturator under vacuum for 24 hours prior to saturation. Cores HCB5 and HCB6 were saturated for

Table 4.1.a

Summary of Consolidated Core Data.

Core Name	Lithology	Length (cm)	Diameter (cm)	X-Sec Area (cm²)	Dry Weight (gm)	Kair (md)	Klinkenberg Corrected Perm (md)	Ruska Bulk Volume (cc)	Beckman Grain Volume (cc)	Porosity (%)	Grain Density (gm/cc)
STB2	Berea ss	3.2656	1.8869	2.7963	19.252	207	181	9.128	7.127	21.92	2.701
STB5	Berea ss	3.2050	1.8875	2.7981	18.879	216	190	8.935	7.050	21.10	2.678
STD2	Dolomite	2.6250	1.8919	2.8111	16.219	94	78	7.310	5.737	21.52	2.827
K5C2*	ss	2.9250	1.9106	2.8671	16.524	14	10	8.187	6.202	24.25	2.664
STB1	Berea ss	3.1256	1.9294	2.9236	18.619	8	5.3	9.099	7.037	22.66	2.646
HCB1	Berea ss	3.3944	1.8863	2.7944	18.389	848	783	9.219	6.957	24.54	2.643
HCB2	Berea ss	3.5350	1.8719	2.7519	18.926	920	851	9.466	7.022	25.82	2.695
HCB3*	Berea ss	3.5175	1.8675	2.7391	18.746	880	813	9.392	7.122	24.17	2.632
HCB4*	Berea ss	3.5938	1.8763	2.7648	19.455	900	832	9.700	7.410	23.61	2.626
HCB5	Berea ss	3.6438	1.8788	2.7722	19.682	925	856	9.740	7.422	23.80	2.652
HCB6+	Berea ss	3.6681	1.8756	2.7630	19.650	920	851	9.767	7.480	23.42	2.627
HCB7	Berea ss	3.6956	1.8844	2.7888	19.856	889	822	9.851	7.427	24.61	2.673
HCB8	Berea ss	3.6931	1.8863	2.7944	19.924	910	842	9.949	7.539	24.22	2.643
HCB9	Berea ss	3.7894	1.8856	2.7925	20.524	925	856	10.219	7.750	24.16	2.648
HCB10	Berea ss	3.8256	1.8775	2.7685	20.618	925	856	10.282	7.772	24.41	2.653
HCB11	Berea ss	3.5869	1.8675	2.7391	19.474	1078	1001	9.581	7.570	20.99	2.573
HCB12	Berea ss	3.6981	1.8725	2.7538	20.244	1060	984	9.965	7.885	20.87	2.567
HCB13	Berea ss	3.7812	1.8700	2.7465	20.546	1026	952	10.128	7.990	21.11	2.572
HCB14	Berea ss	3.4869	1.8663	2.7356	19.033	1066	842	9.396	7.460	20.61	2.551
HCB15	Berea ss	3.5563	1.8550	2.7026	19.036	1066	856	9.420	7.425	21.18	2.564
HCB16	Berea ss	3.5313	1.8700	2.7465	19.285	1000	850	9.510	7.515	20.98	2.566

* Core broken during preparation procedure.
+ Core broken during testing procedure.

Table 4.1.b.
Comparison of Measured Core Properties with Montmayeur's.

Core Name	Measured Porosity (%)	Montmayeur Porosity (%)	Measured Grain Density (gm/cc)	Montmayeur Grain Density (gm/cc)
STB2	21.92	19.10	2.701	2.655
STB5	21.10	20.80	2.678	2.695
STD2	21.52	21.30	2.827	2.862
K5C2	24.25	22.00	2.664	2.655
STB1	22.66	20.30	2.646	2.701

2 days and the rest of the cores were saturated for 5 days. The remaining four Berea cores HCB3, HCB8, HCB9, and HCB10 were saturated with kerosene, a non-reactive fluid, in the high pressure saturator at 2000 psig for two weeks. After measuring the specific gravity of the saturating fluids and the saturated core weights, the percent saturation of each core was calculated (Table 4.1.c).

After saturation, the liquid permeability of the eleven brine saturated cores and four kerosene-saturated cores was measured using a Ruska liquid permeameter. Cores HCB3, HCB4, and K5C2 broke during the liquid permeability test and the liquid permeability of core STB1 was too small to be measured with the available equipment.

The results of the liquid permeability tests showed that the brine saturated cores had a 33 to 54 percent reduction in permeability compared to the air permeability corrected for Klinkenberg effects. The kerosene-saturated cores showed a less than 4 percent change in liquid permeability compared to the Klinkenberg corrected air permeabilities. The 50,000 ppm brine salinity should have been sufficient to prevent clay swelling and further investigation was done to determine other possible reasons for the liquid-air permeability discrepancies (Palmer 1987).

Table 4.1.c.
Summary of Consolidated Core Saturation and Liquid
Permeability Data.

TYPE I	Dried in 130°F oven then saturated with 50,000 ppm NaCl brine at 2000 psig.
TYPE II	Dried in 130°F oven then saturated with kerosene at 2000 psig.
TYPE III	Originally TYPE II; recleaned in Soxhlet extractor with toluene, dried in 130°F oven then saturated with 50,000 ppm NaCl brine at atmospheric pressure.
TYPE IV	Dried in 190°F oven then saturated with 50,000 ppm NaCl brine at atmospheric pressure.
TYPE V	Dried in 190°F oven then saturated with kerosene at atmospheric pressure.
TYPE VI	Originally TYPE V; recleaned in Soxhlet extractor with toluene, dried in 130°F oven then saturated with 150,000 ppm NaCl brine at atmospheric pressure.

Core Name	Core Type	Saturated Density (gm/cc)	Saturating Fluid Density (gm/cc)	Saturation (%)	Liquid Perm (md)	Air Perm (md)
STB2	I	2.3335	1.0376	87.99	116	207
STB5	I	2.3335	1.0376	93.16	108	216
STD2	I	2.4651	1.0376	99.81	52	94
HCB1	I	2.2613	1.0376	94.97	371	848
HCB2	I	2.2607	1.0376	90.07	544	920
HCB5	I	2.2823	1.0364	97.17	422	925
HCB6	I	2.2740	1.0364	99.44	395	920
HCB7	I	2.2820	1.0376	96.38	424	889
HCB8	II	2.2101	0.8028	95.09	871	910
HCB9	II	2.2127	0.8028	96.81	830	925
HCB10	II	2.2220	0.8028	98.46	841	925
HCB8	III	2.2635	1.0326	96.88	408	910
HCB9	III	2.2625	1.0326	97.27	423	925
HCB10	III	2.2710	1.0326	95.57	438	925
HCB11	IV	2.2816	1.0326	98.29	573	1078
HCB12	IV	2.2800	1.0326	99.08	567	1060
HCB13	IV	2.2739	1.0326	97.08	503	1026
HCB14	V	2.2201	0.8002	100.00	997	1066
HCB15	V	2.2123	0.8002	96.60	1019	1066
HCB16	V	2.2198	0.8002	97.70	954	1000
HCB14	VI	2.2861	1.0994	99.11	490	1066
HCB15	VI	2.2845	1.0994	98.16	574	1066
HCB16	VI	2.2871	1.0994	97.19	545	1000

Because the kerosene and brine permeabilities were measured in different permeameters, it was thought that perhaps one of the permeameters or coreholders was not functioning properly. Subsequent tests, running the same core in the same fluid in different permeameters, showed that the problem was not the permeameters. Another possibility was that, because the kerosene-saturated cores were in the high pressure saturator for so much longer that the brine saturated cores, the high pressure was fracturing the cores over time. In order to test this hypothesis, six more Berea cores were cut from the same slab for further testing. These were saturated in the low pressure saturator at atmospheric pressure overnight rather than in the high pressure saturator.

These six cores, HCB11, HCB12, HCB13, HCB14, HCB15, and HCB16, were also cleaned overnight in a Soxhlet extractor with toluene but were dried in a 190°F oven overnight. The other 10 Berea had previously been dried in an 130°F oven overnight. Subsequent air permeabilities measured using the wet test meter showed a 14 percent increase in the air permeability compared to the 10 Berea cores that were dried in the 130°F oven. This increase in the permeability could be due to the higher temperature fracturing the cores or to the dehydration of clays in the rock. Cores HCB8, HCB9, and

HCB10, cores previously saturated in kerosene, were cleaned with the 6 new Berea cores prior to testing in brine solutions.

To examine the possibility of time and high pressure effects causing the discrepancy in the liquid permeabilities, the six new Berea cores and HCB8, HCB9, and HCB10 were saturated at atmospheric pressure for one day. HCB8, HCB9, HCB10 and three of the new Berea cores, HCB11, HCB12, and HCB13, were saturated in 50,000 ppm sodium chloride brine. The remaining three new Berea cores, HCB14, HCB15, and HCB16, were saturated in kerosene. The results showed that there was no advantage to using the high pressure saturator to increase liquid saturation (Table 4.1.c). For example, the high pressure saturations ranged from 88 to 99.5 percent while the low pressure saturations ranged from 95.5 to 100 percent. The liquid permeabilities showed the same results as before; the brine saturated cores had a 42 to 47 percent reduction in permeability and the kerosene cores had less than three percent reduction compared to the Klinkenberg corrected air permeabilities (Table 4.1.c). This ruled out the time and pressure factors as possible causes of the decreased liquid permeability for the brine saturated cores.

The only possibility could then be some type of reaction within the cores causing the permeability to be reduced by

brine but not by the kerosene. Cores HCB14, HCB15, and HCB16, previously saturated with kerosene, were then cleaned in the Soxhlet extractor with toluene, dried in an 130°F oven overnight and saturated in 150,000 ppm sodium chloride brine solution at atmospheric pressure. Liquid permeability of these high salinity brine cores was reduced 41 to 51 percent of the Klinkenberg corrected air permeability. Increasing the salinity of the brine by a factor of three had no effect on the brine permeability of the Berea cores. This would not be unusual if, in fact, clay swelling is causing the permeability reduction. As shown in Figure 4.1 (Core Lab 1973), if the rock has moderate to high clay content, the ratio of brine permeability to air permeability will be not increased by increasing the salinity of the brine over 50,000 ppm. X-ray diffraction tests run on the Berea sandstone sample at Marathon Oil Field Research Lab showed that the Berea sample was 6 percent clay (Table 4.1.d).

The decision was made to continue using 50,000 ppm sodium chloride brine because sodium chloride is suitable for the samples and higher salinities of NaCl do not reduce the swelling of the clay to a greater extent. The investigation of the liquid permeability reduction has been left to further research. Table 4.1.c contains the summary of the saturation and permeability data for all consolidated cores.
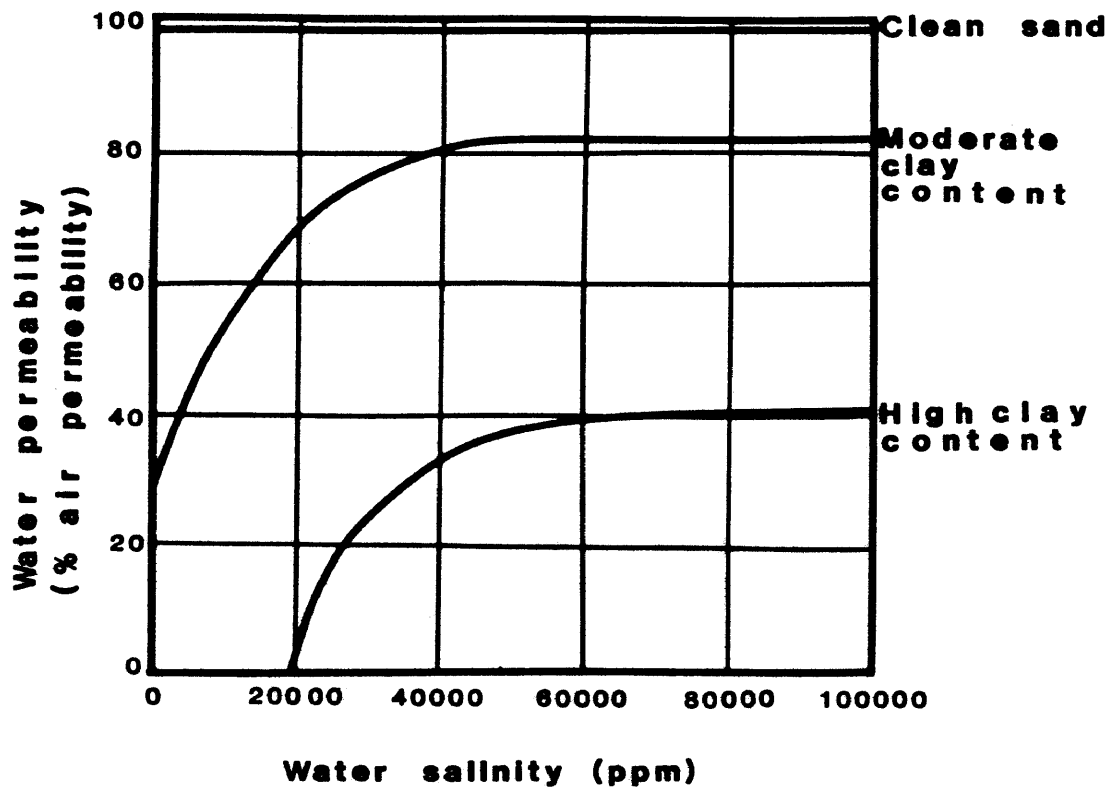
Figure 4.1. Variation of water permeability with salinity and clay content. [After Core Lab (1973)]

Table 4.1.d.
Summary of X-ray Diffraction Results for Berea Rock.

Component	Weight Percent of Component in Whole Rock Sample
Clay	6
Quartz	86
Albite	0
Plagioclase	0
K-Feldspar	8
Calcite	0
Dolomite	0
Pyrite	0
Gypsum	0
Siderite	0
Total	100

Clay Mineral	Percent in 2-8 Micron Fraction	Percent in 0.2-2 Micron Fraction
Montmorillonite	0	0
Chlorite	12	8
Mixed-layer Clays	0	0
Illite	12	38
Kaolinite	76	54
Quartz	0	0
Feldspar	0	0
Total	100	100

4.2. Unconsolidated Sand Cores

4.2.1. Samples

Three types of unconsolidated media were dynamically tested under hydrostatic pressure; glass beads, Ottawa frac sand, and unconsolidated sand from producing reservoirs. Marathon Oil Company provided the glass beads and reservoir sand samples. Additional reservoir sand samples were donated by Mobil Oil Company, and Chevron Oil Company. Information about the reservoir samples including formation name, depth of burial, geologic age, porosity, and permeability for each reservoir sample is found in Table 4.2.1.a.

Glass beads were tested because they are readily available and are often used in laboratories to simulate sand packs. The glass beads were sieved to make unconsolidated core packs in the same size range as the frac sand and the reservoir samples so that comparisons can be made between the different media. Scanning electron microscope (SEM) photographs were taken of the glass beads which illustrate how spherical the beads are. Figures 4.2.1.a and 4.2.1.b show 170/200 mesh glass beads at 150X and 1000X magnifications, respectively.

Ottawa frac sand, another available media used in

Table 4.2.1.a.
Summary of Unconsolidated Sand Sample Geologic Properties.

Property	Reservoir Sample 1	Reservoir Sample 2
Location	U.S. Gulf Coast	U.S. Gulf Coast
Geologic Age	Pliocene	Miocene
Depth (ft)	7500	8250
Porosity (%)	Not measured	30
Permeability (md)	Not measured	500 (range:50-4000)

Property	Reservoir Sample 3	Reservoir Sample 4
Location	Los Angeles, CA	Los Angeles, CA
Geologic Age	Pliocene/Miocene	Pliocene/Miocene
Depth (ft)	3696	3754
Porosity (%)	31	31.7
Permeability (md)	1210	900

Table 4.2.1.a
(Continued)

Property	Reservoir Sample 5	Reservoir Sample 6
Location	Los Angeles, CA	Los Angeles, CA
Geologic Age	Pliocene/Miocene	Pliocene/Miocene
Depth (ft)	3791	3829
Porosity (%)	34	23.8
Permeability (md)	456	826

Property	Reservoir Sample 7	Reservoir Sample 8
Location	Los Angeles, CA	Los Angeles, CA
Geologic Age	Pliocene/Miocene	Pliocene/Miocene
Depth (ft)	3845.8	3902
Porosity (%)	29.6	32
Permeability (md)	517	581
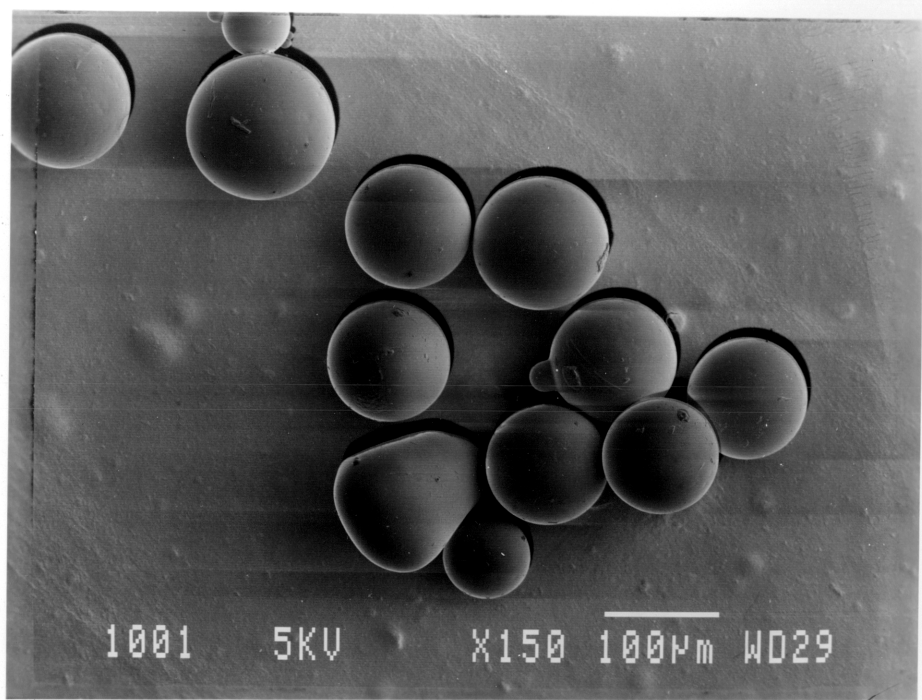
Figure 4.2.1.a.   SEM photograph of 170/200 mesh glass beads
                  magnified 150X.
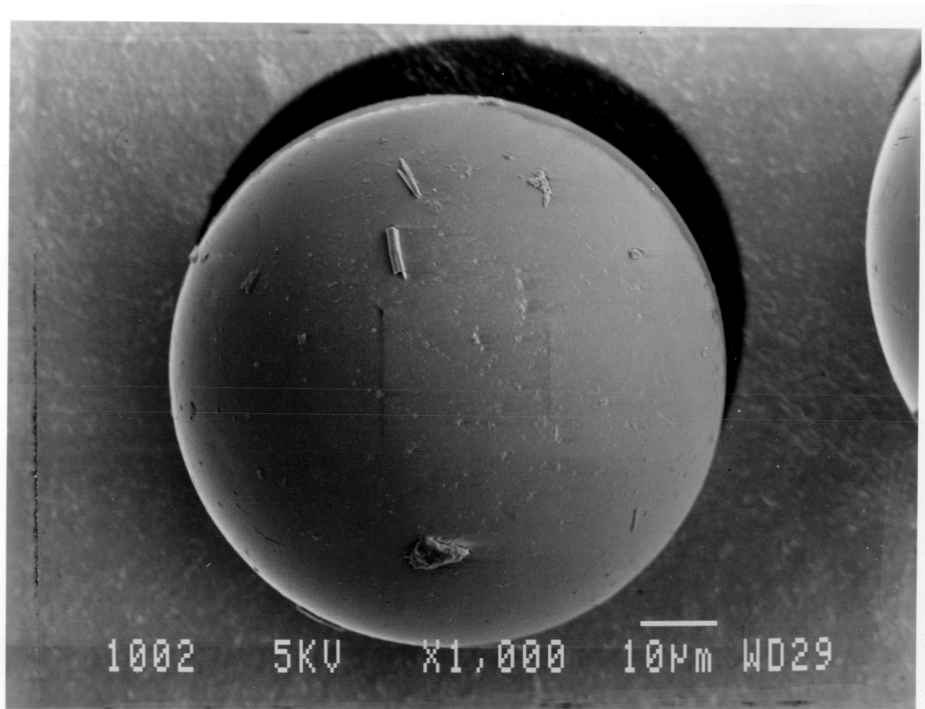
Figure 4.2.1.b.   SEM photograph of 170/200 mesh glass beads
                   magnified 1000X.

laboratory sand pack tests, had to be cleaned and sieved prior to its use in core packs. The sand was rinsed repeatedly in water to remove dust. It was then dried in a low temperature, 80°F, oven to prevent grains from breaking due to high temperatures. No observable differences were noted in the frac sand grains before and after cleaning under 7X magnification. SEM photographs, Figures 4.2.1.c and 4.2.1.d, show the angularity of the frac sand as compared to the glass beads. Figure 4.2.1.c is 170/200 mesh frac sand magnified 100X and Figure 4.2.1.d is 170/200 mesh frac sand magnified 1000X.

The reservoir samples were not cleaned prior to preparation for testing. Table 4.2.1.a contains geologic information about each sample, Tables 4.2.1.b and 4.2.1.c contain the x-ray diffraction test results for Reservoir Samples 1 and 2, and Table 4.1.2.d contains the sieve analysis for each reservoir sample. The size of the other six reservoir samples was not large enough for x-ray diffraction testing. Graphs of sieve analysis data are presented in Figures 4.2.1.e through 4.2.1.l.

SEM photographs taken of Reservoir Sample 1 (Figures 4.2.1.m and 4.2.1.n) show the angularity of the grains as compared to the frac sand and glass beads. Figure 4.2.1.m is a 550X magnification and Figure 4.2.1.n is a 2500X
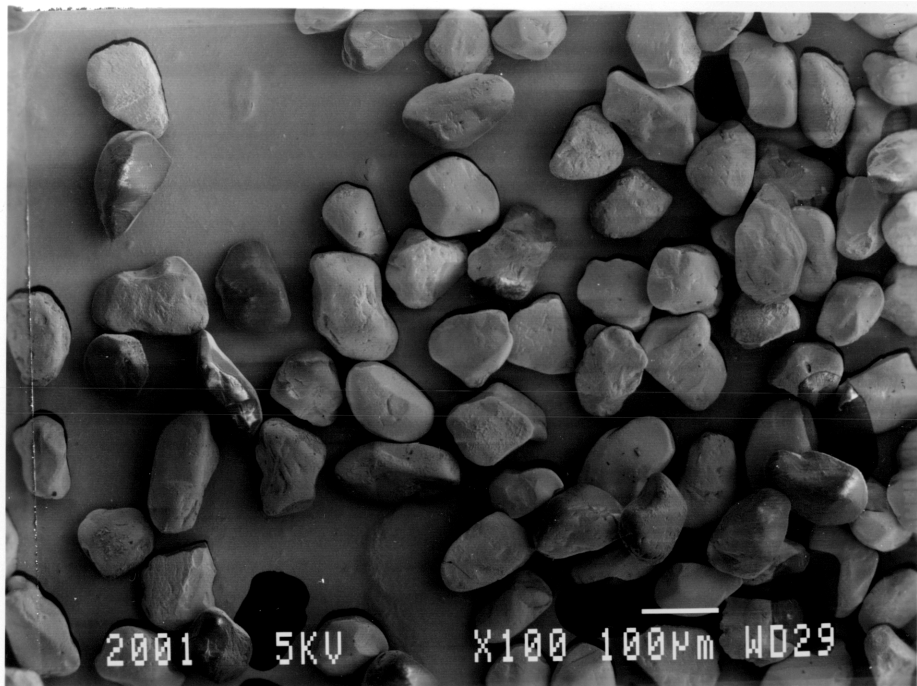
Figure 4.2.1.c.   SEM photograph of 170/200 mesh frac sand magnified 100 X.
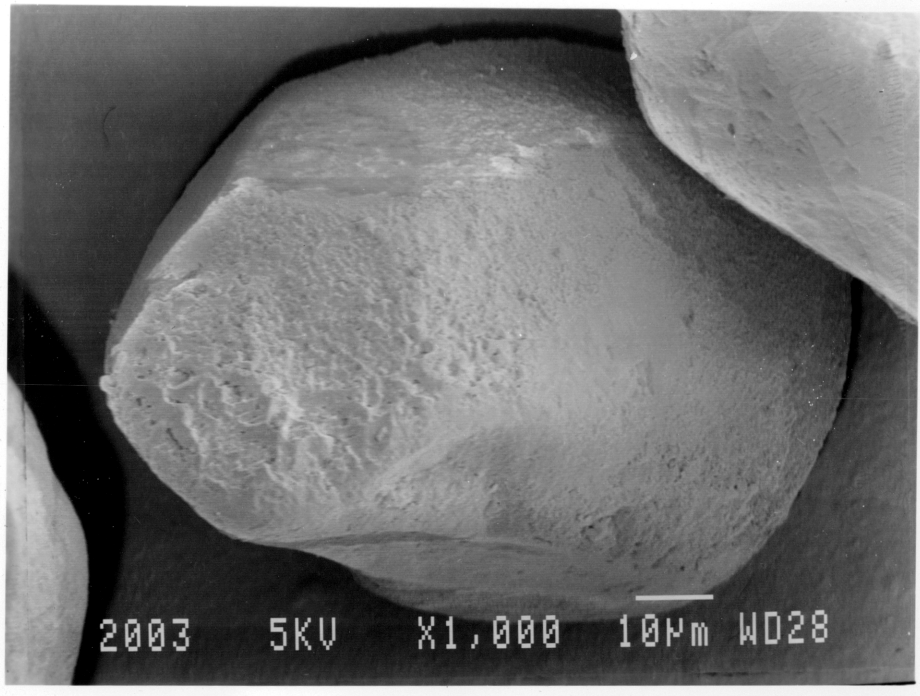
Figure 4.2.1.d.   SEM photograph of 170/200 mesh frac sand.
                   magnified 1000X.

Table 4.2.1.b.
Summary of X-ray Diffraction Results for
Reservoir Sample 1.

Component	Weight Percent of Component in Whole Rock Sample
Clay	14
Quartz	71
Albite	0
Plagioclase	10
K-Feldspar	0
Calcite	5
Dolomite	0
Pyrite	0
Gypsum	0
Siderite	0
Total	100

Clay Mineral	Percent in 2-8 Micron Fraction	Percent in 0.2-2 Micron Fraction
Montmorillonite	66	75
Chlorite	7	5
Mixed-layer Clays	0	0
Illite	24	17
Kaolinite	3	3
Quartz	0	0
Feldspar	0	0
Total	100	100

Table 4.2.1.c.
Summary of X-ray Diffraction Results for
Reservoir Sample 2.

Component	Weight Percent of Component in Whole Rock Sample
Clay	16
Quartz	78
Albite	0
Plagioclase	6
K-Feldspar	0
Calcite	0
Dolomite	0
Pyrite	0
Gypsum	0
Siderite	0
Total	100

Clay Mineral	Percent in 2-8 Micron Fraction	Percent in 0.2-2 Micron Fraction
Montmorillonite	96	97
Chlorite	1	1
Mixed-layer Clays	0	0
Illite	3	2
Kaolinite	trace	trace
Quartz	0	0
Feldspar	0	0
Total	100	100

Table 4.2.1.d.
Summary of Sieve Analysis Results for Reservoir Samples

Sieve Mesh Number	PHI*	Weight Percent							
		Sample 1	Sample 2	Sample 3	Sample 4	Sample 5	Sample 6	Sample 7	Sample 8
10	-1.00	0.00	0.00	0.00	0.00	0.00	0.41	0.00	0.00
20	0.25	0.08	0.00	0.99	3.43	0.00	18.84	0.16	0.07
40	1.25	0.19	0.10	15.37	20.40	1.41	42.03	0.66	1.23
60	2.00	3.85	0.95	24.90	32.62	17.14	16.13	14.57	16.10
80	2.50	15.49	5.38	43.78	26.69	34.43	9.15	40.16	34.54
100	2.75	14.83	3.32	6.37	5.47	13.45	2.79	13.97	14.87
120	3.00	26.90	9.78	5.00	6.92	14.00	3.36	12.28	14.45
170	3.50	24.63	51.44	3.55	3.80	17.03	4.47	13.39	15.62
200	3.75	4.83	9.47	0.04	0.56	1.89	1.02	1.81	1.86
230	4.00	3.23	6.20	0.00	0.11	0.65	0.89	1.40	0.98
325	4.50	4.13	10.32	0.00	0.00	0.00	0.77	1.48	0.28
400	4.75	0.62	0.85	0.00	0.00	0.00	0.10	0.08	0.00
400+	5.00	1.22	2.19	0.00	0.00	0.00	0.04	0.04	0.00
TOTAL		100.00	100.00	100.00	100.00	100.00	100.00	100.00	100.00
MGD**		0.1340	0.1069	0.2316	0.2736	0.1805	0.5176	0.1805	0.1817

* PHI $= -\log_2(mm) = \dfrac{-\log_{10}(mm)}{\log_{10}2}$

where: (mm) = grain size in mm

** MGD = Mean Grain Diameter in mm of sample calculated
for PHI at cumulative frequency at 50%.

For a detailed discussion of grain analysis, please refer
to Leroy, Leroy, and Raese (1977).
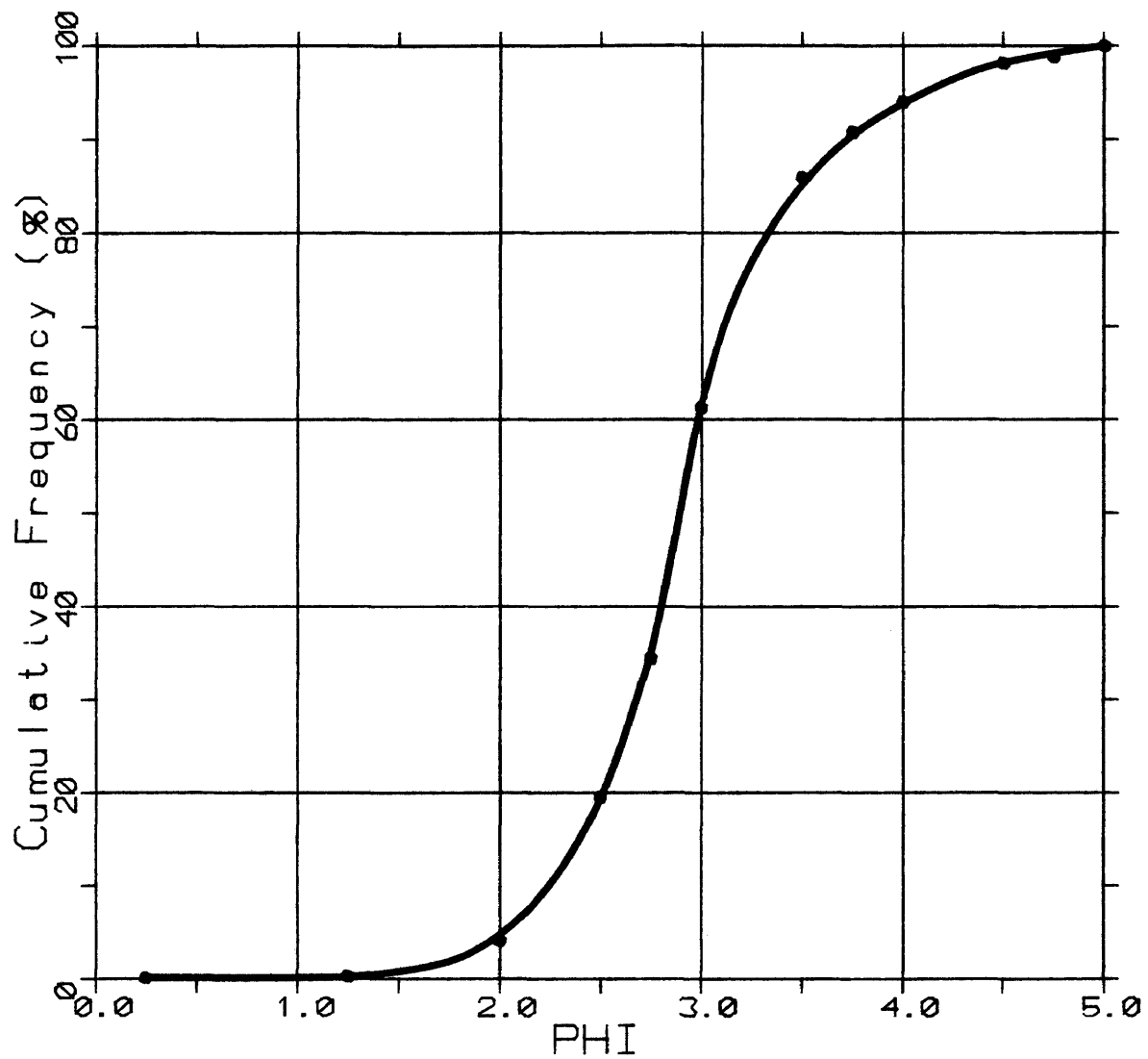
Figure 4.2.1.e. Sieve analysis results for Reservoir Sample 1. [PHI = $-\log_2$(grain size in mm)]
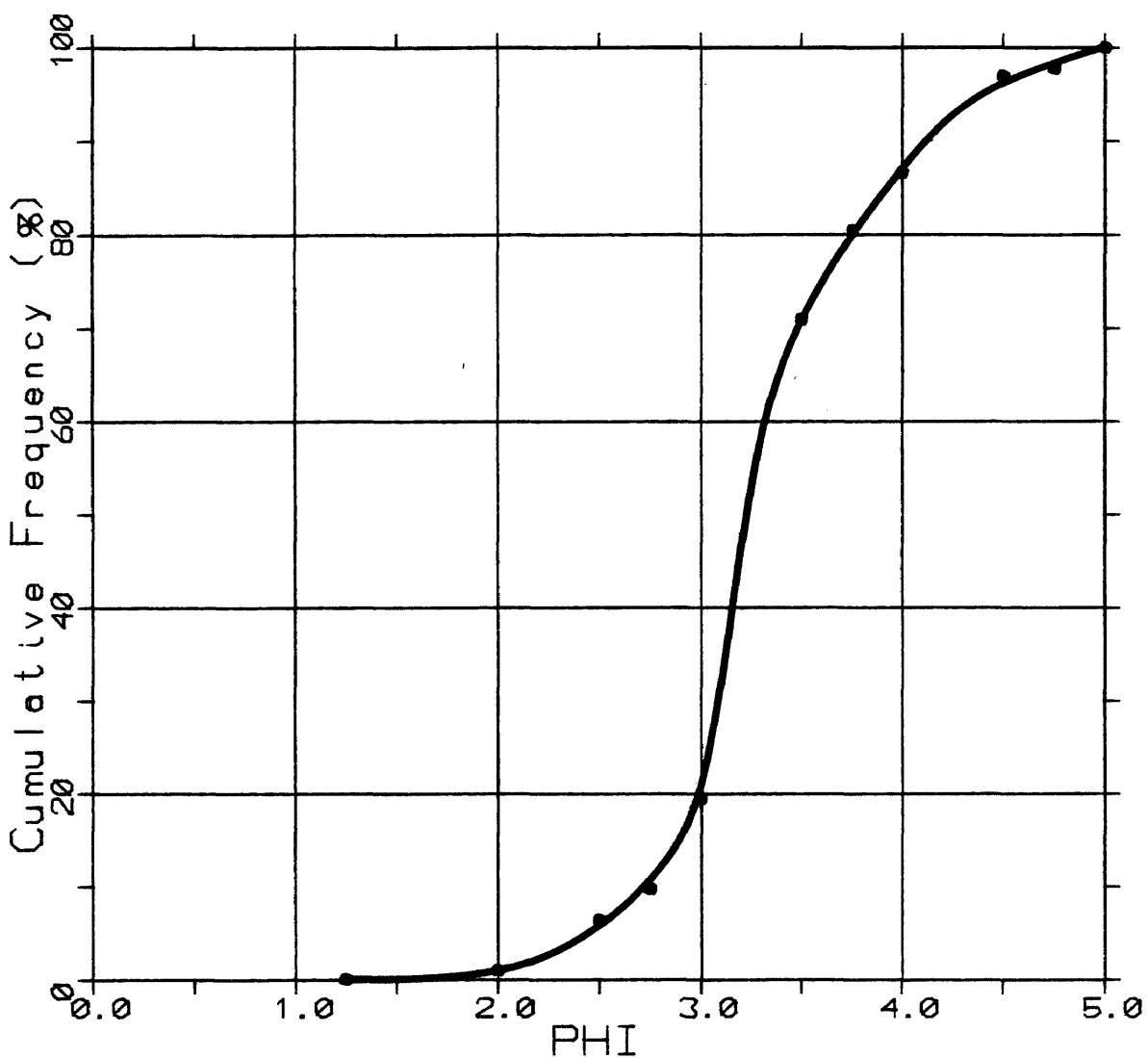
Figure 4.2.1.f. Sieve analysis results for Reservoir Sample
2. [PHI = $-\log_2$(grain size in mm)]
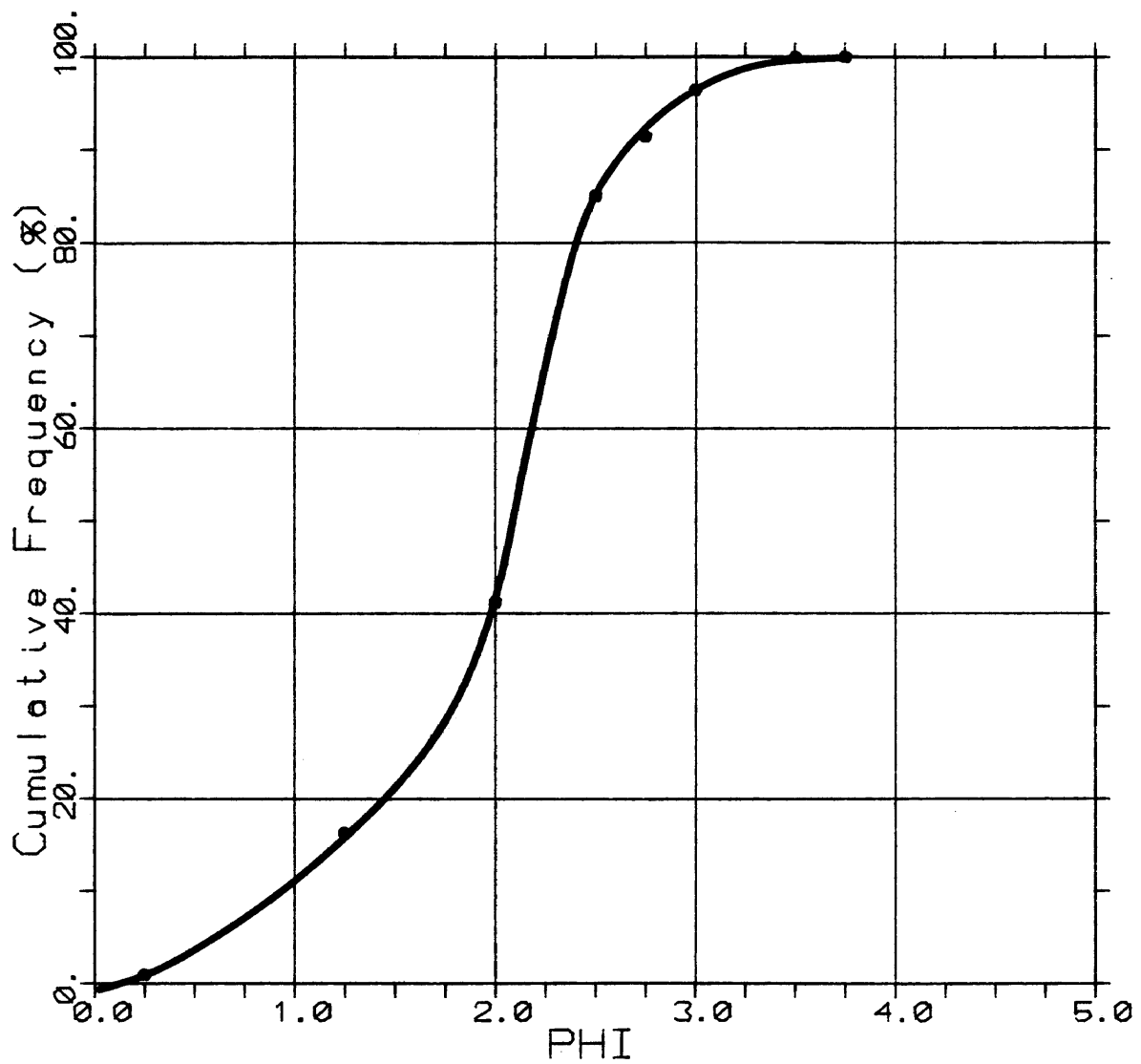
Figure 4.2.1.g.   Sieve analysis results for Reservoir Sample 3. [PHI = $-\log_2$(grain size in mm)]
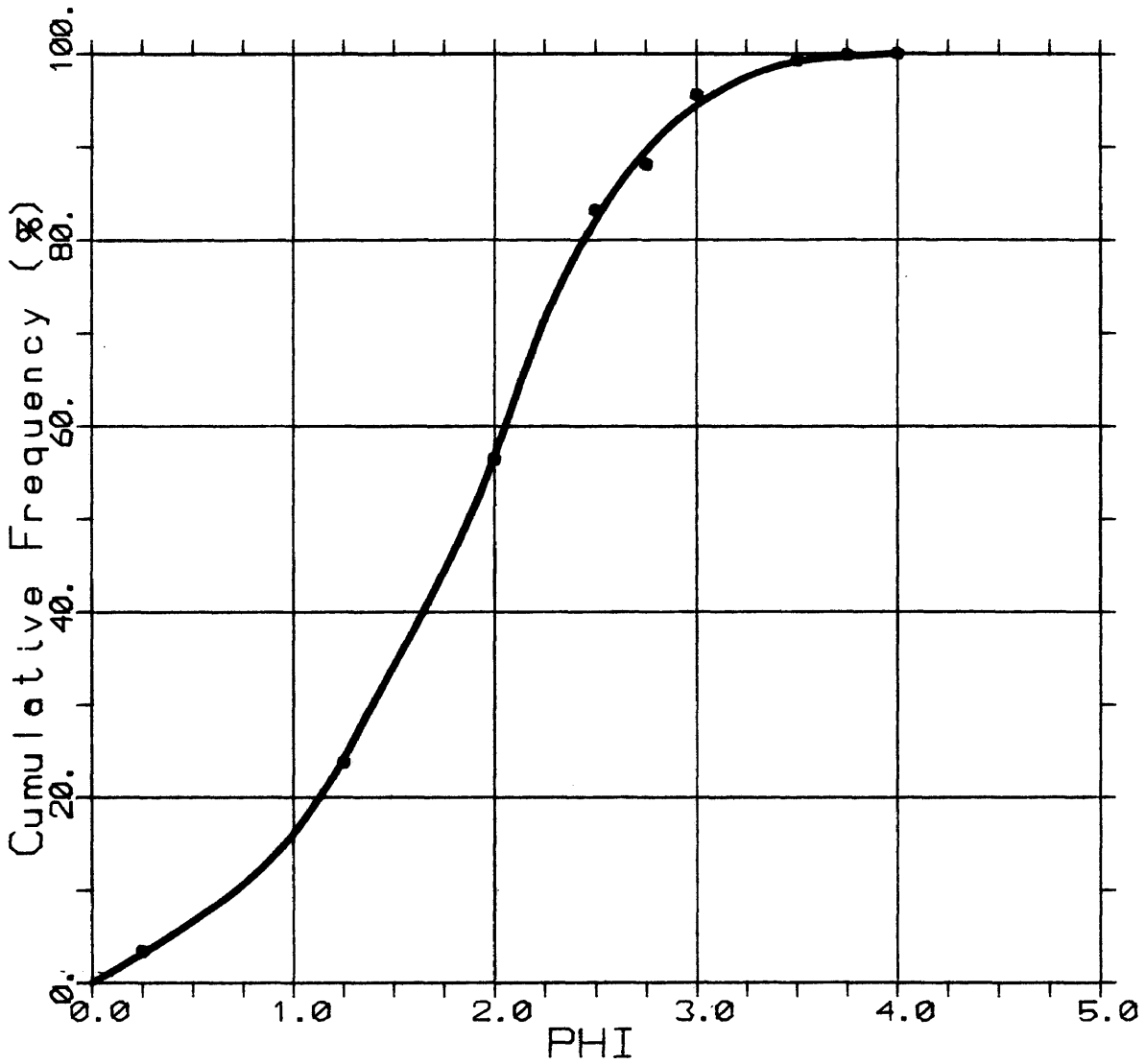
Figure 4.2.1.h.   Sieve analysis results for Reservoir Sample
4. [PHI = log$_2$(grain size in mm)]
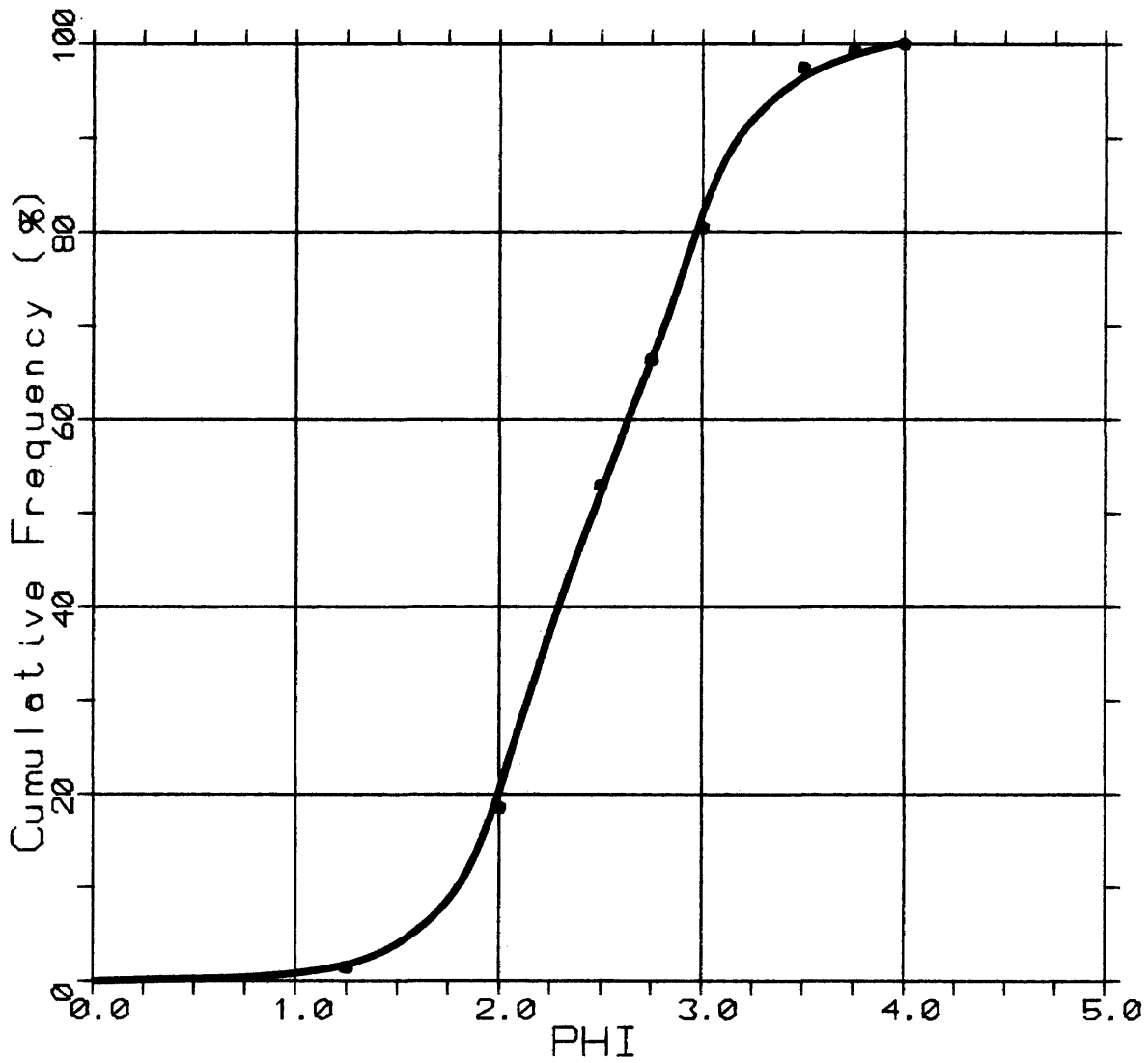
Figure 4.2.1.i.   Sieve analysis results for Reservoir Sample
5. [PHI = $-\log_2$(grain size in mm)]
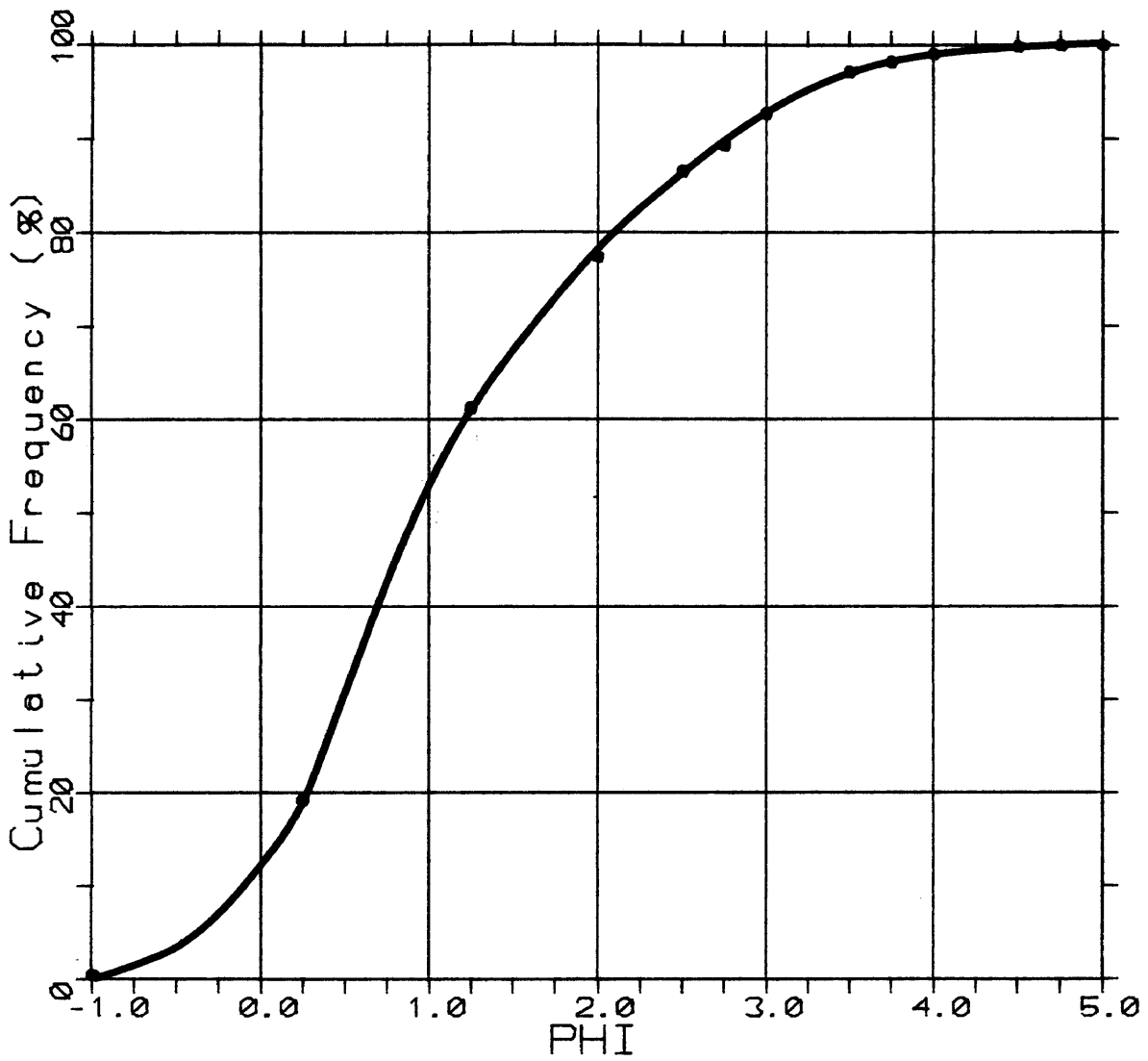
Figure 4.2.1.j.   Sieve analysis results for Reservoir Sample
6. [PHI = -log$_2$(grain size in mm)]
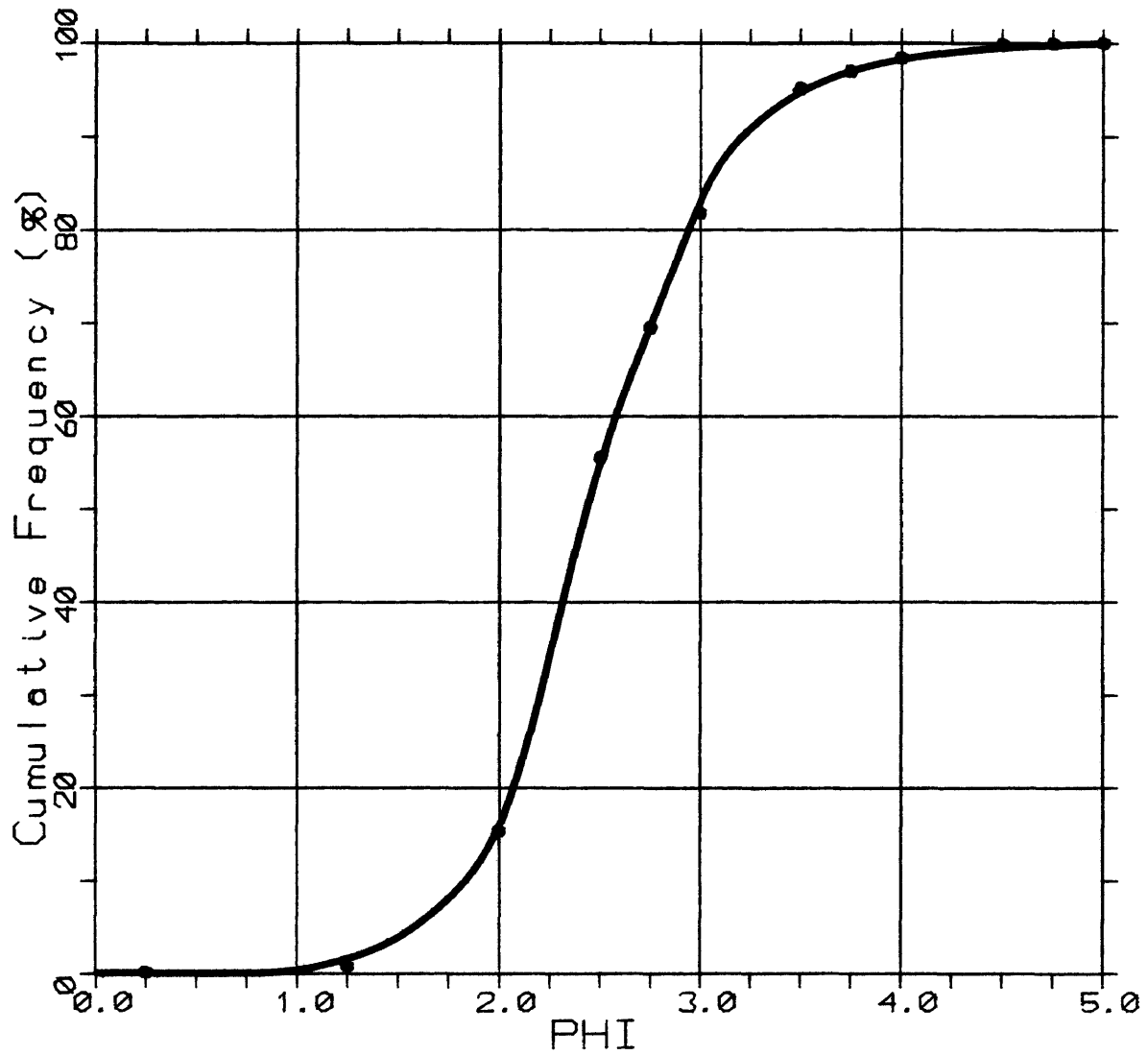
Figure 4.2.1.k.   Sieve analysis results for Reservoir Sample
                  7. [PHI = -log$_2$(grain size in mm)]
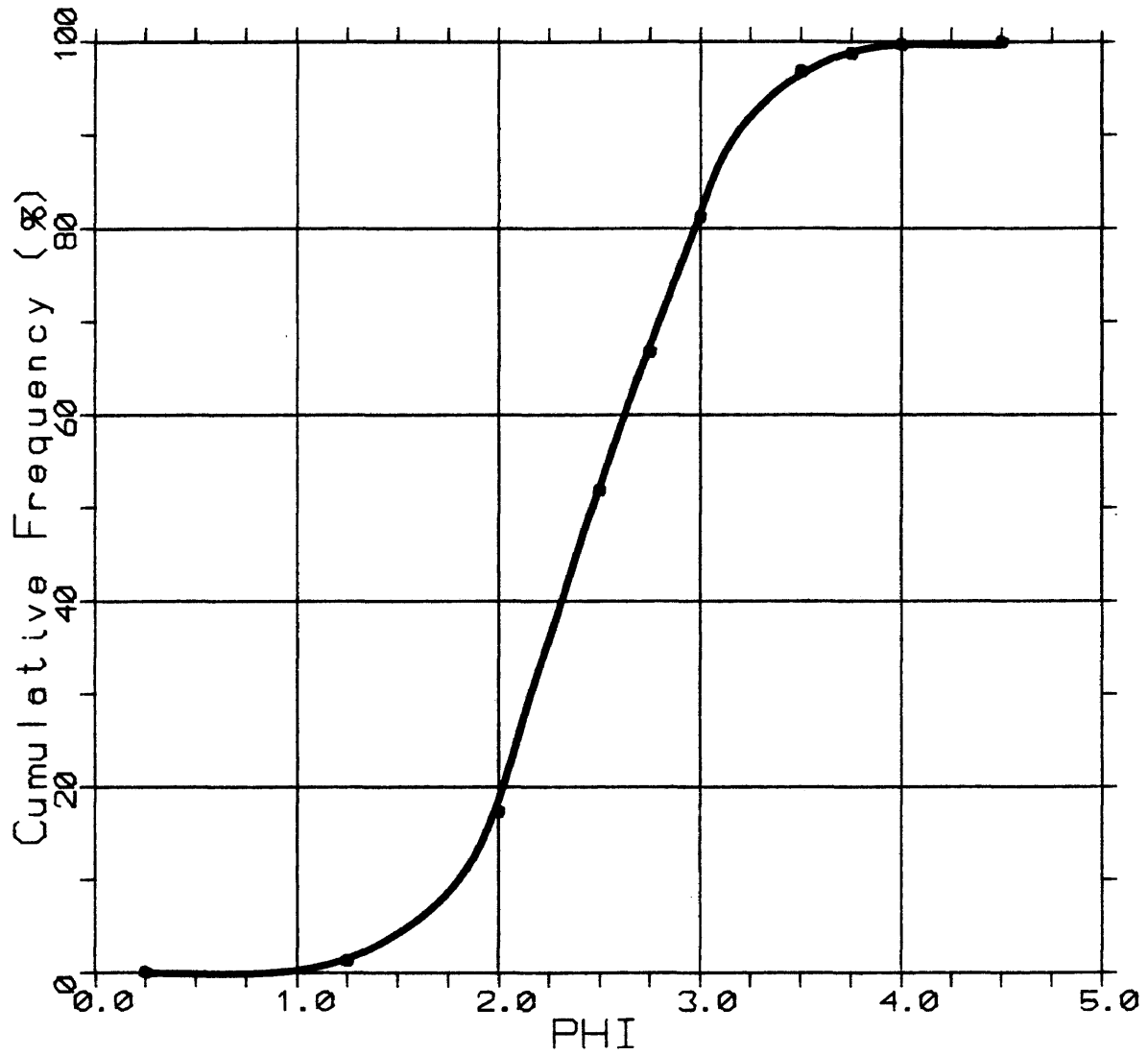
Figure 4.2.1.1.   Sieve analysis results for Reservoir Sample
                   8. [PHI = -log$_2$(grain size in mm)]
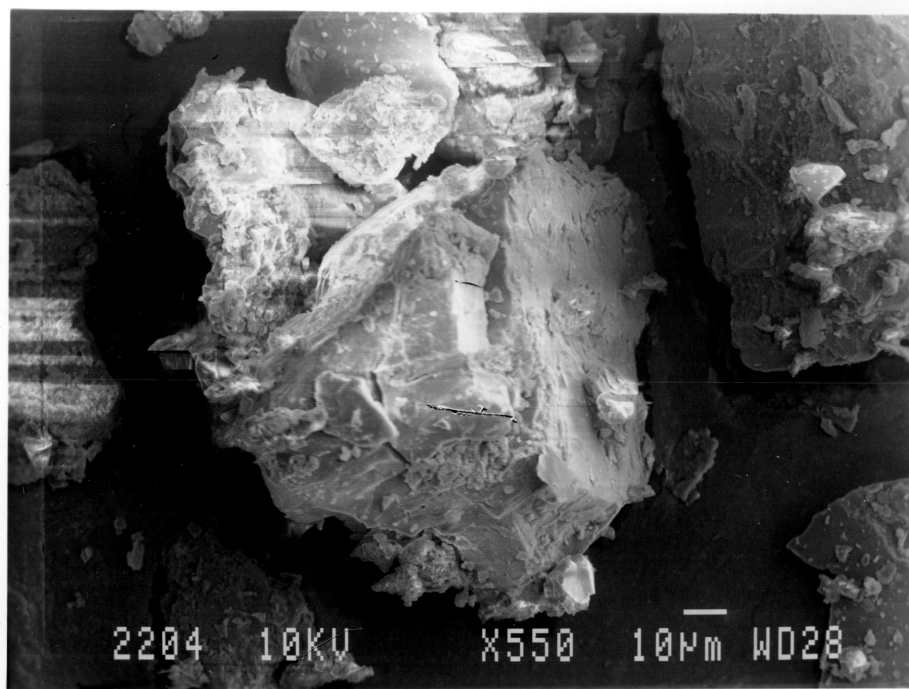
Figure 4.2.1.m.   SEM photograph of Reservoir Sample 1
magnified 550X.
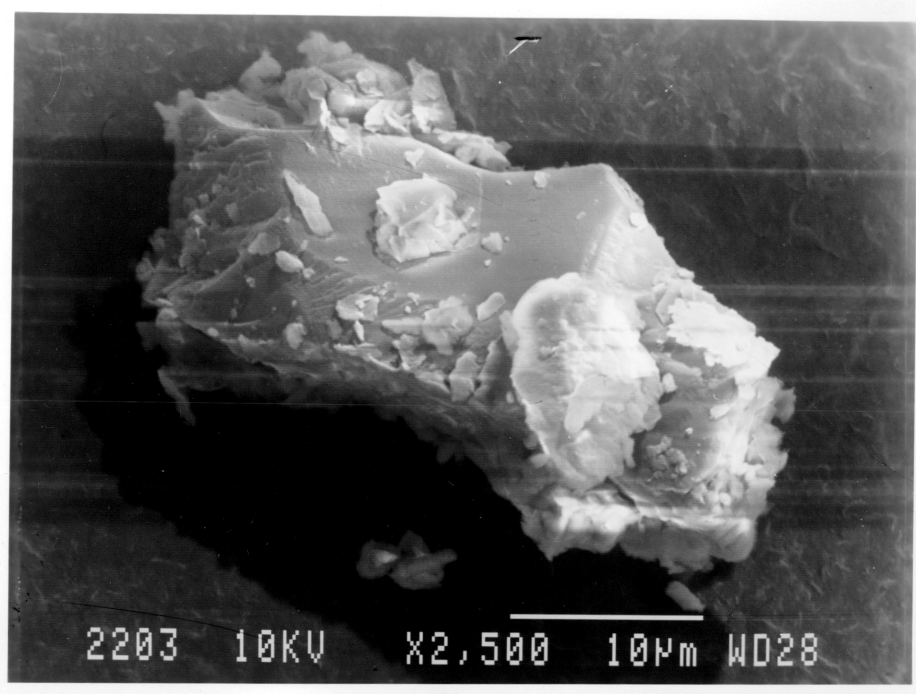
Figure 4.2.1.n.   SEM photograph of Reservoir Sample 1
                   magnified 2500X.

magnification of Reservoir Sample 1.

4.2.2. Sample freezing

Freezing unconsolidated sand samples is accepted

procedure in unconsolidated core analysis, as described by

Jennings (1961), Newman (1973), Mattax (1974), and Swanson

and Thomas (1980). Freezing the pore fluid imparts cohesion

to the sand particles which is maintained until the sample

thaws. But, if the sand core is under isostatic stress as it

thaws, the shear strength of isostatic confinement replaces

the cohesion-induced shear strength (Swanson and Thomas

1980).

Typically, the cores are recovered with rubber sleeved

core barrels, frozen on location, and kept frozen during

transportation to the laboratory where they are stored

frozen. Individual core plugs samples are then drilled out

of the core using liquid nitrogen as the drilling fluid. The

plugs are inserted into the testing apparatus while frozen

and then cleaned by flowing solvents through the core sample

(Jennings 1961; Newman 1973; Swanson and Thomas 1980). There

is some concern among other researchers (Dunn 1986) that

freezing the samples causes cracks in the individual sand

grains.   The effect of freezing was a major point of investigation of this work.

The unconsolidated reservoir samples donated for this research were not frozen when received, but arrived as either loose sand, as were the glass beads and frac sand, or in semiconsolidated chunks. A primary goal was to investigate ways to consolidate the sand thus setting up a stress state which would provide shear strength to the sample core until isostatic stress induced shear strength within the test cell could replace it.

The most obvious way to consolidate the loose sand was to create a core pack by saturating the sand in a fluid and then freezing it in a liquid nitrogen bath, (Montmayeur 1985). It was desired to use a saturating fluid that would have the following properties: 1) it would not react with the minerals, especially clays, in the sample, 2) it would remain in a frozen state for a long enough time to make appropriate measurements and mount the sample in the test cell, 3) it would not cause the grains to crack from the expansion of the fluid within vugs or cracks in the grains, and 4) it was consistent with that used by Montmayeur (1985).

The two saturating fluids examined were toluene and a salt water brine solution. The toluene was chosen because, as a hydrocarbon, it is nonreactive with clays, it can be

frozen with liquid nitrogen, it is readily available, and it does not expand when frozen. Brine was chosen because, with the correct salinity and composition, reaction with clay minerals can be minimized. It can also be frozen quickly with liquid nitrogen and the salt will act to reduce the expansion of the water during freezing.

Initial tests on 20/40 and 170/200 mesh sand packs showed that toluene would be unsuitable as the saturating fluid because the volatile hydrocarbon evaporates quickly as the core thaws. The thawing began as soon as the core was removed from the liquid nitrogen bath and individual grains started falling from the core as it continued to thaw. Ruling out toluene as the saturating fluid left brine as the alternative, but a proper composition and salinity had to be determined.

4.2.2.1. Brine composition

It was desired to use the same saturating fluid for both the consolidated rock cores and the unconsolidated sand samples. In choosing an appropriate brine, the water sensitivity of the samples had to be identified. The glass beads and frac sand are not water sensitive, but X-ray diffraction of the reservoir samples (Tables 4.2.1.b and

4.2.1.c) showed that there were water sensitive clays
present. Reservoir Sample 1, for example, was approximately
14 percent clay, of which 70 percent was montmorillonite and
20 percent was illite, both swelling water sensitive clays.
The remaining 10 percent of the clays in Reservoir Sample 1
were chlorite and kaolinite which are also water sensitive
clays.

Water sensitive clays are commonly categorized as either
swelling or nonswelling. The water sensitivity is a function
of how extensively clay particles separate by swelling and
break off and disperse in the pore fluid. Swelling clays,
such as montmorillonite and mixed layer clays, have a high
surface-area-to-volume ratio and are extremely water
sensitive. As they swell, flow is restricted and effective
porosity is reduced. Permeability is further reduced by the
montmorillonite and mixed-layer clay particles that break
off, become entrained in the moving fluid, and form
microscopic filter cakes at the pore throats. Nonswelling
clays, such as illite, kaolinite, and chlorite, also have
reduced permeability when contacted with fresh water causes
clumps of clay particles to break off and migrate to block
off pore channels (Holcomb 1985).

In field and laboratory work, three salts commonly used
to reduce the watersensitivity of clays are sodium chloride,

potassium chloride, and ammonium chloride. When the clays are predominantly illite, potassium chloride works best to stabilize the clay because the potassium ion replaces any exchangeable cation impurities in the structure and the clay is then in an environment which is the same as the cation binding it together (O'Brien 1973). Primarily montmorillonite clays will swell appreciably even with potassium ions present and the degree of improvement over sodium chloride and ammonium chloride salts may not be sufficient to justify the costs involved. Ammonium chloride salts are also more expensive and are more temperature sensitive than sodium chloride or potassium chloride, so their use is limited (Hower 1974).

Because the samples were predominantly montmorillonite clays sodium chloride was chosen as the salt to use in the brine solution. Krug (1977), Graves (1982), and Montmayeur (1985) used NaCl and according to scientists at Marathon Oil Company Research laboratory who also worked with Reservoir Sample 1, sodium chloride is acceptable to use to retard the clay swelling in that sample (Palmer 1987).

4.2.2.2. Brine salinity

The salinity of the brine solution must meet two criteria: 1) it must be sufficient to retard clay swelling; and 2) it must be low enough so that the salt does not precipitate out of solution. Precipitation of salt can block off pore channels, thus reducing effective porosity and permeability and changing test results.

At laboratory temperature conditions, 70-80°F, a sodium chloride solution is saturated at approximately 250,000 ppm. According to Graves (1987), when she tried to use a saturated salt brine, the salt did precipitate out of solution.

Krug (1977) and Graves (1982) both used 50,000-70,000 ppm NaCl and Montmayeur (1985) used a 50,000 ppm sodium chloride solution. This salinity is close to that of most seawater which is in the range of 34,000-36,000 ppm sodium chloride, Stowe (1972). According to Palmer (1987), and Figures 4.1 and 4.2.2.2 (Core Lab 1973), this salinity should be sufficient to retard clay swelling as much as possible. These figures show that 50,000 ppm is the minimum salinity required to maximize retardation of clay swelling for water sensitive rocks. As shown in Figure 4.1, if the salinity is increased up to 100,000 ppm, the ratio of water
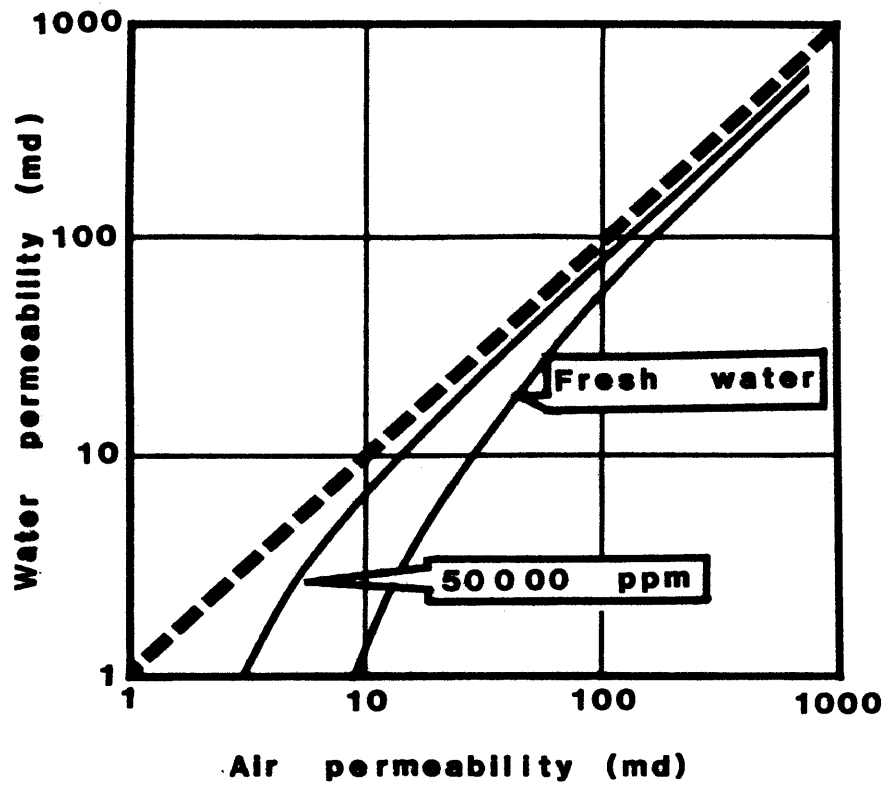
Figure 4.2.2.2. Variation in water permeability with salinity
and air permeability. [After Core Lab (1973)]

permeability to air permeability does not increase. This was verified on the Berea consolidated cores.

The air permeability was measured on six cores. The liquid permeability of three of the cores (HCB11, HCB12, and HCB13) was measured for a 50,000 ppm sodium chloride solution and the liquid permeability was measured for the other three cores (HCB14, HCB15, and HCB16) using a 150,000 ppm NaCl brine solution. The ratio of water permeability to air permeability for the 50,000 ppm cores were 49%, 53%, and 53%, the ratios for the 150,000 ppm brine cores were 46%, 54%, and 54%. This difference is negligible.

4.2.3. Effects of Freezing on Unconsolidated Sand Packs

The effects of freezing on unconsolidated frac sand and glass bead packs were investigated both microscopically and macroscopically. Rapid freezing can cause mechanical rupture due to stress differences between the external and internal grains. SEM analysis was performed to determine what, if any, effects freezing had on individual grains of frac sand and glass beads. On a macroscopic level, the effect of freezing time in a liquid nitrogen bath on the time a core pack would remain solidly frozen was examined.

4.2.3.1. Microscopic analysis

Previous work studying quick freezing effects on cores (Lebeaux 1952; Kelton 1953) was concerned with consolidated rocks. This work was directed toward identifying the effect freezing had on the permeability and porosity of rocks. Lebeaux (1952) quick-froze 100% water saturated and 100% oil saturated consolidated oil well cores. All of the 100% water saturated cores broke during the freezing process while the partially water-partially oil-saturated cores increased in permeability and porosity. Kelton (1953) found that core preparation procedures, such as cleaning, drying, and resaturating, actually had five to six times the effect on the core in terms of increasing the permeability and porosity as did the quick-freezing process. Quick-freezing the cores increased both the permeability and porosity by about 2.5%.

More recently, Torsaeter and Beldring (1985) investigated freezing effects on slightly consolidated sandstone cores. They contend that when the water expands during the freezing and thawing processes, internal grain structure and orientation might change.

Swanson (1980) supports the practice of freezing unconsolidated sand upon removal from the wellbore and maintains that, as long as the gas saturation in the core is

at least 10%, the expansion of water in the core when frozen
will have no effect. This gas saturation buffer action could
be limited though, because, for water wet sands, the water
occupies the smallest pores and cracks. Thus, freezing
effects would be even more pronounced for cores with
microfractures where gas is in the larger pores, unable to
act as a buffer during freezing expansion. When there are
clays present, fine migrating particles could be produced
when freezing water within the clay mineral bursts the clay
layers apart. Freezing effects should be minimal for smooth,
well rounded grains with no surface vugs.

    With these concerns in mind, SEM analysis was conducted
for brine saturated glass bead and frac sand packs. There
were problems analyzing the reservoir samples in the
microscope; particles would dislodge from the sample, float
up and hit the filament, and cause the microscope to shut
itself down. Expensive damage would have resulted to the SEM
if this continued, so the decision was made to analyze only
the frac sand and glass beads packs. In addition, as
illustrated in Figure 4.2.1.m, the reservoir sample grains
prior to freezing are irregularly shaped compared to the
glass beads and the frac sand before freezing (Figures
4.2.1.b and 4.2.1.c). Because of this, it would be nearly
impossible to identify whether the reservoir sample grains

were changed by freezing. Torsaeter and Beldring (1985) analyzed thin sections of their samples in an SEM and found that, while beneficial information was obtained, it would be only speculative to use it as documentation of freezing effects on core material.

The SEM analysis was performed on the glass bead and frac sand packs saturated in 50,000 ppm sodium chloride brine and frozen for 3 minutes in a liquid nitrogen bath at -364°F. The freezing time was determined experimentally. Sand packs were frozen for various times from 1 to 3 minutes to determine how long they should be frozen to maximize the time they would remain solidly frozen after removal from the bath. The cores remained frozen for 18 to 20 minutes after being in the bath for 2 or more minutes. The larger the grain size of the pack, the longer the pack stayed frozen. Lebeaux (1942) froze smaller cores, 1.8 cm diameter by 2 cm long, with dry ice which freezes at -69°F. He found that 5 minutes was ample time to reduce the temperature of his water and oil and water saturated cores to 0° F.

Analysis of SEM photographs indicates that freezing does not damage the frac sand and glass bead grains, see Figures 4.3.1.a and 4.3.1.b. The frac sand grains appear to be of the same general shape as before freezing (Figure 4.3.1.a). There is visible evidence of crystal growth on the grains.
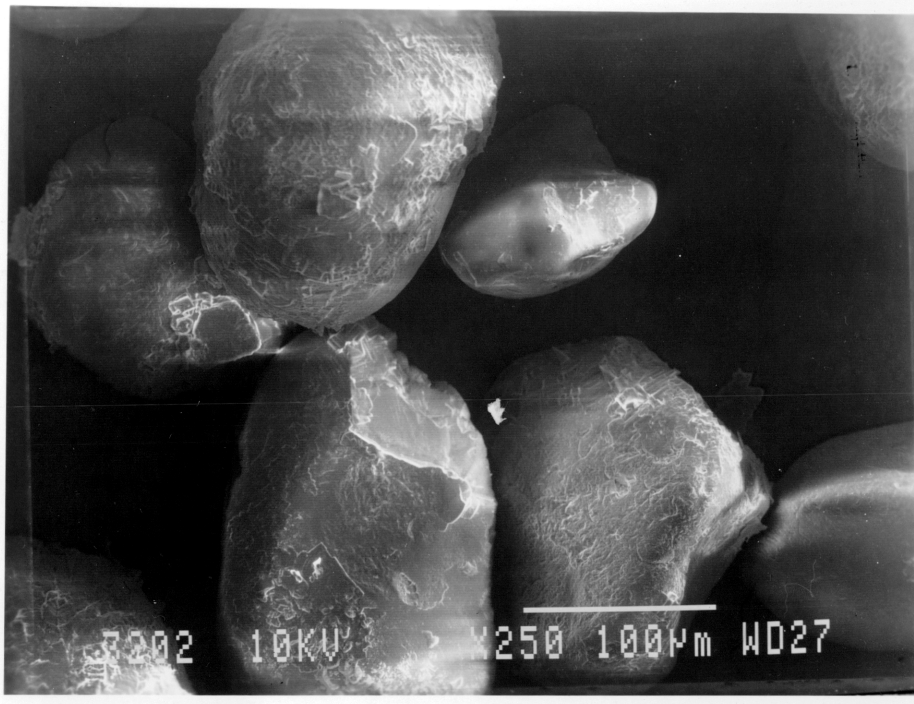
Figure 4.3.1.a.   SEM photographs of 80/100 mesh frac sand
                 after freezing in 50,000 ppm NaCl brine
                 magnified 250X.
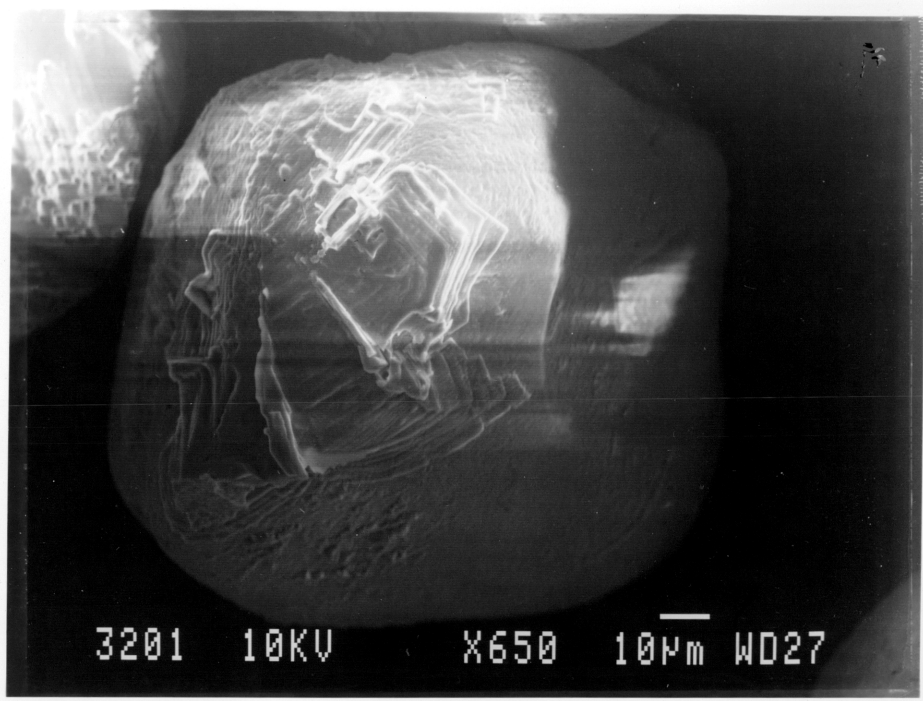
Figure 4.3.1.b.   SEM photograph of 80/100 mesh frac sand after
                   freezing in 50,000 ppm NaCl brine magnified
                   650X.

X-ray analysis showed that, as expected, these are sodium chloride crystals grew on the grains as the salt precipitated out of solution as the sand packs thawed and the water evaporated.

4.2.3.2. Macroscopic analysis

It is interesting to note that while the toluene saturated cores were reduced to a pile of loose sand after thawing as the toluene vaporized, the 50,000 ppm sodium chloride saturated cores retained their shape after thawing and air drying. When small stress was applied to these brine saturated cores, they would break up into clumps still bound together. Tiny salt grains were observed on the surface edges of the brine saturated cores suggesting that the salt was acting as a cementing agent holding the core grains together. To test this hypothesis, sand packs were saturated and frozen with reduced salinity brine, 5000 ppm sodium chloride and fresh water. As expected, the fresh water core was also reduced to a pile of loose sand after thawing and allowing the core to air dry. The lower, 5000 ppm, salinity core, however, retained its shape on surface edges after thawing and air drying undisturbed at room temperature. This

supports the idea that the salt was holding the grains together.

The presence of salt grains on the edges of the sodium chloride brine cores can be explained by the physical processes taking place when salt water freezes. For example, as sea water freezes, approximately 70% of the salt leaves the ice crystal. The remaining 30% is trapped in between the water crystals. The freezing process forces the salt out of the pores to the outside of the core. This is very similar to what occurs when ice freezes on the surface of the ocean (Stowe 1983). So, for the 50,000 ppm NaCl saturated core there were sufficient amounts of salt left between the internal grains to hold them together. But, for the 5000 ppm brine cores, there was enough salt pushed out toward the edges to hold the grains together, but not enough to hold the internal grains together.

4.2.4. Unconsolidated Core Data

In all, seventeen unconsolidated packs were successfully tested. These included six frac sand packs, two glass bead packs, and nine natural reservoir sand packs. SEM, sieve, and some x-ray diffraction analyses have been presented on these samples as has the assembly procedure followed. Table

4.2.4.a summarizes the basic data for the seventeen
unconsolidated cores including grain type, length, diameter,
porosity, grain and brine density, and bulk volume. Table
4.2.4.b, reproduced from Montmayeur (1985), contains basic
core data for his unconsolidated frac sand packs. These
cores were used as a comparison data base for this work.

Table 4.2.4.a.
Summary of Basic Unconsolidated Core Data*

Core Name	Grain** Type	Grain Size (Mesh)	Core Length (cm)	Core Diameter (cm)	Bulk Volume (cc)	Grain Density (gm/cc)	Pore Fluid Density (gm/cc)	Bulk Density (gm/cc)	Sand Pack Porosity (%)	Reported Porosity (%)***
F2040C	1	20/40	3.350	1.900	9.4982	2.6222	1.0185	2.0410	36.24	–
F6080A	1	60/80	3.540	1.865	9.6705	2.6089	1.0185	2.1059	31.63	–
F6080B	1	60/80	2.970	1.880	8.2445	2.6089	1.0185	2.0833	33.05	–
F6080D	1	60/80	3.370	1.900	9.5549	2.6089	1.0185	2.0712	33.81	–
F1014A	1	100/140	2.840	1.925	8.2655	2.6396	1.0255	2.0086	39.09	–
F1014B	1	100/140	3.400	1.880	9.4381	2.6396	1.0255	2.0803	34.65	–
RS1A	2	–	3.435	1.880	9.5353	2.5897	1.0255	1.9529	40.71	–
RS2B	2	–	2.910	1.905	8.2942	2.6431	1.0255	2.0298	37.92	30
RS3A	2	–	3.265	1.905	9.3060	2.5765	1.0255	1.9699	39.11	31
RS4A	2	–	3.265	1.905	9.3060	2.5981	1.0255	2.0265	36.35	31.7
RS5A	2	–	3.525	1.905	10.0471	2.5908	1.0255	1.9090	43.56	34
RS5B	2	–	2.965	1.905	8.4509	2.5908	1.0255	1.9270	46.41	34
RS6A	2	–	3.515	1.905	10.0186	2.6586	1.0255	2.0433	37.68	23.8
RS7A	2	–	3.205	1.905	9.1350	2.6060	1.0255	1.9770	39.80	29.6
RS8A	2	–	3.300	1.875	9.1118	2.5530	1.0255	1.9310	40.72	32
G2040A	3	20/40	3.485	1.905	9.9331	2.4703	1.0255	1.9187	38.18	–
G1014A	3	100/140	3.485	1.905	9.9331	2.4649	1.0255	1.8937	39.68	–

*   Appendix D contains the core nomenclature code for all samples

** 1-Ottawa Frac Sand
    2-Reservoir Samples
    3-Glass Beads

*** Reported by Company providing sample

Table 4.2.4.b.
Summary of Montmayeur's Basic Core Data
for Unconsolidated Sand Packs* [After Montmayeur (1985)]

Core Name	Grain* Type		Grain Size (Mesh)	Core Length (inches)	Core Diameter (inches)	Saturated Density (gm/cc)	Skeleton Density (gm/cc)	Brine Density (gm/cc)	Porosity (fraction)	Saturation (fraction)
20403	Frac	Sand	20/40	1.482	0.751	2.124	2.648	1.036	0.326	1.00
20404	Frac	Sand	20/40	1.450	0.750	2.116	2.648	1.036	0.330	1.00
4060	Frac	Sand	40/60	1.444	0.750	2.095	2.646	1.036	0.342	1.00
6080	Frac	Sand	60/80	1.429	0.751	2.098	2.650	1.036	0.342	1.00
8010	Frac	Sand	80/100	1.393	0.748	2.126	2.650	1.036	0.325	1.00
1012	Frac	Sand	100/120	1.444	0.750	2.070	2.650	1.036	0.359	1.00
1217	Frac	Sand	120/170	1.441	0.748	2.081	2.650	1.036	0.353	1.00
1720	Frac	Sand	170/200	1.427	0.749	2.111	2.650	1.036	0.334	1.00

* Appendix D contains the core nomenclature code for all samples

5. EXPERIMENTAL TESTING PROCEDURE

Both the consolidated rocks and unconsolidated sand
samples were subjected to "long" hydrostatic pressure cycles
as defined by Montmayeur (1985). There were differences in
the way the consolidated rocks and unconsolidated sands were
tested so they will be discussed separately. Because the
data was compared to Montmayeur's (1985) the core preparation
and testing procedures followed his as closely as possible.
The only difference between Montmayeur's core preparation and
that of this research is that he dried his consolidated cores
in a 600°F oven and the consolidated cores in this study were
dried in ovens at less than 200°F.

5.1. Consolidated Rocks

Six consolidated rocks were tested: two previously
tested by Montmayeur (1985); STD2 and STB5, and five
previously untested Berea cores; HCB5, HCB6, HCB11 and
HCB13. Preparation procedure for these cores was discussed
in detail in Chapter 4 of this study. After mounting the
cores in the cell, Section 3.3, and sealing the triaxial
cell, the confining fluid was circulated to remove air from
the confining fluid system and 500 psig hydrostatic pressure

was applied to the core. Montmayeur (1985) subjected his cores to 500 psig confining pressure for 8-12 hours to allow epoxy glue to harden as part of his mounting procedure. The absence of epoxy in this core mounting procedure precluded the 8-12 hour wait. While the cores were under 500 psig hydrostatic pressure, brine pore fluid was circulated through the core for 30 minutes to remove any air from the core and pore fluid system. After the flow was stopped, the core was allowed to equilibrate and stabilize for another 30 minutes prior to the test cycles.

The cores were subject to three hydrostatic pressure cycles; cycles 1 and 2 were stabilization cycles and cycle 3 was the actual test cycle. For cycles 1 and 2 dynamic measurements, described below, were first taken at 500 psig hydrostatic pressure which was the beginning of the first cycle. The ENERPAC pump was used to increase the hydrostatic pressure to 5000 psig at which point another set of dynamic data was taken. The pressure was bled off to 500 psig and at that pressure a third set of dynamic data was taken which was the beginning of cycle 2. Again the hydrostatic pressure was increased with the ENERPAC pump to 5000 psig and dynamic data was taken prior to bleeding off the pressure to 500 psig, which was the end of cycle 2 and the first data point for cycle 3. Data was taken at the two extreme pressures so that

measurements could be compared to ensure a good test and to check for hysteresis.

Cycle 3 data was taken at increasing pressures: 500, 1000, 2000, 3000, 4000, and 5000 psig. Data was taken during decreasing pressure at 4000, 3000, 2000, 1000, and 500 psig. The fast ENERPAC pump system was used on cycle 3 for the consolidated rock cores. 500 psig was the lowest pressure that data was taken because of wave attenuation problems on rock and sand samples which occurs when pressures are too low to ensure sufficient grain to grain contact. Only one core, HCB6, broke during testing. It is assumed that the ends of the core were not cut parallel and the unequal stress distribution on the ends of the core caused it to shear.

Data Measurement Process:

   Step 1: Record pressure

   Step 2: Trigger p-wave through core

   Step 3: View p-wave on oscilloscope
          a. If wave is attenuated adjust pulse
            amplitude, adjust horizontal and vertical
            expansion of waveform
          b. Plot p-wave train and mark wave arrival
            time on plot

   Step 4: Trigger s-wave through core

   Step 5: View s-wave on oscilloscope

             a. If wave is attenuated, adjust pulse
                amplitude, adjust horizontal and vertical
                expansion of wave form.
             b. Plot s-wave train and mark arrival time on
                plot

Step 6: Record pressure. The first five steps take from 5
to 7 minutes during which time the hydrostatic
pressure might decrease due to leaks in the
pressure system. The pressure for each data point
for analysis is the average of two pressures
recorded in steps 1 and 6.

5.2. Unconsolidated Sand Samples

Seventeen unconsolidated samples were tested: two glass
bead sand packs, six frac sand packs and nine reservoir sand
samples. The unconsolidated cores were molded to be
approximately 0.75 inches in diameter by 1.5 inches as
detailed in Section 3.3.

Testing of the unconsolidated samples was the same as
for the consolidated rocks except for Cycle 3, the actual
test cycle. While the pressure data points were the same,
the slower, easier to control pump system was employed.
This system allowed for variable pressure rates up to a
maximum of approximately 4000 psi/hour. Additionally,
digital pressure gauges ensured more accurate pressure
readings.

6. DISCUSSION OF RESULTS

The first section will detail gross observations on both microscopic and macroscopic scales. The second section will be a comparative analysis and will be divided into four parts: A) a comparison between Montmayeur's (1985) data and that from this research for consolidated rocks, B) a comparison between Montmayeur's frac sand data and that of this study, C) a comparison between frac sand and glass bead data from this study, and D) a comparison of measurements from glass beads, frac sand and the natural sand samples from this study with regard to grain size. The third section will be a theoretical analysis of the data using the three models described in Section 2.4.9. of this report; Wyllie's time average, Gassmann's and Biot's. The core sample nomenclature code is found in Appendix D.

6.1. Gross Observations

6.1.1. Microscopic (SEM) results

Grain crushing has been shown to occur when sand packs are subject to high stress (Roberts and de Souza 1958). Grain failure within frac sand and glass bead packs as a

result of thermal expansion when saturated in sodium brine solution was investigated in Chapter 4. As a follow up, additional SEM analyses was performed to determine whether grain failure occurred in the frac sand and glass bead packs as a result of the imposed hydrostatic stress load. Five samples were studied with SEM; one from Montmayeur, the 80/100 frac sand (Figure 6.1.1.a) and four from this work, the 20/40 frac sand (Figure 6.1.1.b), the 100/140 frac sand, (Figure 6.1.1.c), the 20/40 glass beads (Figure 6.1.1.d) and the 100/140 glass beads (Figure 6.1.1.e). Upon examination of these figures it is apparent that there was no grain crushing of either the glass beads or of the frac sand samples during freezing or pressure loading.

The surface features observed in the frac sand photographs (Figures 6.1.1.a, 6.1.1.b and 6.1.1.c) are consistent with those observed before and after freezing and are not a result of either preparation or experimental procedure. There is no evidence of sodium chloride crystals on these post-stress samples. These samples were carefully rinsed with fresh water to remove any residual salt. This was necessary so that the grains could be magnified and photographed without any masking of cracks by salt crystals. No reservoir samples were analyzed after the loading cycles because of previously discussed problems with the SEM. When

Figure 6.1.1.a.   SEM photograph of Montmayeur's 8010 frac sand
                  after loading magnified 150X.
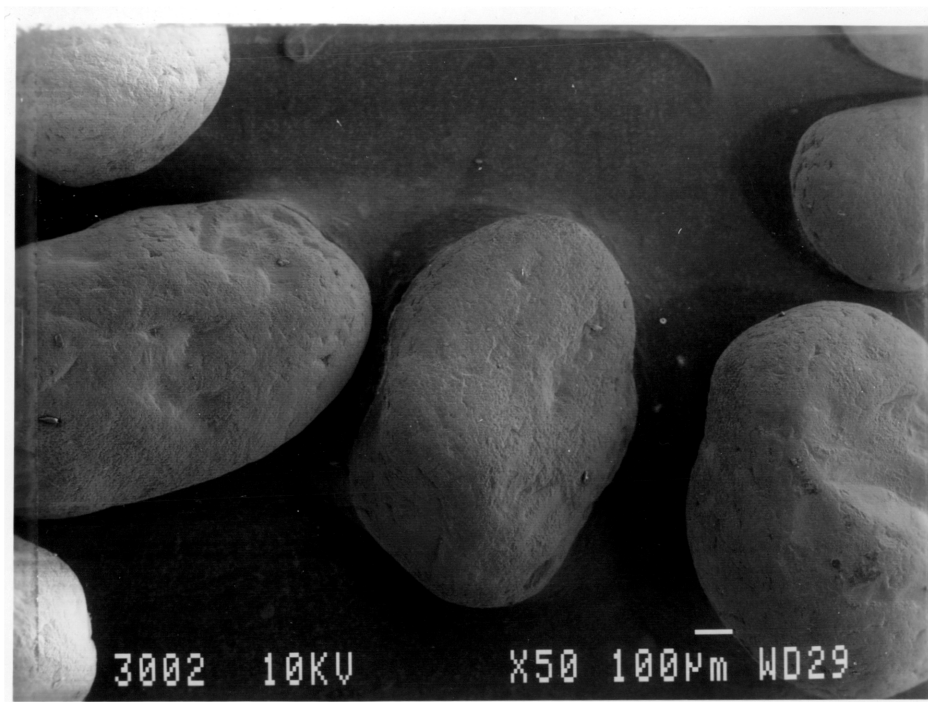
Figure 6.1.1.b. SEM photograph of sample F2040C after loading
magnified 50X.
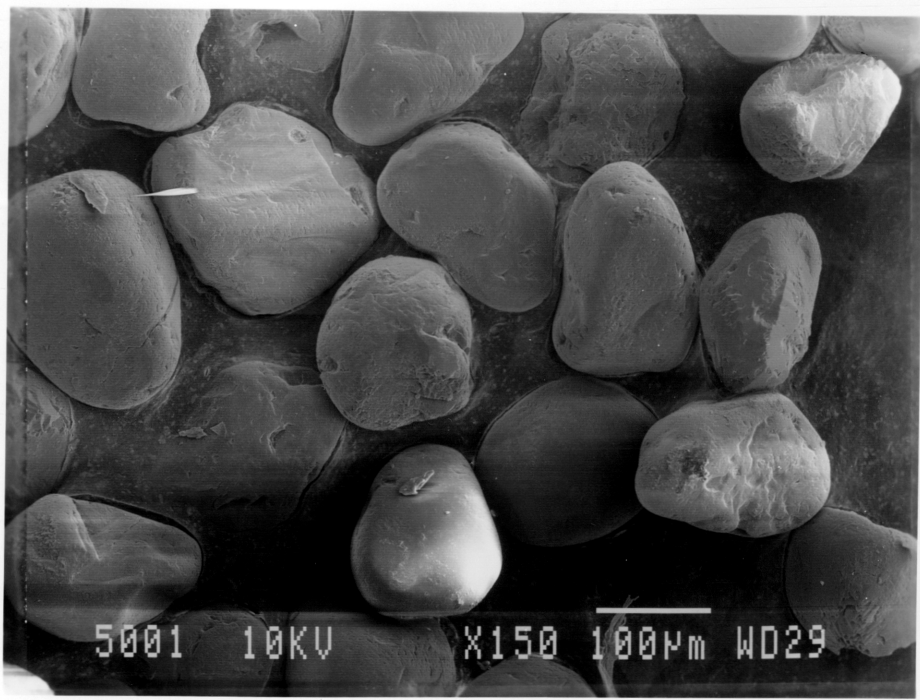
Figure 6.1.1.c. SEM photograph of sample F1014B after loading
             magnified 150X.
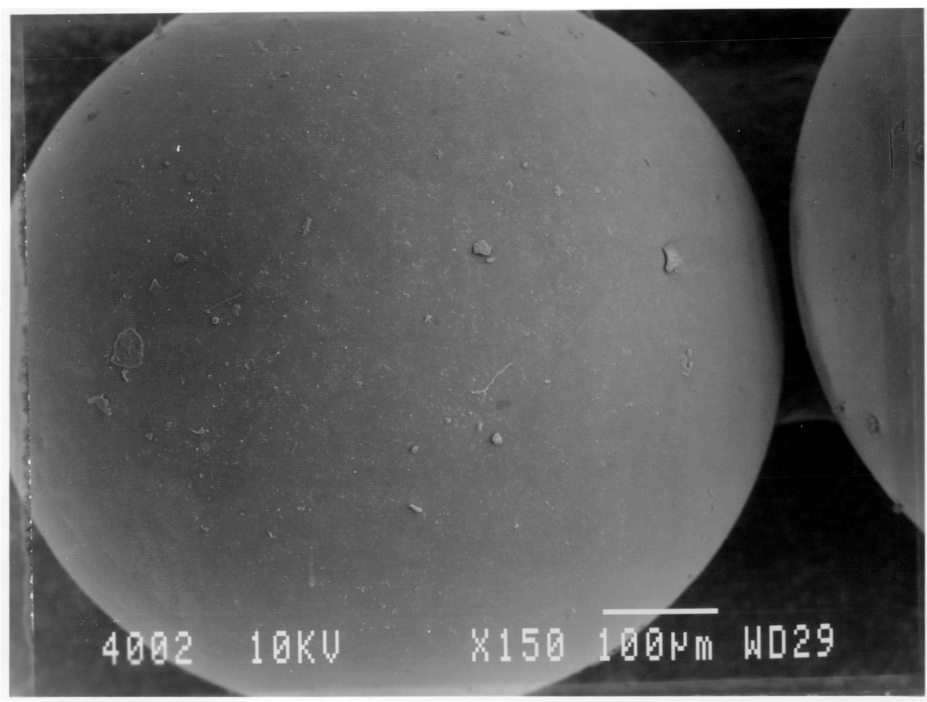
Figure 6.1.1.d.   SEM photograph of G2040A glass beads after
                  loading magnified 150X.
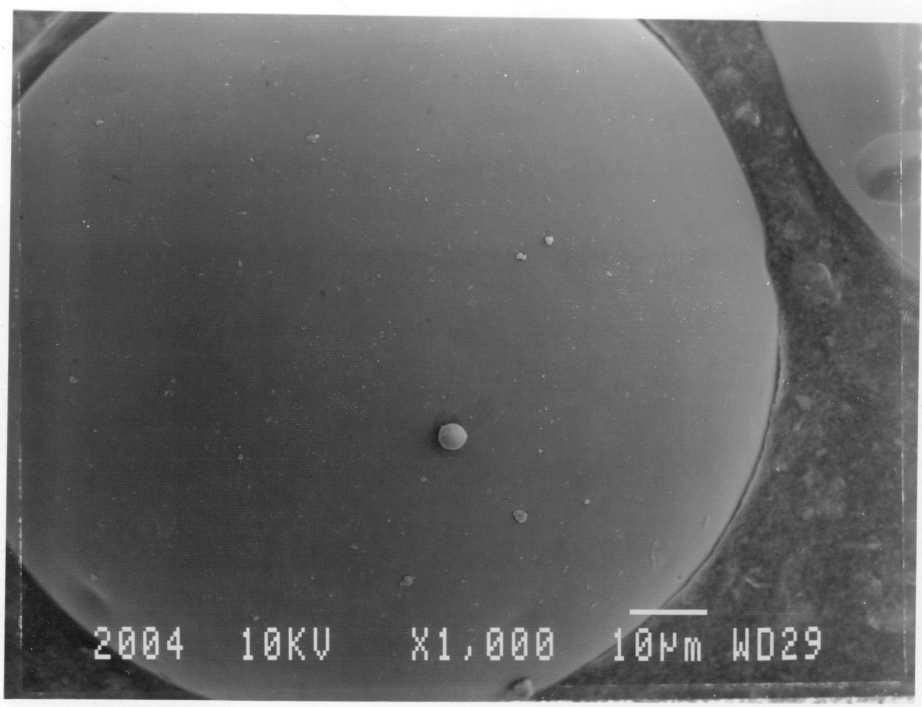
Figure 6.1.1.e. SEM photograph of G1014A glass beads after loading magnified 1000X.

reservoir samples were inside the microscope under vacuum, particles would dislodge and damage the microscope filament causing the SEM to shut down.

6.1.2. Macroscopic results

While measuring the longitudinal and shear wave travel times through the cores there were some very obvious differences between the consolidated rocks and unconsolidated sand packs and among the three different unconsolidated sand packs; glass beads, frac sand and reservoir samples. These will be illustrated and discussed in this section and explained using theoretical models in Section 6.3.

The p-wave arrivals for the consolidated rock cores, STD2, STB5, HCB5, HCB11 and HCB13 were sharp and easy to identify at all pressures from 500 to 5000 psig (Figure 6.1.2.a). However, for the unconsolidated cores the p-wave arrivals were difficult if not impossible to pick at 500 psig (Figures 6.1.2.b and 6.1.2.c). For example, in Figure 6.1.2.b it appears that the p-wave arrival is at point A which is physically impossible. The p-wave arrival indicated by A results in a p-wave velocity greater than the measured s-wave velocity. Instead, upon examination of the p-wave arrival peak at higher pressures the p-wave actually arrives
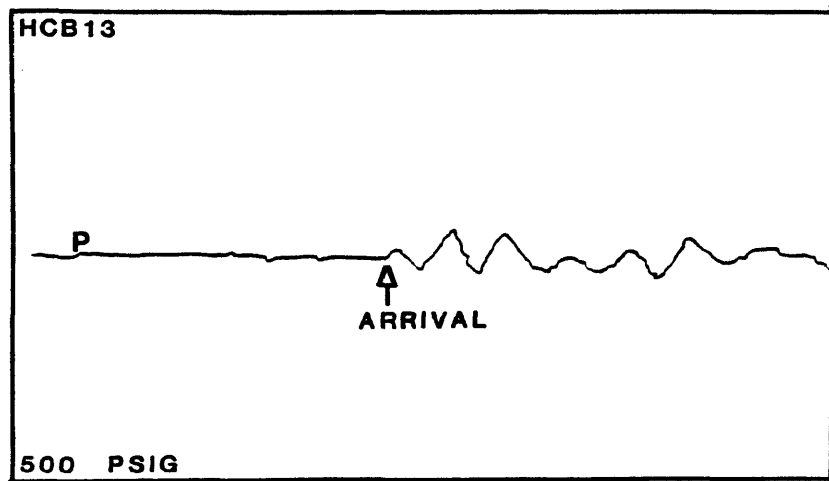
Figure 6.1.2.a. P-wave through Berea rock, HCB13, at 500
                 psig.
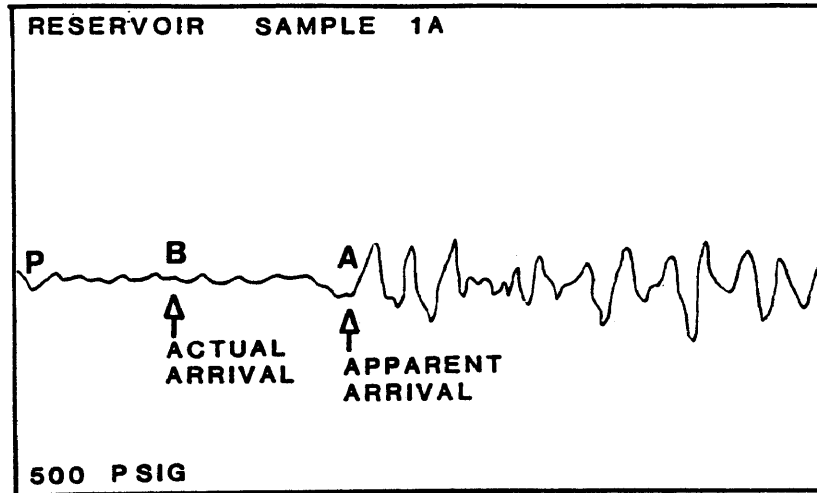
Figure 6.1.2.b. P-wave through Reservoir Sample 1A at 500
                 psig.
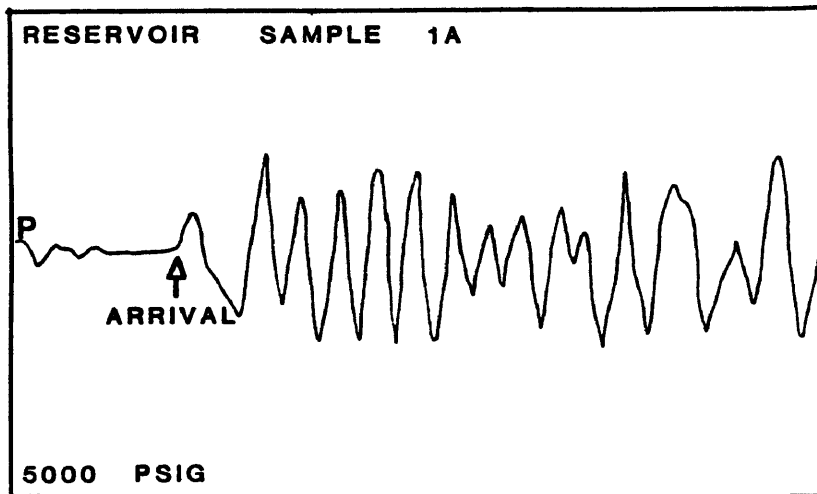
Figure 6.1.2.c. P-wave through Reservoir Sample 1A at 5000
                 psig.

in the vicinity of point B. As the pressure was increased to
1000 psig and above, the p-wave arrivals become more apparent
and were increasingly easier to identify (Figure 6.1.2.c) for
the natural reservoir samples and the smaller (60/80 mesh and
smaller) frac sand and glass bead packs.

For the large, 20/40 mesh, frac sand and glass bead
packs, however, increasing pressure was not as effective in
reducing the wave attenuation and p-wave arrivals were
difficult to identify at both 500 psig (Figure 6.1.2.d) and
at 5000 psig (Figure 6.1.2.e). The actual p-wave arrivals
are indicated by point B on Figures 6.1.2.d and 6.1.2.e.
Thus, grain size appears to be a factor in the attenuation of
longitudinal waves at all pressures investigated for sand
packs of large uniform grain size.

Shear wave arrivals were easiest to identify on the
natural reservoir samples and small grain size (60/80 mesh
and smaller) glass beads and frac sand packs at all pressures
(Figure 6.1.2.f) than for consolidated rocks (Figure
6.1.2.g). With increasing pressure, 3000 psig or greater,
the s-wave amplitude through the cores increased and sharper
peaks formed (Figure 6.1.2.h) except for the large uniform
size grain packs on frac sand and glass beads. Shear wave
arrivals for these large uniform grain packs were not
difficult to pick at low pressures. The increasing amplitude
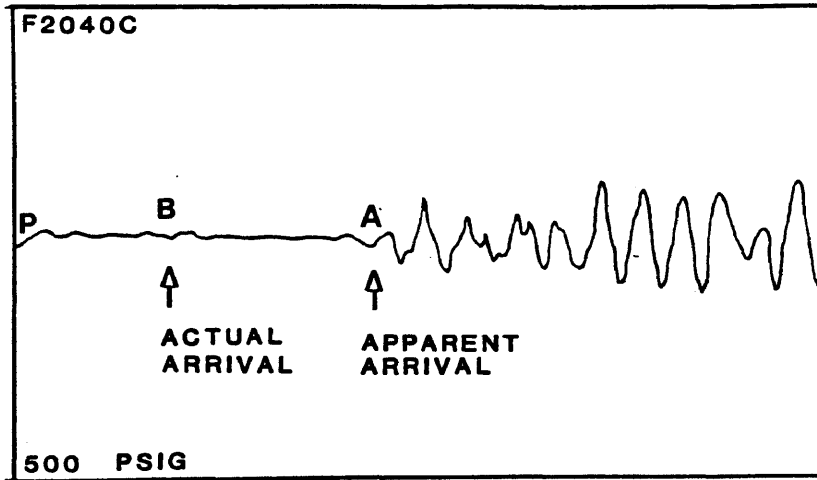
Figure 6.1.2.d. P-wave through F2040C at 500 psig.
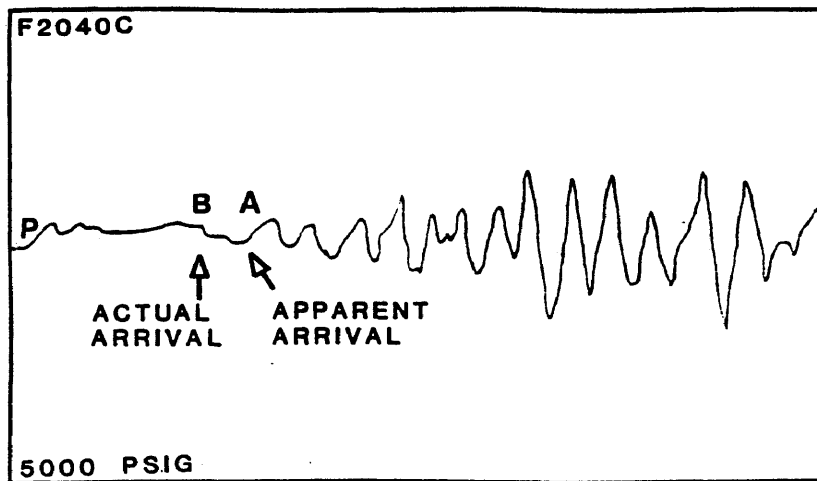
Figure 6.1.2.e. P-wave through F2040C at 5000 psig.
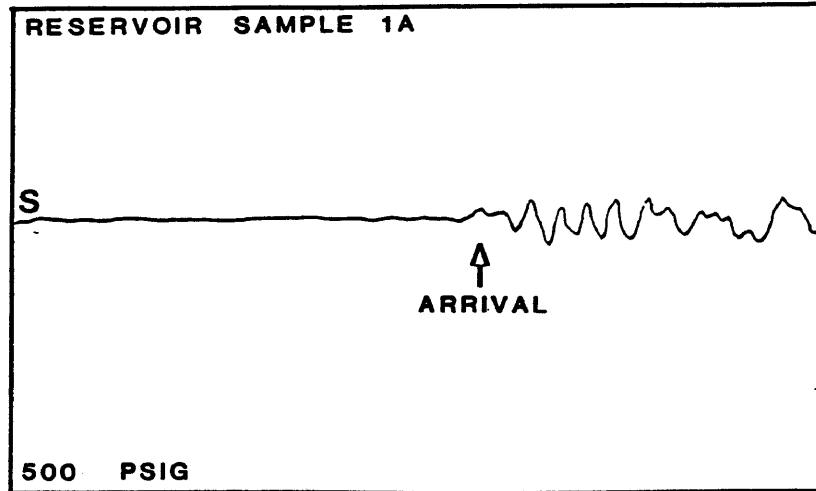
Figure 6.1.2.f. S-wave through Reservoir Sample 1A at 500
                 psig.
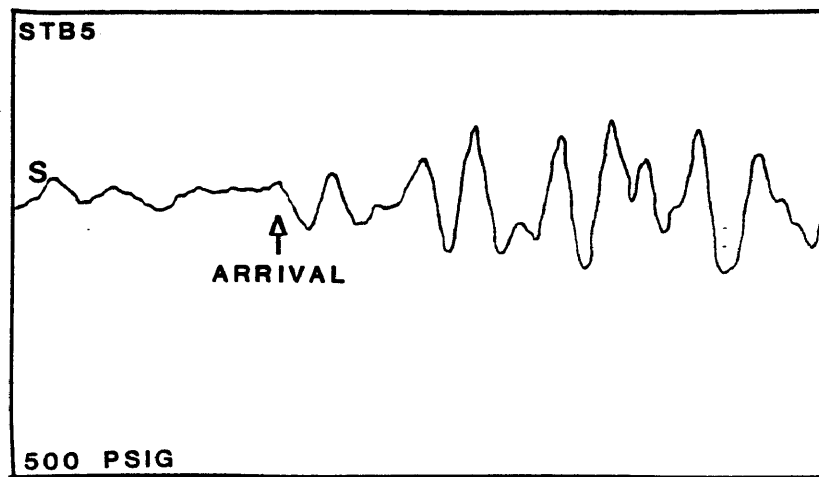
Figure 6.1.2.g. S-wave through STB5 at 500 psig.
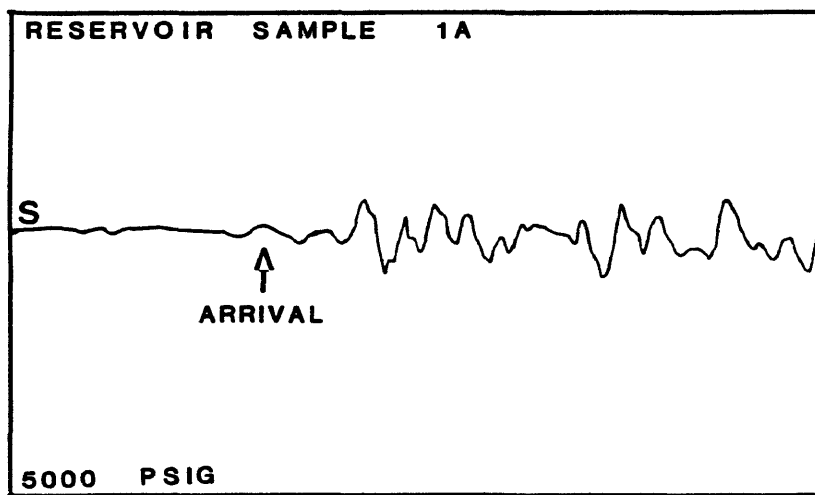
Figure 6.1.2.h. S-wave through Reservoir Sample 1A at 5000
                 psig.

with pressure was observed for the p-wave did not occur for the s-wave.

The problem of p-wave attenuation in the uniform large grain size glass bead and frac sand packs can be explained by the dominant effect of one of the two wave energy dissipation models. The first one is viscous energy loss in the pore fluid and relative movement between pore fluid and the grain (matrix or frame) material. The second one is due to friction in the skeletal frame of the grains during compaction. Stoll (1977) shows that for coarse, high permeability sands, the viscous fluid losses dominate, especially at high frequency. He shows that for a given frequency, coarser sands will have greater wave attenuation than will the finer-grained sands. For the latter sands energy losses due to friction dominate viscous fluid energy losses.

The relationship between p-wave attenuation and grain size can be explained on a conceptual basis, remembering that as a p-wave travels through a medium, the particles of that medium are displaced in the direction of propagation. Referring to Figure 6.1.2.i, assume the p-wave starts traveling at point A and continues through the grain to point B. At point B the wave reaches the grain-pore-fluid interface where energy loss occurs due to refraction. The p-
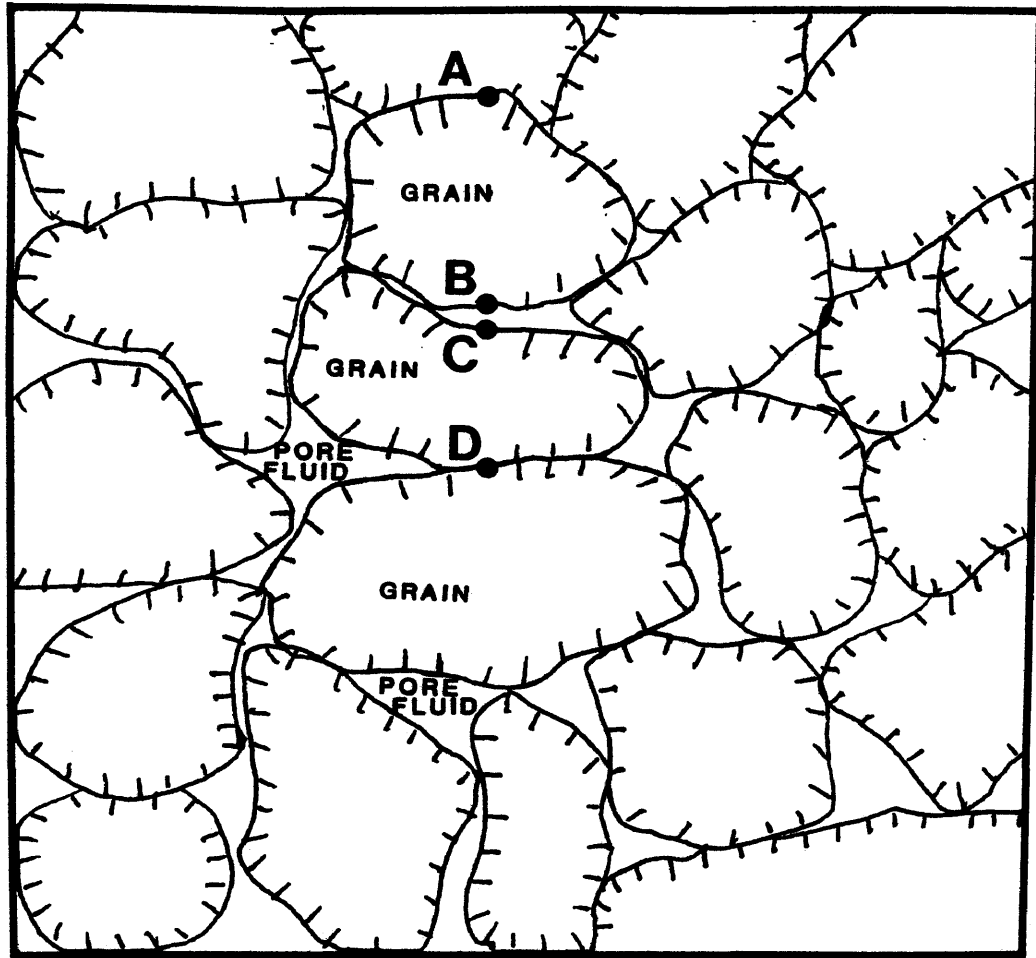
Figure 6.1.2.i. Wave travel path example, see text of
                 discussion.

wave continues through the pore fluid to point C. While traveling through the pore fluid, it attenuates, due to fluid viscous effects, and slows down. When the wave reaches point C energy is lost again at the pore fluid-grain interface due to refraction. The wave continues through a second grain to point D where wave energy losses occur due to the grain-to-grain interface but none to fluid.

It is easy to imagine that for a given porosity, the relative volume of fluid present between large grains in a uniform size pack will be greater than that of fluid present between small grain in a uniform grain size pack at a microscopic level. For large grain packs, then, there are less grain-to-grain contacts per unit area and larger volume of pore fluid present so the viscous fluid effects dominate the energy loss. With increasing confining pressure the volume of pore fluid does not change appreciably and the wave is still attenuated. For the smaller grain packs, the viscous fluid losses are smaller due to the smaller relative volume of water present between the grains but there is a larger number of grains present so the grain-to-grain contact friction losses will dominate over fluid energy losses. As confining pressure is applied, the grains are pushed closer together and the energy loss at the grain contact interfaces

is decreased. This phenomenon reduces attenuation and increases p-wave velocity through the sand pack.

6.2. Comparative Analysis

6.2.1. V_p and V_s measurements in consolidated rocks

Shear and longitudinal wave travel times were measured for the five consolidated rock samples. As can be seen in Figure 6.2.1.a, the longitudinal wave travel times measured by Howarth and Montmayeur are consistent; the dolomite travel times as measured by Montmayeur, sample MSTD2, agree with those of this study for sample HSTD2, and the Berea samples were similarly consistent. The shear-wave travel time measurements on the same cores by Montmayeur and in this research are less consistent (Figure 6.2.1.b). This is primarily due to the difficulty in identifying shear wave arrivals on Berea samples. It was not expected that all the travel times measured by Montmayeur would agree with those of this study for STB5 and STD2 because of the core preparation processes on the cores for this research after Montmayeur made his measurements. Both the shear and longitudinal wave travel times were within the ranges of values measured
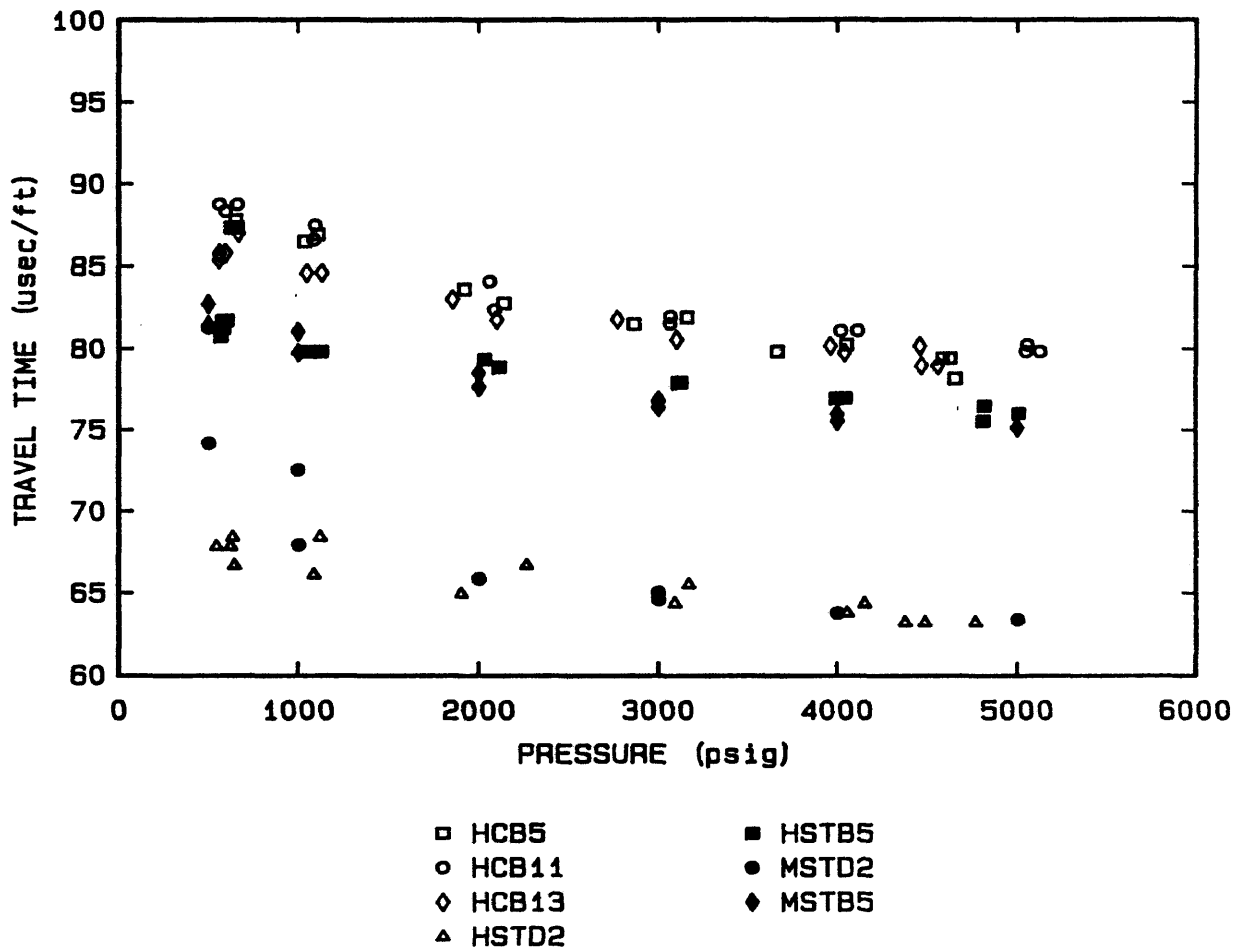
Figure 6.2.1.a. P-wave travel times for all consolidated
                 rocks.

Figure 6.2.1.b.   S-wave travel times for all consolidated
                  rocks.

by other researchers, as discussed in section 2.4.9.

6.2.2. V_p and V_s measurements in frac sand

While Montmayeur ran a series of eight sand grain packs with sizes ranging from 20/40 mesh to 170/200 mesh, only three sizes were run in this study; 20/40, 60/80 and 100/140. Three 60/80 mesh samples were formed and tested in this study. As shown in Figure 6.2.2.a, the p-wave travel times for the 60/80 packs were reproducible for F6080A and F6080D, but not for F6080B which had a lower travel time at high pressures. This indicates that cores were not packed consistently for each experiment. The smaller grain size packs showed shorter p-wave travel time as would be expected due to the attenuation and travel time to grain size relationship discussed in section 6.1.2. The large (20/40) grain size packs had intermediate p-wave travel times between those measured for the 60/80 and 100/140 packs but, because of wave attenuation problems on the large grain size packs, this observation is inconsequential.

Values of p-wave travel time ranged from 150 to 300 microseconds per foot at 500 psig to 100 to 200 microseconds per foot at 5000 psig. There was no obvious trend between s-wave travel time and grain size for the frac sand packs (Figure 6.2.2.b).
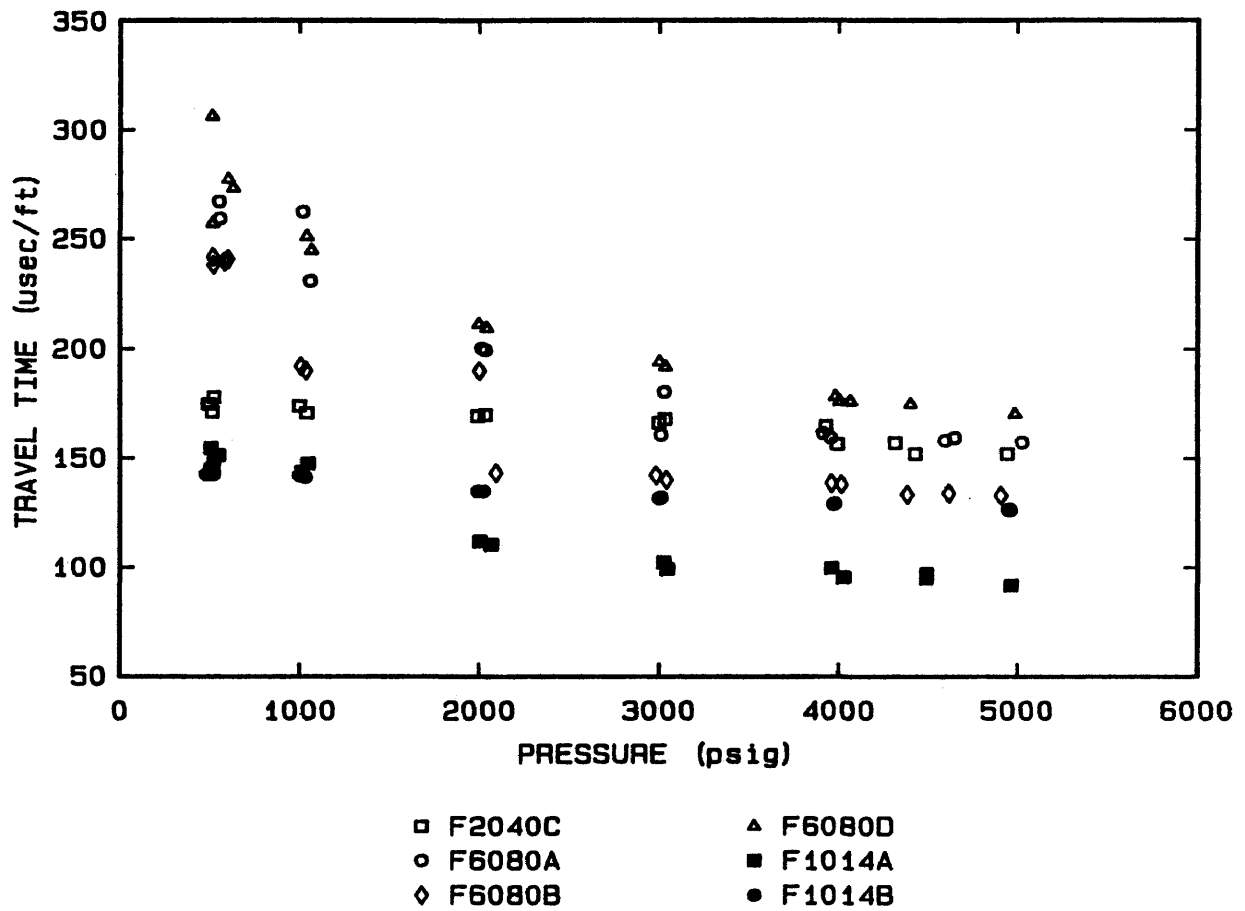
Figure 6.2.2.a. Howarth frac sand p-wave travel time.
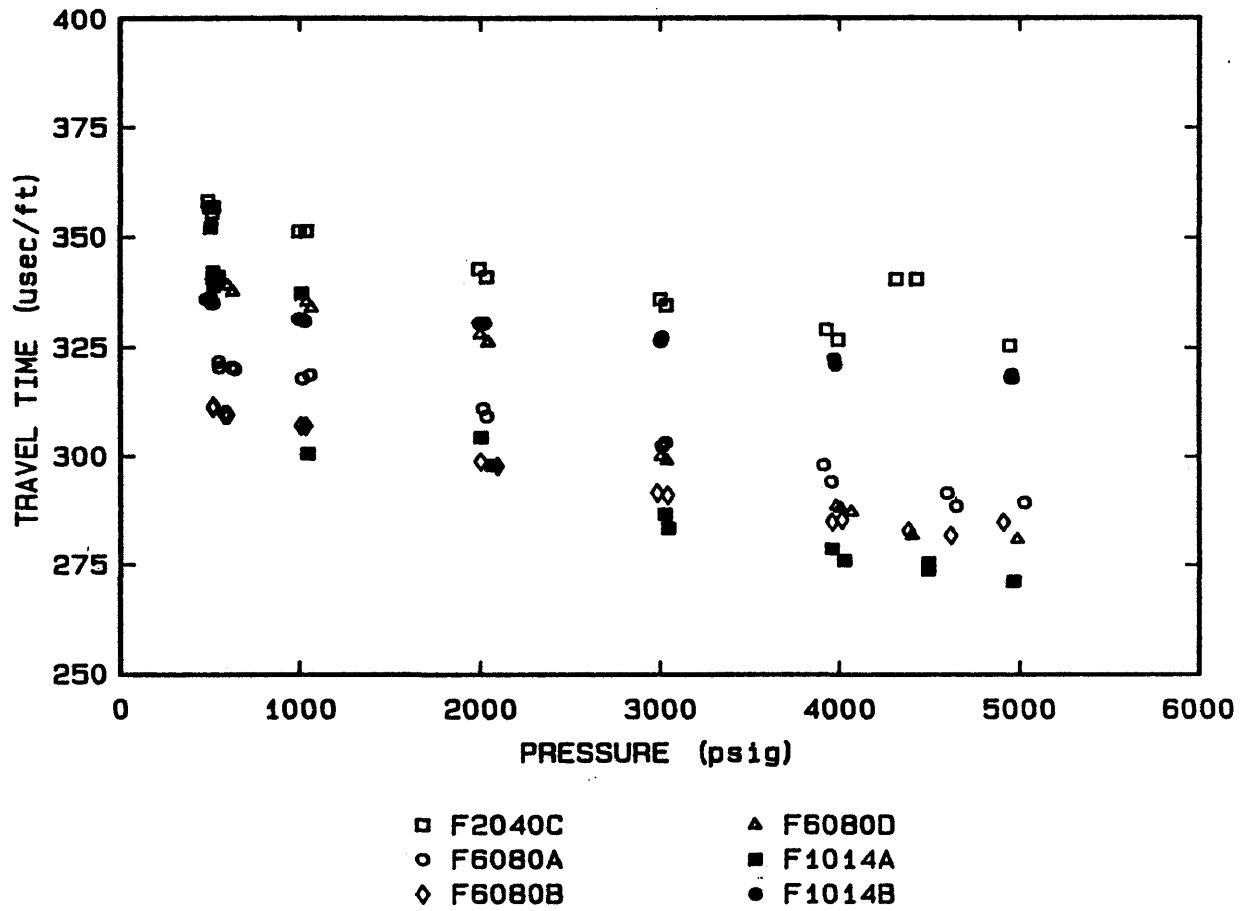
Figure 6.2.2.b. Howarth frac sand s-wave travel time.

Montmayeur's frac sand-pack travel times for different

grain sizes were so close that they are virtually

indistinguishable from each other on a grain size basis. The

only anomalous data on both the p-wave and s-wave

measurements were the large 20/40 frac sand pack which had

lower travel times for both waves (Figures 6.2.2.c and

6.2.2.d). Montmayeur's frac sand travel times were higher

than those of this research for the shear waves but were

lower for the p-wave travel times. It is suspected that

Montmayeur's samples may not have been sieved sufficiently,

which would result in a more poorly sorted sample pack and

different wave travel times. The measurements for his coarse

(20/40) grain packs were inconsistent with those measured in

this study and it is suspected that he also had trouble

identifying wave arrivals on these samples due to wave

attenuation problems.

6.2.3. V_p and V_s measurements in frac sand and glass bead packs

Because frac sand and glass beads are routinely used in

laboratory experiments, 60/80 frac sand packs and 100/140

glass bead and frac sand packs were tested to determine if
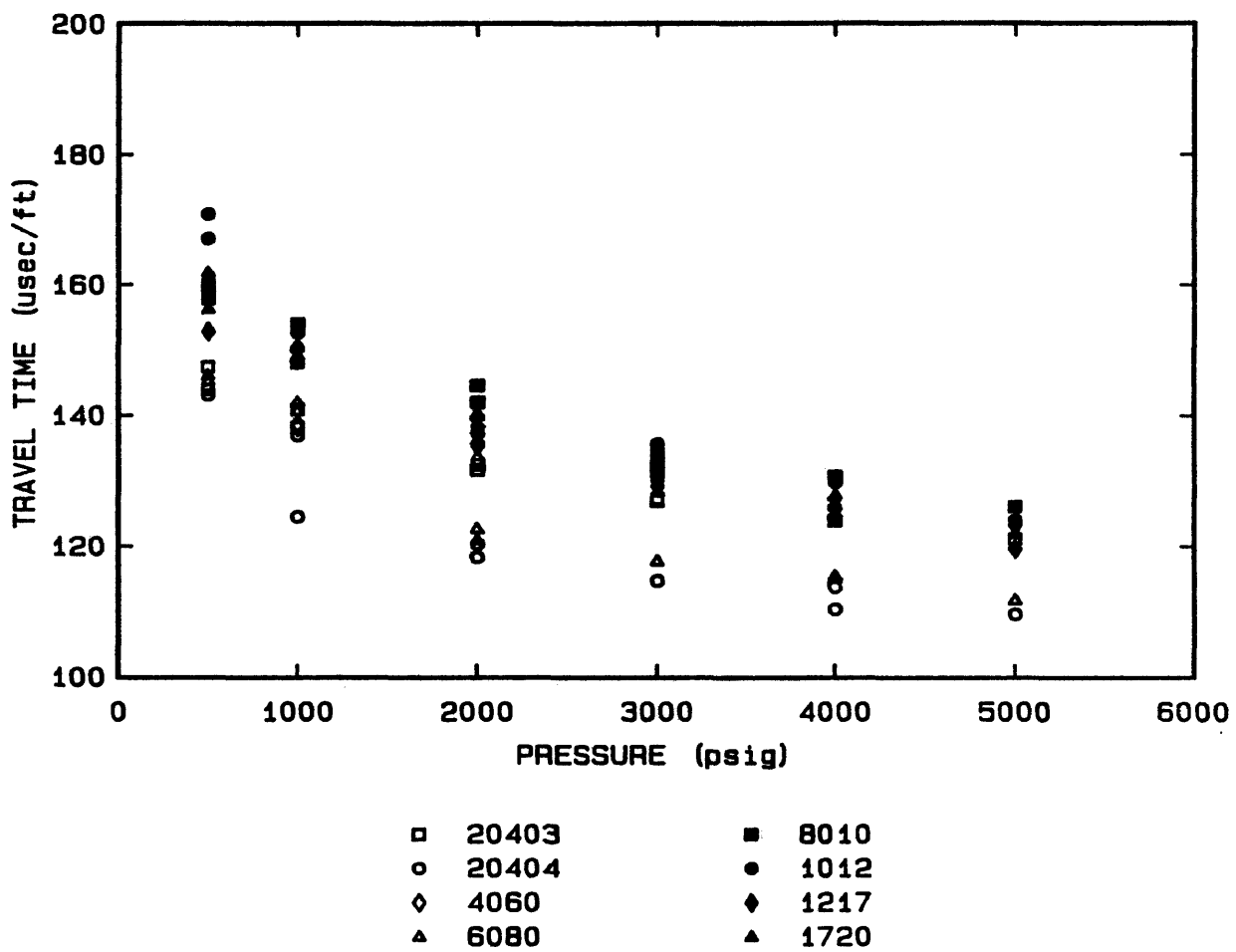
Figure 6.2.2.c. Montmayeur (1985) frac sand p-wave travel
                 times.
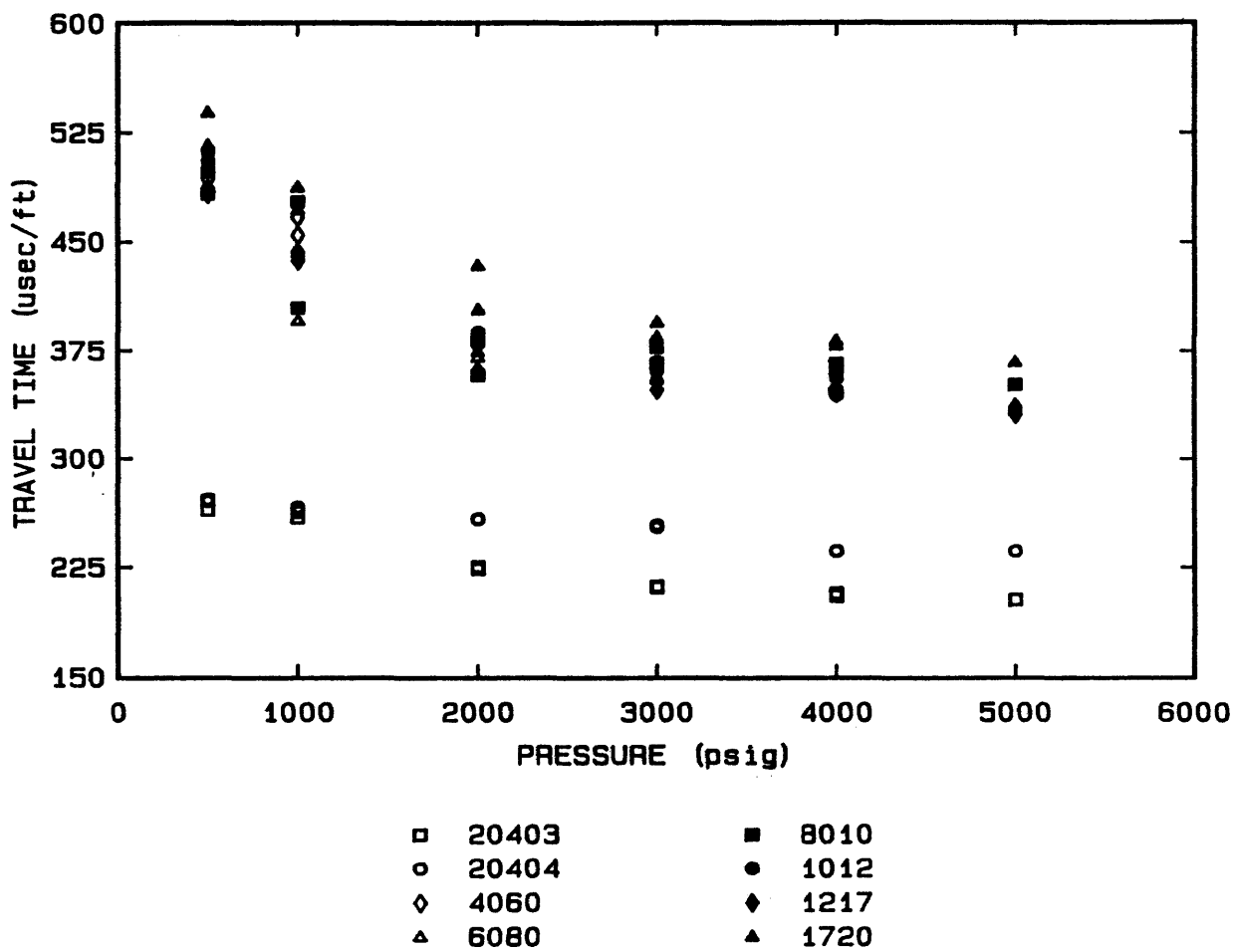
Figure 6.2.2.d. Montmayeur (1985) frac sand s-wave travel
times.

there was any relationship in measured wave travel times and grain shape.

There does not appear to be any conclusive trend in the longitudinal wave travel times with grain shape; although the 20/40 mesh glass beads and frac sand had very nearly the same travel times (Figure 6.2.3.a). The glass beads and the frac sand packs had different arrival times. The 100/140 mesh glass bead travel times were nearly twice those of the 100/140 frac sand. The shear wave travel times were more reproducible than the p-waves. The 20/40 values were nearly the same and slightly higher than the 100/140 glass bead and frac sand packs (Figure 6.2.3.b). The 60/80 frac sand packs had slower travel times than both the 100/140 and 20/40 packs. Again, because of the difficulty encountered in measuring p-wave travel times through large uniform grain size packs, the confidence in the arrival time selection for 20/40 glass bead and frac sand packs of this experiment is low.

6.2.4. V_p and V_s measurements in reservoir sand samples

Nine reservoir sand packs were tested and wave velocity measurements were made for each (Figures 6.2.4.a and b).
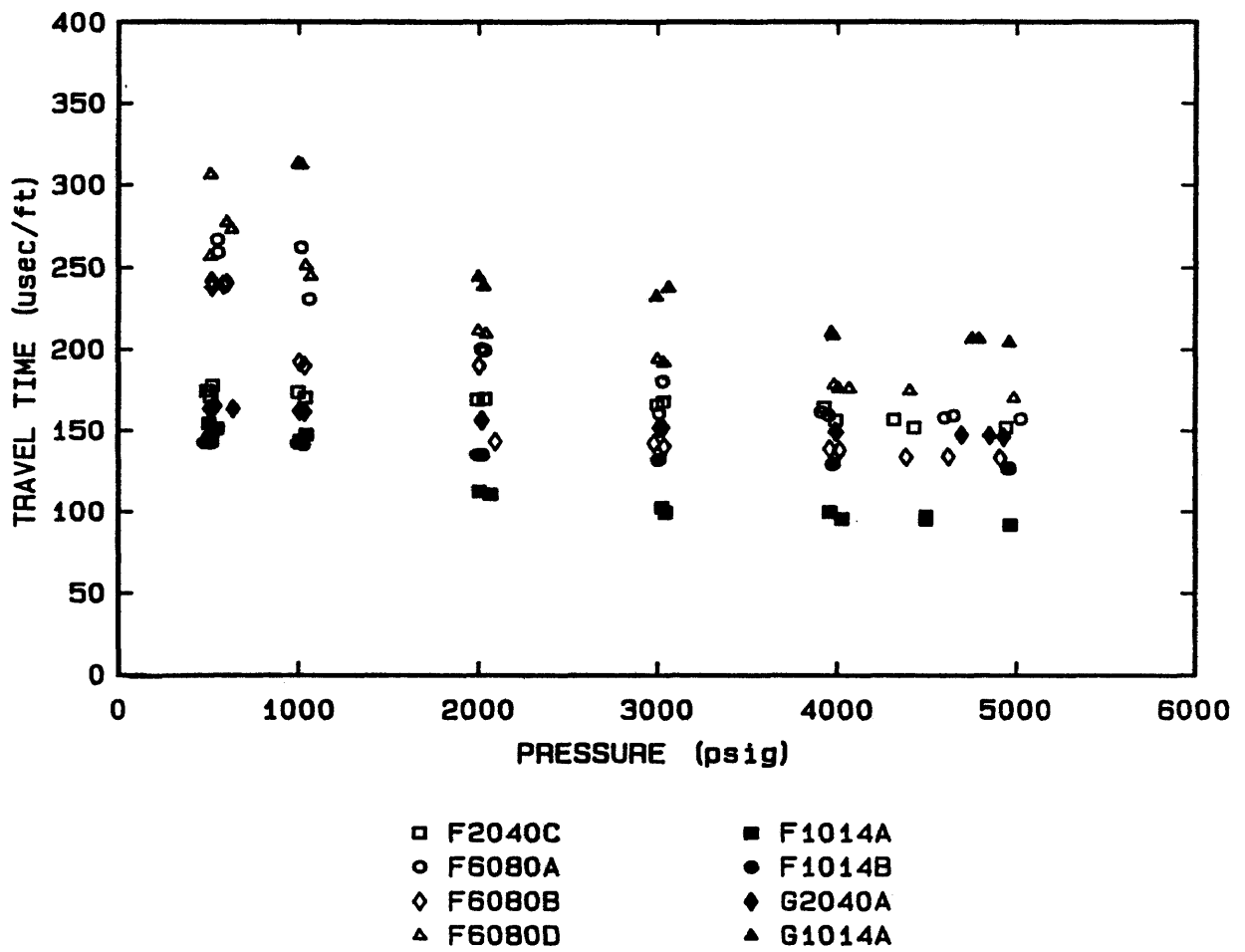
Figure 6.2.3.a.   P-wave travel time for glass bead and frac
                  sand packs.
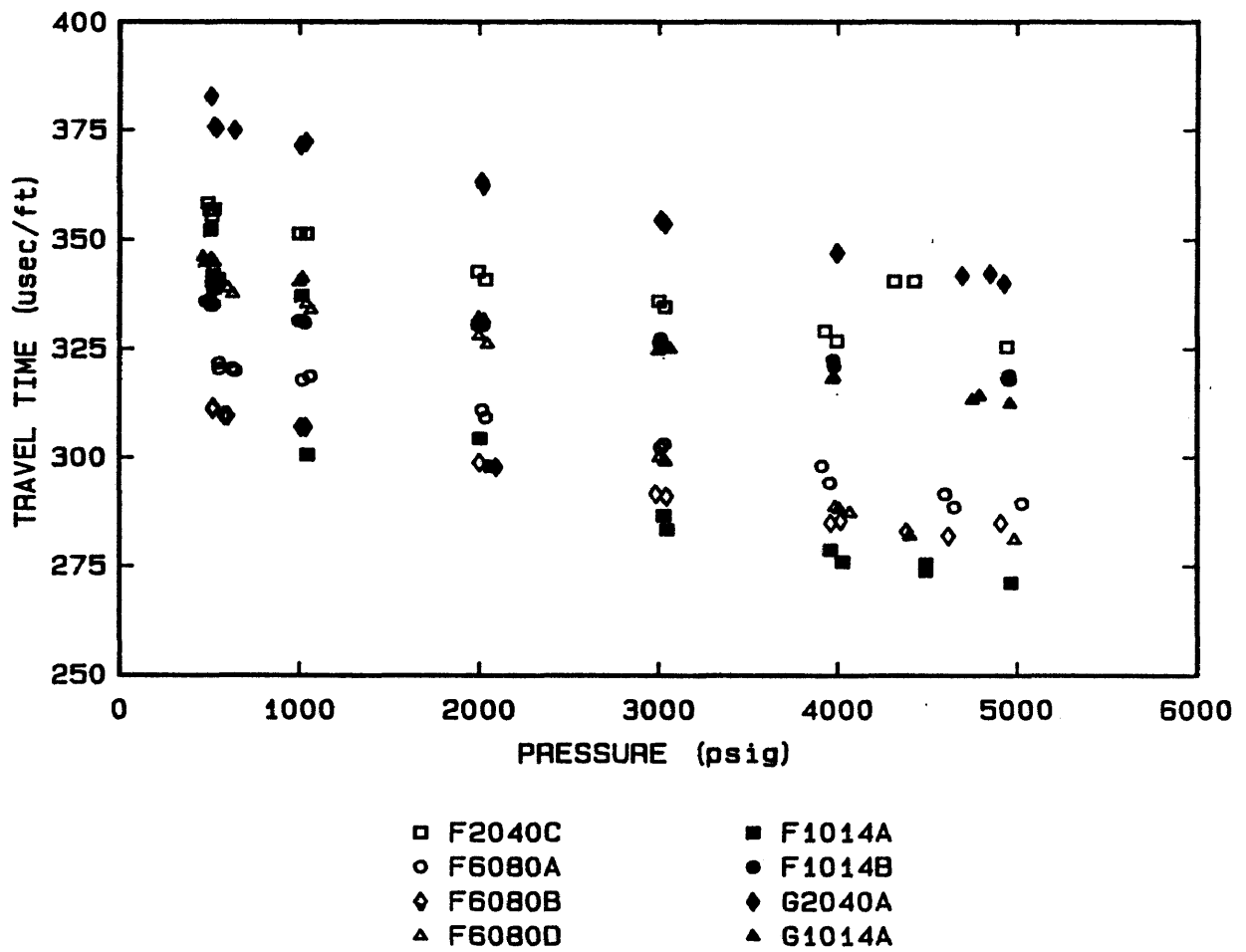
Figure 6.2.3.b. S-wave travel times for glass bead and frac
                 and packs.
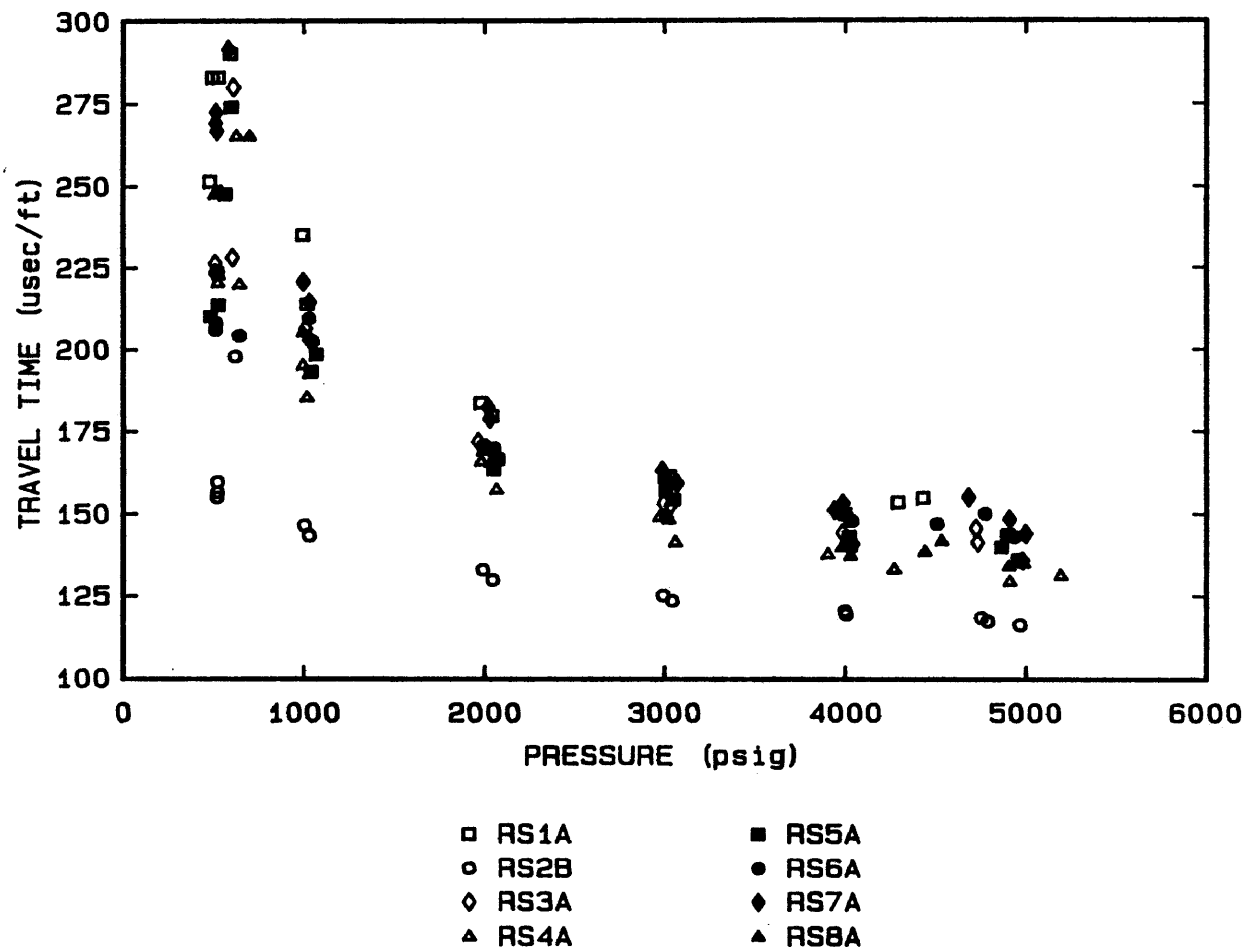
Figure 6.2.4.a. P-wave travel time for Reservoir Samples.
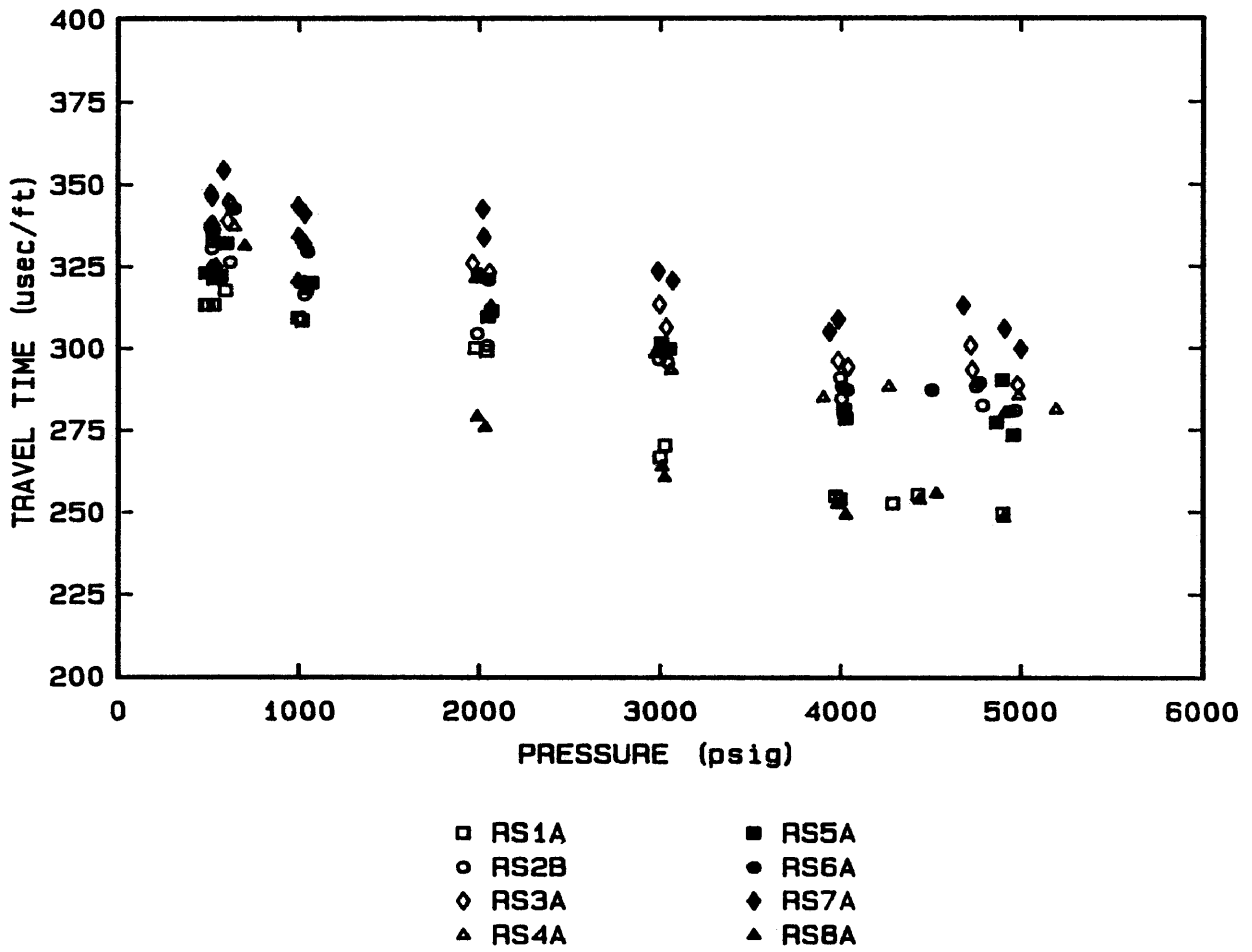
Figure 6.2.4.b. S-wave travel times for Reservoir Samples.

One purpose of testing various frac sand and glass bead packs
was to determine how their travel times compare to those for
reservoir samples.

Table 6.2.4 contains a list of the reservoir samples,
their mean grain diameters, and the mesh size equivalent to
that mean grain diameter. The 20/40, 60/80 and 100/140 mesh
size packs were chosen because they are in the same size
range as the reservoir samples. Comparing the p-wave travel
times for the different reservoir samples (Figure 6.2.4.a),
the individual travel times for all samples are grouped
together except for Reservoir Sample 2B. This pack had the
smallest mean grain diameter and lower p-wave travel times
than the other packs over the entire pressure range.
Correspondingly, the 100/140 mesh frac sand had lower p-wave
travel times than did the larger grain packs. One would
expect Reservoir Sample 6A to also be anomalous based on its
higher values of mean grain diameter but its measurements
were close to the other samples. This may be due to the core
tested not being a representative sample of the sand.

The shear wave travel times did not indicate any trend
with grain size. The travel times were very comparable to
those for the frac sand and glass bead samples. Reservoir
Samples 2 and 6 was clustered with the other sands on the

Table 6.2.4.
Reservoir Sample Mean Grain Diameter and Equivalent Mesh Size

Reservoir Sample	Mean Grain Diameter (mm)	Equivalent Mesh Size
1A	0.1340	100/120
2B	0.1069	140
3A	0.2316	60/70
4A	0.2736	50/60
5A, B	0.1805	70/80
6A	0.5176	35
7A	0.1805	80
8A	0.1817	80

shear wave measurements, indicating that travel time there is
not a definite relationship between grain size and shear wave
travel time.

In summary, there does appear to be a slight trend
between grain size and p-wave travel time. The smaller grain
size packs have shorter travel times than the larger grain
packs. The 20/40 mesh grain packs did not fit this trend but
this is considered to be due to the difficulty in identifying
p-wave arrivals on these packs because of wave attenuation.
The small grain size frac sand and glass bead packs in the
same size range as the reservoir samples had similar wave
travel times. There did not appear to be any trend between
s-wave travel time and grain size or angularity.

6.2.5. Bulk compressibility measurements

Bulk compressibilities of all cores were calculated
using the shear and longitudinal travel time measurements
(Appendix B). These calculations will be referred to as the
measured dynamic bulk compressibility, C_b, values. In a
later section of this chapter, 6.3., the calculations of bulk
compressibility using wave measurements and corrections using
the Biot and Gassmann models will be discussed. Graphs and
tables of dynamic bulk compressibility versus pressure were

made for all samples and are found in Appendix B. While the
measured dynamic bulk compressibilities may appear to be low,
it should be remembered that the static bulk compressibility
can be at lease twice as high as the dynamic (Montmayeur
1985).

6.2.5.1. Consolidated rocks

The bulk compressibility of the dolomite sample STD2 was
very nearly linear for high pressures. Montmayeur's (1985)
values for STD2 were slightly higher than those of this study
which can be attributed to core preparation procedures. The
Montmayeur measured value for STD2 at 5000 psig was 0.17 •
10^{-6} per psi and the bulk compressibility measured in this
research was 0.15 • 10^{-6} per psi. Similarly, Montmayeur's
values for the Berea sample STB5, were also slightly higher,
0.31 • 10^{-6} per psi versus 0.27 • 10^{-6} per psi. The three
new Berea cores showed that the higher permeability cores,
HCB11 and HCB13 had nearly identical compressibilities at
high pressure, 0.29 • 10^{-6} per psi while the lower
permeability core HCB5 had slightly higher compressibility at
high pressure, 0.32 • 10^{-6} per psi. All of these three cores
were cut from the same Berea slab but higher permeabilities
resulted for HBC11 and HBC13 due to higher oven drying
temperatures during core preparation, see Table 4.1.

6.2.5.2. Montmayeur's (1985) frac sand packs

The bulk compressibilities of Montmayeur's frac sand packs are nearly identical except for core 20403. All cores, except 20403, show bulk compressibility at high pressure to be $0.60 \cdot 10^{-6}$ per psi while 20403 has a higher value, approximately $1 \cdot 10^{-6}$ per psi. Careful analysis of Montmayeur's raw data files show that 20403 may have been only 95% water saturated while the other cores were 100% water saturated. The higher compressibility could be attributed to the presence of gas in the pores.

6.2.5.3. Glass bead and frac sand packs

The three 60/80 frac sand packs from this study had comparable bulk compressibilities of $1.0 \cdot 10^{-6}$ per psi at high pressures. The 20/40 frac sand packs and glass beads had higher compressibilities of $1.2 \cdot 10^{-6}$ and $1.1 \cdot 10^{-6}$ per psi, respectively. The difference between these values and Montmayeur's (1985) may be due to quality control during sieving. The smaller grain size packs 100/140 had interesting results. The two frac sand samples had different compressibilities, F1014A was much lower, $0.4 \cdot 10^{-6}$ per psi at 5000 psi, versus $0.75 \cdot 10^{-6}$ per psi at 5000 psi for

F10104B. The 100/140 glass bead pack had much higher values for compressibility than the other packs with C_b at 5000 psi of $4 \cdot 10^{-6}$ per psi.

6.2.5.4. Reservoir Samples

The reservoir samples could be grouped according to their compressibilities. Samples 1A, 3A, 4A, 5A, 5B, 7A and 8A had nearly the same compressibilities, $1.0 \cdot 10^{-6}$ per psi at high pressures. The mean grain diameters of all these samples is in the 60/80 mesh size range (Table 6.2.4) and these reservoir samples have the same bulk compressibilities at high pressure as the 60/80 frac sand samples.

Reservoir Sample 2B, whose mean grain diameters was about 140 mesh had bulk compressibility at 5000 psig of $0.65 \cdot 10^{-6}$ per psi. This value was halfway between the two 100/140 mesh frac sand values of $0.4 \cdot 10^{-6}$ for F1014A and $0.75 \cdot 10^{-6}$ per psi for F1014B. Reservoir Sample 6A had higher values of bulk compressibility than any of the other reservoir samples at high pressure, $1.2 \cdot 10^{-6}$ per psi. The mean grain diameter of this pack was comparable to 20/40 mesh frac sand which had compressibility of $1.2 \cdot 10^{-6}$ per psi.

In summary, it appears that the measured bulk dynamic compressibility for the reservoir sample can be closely

approximated based on the values measured for frac sand pack

samples whose mesh/grain size is comparable to the mean grain

diameter of the reservoir sample. There also appears to be a

trend between grain size and dynamic bulk compressibility

where increasing bulk increases compressibility with

increasing mean grain diameter.

6.3. Theoretical Analysis-Application of Models

The three models described in Chapter 2.5 were: 1) the

Wyllie time average model, 2) the Gassmann (1951) model, and

3) the Biot (1956) model. The Wyllie time average model is

used, under specified conditions, to calculate formation

porosity using acoustic wave velocity and the rock matrix and

pore fluid p-wave travel times. Both the Gassmann and Biot

models are used to calculate static bulk compressibility

using acoustic p-wave velocity together with bulk density,

porosity, and compressibilities of the dry rock skeleton, the

pore fluid and the matrix material. The assumptions of the

two models differ in that the Gassmann model assumes that

there is no relative motion between the pore fluid and the

rock matrix material during compression. The Biot model

allows for relative motion between the pore fluid and rock

matrix material and includes two other factors; 1) a mass

coupling coefficient which is a function of pore geometry, and 2) a structural factor which is related to tortuosity and flow path. Gassmann's model describes low frequency wave propagation through fluid-saturated porous media, but Biot's model allows for high frequency wave propagation. Gassmann's model is easier to use than the Biot model and is used in the industry to predict static bulk compressibility from dynamic measurements. This may not be correct because laboratory dynamic measurements are made at very high frequencies (on the order of 500 to 1000 kHz). Noting that Gassmann's model is for low frequency wave propagation, it may not be applicable for high frequency laboratory measurements.

In order to test the use of and compare the two models to determine the applicability of the Gassmann model (for laboratory measurements of unconsolidated sand bulk compressibility) as a simplified form of the Biot equation two sets of measurements are necessary. They are: 1) static measurements of bulk compressibility, and 2) simultaneous dynamic p- and s-wave measurements. Montmayeur (1985) provides both sets of data for his unconsolidated frac sand samples and, using the dynamic measurements, he calculated static bulk compressibility with Biot's model.

This section is broken up into three parts. The first section uses the Wyllie time-average equation to calculate

the porosity of the consolidated and unconsolidated cores

from dynamic measurements. In the second part, calculations

were made using the formation strength predictor models to

determine whether the sand packs would flow based on accepted

cutoff values of G and G/C_b. The third part includes the

calculation of static bulk compressibility for Montmayeur's

(1985) unconsolidated frac sand samples and a comparison of

the measured static bulk compressibility, the Biot calculated

static bulk compressibility, and the Gassmann calculated

static bulk compressibility.

6.3.1. Wyllie time-average equation

Wyllie et al. (1956) presented their well known "time-

average equation" from which porosity can be calculated from

the longitudinal wave travel time, Equation 6-1.

$$\phi = \frac{t_p - t_{ma}}{t_f - t_{ma}} \qquad (6-1)$$

where:

t_p = Travel time through rock and fluid

t_f = Travel time through fluid only

t_{ma} = Travel time through rock matrix material

Wyllie et al. (1956) found that the time-average calculated results were consistently higher than the observed wave velocity at atmospheric pressure. They found that for consolidated rocks at high pressures (usually greater than 4000 psig) a limiting velocity could be reached that agreed well with the calculated time average velocity. Elliott and Wiley (1978) found that the Wyllie time-average equation was not applicable for determination of p-wave velocity in partially saturated unconsolidated sands. Wyllie et al. (1956) had addressed this problem earlier and found that, for unconsolidated samples, higher pressures were required to reach the limiting velocity. Unfortunately, grain failure from crushing occurred before that pressure could be reached.

P-wave velocities measured at 5000 psig were used to calculate porosity for both the consolidated and unconsolidated samples used in this study (Table 6.3.1). Wyllie's equation predicts reasonable porosity values for the consolidated Berea sandstone samples but grossly under-predicts the dolomite (STD2) porosity and over-predicts unconsolidated sand porosity.

According to Hilchie (1978), Wyllie's equation gives good porosity values for carbonates with homogeneous porosity but underestimates porosity for carbonates with vugs or secondary porosity. As expected the porosities calculated

Table 6.3.1.
Comparison of Wyllie Time-Average Porosity at 5000 psig
to Laboratory Measured Porosity at 0 psig

Core	Wyllie Porosity (%) (5000 psig)	Laboratory Porosity (%) (0 psig)	Percent Difference
Consolidated:			
STD2- Howarth	13.42	21.52	60.36
STB5- Howarth	17.98	21.10	17.35
HCB5	20.42	23.80	16.55
HCB11	20.71	20.99	1.55
HCB13	20.09	21.11	5.68
STD2- Montmayeur	13.55	21.30	57.20
STB5- Montmayeur	17.34	20.80	19.95
Unconsolidated:			
G2040A	68.32	38.18	44.12
G1014A	110.17	39.68	63.98
F2040C	72.55	36.24	50.05
F6080A	76.25	31.63	58.54
F6080B	58.85	33.05	43.84
F6080D	85.58	33.81	60.49
F1014A	29.24	39.09	33.69
F1014B	54.18	34.65	36.05
Res. Sample 1A	66.66	40.71	38.93
Res. Sample 2B	46.88	37.92	19.11
Res. Sample 3A	60.96	39.11	35.84
Res. Sample 4A	56.26	36.35	35.38
Res. Sample 5A	61.22	43.56	28.85
Res. Sample 5B	56.05	42.41	24.34
Res. Sample 6A	66.18	37.68	43.06
Res. Sample 7A	66.89	39.80	40.50
Res. Sample 8A	59.59	40.72	31.67
20403- Montmayeur	50.45	32.60	35.38
20404- Montmayeur	42.14	33.00	21.69
4060- Montmayeur	51.97	34.20	34.19
6080- Montmayeur	43.63	34.20	21.61
8010- Montmayeur	53.97	32.50	39.78
1012- Montmayeur	52.50	35.90	31.62
1217- Montmayeur	54.96	35.30	35.77
1720- Montmayeur	50.91	33.40	34.39

using the Wyllie equation for unconsolidated sands were too
high, indicating that the confining pressure was not high
enough to reach a terminal velocity. Hilchie (1978) suggests
using travel times through adjacent shales to determine
whether a formation is compacted. He suggests using a cut-
off value of 100 microseconds per foot; if the travel time
through the shales is greater than this value the sand is
usually unconsolidated. Further, the deviation between the
Wyllie calculated porosity and true porosity is a good
indicator of the "uncompactedness" of the formation.
Tixier's formula exists (Equation 6-2) to calculate the
proper porosity in uncompacted formations which takes into
account the travel time through adjacent shales.

$$\emptyset = \left(\frac{t_p - t_{ma}}{t_f - t_{ma}} \right) \cdot \left(\frac{1}{B_{cp}} \right) \tag{6-2}$$

where:

$$B_{cp} = \frac{t_{sh} \cdot c}{100}$$

t_{sh} = Travel time through shale

c = 1, unless more correction is necessary

6.3.2. Determination of formation strength

Tixier, Loveless and Anderson (1973) presented limiting values of shear modulus, G, and a ratio of shear modulus to bulk compressibility, G/C_b, that are used to determine the formation strength and susceptability to sand flow. If G/C_b is greater than $8 \cdot 10^{11}$ psi^2 no sand flow will occur and if G/C_b is less than $7 \cdot 10^{11}$ psi^2 sand flow control will be necessary. Additionally, if G is greater than $6 \cdot 10^5$ psi sand flow should not be a problem. The values of G and G/C_b were calculated for all the unconsolidated samples to predict sand flow problems and are given in Appendix B. Using the G/C_b limiting values, F1014A and Montmayeur's 20404 would not flow at pressures greater than 2000 psi. Using the G limiting value, Montmayeur's 20403 would not flow at pressures greater than 3000 psi. All of the other unconsolidated sand packs would flow at all pressures. One of the assumptions of these formation strength predictive methods is that there are two phases present in the pore fluid. This assumption was not met and, because interfacial tension plays a large role in sand flow, the prediction of formation sand flow from this test is not generally applicable.

6.3.3. Comparison of C_b from Biot and Gassmann models.

The Biot model was used by Montmayeur (1985) to calculate the static bulk compressibility of his samples using rock properties and dynamic wave travel times. At high pressures, where wave arrivals are easier to identify, he found that his Biot calculated and static measured values of bulk compressibility were very similar. The Biot model is cumbersome to use and must be solved on a computer because of the required iterative procedures (Montmayeur 1985), as shown in Equation 2-34. The Biot model takes into account high frequency wave propagation and includes a mass coupling factor, which relates the coupling between the grain matrix and the pore fluid. The Biot model is applicable for most conditions for calculating bulk compressibility for either consolidated or unconsolidated media at high or low frequencies.

The Gassmann model, which is generally considered to be applicable in low frequency ranges, is a simplified form of the Biot model and both are applicable in low frequency ranges. The question then becomes, when do we need to use the cumbersome Biot model and when will the Gassmann model suffice?

In comparing the two models, the most important difference is the frequency term. Montmayeur found that when cores are 100% water saturated, dynamic measurements are not function of the mass coupling factor. A brief discussion on the relationship between frequency and wavelength follows which provides insight into why frequency plays such a dominant role in wave propagation through reservoir and core samples.

The frequency and wavelength are related to travel time by Equation 6-3.

$$\lambda = \frac{V_p}{f} \qquad\qquad (6-3)$$

where: λ = Wavelength

V_p = P-wave velocity

f = Frequency

There is also a relationship between frequency and attenuation. In the reservoir, low frequency waves (20,000 Hz and below) with long wavelengths are propagated because they will travel farther into the formation before attenuating. In the laboratory, high ultrasonic frequencies are used because core samples are so small that a long wavelength wave might "pass over" the sample. Longitudinal

waves can be generated within a large frequency range and if the frequency is above the audible range (20-20,000Hz) it is termed ultrasonic. High frequency ultrasonic waves are produced when a quartz crystal is elastically vibrated by resonance with an applied alternating electric field (Halliday and Resnick 1974). This is also known as the piezoelectric effect.

One of the basic assumptions of both the Biot and the Gassmann theories is that the wavelength of the longitudinal wave must be greater than the grain diameter of the particles comprising the matrix material. Using high frequency waves in the laboratory on large uniform grain size frac sand and glass bead packs may invalidate the use of Gassmann's model. If the wavelength is too small, approximately the size of a single grain, the measured rock property would be representative of the grain and not the whole rock or sand sample. Murphy (1982) suggests using a 100 to 1 ratio of core length to grain diameter to obtain wave measurements which truly represent the rock sample. The ratio of mean grain diameter to core length was greater than 100-to-1 for all unconsolidated samples except the 20/40 frac sand and glass beads.

Following is a comparative analysis which illustrates the grain size-wavelength relationship given typical frac

sand longitudinal wave travel time of approximately 2000
meters per second for a 750 kHz frequency. Using Equation
6-3 the wavelength is calculated to be 0.00276 meters. Table
6.3.3 shows the ratio of wavelength to grain diameter for the
sand mesh sizes used in this study. For the large grain
sizes used, 20 mesh, the wavelength is only three times as
long as the grain diameter whereas for the small grains, 200
mesh, the wavelength is almost 40 times the grain diameter.

White's formulation of the Gassmann model was used to
calculate the static bulk modulus, K_S, from p-wave velocity,
V_p, and is presented here as Equation 6-4.

$$V_p^2 = \left\{ \frac{1}{\rho_b} \left[K_S + \frac{\left(1 - \frac{K_g}{K_{ma}}\right)^2}{\left(\frac{\phi}{K_f} + \frac{(1-\phi)}{K_{ma}} - \frac{K_g}{K_{ma}^2}\right)} \right] \right\} \qquad (6-4)$$

where:

ρ_b = Bulk density

ϕ = Porosity

K_g = Bulk modulus of grain

K_{ma} = Bulk modulus of grain (matrix or framework)

K_f = Bulk modulus of pore fluid

Table 6.3.3
Comparison of Mean Grain Diameter to Wavelength*

Sieve Mesh Size	Grain Size (mm)	Wavelength/ Grain Size
20	0.841	3.17
40	0.420	6.35
60	0.250	10.67
80	0.177	15.07
100	0.149	17.90
120	0.125	21.33
140	0.105	25.40
170	0.088	30.30
200	0.074	36.04

* Velocity = 2000 m/sec

  Frequency = 750 kHz

  Wavelength = 2.76 mm

White and Sengbush (1986) suggest using Equation 6-5
to estimate K_{ma}/K_g from porosity for clean sand. This
empirical relationship was defined by Geertsma (1961).
Sample calculations are found in Appendix A for the Gassmann
model calculations.

$$K_{ma}/K_g = 1/(1+50 \; \phi) \hspace{4cm} (6\text{-}5)$$

Typical values of the bulk moduli used in Equation 6-4
for frac sand are listed below:

Modulus	Value (Pa)	Source
K_g	$3.5 \cdot 10^{11}$	White and Sengbush (1986)
K_f	$2.0 \cdot 10^9$	Montmayeur (1985)
K_{ma}	$2.0 \cdot 10^{10}$	Equation (6-5)

Noting that the bulk moduli of the pore fluid, K_f, is one to
two orders of magnitude greater than the others, it can be
shown that the pore fluid bulk modulus, or the pore fluid
compressibility, is the dominant term in the denominator of
the second term in Equation 6-4 (see Zimmerman 1985). It can
also be shown that if there is any gas present in the pore
fluid the bulk modulus becomes an even more dominant
variable.

Bulk compressibility, the inverse of bulk modulus, was calculated four ways for Montmayeur's frac sand samples. He calculated the static bulk compressibility from core deformation measurements, the dynamic bulk compressibility from shear and longitudinal wave measurements, and estimated static bulk compressibility from dynamic measurements using the Biot model. The fourth calculation was the estimation of static bulk compressibility from dynamic p-wave travel time using the Gassmann model in this research. All of these calculated values are found in tabular form in Appendix B for Montmayeur's frac sand packs. Crossplots of dynamic bulk compressibility (measured, Biot predicted, and Gassmann predicted) versus measured static bulk compressibility for each of Montmayeur's frac sand packs are also included in Appendix B and Figures 6.3.3.a, 6.3.3.b, and 6.3.3.c.

Montmayeur's (1985) computational method for Biot's model is included as Appendix C. Further discussion is found in his Ph.D. dissertation, T-3099, at Colorado School of Mines.

Figures 6.3.3.a, 6.3.3.b, and 6.3.3.c show the described crossplots for the large (20404), medium (1012), and the small (1720) frac sand packs, respectively. Figure 6.3.3.a shows that at pressures greater than 2000 psig on large
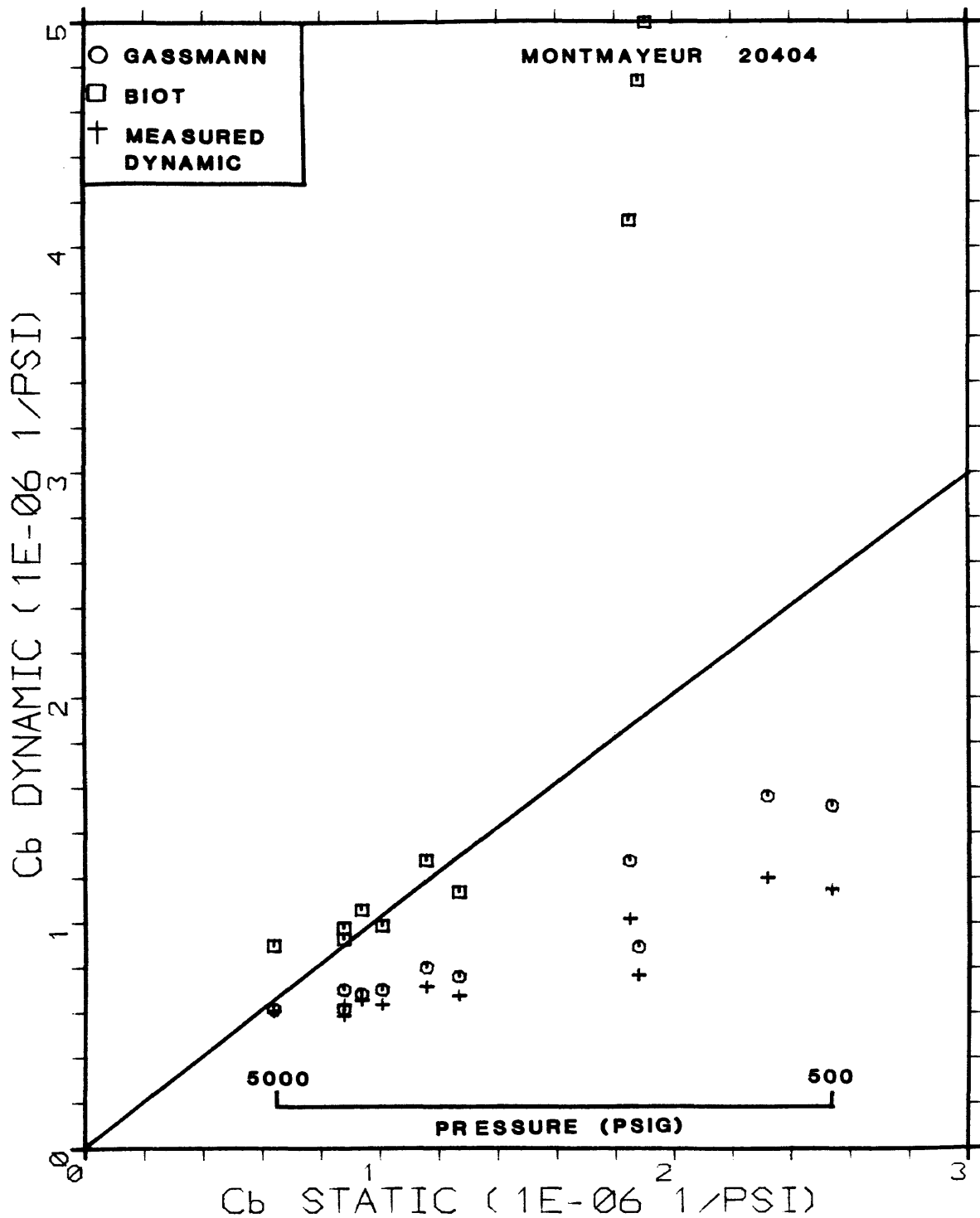
Figure 6.3.3.a. Bulk compressibility crossplot for 20404 frac
sand (20/40 mesh).
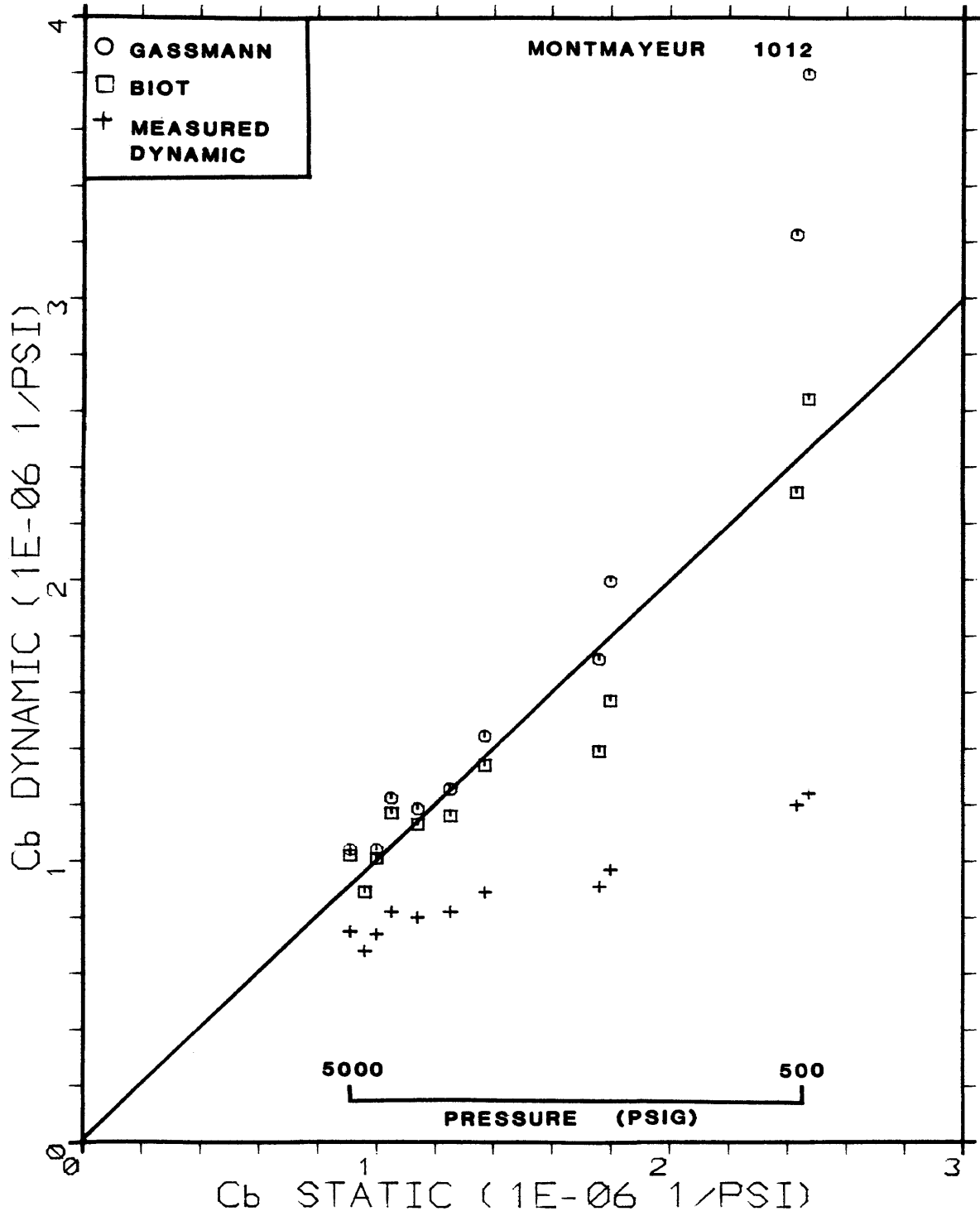
Figure 6.3.3.b. Bulk compressibility crossplot for 1012 frac
sand (100/120 mesh).
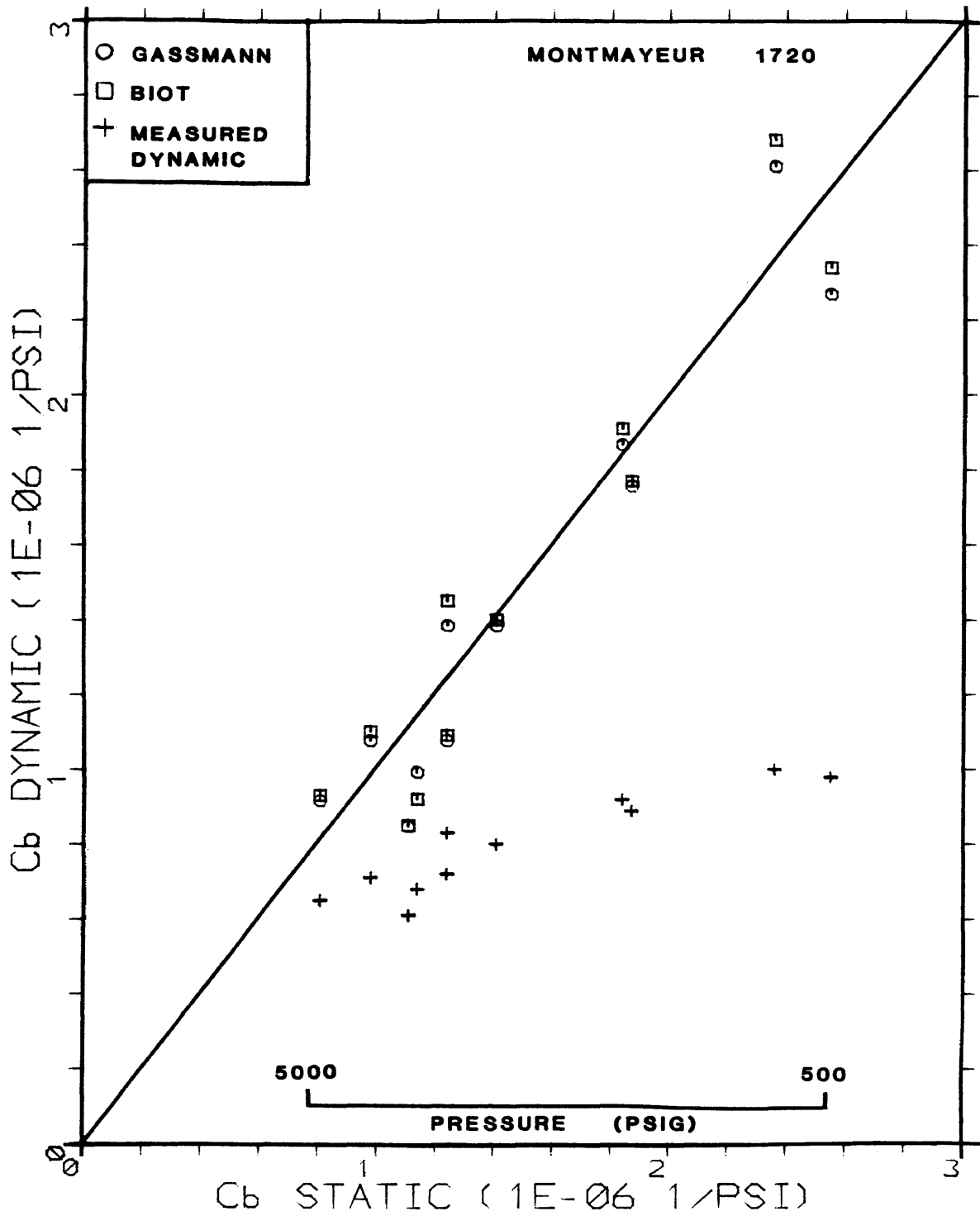
Figure 6.3.3.c.   Bulk compressibility crossplot for 1720 frac
                  sand (170/200 mesh).

uniform grain samples, the Biot model predicts bulk
compressibility closer to Montmayeur's measured static bulk
compressibility than does the Gassmann model. Dynamic bulk
compressibility calculated from measured shear and
longitudinal wave travel times are consistently lower than
both those calculated from the Biot and the Gassmann models
for all sand packs. As the grain size of the sand packs
decreases, the difference between the Gassmann and Biot
calculated bulk compressibilities decreased (Figures 6.3.3.a,
6.3.3.b, and 6.3.3.c). These figures illustrate that for
small grain size packs at high hydrostatic pressures,
generally greater than 2000 psig, the Gassmann model
effectively predicts static bulk compressibility from dynamic
p-wave measurements. These results are comparable to those
calculated using the Biot model for Montmayeur's frac sand
packs with grain sizes smaller than 20/40 mesh.

It appears then, that the Gassmann model could be used
to calculate static bulk compressibility from p-wave dynamic
measurements. This method should be applicable in both the
reservoir for in-situ acoustic log p-wave measurements when
frequencies are low and in the laboratory on small grain size
samples even at ultrasonic frequencies. Further testing both
in-situ and in the laboratory of reservoir samples are
needed.

7. CONCLUSIONS

1.   Gassmann's model is as effective for predicting static bulk compressibility from dynamic p-wave measurements as Biot's model for Montmayeur's (1985) frac sand packs when the sand is smaller than 20/40 mesh. Biot's (1956) model is better for predicting static bulk compressibility on coarse (20/40 mesh) grain packs. A relationship between grain size and wave frequency/wave length is indicated.

2.   P-waves through all unconsolidated sand packs were severely attenuated at confining pressures below 2000 psi. P-waves were attenuated for large (20/40 mesh) uniform grain size packs at confining hydrostatic pressures to 5000 psi. There was a slight trend between grain size and p-wave travel time, but none between grain size or sorting and s-wave travel time. The dynamic bulk compressibility of natural reservoir samples was the same as that of uniform sized frac sand or glass bead packs with the same mean grain diameter as the reservoir sample.

3.   SEM analysis on unconsolidated glass bead and frac sand packs showed that individual grains were not cracked or crushed during freezing or hydrostatic pressure loading

cycles. This indicates that attributing and modeling core behavior to microcrack closing and opening would be erroneous. Throughout the literature researchers have attributed the near-linear elastic behavior of rocks at pressures greater than 3500-4000 psi to the closure of microcracks and to the maximum depth of burial. Wave propagation through small grain size (less than 20/40 mesh) is affected by confining pressures above 3000 psi but it appears to be due to better grain-to-grain contact with pressure. This is supported by the absence of microcracks in the frac sand and glass bead samples, but if undetected microcracks are present, they may also close in the same pressure range as that needed to give good grain contact, 3500-4000 psig.

4. Berea sandstone is extremely sensitive to core preparation techniques. The air permeability of samples tested in this research was increased by nearly 25% when oven drying temperature was increased from 130° to 190° F. The liquid permeability of Berea samples to kerosene was nearly double the liquid permeability to 50,000 ppm NaCl brine. The low pressure saturator was as effective in saturating Berea cores as the high pressure saturator.

5.   Wyllie's time-average model predicts porosities for
Berea sandstone which are close to the values measured in the
laboratory. Wyllie's model under-predicted porosity for the
dolomite sample and over-predicts porosity for all
unconsolidated sand packs.

8. RECOMMENDATIONS FOR FUTURE WORK

1.   Install a working static measurement system to measure
core deformation simultaneously with dynamic wave
measurements on unconsolidated sand samples.

2.   Investigate the use of Gassmann's and Biot's models to
predict static bulk compressibility from dynamic measurements
on reservoir samples.

3.   Increase the number of unconsolidated cores tested to
establish a statistical data base.

4.   Investigate the relationship between hydrostatic
compressibility and uniaxial constrained compressibility on
unconsolidated frac sand, glass beads and natural reservoir
samples.

5.   Test unconsolidated sand cores under conditions
representative of reservoir depletion.

6.   Investigate the effects on bulk compressibility of
reconstructing reservoir sand samples by taking static and

dynamic measurements on reconstructed samples and
unreconstructed samples, those cut frozen (using liquid
nitrogen as drilling fluid) and tested.

7.   Investigate the sensitivity of Berea sandstone to core
preparation with respect to temperature effects and
saturating fluid salinity and composition.

8.   Install a fluid extrusion system to measure the pore
fluid expelled during testing.

9. NOMENCLATURE

[All attempts were made to maintain consistency in nomenclature with Montmayeur and Graves (1985 and 1986)]

GREEK SYMBOLS:

α	Ratio of compressibilities
ε	Strain
$\emptyset$	Porosity
$\emptyset_m$	Microcrack porosity
ρ	Density
σ	Stress
λ	Lame's coefficient
ν	Poisson's ratio
ν_d	Dynamic Poisson's ratio
ω	Frequency
ω_c	Critical frequency (on the order of 0.1 MHz)
τ	Shear stress

ENGLISH SYMBOLS:

C_b	Bulk compressibility
C_{bc}	Static bulk compressibility calculated with Biot's relationship

C_{bdc} Corrected dynamic bulk compressibility (computed static)

C_{bs} Measured static bulk compressibility

C_{bi} Static bulk compressibility at high pressures, for C_{bdc1} = terminal compressibility

C_{bdc1} Static bulk compressibility at high pressures, for C_{bi} = terminal compressibility

C_{ma} Rock matrix compressibility

C_p Pore volume compressibility

C_u Uniaxial compressibility

e   Fluid displacement

E   Young's modulus

E_D Dynamic Young's modulus

G   Shear modulus

G_D Dynamic shear modulus

k   Permeability of rock

K_d Dynamic bulk modulus (inverse of compressibility)

K_s Static bulk modulus

P_p Pore pressure

P_c Confining pressure

t   Time

T   Temperature

V_b Bulk volume

V_s Rock volume

V_p Pore volume

V_p Longitudinal wave velocity

V_s Shear wave velocity

W   Frequency ratio

x,y,z Principal directions in cartesian coordinates

REFERENCES

Adams, B.H., 1983: "Stress-sensitive permeability in a high permeability sandstone reservoir - the Kaparuk Field", SPE 11718.

Aktan, T. and Farouq Ali, S.M., 1975: "Effect of cyclic and in-situ heating on the absolute permeabilities, elastic constants, and electrical resistivities of rocks", SPE 5633.

Allen, D.R., 1967: "Physical changes of reservoir properties caused by subsidence and repressuring operations, Wilmington Field, California", SPE 1811.

American Petroleum Institute, 1983: API recommended practices for testing sand used in hydraulic fracturing operations, API, Washington, D.C., API RP 56.

Anderson, M.A., 1985: "Predicting reservoir condition pore-volume compressibility from hydrostatic-stress laboratory data", SPE 14213.

Anderson, M.A., and Jones, F.O., 1985: "A comparison of hydrostatic-stress and uniaxial-strain pore-volume compressibilities using nonlinear elastic theory", 26th U.S. Symposium on Rock Mechanics, Rapid City, S.D., June 26-28, p. 403-410.

Anderson, R.A., Ingram, D.S., and Zanier, A.M., 1972: "Fracture pressure gradient determination from well logs", 47th Annual Fall Meeting, Society of Petroleum Engineers of AIME, October 8-11, SPE 4135.

Bacri, J.C. and Salin, D., 1986: "Sound velocity of a sandstone saturated with oil and brine at different concentrations", Geophysical Research Letters, Vol. 13, No. 4, April, p. 326-328.

Barton, N., Harvik, L., Cristianson, M., Bandis, S.C., Makurat, A., Chryssanthakis, P., and Vik, G., 1986: "Rock mechanics modeling of the Ekofisk reservoir subsidence", Presented at the 27th U.S. Symposium on Rock Mechanics, Tuscaloosa, Alabama, June 23-25.

Biot, M.A., 1941: "General theory of three-dimensional consolidation", Journal of Applied Physics, Vol. 12, February, p. 155-164.

Biot, M.A., 1954: "Theory of elasticity and consolidation for a porous anisotropic solid", Journal of Applied Physics, Vol. 26, February, p. 182-185.

Biot, M.A., 1956a: "Theory of propagation of elastic waves in a fluid-saturated porous solid: 1.Low frequency range", Journal of the Acoustical Society of America, Vol. 28, February, p. 168-178.

Biot, M.A., 1956b: "Theory of propagation of elastic waves in a fluid-saturated porous solid: 1.High frequency range", Journal of the Acoustical Society of America, Vol. 28, February, p. 179-191.

Biot, M.A., 1962: "Mechanics of deformation and acoustic propagation in porous media", Journal of Applied Physics, Vol. 33, p. 1482-1498.

Biot, M.A., 1962: "Generalized theory of acoustic propagation in porous dissipative media", Journal of Applied Physics, Vol. 34, February, p. 1254-1264.

Bishop, A.W., 1973: "The influence of an undrained change in stress on the pore pressure in porous media of low compressibility", Geotechnique, Vol. 23, p. 435-442.

Botset, H.G. and Reed, D.W., 1935: "Experiment on compressibility of sand", Bulletin AAPG, Vol. 19, p. 1053.

Brace, W.F., 1964: "Some new measurements of linear compressibility of rocks" Journal of Geophysical Research, Vol. 70, No. 2, January 15, p. 391-398.

Brandt, H., 1955: "A study of the speed of sound in porous granular media", Presented at the West Coast Conference of the Applied Mechanics Division of ASME, Monterey, California, September 12-13.

Brandt, H., 1967: "Compressional wave velocity and compressibility of aggregates of particles of different materials", Transactions of the ASME, December, p. 886-872.

Brighenti, G., 19??: "Influence of pore pressure deline on the behavior of petroleum reservoir rocks". Source unknown.

Brighenti, G., 1972: "Influence of the viscoelastic properties of the overlying rocks on the behavior of the deep aquifers", SPE 3727.

Carroll, M.M., 1979: "An effective stress law for anisotropic elastic deformation", Journal of Geophysical Research, Vol. 84, No. B13, December 10, p. 7510-7512.

Cheng, C.H. and Johnston, D.H., 1979: "Inversion of seismic velocities for the pore aspect ratio spectrum of a rock", Journal of Geophysical Research, Vol. 84, p.7533-7543

Cheng, C.H. and Johnston, D.H., 1981: "Dynamic and static moduli", Geophysical Research Letters, Vol. 8, No. 1, January, p. 39-42.

Chierici, C.L., Ciucci, G.M., Eva, F. and Long, G., 1967: "Effect of the overburden pressure on some petrophysical parameters of reservoir rocks", Proceedings 7th World Petroleum Congress, Elsevier, London, Vol. 2, p.309.

Christensen, N.I. and Wang, H.F., 1985: "The influence of pore pressure and confining pressure on dynamic elastic properties of Berea sandstone", Geophysics, Vol. 50, No. 2, February, p. 207-213.

Cleary, M.P., Melvan, J.J., and Kohlhaas, C.A., 1979: "The effect of confining stress and fluid properties on arch stability in unconsolidated sands", SPE 8426.

Coates, G.R. and Denoo, S.A., 1980: "Log derived mechanical properties and rock stress", SPWLA Twenty-first Annual Logging Symposium, July 8-11.

Coffen, J.A., 1986: Seismic Exploration Fundamentals, Tulsa, Oklahoma, PennWell Publishing Company.

Core Lab, 1973: Fundamentals of Core Analysis, p. 2-24.

Coyner, K. and Cheng, C.H., 1984: "New laboratory
      measurements of seismic velocities in porous rocks",
      Presented at the 54th annual meeting of the Society of
      Exploration Geophysicists at Atlanta, December 2-6.

Davies, D.R. and Meijs, F.H., 1980: "'SILICALOCK'-A novel
      sand-control process for gas wells'", SPE 9423.

DeMartini, D.C., Beard, D.C., Danburg, J.S., and Robinson,
      J.H., 1976: "Variation of seismic velocities in
      sandstones and limestones with lithology and pore fluid
      at simulated in situ conditions", Proceedings E.G.P.C.
      Exploration Seminar, November 15-17.

De Waal, J.A. and Smits, R.M.M., 1985: "Prediction of
      reservoir compaction and surface subsidence: Field
      application of a new model", SPE 14214.

Dobrynin, V.M., 1962: "Effect of overburden pressure on
      some properties of sandstone", SPEJ, Vol. 2, No. 4,
      December 1962, p. 360-366.

Domenico, S.N., 1974: "Effect of water saturation on seismic
      reflectively of sand reservoirs encased in shale",
      Geophysics, Vol. 39, p. 759-769.

Domenico, S.N., 1976: "Effect of brine-gas mixture on
      velocity in an unconsolidated sand reservoir",
      Geophysics, Vol. 41, No. 5, October, p. 882-894.

Domenico, S.N., 1977: "Elastic properties of unconsolidated
      porous sand reservoirs", Geophysics, Vol. 42, No. 7,
      December, p. 1339-1368.

Domenico, S.N., 1984: "Rock lithology and porosity
      determination from shear and compressional wave
      velocity", Geophysics, Vol. 49, No. 8, August, p. 1188-
      1195.

Dunn, K.J., 1986: "Acoustic attenuation in fluid-saturated
      porous cylinders at low frequencies", Journal Acoustic
      Society of America, Vol. 79, No. 6, June, p. 1709-1721.

Dunn, K.J., 1986: Personal Communication, Chevron Oil Field
      Research Company, July 15.

Dvorak, A., 1970: "Seismic and static modulus of rock
    masses", Proceedings of the 2nd Congress on Rock
    Mechanics.

Elliott, S.E. and Wiley, B.F., 1975: "Compressional
    velocities of partially saturated, unconsolidated
    sands", Geophysics, Vol.40(6), p. 949-954.

Fatt, I., 1953: "The effect of overburden pressure on
    relative permeability", Petroleum Transactions,
    AIME, Vol. 198, p. 325-326.

Fatt, I., 1958: "Pore volume compressibilities of sandstone
    reservoir rocks", Petroleum Transactions, AIME, Vol.
    213 , p. 362-364.

Fatt,I. and Davis, D.H., 1952: "Reduction in permeability
    with overburden pressure", Petroleum Transactions, AIME,
    Vol. 195, p. 329.

Fountain, J., 1985: Oceanography 408, Colorado School of
    Mines, Class notes, Fall Semester.

Frost, E., Jr. and Fertl, W.H., 1982: "Shear wave travel
    time determination using an unconventional
    approach", SPE 11032.

Gardner, G.H.F., Willie, M.R.J., and Droschak, D.M., 1964:
    "Effects of pressure and fluid saturation on the
    attenuation of elastic waves in sands", Journal of
    Petroleum Technology, February, p. 189-198.

Gardner, G.H.F., Wyllie, M.R.J., and Droschak, D.M., 1965:
    "Hysteresis in the velocity-pressure characteristics of
    rocks", Geophysics, Vol. 30, No. 1, February, p. 111-
    116.

Gardner, G.H.F. and Harris, M.H., 1968: "Velocity and
    attentuation of elastic waves in sand", SPWLA Ninth
    Annual Logging Symposium, June 23-26.

Gardner, G.H.F., Gardner, L.W., and Gregory, A.R., 1974:
    "Formation Velocity and Density-The Diagnostic Basics
    for Stratioprophic Trops", Geophysics, Vol. 39, p. 770-
    780.

Garg, S.K., 1971: "Wave propagation effects in a fluid-saturated porous solid", Journal of Geophysical Research, Vol. 76, No. 32, November 10, p. 7947-7962.

Garg, S.K. and Nur, A., 1973: "Effective stress law for fluid-saturated porous rocks", Journal of Geophysical Research, Vol. 78, No. 26, p. 5911-5921.

Gassmann, F., 1951: "Elastic waves through a packing of spheres", Publication unknown, p. 673-685.

Gassmann, F., 1951: "Elasticity of Porous Media", Vierteljahrsschr. natur forsch. Ges Zurich, Vol. 96, No.1, p. 1-21.

Geertsma, J., 1957: "The effect of liquid pressure decline on volumetric change of porous rocks", Petroleum Transactions, AIME, Vol. 210, p. 331-340.

Geertsma, J., 1966: "Problems of rock mechanics in petroleum production engineering", Proceedings First Congress of the International Society of Rock Mechanics, Lisbon, Vol. 1, p. 585.

Geertsma, J. and Smit, D.C., 1961: "Some aspects of elastic wave propagation in fluid-saturated porous solids", Geophysics, Vol. 26, No. 2, April, p. 169-181.

Geyer, R.L. and Myung, J.I., 1970: "The 3-D velocity log; A tool for in-situ determination of the elastic moduli of rocks", Proceedings of the Twelfth Symposium on Rock Mechanics, University of Missouri, November 16-18.

Graves, R.M., 1982: "Biaxial acoustic and static measurement of rock elastic properties", Ph. D. Dissertation (T-2596), Colorado School of Mines, Golden, CO.

Graves, R.M., 1987: Personal communication, Colorado School of Mines, Golden, CO, May, 1987.

Gray, D.H., Fatt, I., and Bergamini, G., 1963: "The Effect of stress on permeability of sandstone cores", Society of Petroleum Engineers Journal, June, p. 95-100.

Gregory, A.R., 1962: "Shear wave velocity measurements of
      sedimentary rock samples under compression", Fifth Rock
      Mechanics Symposium, University of Minnesota, May 3-5,
      p. 439-467.

Gregory, A.R., 1962: "Fluid Saturation effects on dynamic
      elastic properties of sedimentary rocks", Geophysics,
      Vol. 41, No.5, October, p. 895-921.

Gregory, A.R. and Podio, A.L., 1970: "Dual-mode ultrasonic
      apparatus for measuring compressional and shear wave
      velocities of rock samples", IEEE Transactions on Sonics
      and Ultrasonics, Vol. SU-17, No. 2, April, p. 77-85.

Hall, C.D. and Harrisberger, W.H., 1970: " Stability of sand
      arches:"A key to sand control", Journal of Petroleum
      Technology, July, p. 821-829.

Hall, H.N., 1953: "Compressibility of reservoir rocks",
      Petroleum Transactions, AIME, Vol. 198, p. 309-311.

Hamilton, E.L., 1971: "Elastic properties of marine
      sediments", Journal of Geophysical Research, Vol. 76,
      No. 2, January 10, p. 579-604.

Hamilton, E.L., 1976: "Shear-wave velocity versus depth in
      marine sediments: A review", Geophysics, Vol. 41, No. 5,
      October, p. 985-996.

Hamilton, E.L., 1978: "Sound velocity-density relations in
      sea-floor sediments and rocks", Journal Acoustic Society
      of America, Vol. 63, No. 2, February, p. 366-377.

Hamilton, E.L., 1979: "Sound velocity gradients in marine
      sediments", Journal Acoustic Society of America, Vol.
      65, No. 4, April, p. 909-922.

Hamilton, E.L., Bucker, H.P., Keir, D.L., and Whitney, J.A.,
      1970: "Velocities of compressional and shear waves in
      marine sediments determined is situ from a research
      submersible", Journal of Geophysical Research, Vol. 75,
      No. 20, Jully 10, p. 4039-4049.

Harville, D.W. and Hawkins, M.F., 1967: "Rock
      Compressibility and failure as reservoir mechanisms in
      geopressured gas reservoirs", SPE 2500.

Hicks, W.G. and Berry, J.E., 1956: "Application of contrinuous velocity logs to determination of fluid saturation of reservoir rocks", Geophysics, Vol. 21, No. 3, July, p. 739-754.

Higdon, A., Ohlsen, E.H., Stiles, W.B., Weese, J.A., and Riley, W.F., 1976: Mechanics of Materials; John Wiley and Sons, Inc., New York.

Hilchie, D.W., 1978: Applied Openhole Log Interpretation, Douglas W Hilchie Inc., Golden, CO.

Holcomb, D.L.: "Minimizing well damage by formation clay control", Presentation for Smith Energy, a Division of Smith International, Inc., Golden, CO.

Holzer, T.L. and Bluntzer, R.C., 1984: "Land Subsidence near oil and gas fields, Houston, Texas", Gound Water, Vol. 22, No. 4, July-August, p. 450-459.

Horn, I.W., 1980: "Some laboratory experiments on shear wave propagation in unconsolidated sands", Marine Geotechnology, Vol. 4, No. 1., p. 31-54.

Howarth, D.F., 1984: "Apparatus to determine static and dynamic elastic moduli", Rock Mechanics and Rock Engineering, Vol. 17, p. 255-264.

Hower, W.F, 1974: "Influence of clays on the production of hydrocarbons", SPE 4785.

Ide, J.M., 1936: "The elastic properties of rocks: A correlation of Theory and Experiment", Proceeding of the National Academy of Science, Vol. 22, p. 482-496.

Jaeger, J.C. and Cook N.G.W., 1971: "Fundamentals of Rock Mechanics, John Wiley and Sons, New York.

Jennings, H.Y., Jr., 1965: "How to handle and process soft and unconsolidated cores", World Oil, June, p. 116-119.

Johnston, D.H., Toksoz, M.N. and Timur, A., 1979: "Attenuation of seismic waves in dry and saturated rocks: II. Mechanisms", Gephysics, Vol. 44, No. 4, April, p. 691-711.

Jones, S.C., 1972: "A rapid accurate unsteady-state
     Klinkenberg permeameter",SPEJ, October, p. 383-
     397. (SPE 3535)

Jones, T. and Nur, A., 1983: "Velocity and attenuation in
     sandstone at elevated temperatures and pressures",
     Geophysical Research Letters, Vol. 10, No. 2, February,
     p. 140-143.

Jorden, J.R., and Campbell, F.L., 1986: Well Logging II-
     Electric and Acoustic Logging, Society of Petroleum
     Engineers Inc., Dallas, TX.

Keller, G.V., 1981: "Elastic, mechanical, and electrical
     properties of low-porosity rocks", The Log Analyst,
     November-December, p. 13-21.

Kelton, F.C., 1953: "Effect of Quick-freezing vs saturation
     of oil well cores", JPT, January.

King, M.S., 1966: "Waves velocities in rocks as a functions
     of changes in over burden pressure and pore fluid
     saturants" Geophysics, Vol. 31, No. 1, February, p. 50-
     73.

King, M.S., 1969: "Static and dynamic elastic moduli of rocks
     under pressure", Proceedings of the 11th Symposium on
     Rock Mechanics, University of California at Berkeley,
     June 16-19.

Koerperich, E.A., 1979: "Shear wave velocities determined
     from long and short spaced borehole acoustic devices",
     SPE 8237.

Kohlhaas, C.A. 1980: Oil and Gas Well Design: Completions,
     Colorado School of Mines, Golden, CO.

Kowallis, B.J., Jones, L.E.A. and Wang, H.F., 1984:
     "Velocity-porosity clay content systematics of poorly
     consolidated sandstones", Journal of Geopysical
     Research, Vol. 89, No. B12, November 10, p. 10355-10364.

Kowalski, J., 1975: "Formation strength parameters from well
     logs", SPWLA Sixteenth Annual Logging Symposium, June 4-
     7.

Kranz, R.L., 1983: "Microcracks in rocks: A review",
     Technophysics, Elsevier Science Publishers, B.V.,
     Amsterdam, Netherlands, 100(1983), p. 449-480.

Krug, J.A., 1977: "The effects of stress on the
     petrophysical properties of some sandstones", Ph. D.
     Dissertation (T-1964), Colorado School of Mines,
     Golden, CO.

Kumar, J., 1976: "The Effect of Poisson's ratio on rock
     properties", SPE 6094.

Lebeaux, J.M., 1952: "Some effects of quick-freezing upon
     the permeability and porosity of oil well cores",
     Journal of Petroleum Technology, November,
     p. 19-20.

LeRoy, L.W., LeRoy,D.O., and Raese, J.W.,1977:   Subsurface
     Geology, Golden, CO, Colorado School of Mines, Chapter
     5.

Lelie, H.D. and Mons, F., 1982: "Sonic wave form analysis:
     Applications", SPWLA, Twenty-third Annual Logging
     Symposium, July 6-9.

Lin, W., 1985: " Strength and static elastic moduli of
     Mesaverde rocks", Lawrence Livermore National
     Loboratory, UCID-20370, March.

Lin, W., 1985: "Ultrasonic velocities and dynamic elastic
     moduli of Mesaverde rocks", Prepared for Morgantown
     Energy Technology Center, Morgantown, WV, March (UCID-
     20273-Rev.1.).

Lin, W. and Hauze, F.E., 1986: "In-situ dynamic moduli of
     Mesaverde rocks, compared to static and dynamic
     laboratory moduli", Presented at the 27th U.S. Symposium
     on Rock Mechanics at the University of Alabama,
     Tuscaloosa,Alabama, June 23-25. Published by Society of
     Mining Engineers, Inc., Littleton, CO.

Ludwig, W.J.,Nafe J.E. and Drake C.C., 1970: "Seismic
     Refraction in the Sea", in The Sea, Edited by A.E.
     Maxwell, Wiley, New York, Vol.4., Pt.1., p. 53-84.

Mann, R.L. and Fatt, I. 1960: "Effect of pore fluids on the elastic properties of sandstone", Geophysics, Vol. 25, No. 2, April, p. 433-444.

Marek, B.F., 1973: "Predicting pore compressibility of reservoir rock", SPE 3354.

Mattax, C.C. and Clothier, A.T., 1974: "Core analysis of unconsolidated and friable sands", SPE 4986.

Maxwell, J.C., 1960: "Experiments on compaction and cementation of sand", The Geoloic Society of America, Memoir 79, March, p. 105-132.

McCabe, C., 1986: "How Phillips is dealing with subsidence at Ekofisk", Ocean Industry, Vol. 21, No. 2, p. 30-34.

McCann, C. and McCann, D.M., 1985: "A theory of compressional wave attenuation in noncohesive sediments", Geophysics, Vol. 50, No. 8, August, p. 1311-1317.

McLatchie, A.S., Hemstock, R.A., and Young, J.W., 1957: "The effective compressibility of reservoir rock and its effects on permeability", Petroleum Transactions, AIME, p. 386-388.

Minear, J.W. 1982: "Clay models and acoustic velocities", SPE 11031.

Mons, F. and Babour, K., 19??: "Vertical seismic profiling Recording Processing Applications", Schlumberger Wireline Atlantic.

Montmayeur, H., 1985: "Prediction of static elastic/mechanical properties of consolidated and unconsolidated sands from acoustic measurements", Ph. D. Dissertation (T-3099), Colorado School of Mines, Golden, CO.

Montmayeur, H. and Graves, R.M., 1985: "Prediction of static elastic/mechanical properties of consolidated and unconsolidated sands from acoustic measurements: Basic measurements", SPE 14159.

Montmayeur, H. and Graves, R.M., 1986: "Prediction of static elastic/mechanical properties of consolidated and unconsolidated sands from acoustic measurements: Correlations", SPE 15644.

Morita, N., Gray, K.E., Srouji, F.A.A., and Jogi, P.N., 1984: "Rock property change during reservoir compaction", SPE 13099.

Morris, R.L., Grine, D.R., and Arkfeld, T.E., 1964: "Using compressional and shear acoustic amplitudes for the location of fractures", Journal of Petroleum Technology, June, p.623-632

Myung, J.I. and Helander D.P., 1972: "Correlation of elastic moduli dynamically measured by in-situ and loboratory techniques", SPWLA Thirteeth Annual Logging Symposium, May 7-10.

Nasu, N., 1940: "Studies on the propagation of an artificial earthquake wave through superficial soil or sand layers and the elasticity of soil and sand", Bulletin Earthquake Research Institute (in Japanese), Tokyo Imperial University, Vol. 18, pp. 289-304.

Newman, G.H., 1973: "Pore volume compressibility of consolidated, friable, and unconsolidated reservoir rocks under hydrostatic loading", JPT, February, p. 129-134.

Newman, G.H. and Martin, J.C. 1977: "Equipment and experimental methods for obtaining loboratory compression characteristics of reservoir rocks under various stress and pressure condition", SPE 6855.

Nur, A. and Byerlee, J.D. 1971: "An exact effective stress law for elastic deformation of rock with fluids", Journal of Geophysical Research, Vol. 26, September 10, p. 6414-6419.

Nur, A.M., Winkler, K., DeVilbiss, J. and Walls, J.D., 1979: "Effects of fluid saturation on waves in porous rock and relation to hydraulic permeability", SPE 8235.

O'Brien, D.E. and Chenevert, M.E., 1973: "Stabilizing sensitive shales with inhibited potassium based drilling fluids", JPT, September 1973, p. 1089-1100.

Offshore, 1985: "Ekofisk Subidence: A big problem but little danger", Vol.45, No. 9, September, p. 74-77.

Palmer, D., 1987: Personal communication, Marathon Oil
    Company, January 27.

Pickett, G.R., 1963: "Acoustic character logs and their
    application in formation evaluation", Journal of
    Petroleum Technology, June, p. 659-667.

Pilbeam, C.C. and Vaisnys, J.R., 1973: "Acoutic velocities
    and energy losses in granular aggregates", Journal of
    Geophysical Research, Vol. 78, No. 5, February 10, p.
    810-823.

Plona, T.J. and Johnson, D.L., 1980: "Experimental study of
    the two bulk compressional modes in water-saturated
    porous structures", IEEE Ultrasonic Symposium.

Podio, A.L., 1968: "Experimental determination of the dynamic
    elastic properties of anisotropic rocks, ultrasonic
    pulse method", Ph.D. dissertation at University of Texas
    at Austin

Rike, J.L., 1966: "Review of sand consolidation experience in
    South Louisiana", Journal of Petroleum Technology, May,
    p. 545-550.

Roberts, J.E. and de Souza, J.M., 1958: "The copmressibility
    of sands", Proceedings ASTM, Vol. 58, p. 1269.

Robin, P.F., 1973: "Note on effective pressure", Journal of
    Geophysical Research, Vol. 78, No. 14, May, p. 2434-
    2437.

Rogers,E.B., 1971a: "Sand control in oil and gas wells-1",
    Oil and Gas Journal, November 1, p. 54-60.

Rogers,E.B., 1971b: "Sand control-2: Sizing gravel-pack-
    liners in oil and gas wells", Oil and Gas Journal,
    November 8, p. 58-60.

Rogers,E.B., 1971c: "Sand control-3: Chemical consolidation",
    Oil and Gas Journal, November 15, p. 152-161.

Sawabini, C.T., Chilingarian, G.V., Allen, D.R., 1972:
    "Compressibility of unconsolidated, orkosic oil sands",
    SPE 4058

Sawabini, C.T., Chilingarian, G.V., Allen, D.R., and Yen, T.F., 1986: "Compressibility of unconsolidated oil producing sands and subsidence", Energy Sources, Vol. 8, No. 2/3, p. 125-138.

Scorer, J.D.T. and Miller, F.G., 1974: "A review of reservoir rock compressibility, and its relationship to oil and gas recovery", Institute of Petroleum, London, IP 74-003.

Sethi, D.H., 1981: "Well log applications in rock mechanics", SPE/DOE 9833.

Shirley, D.J. and Hampton, L.D., 1978: "Shear wave measurements in laboratory sediments", Journal of the Acoustical Society of America, Vol. 63., February.

Shumway, G., 1958: "Sound velocity vs. temperature in water-saturated sediments", Geophysics, Vol. 23, No. 3, July, p. 494-505.

Simmons, G. and Brace, W.F., 1965: "Comparison of static and dynamic measurements of copmressibility of rocks", Journal of Geophysical Research, Vol. 70, No. 22, November 15, p. 5649-5657.

Simmons, G. and Richter, D., 1976: The physics and Chemistry of Minerals and Rocks, "Microcracks in rocks",Wiley, New York, NY, p. 105-137.

Simons, L.H., 19??: "Elastic properties of shales", SPE 496.

Stein, N., Odeh, A.S., and Jones, L.G., 1974: "Estimating maximum sand-free production rates from friable sands for different well completion geometries", Journal of Petroleum Technology, October, p.1156-1158.

Stein, N., 1976: "Mechanical properties of friable sands from conventional log data", JPT, July, p. 757.

Stein, N. and Hilchie, D.W., 1972: "Estimating the maximum production rate possible from friable sandstones without using sand control", JPT, September, p. 1157-1160.

Stoll, R.D., 1977: "Acoustic waves in ocean sediments",
    Geophysics, Vol. 42, No. 4, June, p. 715-725.

Stoll, R.D., 1979: "Experimental studies of attenuation in
    sediments", Journal Acoustic Society of American, Vol.
    66, No. 4, p. 1152-1160.

Stowe, K.,1983: Ocean Science, John Wiley and Sons, New
    York, NY, p. 269-274.

Stuivenwold, P.A. and Mast, H., 1980: "New instrumentation
    for managing sand-problem prone fields", SPE 9368.

Suman, G.O., Ellis, R.C., and Snyder, R.E., 1983: Sand
    Control Handbook, Gulf Publishig Company Book Division,
    Honston, Texas.

Swanson, B.F. and Thomas, E,C., 1980: "The measurement of
    petrophysical properties of unconsolidated sand
    cores", The Log Analyst, September-October 1980,
    p. 22-31.

Teeuw, D. 1971: "Prediction of formation compaction from
    laboratory compressibility data", Society of Petroleum
    Engineers Journal, September, p. 263-271.

Terzaghi, K., 1943: Theoretical Soil Mechanics, New York, NY,
    John Wiley and Sons, Inc.

Terzaghi, K. and Peck, R.B., 1948: Soil Mechanics in
    Engineering Practice, New York, NY, John Wiley and Sons,
    Inc., p. 52.

Timur, A., 1972: "Temperature dependence of compressional and
    shear wave velocities in rocks", Geophysics, Vol. 42,
    No. 5, August, p. 950-956.

Tippie, D.B. and Kohlhaas, C.A., 1973: "Effect of flow rate
    on stability of unconsolidated producing sands" SPE
    4533.

Tixier, M.P., Loveless, G.W., and Anderson, R.A., 1973:
    "Estimation of formation strength from the mechanical
    properties log", SPE 4532.

Toksoz, M.N., Cheng, C.H., and Timur, A., 1976: "Velocities of seismic waves in porous rocks", Geophysics, Vol. 41, No. 7, August, p. 621-645.

Toksoz, M.N., Johnston, D.H., and Timur, A., 1979: "Attenuation of seismic waves in dig and saturated rocks: 1. Laboratory measurements", Geophysics, Vol. 44, No. 4, April, p. 681-690.

Torsaeter, O. and Beldring, B., 1985: "The effect of freezing of slightly consolidated cores", SPE 14300.

Tosaya, C. and Nur, A., 1982: "Effects of diagenesis and clays on compressional velocities in rocks", Geophysical Research Letters, VOl. 9, No. 1, January, p. 5-8.

Tosaya, C.A., Nur, A.M., and Prat, G.D., 1984: "Monitoring of thermal EOR fronts by seismic methods", SPE 12744.

Towle, G.F., 1978: "Stress effects on acoustic velocities of rocks", Ph.D. Dissertation (T-1702), Colorado School of Mines, Golden, CO

Tuman, V.S. and Alm, R.F., early 1960's: "Dynamic and static elastic properties of saturated sandstone samples", SPE number illegible. (Early SPE paper found in microfiche without date or publication.)

van der Knaap, W., 1960: "Effect of a change in the pore volume in oil-bearing rock on the estimate of oil reserves", Erdoel Kohle 13, No. 5, p. 305-312. (Paper delivered at the annual meeting of the Deutsche Gesellschaft fur Mineral ol wissenschaft und Kohlechemie in Goslav, October 8, 1959.)

van der Knaap, W., 1959: "Nonlinear behavior of elastic porous media", Petroleum Transactions, AIME, Vol. 216, p. 179-187.

Von Gonten, W.D. and Choudhary, B.K., 1969: "The effect of pressure and temperature on pore volume compressibility", SPE 2526.

Walsh, J.B., 1965a: "The effect of cracks on the compressibility of rock", Journal of Geophysical Research, Vol. 70, No. 2, January 15, p. 381-389.

Walsh, J.B., 1965b: "The effect of cracks on the uniaxial elastic compression of rocks", Journal of Geophysical Research, Vol. 70, No. 2, January 15, p. 399-410.

Walsh, J.B., 1965c: "The effect of cracks in rocks on Poisson's ratio", Journal of Geophysical Research, Vol. 70, No. 20, October 15, p. 5249-5256.

White, J.E. and Sengbush, R.L., 1955: "Velocity measurements in near-surface formations", Geophysics, Vol. 18, p.54-69.

White, J.E. and Sengbush, R.L., 1987: <u>Production Seismology, Handbook of Geophysical Exploration Volume 10</u>, Geophysical Press, London.

Wiborg, R. and Jewhurst, J., 1986: "Ekofisk subsidence detailed and solutions assessed", Oil and Gas Journal, Vol. 184, No. 7, pp. 47-51.

Wilhelmi, B. and Somerton, W.H., 1967: "Simultaneous measurement of pore and elastic properties of rocks under triaxial stress conditions", SPE 1706.

Wilkens, R.H., Cheng, C.H., Simmons, G, and Caruso, L.J.: "Modeling sandstone velocties using direct observations of pore geometry", Rock Physics, Volume unknown, p. 359-360.

Winkler, K.W. and Nur, A., 1982: "Seismic attenuation: Effects of pore fluids and frictional sliding", Vol. 47, No. 1, January, p. 1-15.

Wyllie, M.R.J., Gregory, A.R., and Gardner, G.H.F., 1956: "Elastic wave velocities in heterogeneous and porous media", Geophysics, Vol. 21, No. 1, January, p. 41-70.

Wyllie, M.R.H., Gregory, A.R., and Gardner, G.H.F., 1958: "An experimental investigation of factors affecting elastic wave velocities in porous media", Geophysics, Vol. 23, July, p. 459-493.

Wyble, D.O., 1958: "Effect of applied pressure on the conductivity , porosity, and permeability of sandstone", Petroleum Transactions AIME, Vol. 213, p. 430-432.

Yale, D.P. 1985: "Recent advances in rock physics",
     Geophysics, Vol. 50, No. 12, December, p. 2480-2491.

Youash, Y.Y., 19??: "Dynamic physical properties of rocks:
     Part II, Experimental Results", Proceedings Second
     Congress.

Zimmerman, R.W., 1985: Comment on: "The constitutive theory
     of fluid-filled porous materials", Journal of Applied
     Mechanics, Vol.52., December, p. 983.

APPENDIX A: Sample Calculations

A.1.   Wyllie's time average model.

This model predicts porosity from p-wave travel time measurements.

$$\phi = \frac{t_p - t_{ma}}{t_f - t_{ma}} \cdot (100\%)$$

For unconsolidated core F6080A, the values used were p-wave travel time at 5025 psig:

t_p = 157.05 (microseconds/ft)

t_{ma}* = 51.0 (microseconds/ft)

t_f = 190 (microseconds/ft)

$$\phi = \frac{157.05 - 51}{190 - 51} \cdot 100\% = 76.29$$

Note that this value of porosity is too high. Wyllie's time-average model does not correctly predict porosity for unconsolidated sands.

* These values were taken from Hilchie (1978) and used for all cores except STD2. For STD2 the value of t_{ma} was 43.5 microseconds/ft.

A.2.   Calculation of dynamic bulk compressibility for core
       F6080A at 5025 psig.

$$G = \frac{1.34 \cdot 10^{10} \, \rho_b}{(V_s)^2} \quad \text{(psi)}$$

$$= \frac{1.34 \cdot 10^{10} (2.1059 \text{ gm/cc})}{(289.39 \text{ microseconds})^2} = 3.37 \cdot 10^5 \text{ psi}$$

$$\lambda + 2G = \frac{1.34 \cdot 10^{10} \, \rho_b}{(V_p)^2} \quad \text{(psi)}$$

$$= \frac{1.34 \cdot 10^{10} (2.1059 \text{ gm/cc})}{(157.05 \text{ microseconds/ft})^2} = 11.4 \cdot 10^5 \text{ psi}$$

$$\lambda = \lambda + 2G - 2G$$
$$= [11.4 - 2 \cdot (3.37)] \cdot 10^5 = 4.66 \cdot 10^5 \text{ psi}$$

$$K_D = \lambda + \frac{2}{3} G$$
$$= [4.66 + \frac{2}{3} \cdot (3.37)] \cdot 10^5 \text{ psi} = 6.91 \cdot 10^5 \text{ psi}$$

$$C_{bD} = \frac{1}{K_D}$$
$$= 1/(6.91 \cdot 10^5) = 1.44 \cdot 10^{-5} \text{ (1/psi)}$$

A.3.   Gassmann model

The modified Gassmann model in Jorden and Campbell

(1986) on page 106 was used to calculate static bulk modulus,

K_s, from compression wave velocity, V_p, for Montmayeur's

(1985) unconsolidated frac sand packs. This example is for

Montmayeur core 6080 at 500 psi.

$$K_S = V_p^2 \rho_b - \left[\frac{\left(1 - \frac{C_g}{C_{ma}}\right)^2}{C_g(1-\phi) + C_f\phi - C_g^2/C_{ma}} \right]$$

for: K_S (Pa)   = static bulk modulus

V_p (m/sec) = p-wave velocity

ρ_b (kg/m3) = Bulk density

ϕ (fraction) = Porosity

C_{ma} (1/Pa) = Rock matrix compressibility

C_f (1/Pa) = Pore fluid compressibility

C_g (1/Pa) = Rock grain compressibility

For all cores the following values were used:

$C_g = 2.857 \cdot 10^{-11}$ (1/Pa)

$C_f = 4.786 \cdot 10^{-10}$ (1/Pa)

$C_g/C_{ma} = (1 + 50\phi)^{-1}$

For core 6080: $\phi = 0.342$

$\rho_b = 2.098$ g/cc

$$K_S = (2088)^2(2098)$$

$$- \left[\frac{(1 - 0.055)^2}{(2.857 \cdot 10^{-11}).658 + (4.786 \cdot 10^{-10})(.342) - \frac{(2.857 \cdot 10^{-11})^2}{5.171 \cdot 10^{-10}}} \right]$$

$$= 4.211 \cdot 10^9 \text{ (Pa)}$$

$$C_{bs} = 1.637 \cdot 10^{-6} \text{ (psi}^{-1})$$

APPENDIX B: Raw Dynamic Core Data

This appendix contains the raw core data measurements used in the calculation of dynamic properties. Included is the data for all the cores used in this research:

Howarth's consolidated cores:

Howarth STD2

Howarth STB5

HCB5

HCB11

HCB13

Howarth's unconsolidated cores:

G2040A (glass beads)

G1014A (glass beads)

F2040C (frac sand)

F6080A (frac sand)

F6080B (frac sand)

F6080D (frac sand)

F1014A (frac sand)

F1014B (frac sand)

Reservoir Sample 1A

Reservoir Sample 2B

Reservoir Sample 3A

Reservoir Sample 4A

Reservoir Sample 5A

Reservoir Sample 5B

Reservoir Sample 6A

Reservoir Sample 7A

Reservoir Sample 8A

Montmayeur's consolidated cores:

Montmayeur STD2

Montmayeur STB5

Montmayeur's unconsolidated frac sand cores:

Montmayeur 20403

Montmayeur 20404

Montmayeur 4060

Montmayeur 6080

Montmayeur 8010

Montmayeur 1012

Montmayeur 1217

Montmayeur 1720

Included in the data for each pressure step, P in psig, are the measured longitudinal and shear wave travel times, t_p and t_s, through the core. These values are then corrected for the travel time through the heads (see chapter 3) using the following equations, A-1a-f.

Howarth (consolidated and unconsolidated cores):

$$t_{pc}=t_p-8.661 \text{ (microseconds)} \qquad \text{(A-1a)}$$
$$t_{sc}=t_s-15.840 \text{ (microseconds)} \qquad \text{(A-1b)}$$

Montmayeur consolidated cores:

$$t_{pc}=t_p-5.888 \text{ (microseconds)} \qquad \text{(A-1c)}$$
$$t_{sc}=t_s-3.638 \text{ (microseconds)} \qquad \text{(A-1d)}$$

Montmayeur unconsolidated cores:

$$t_{pc}=t_p-(10.05+0.005487(5-P/1000)^3) \text{ (microseconds)} \quad \text{(A-1e)}$$
$$t_{sc}=t_s-(8.41+0.0021968(5-P/1000)^3) \text{ (microseconds)} \quad \text{(A-1f)}$$

The wave velocities, V_p and V_s are calculated by dividing the corrected travel times, t_{pc} and t_{sc}, by the core length in feet. The shear modulus, G, and combined modulus,

1+2G, and dynamic bulk compressibility are calculated using Equations 2- 17b, 2-17a, and 2-17f, respectively.

Also included in this appendix are two graphs for each core, one is the travel time (V_p and V_s) versus pressure and the other is dynamic bulk compressibility versus pressure. Calculated values of static bulk compressibility from measured core deformation, Biot's model and Gassmann's model are listed with the computed dynamic bulk compressibility for all of Montmayeur's frac sand packs. The compressibility crossplots are also included in this appendix.

Please note that the order of magnitude of the bulk compressibility units on Figures B.33 through B.64 vary from 10^{-5} to 10^{-7} per psi.

STD2 — Howarth
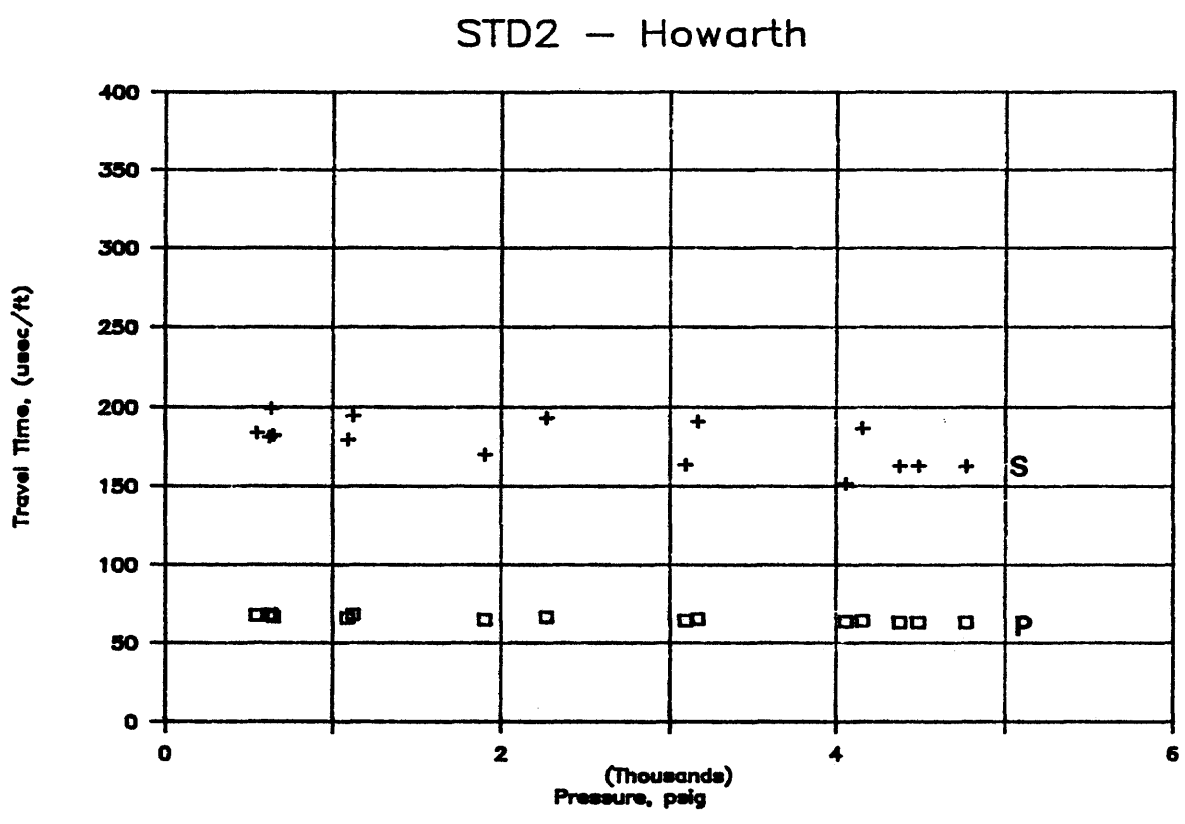
Figure B.1.   Longitudinal and shear wave travel time versus
               pressure.

STB5 — Howarth
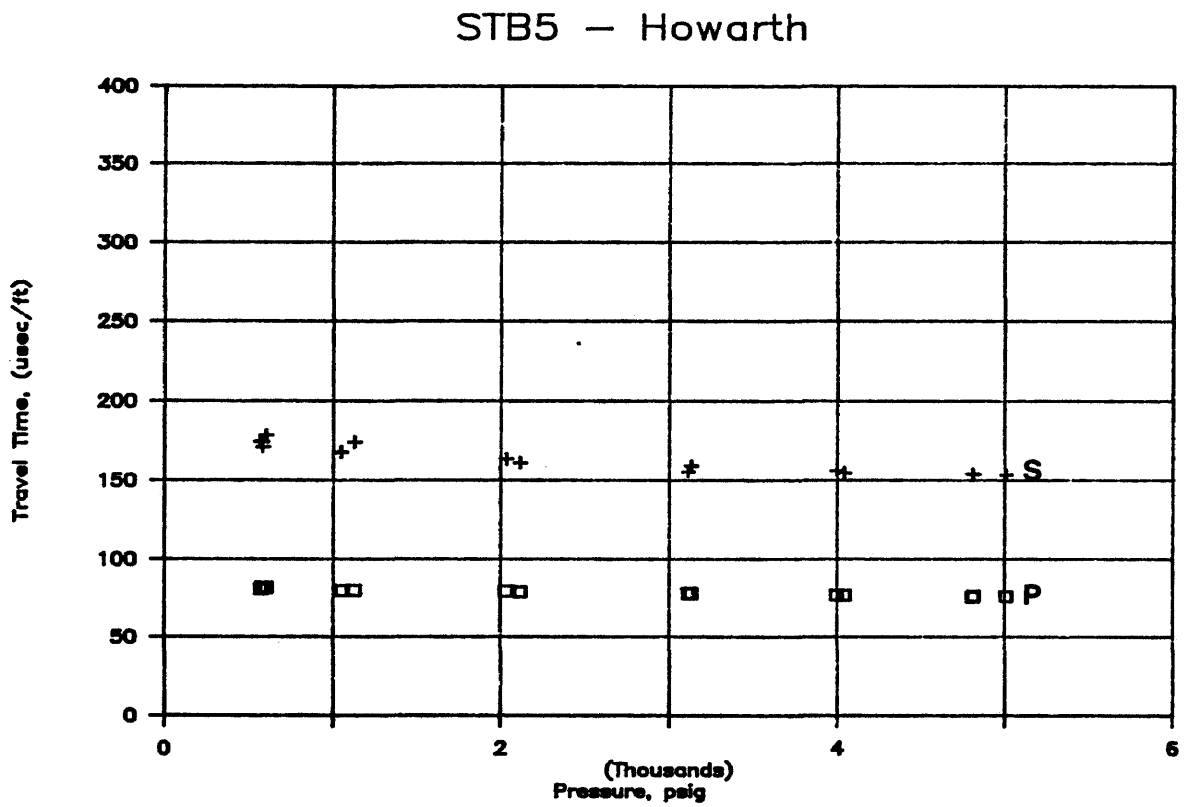
Figure B.2.   Longitudinal and shear wave travel time versus pressure.

HCB5
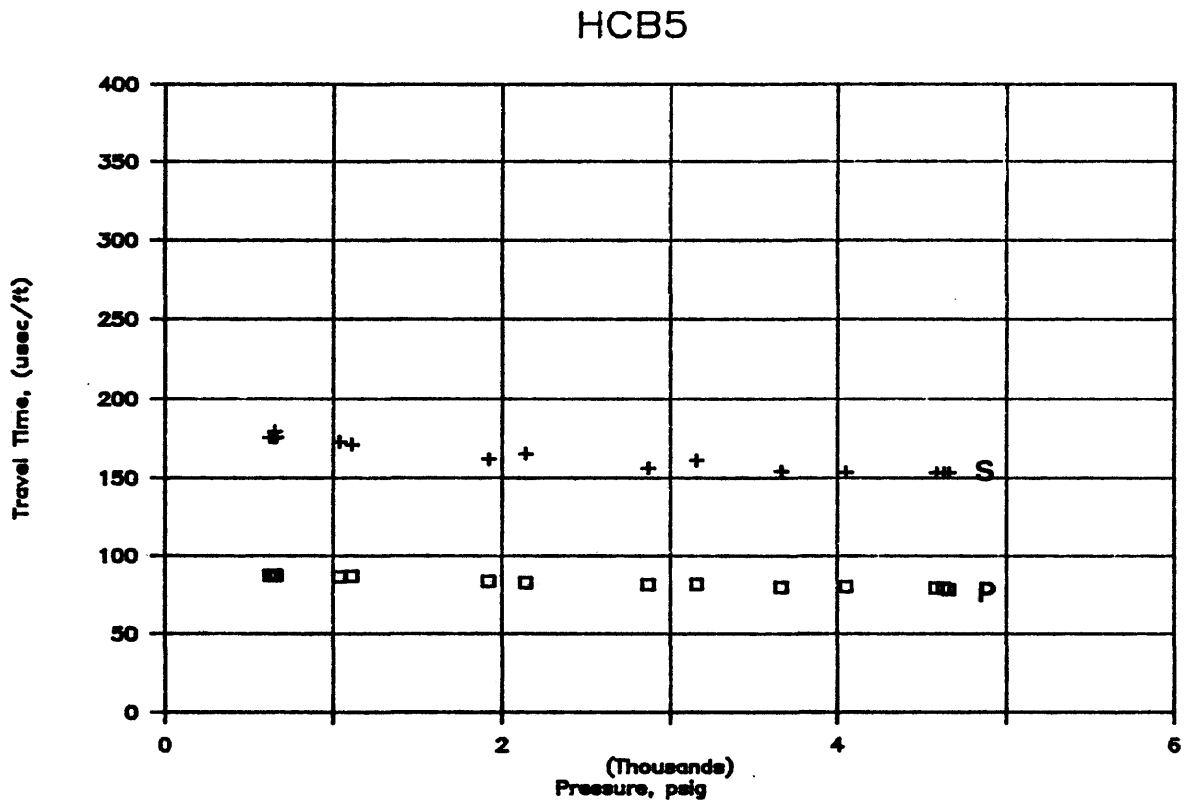
Figure B.3.   Longitudinal and shear wave travel time versus
               pressure.

HCB11
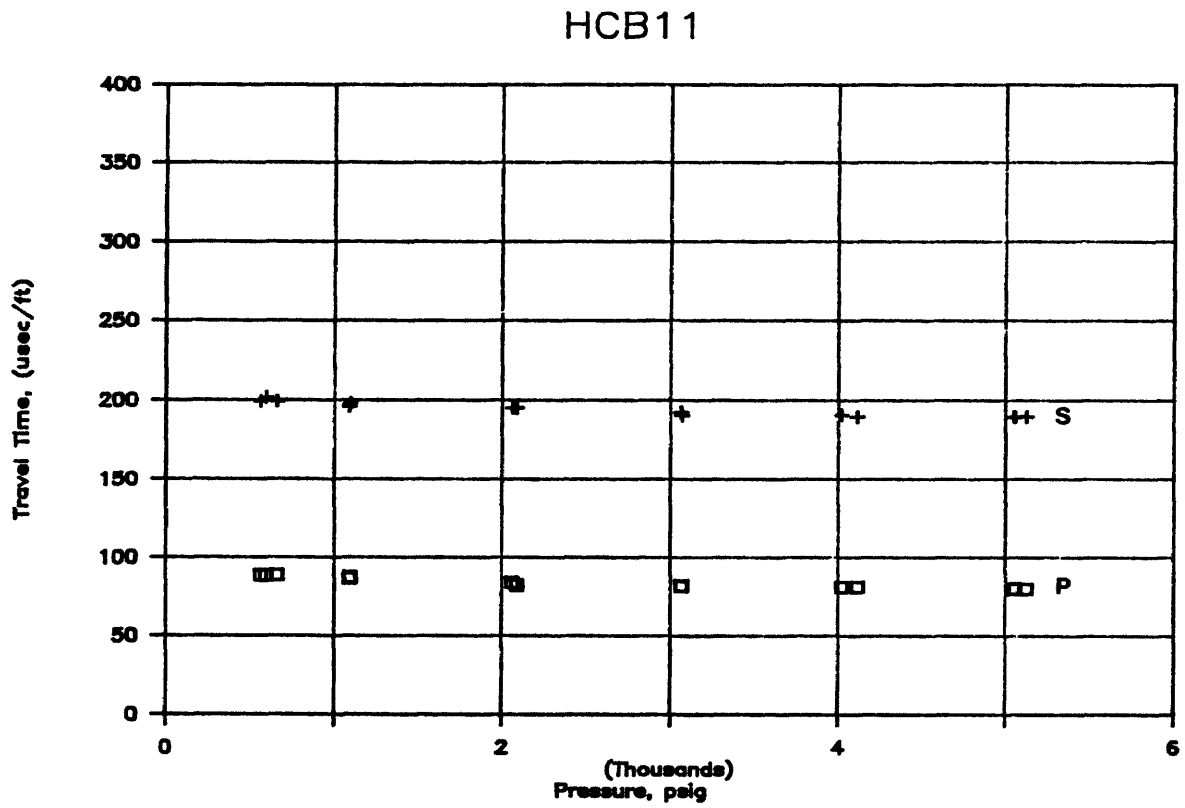
Figure B.4.   Longitudinal and shear wave travel time versus
               pressure.

HCB13
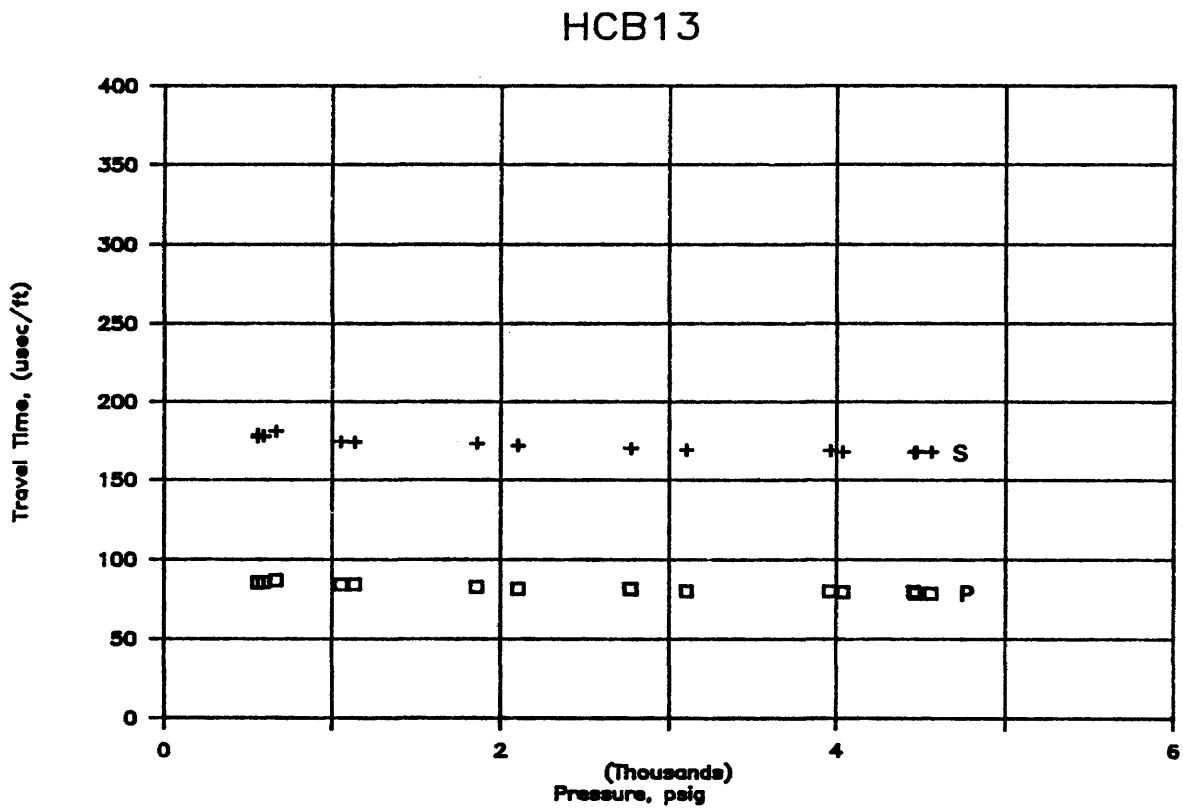
Figure B.5.   Longitudinal and shear wave travel time versus
               pressure.

G2040A
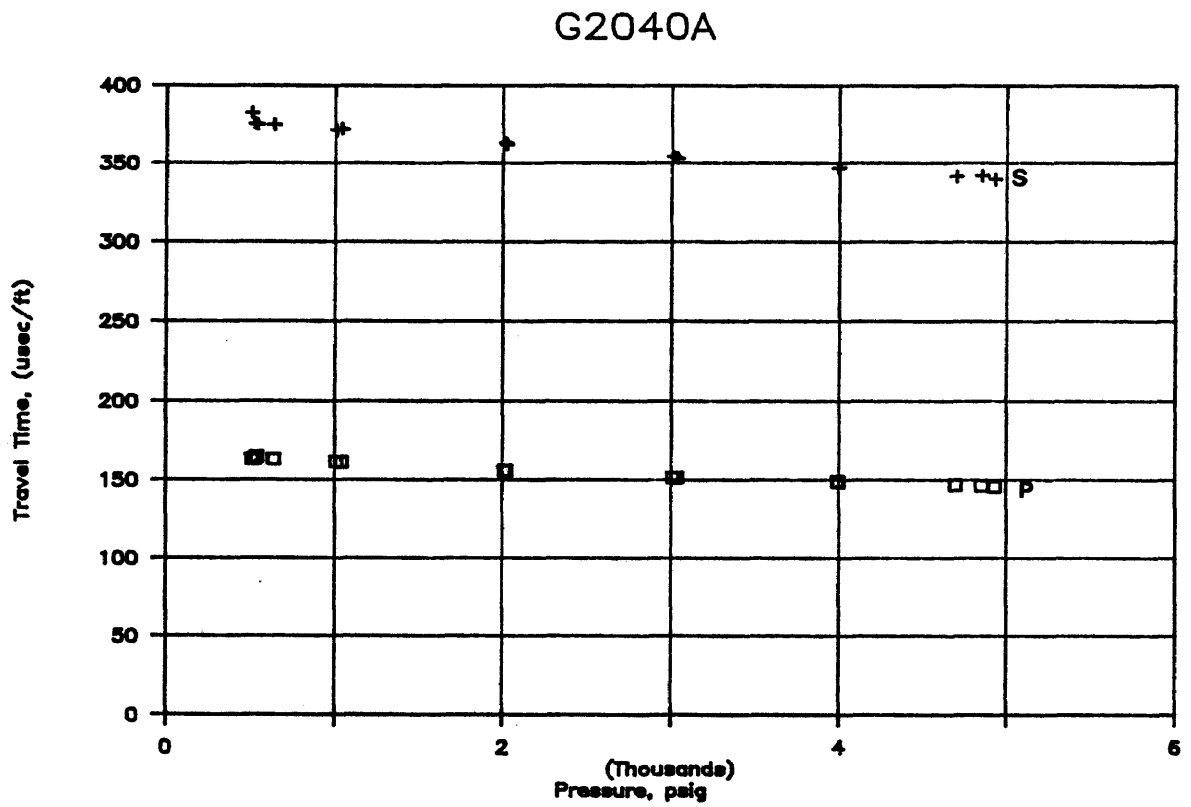
Figure B.6.   Longitudinal and shear wave travel time versus
               pressure.

G1014A
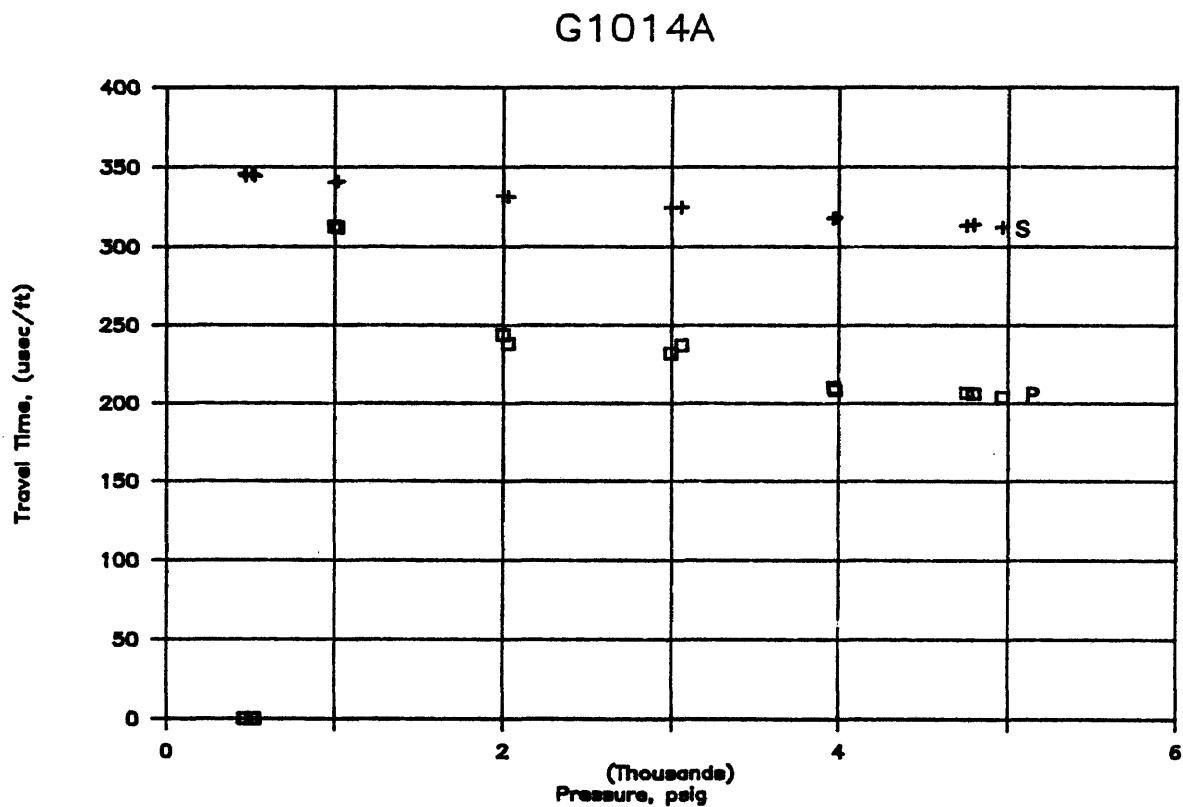
Figure B.7.   Longitudinal and shear wave travel time versus
pressure.

F2040C
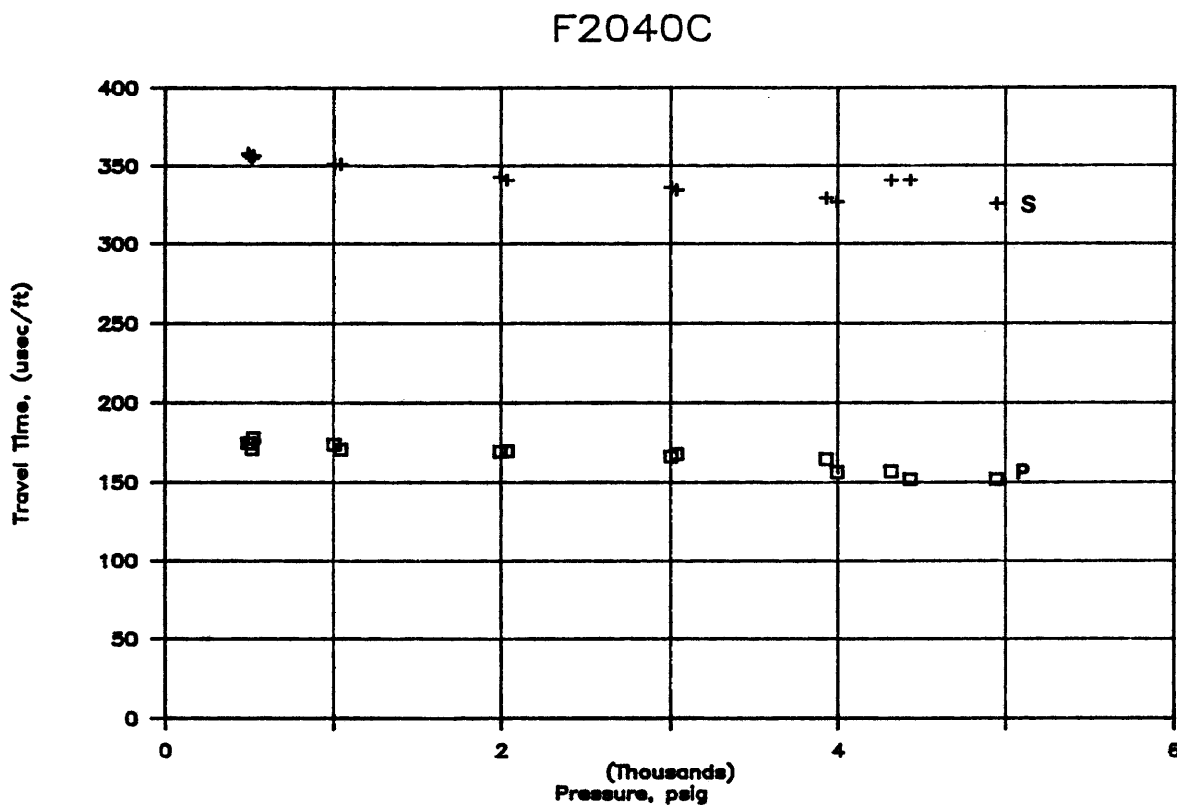
Figure B.8.   Longitudinal and shear wave travel time versus
             pressure.

F6080A
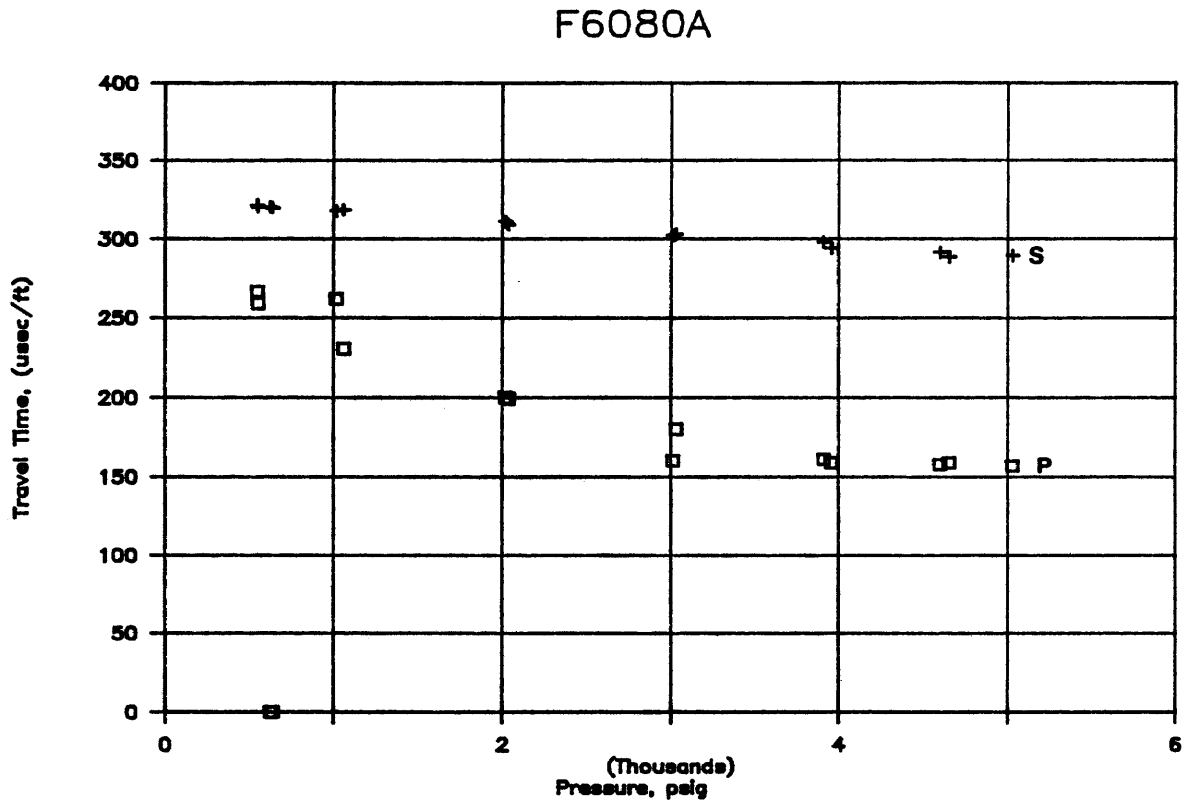
Figure B.9.   Longitudinal and shear wave travel time versus
               pressure.

F6080B
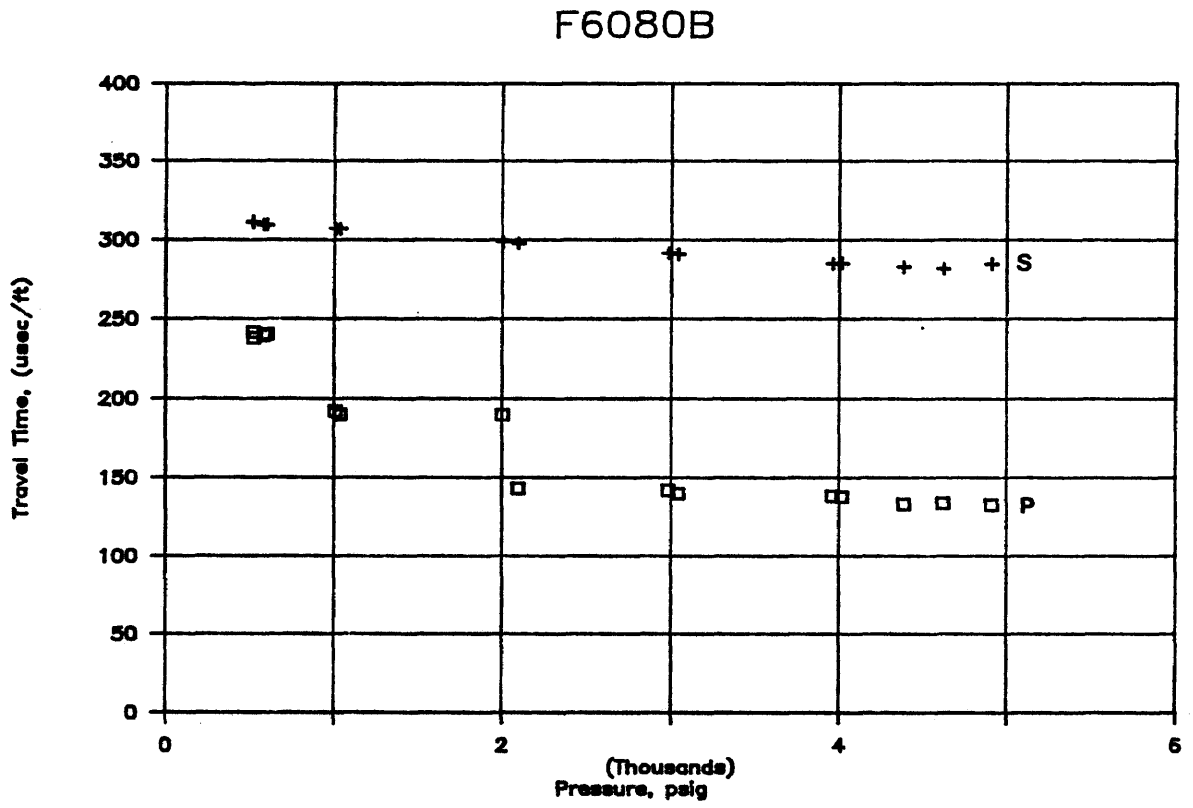
Figure B.10.   Longitudinal and shear wave travel time versus
               pressure.
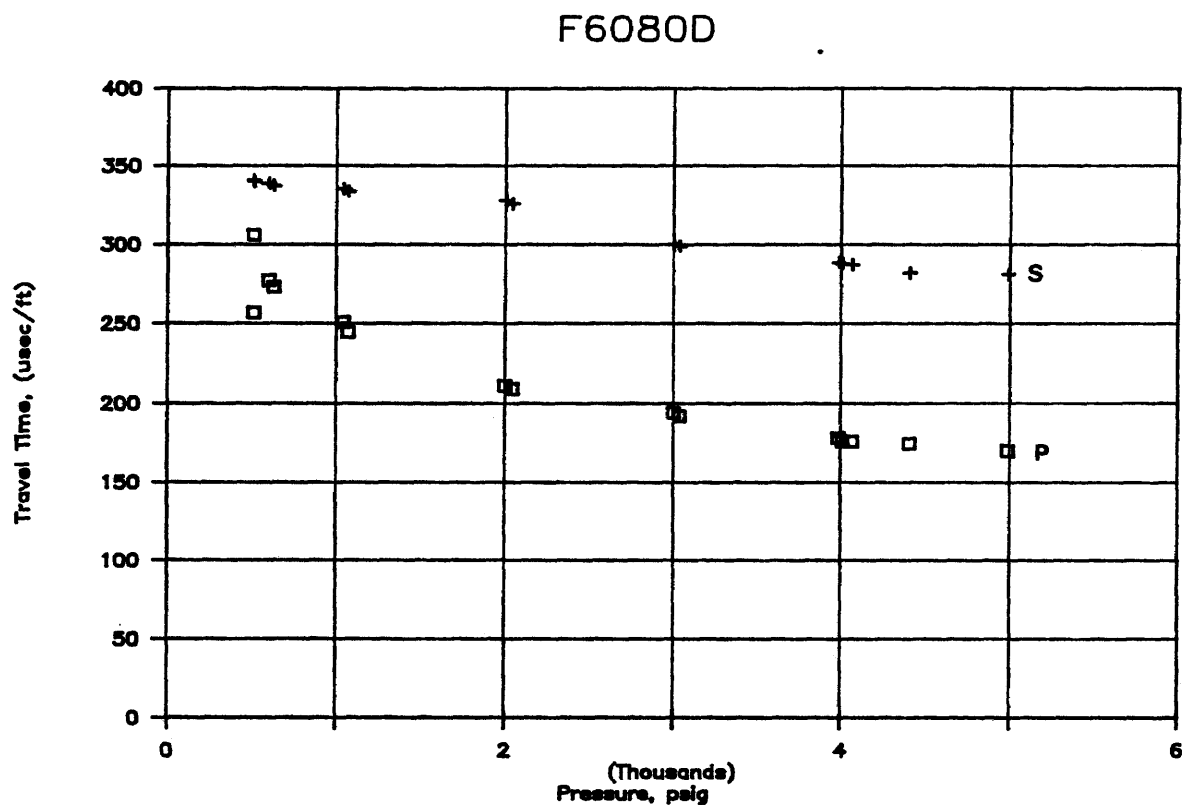
Figure B.11.   Longitudinal and shear wave travel time versus
pressure.

F1014A
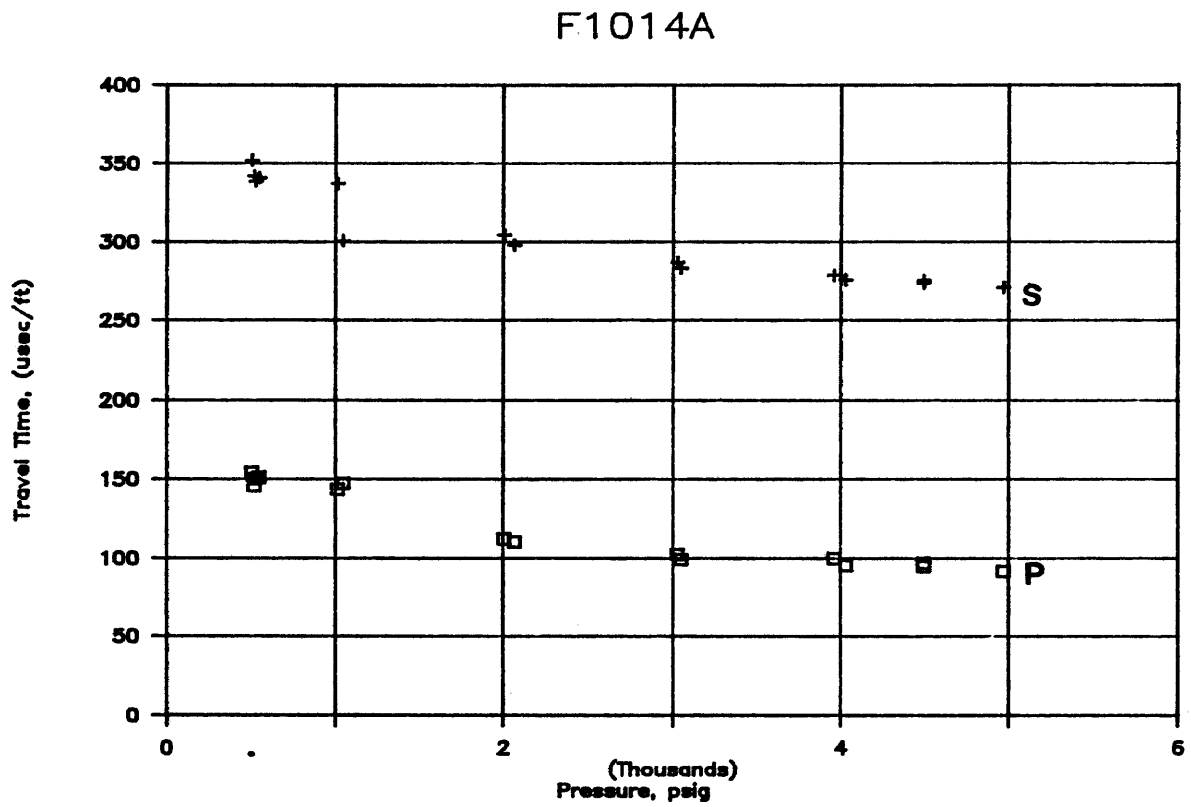
Figure B.12. Longitudinal and shear wave travel time versus
            pressure.

F1014B
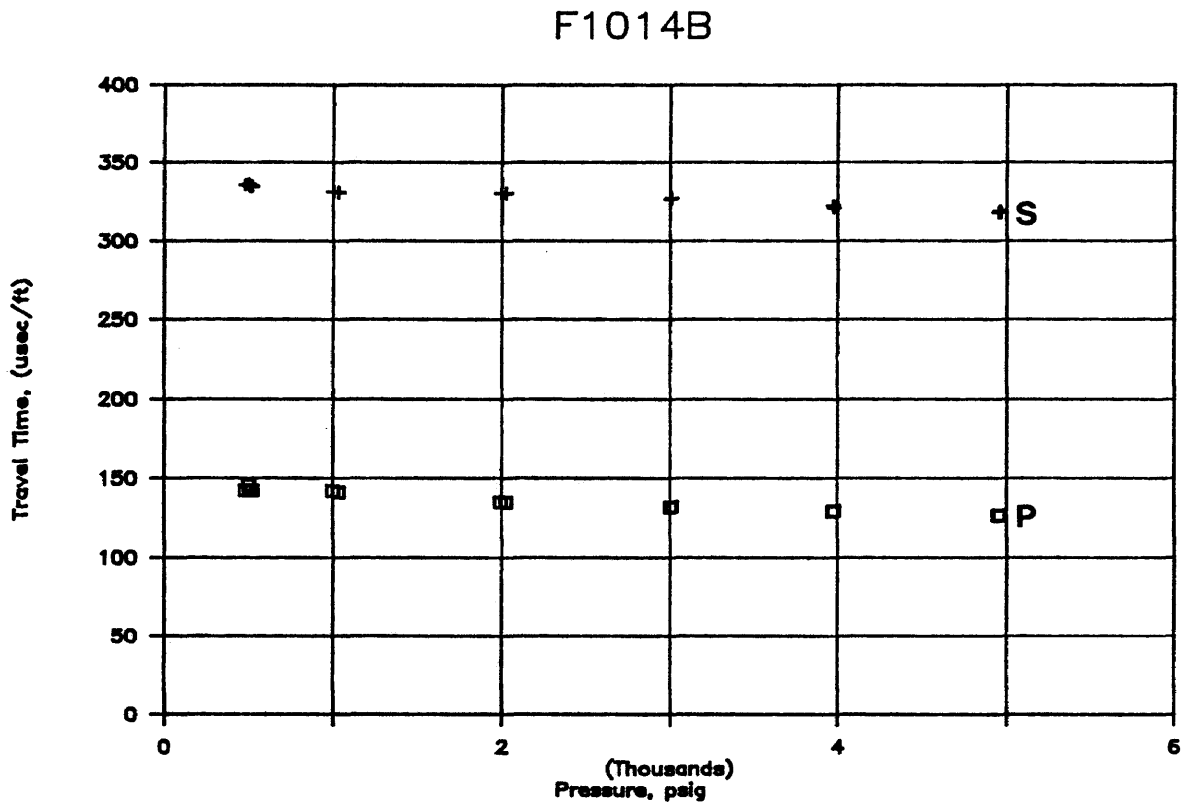
Figure B.13.   Longitudinal and shear wave travel time versus
               pressure.

RESERVOIR SAMPLE 1A
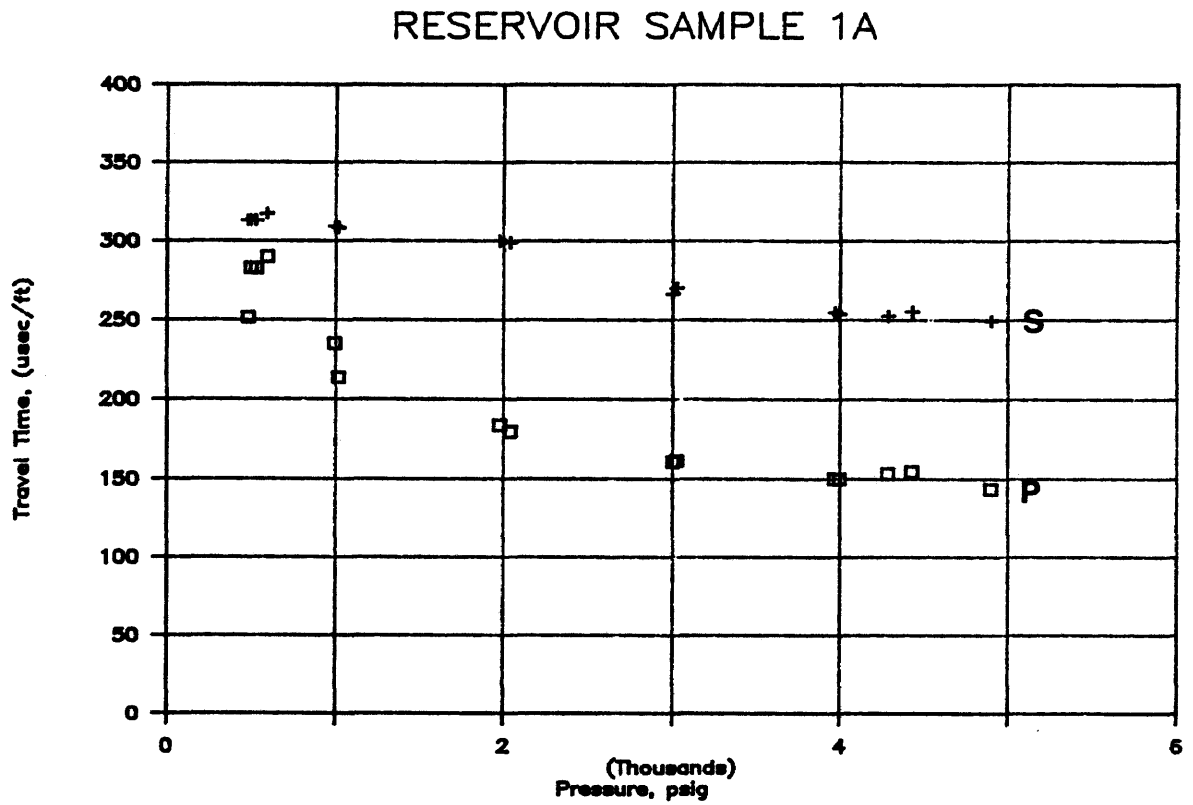
Figure B.14.   Longitudinal and shear wave travel time versus
                pressure.

RESERVOIR SAMPLE 2B
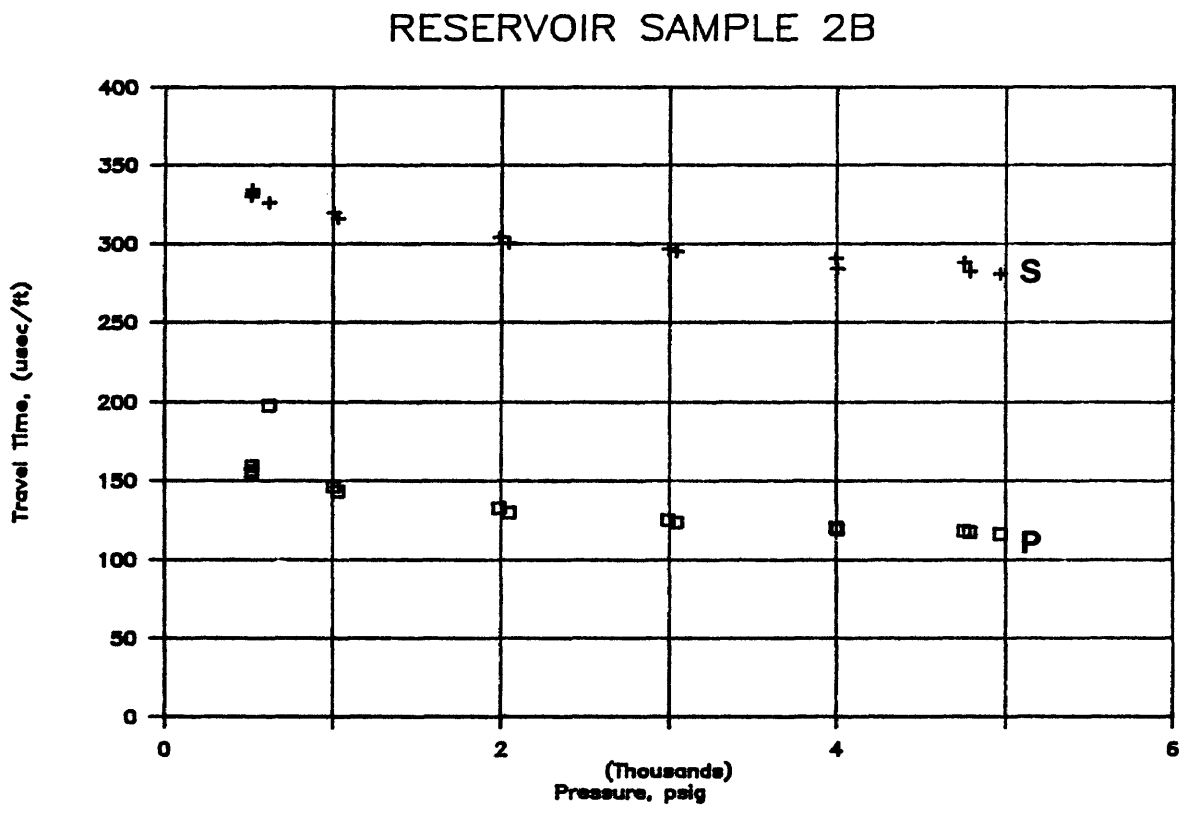
Figure B.15.   Longitudinal and shear wave travel time versus
                pressure.

RESERVOIR SAMPLE 3A
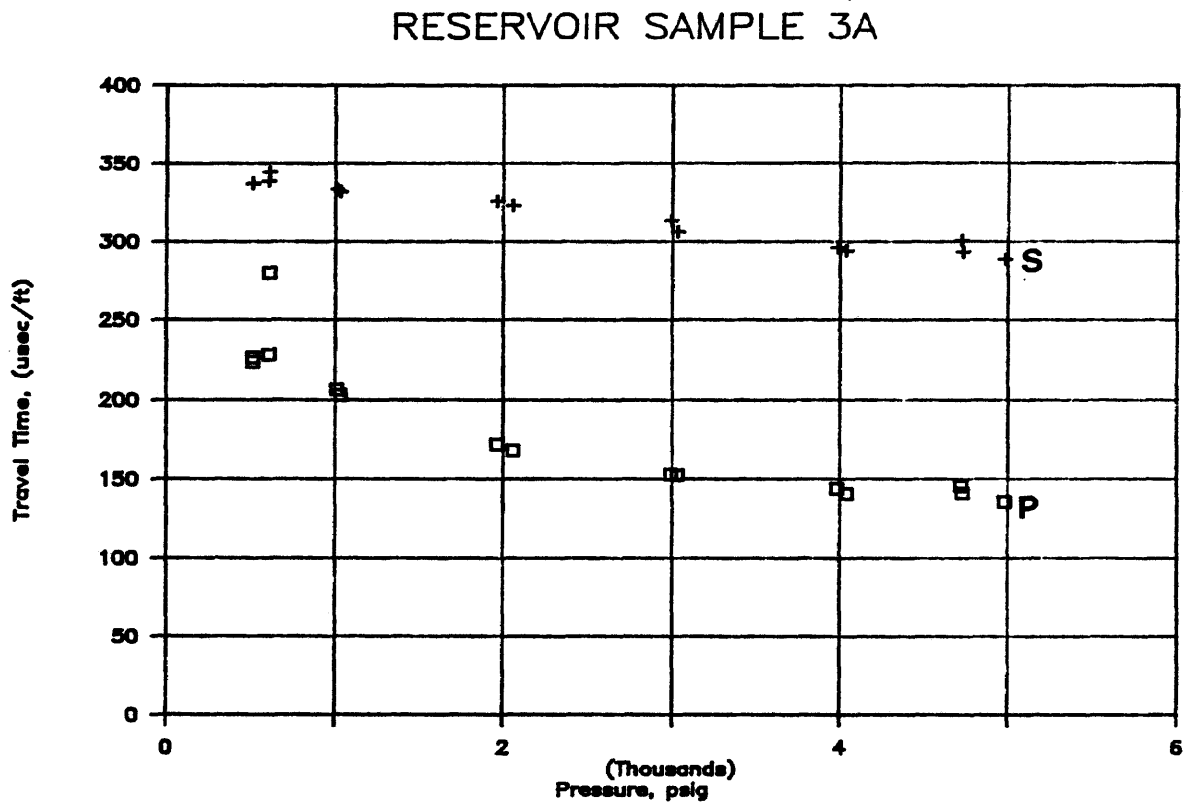
Figure B.16. Longitudinal and shear wave travel time versus
             pressure.

RESERVOIR SAMPLE 4A
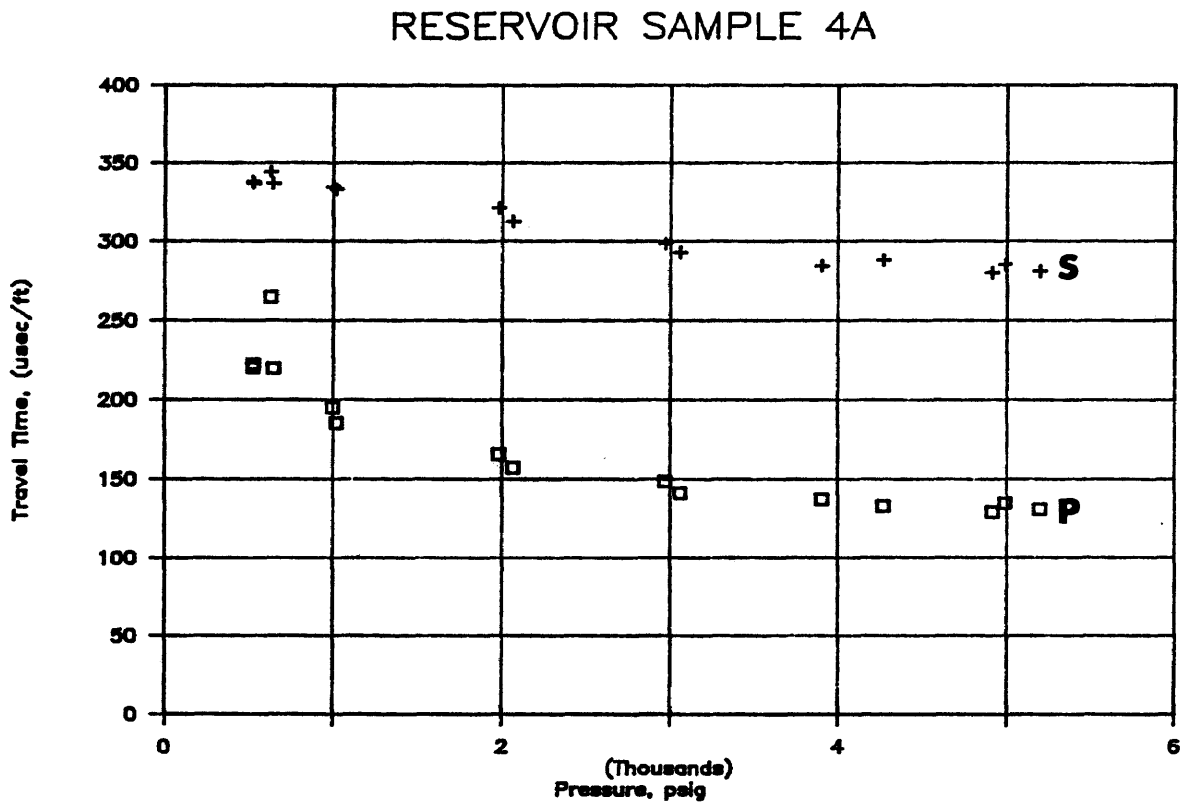
Figure B.17. Longitudinal and shear wave travel time versus
              pressure.

RESERVOIR SAMPLE 5A
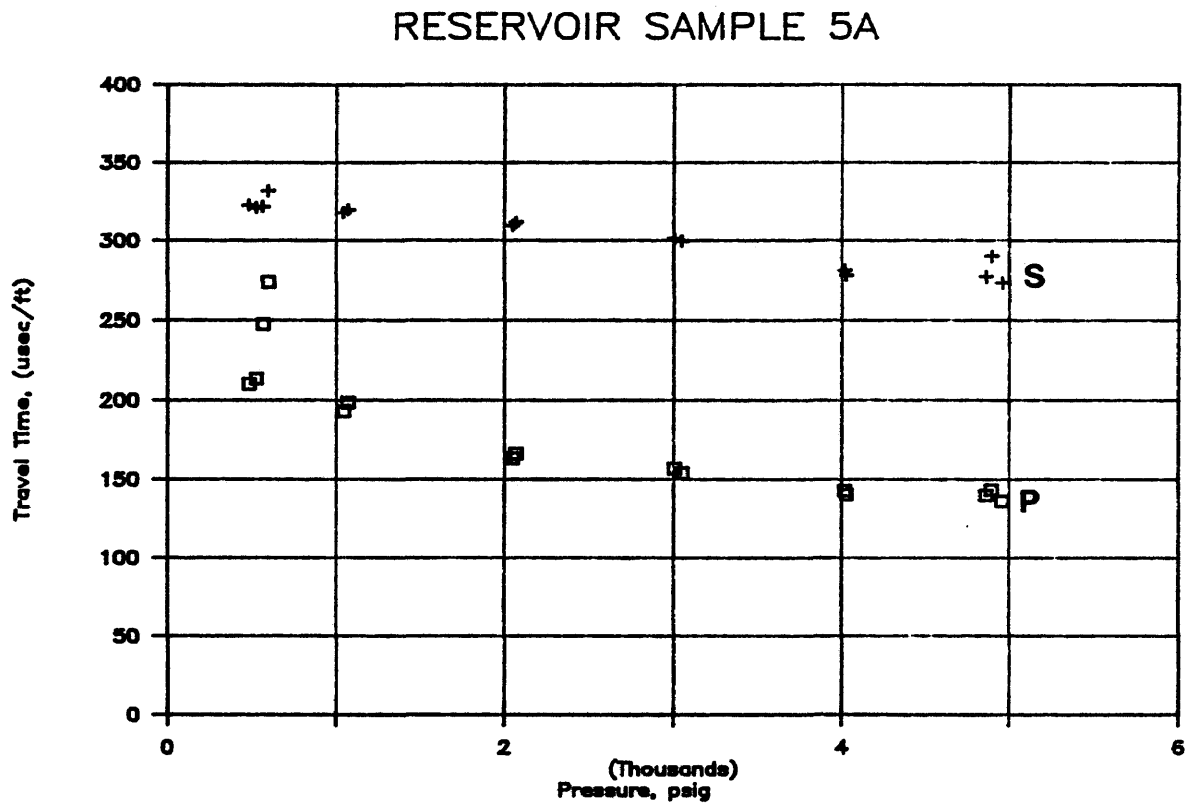
Figure B.18.   Longitudinal and shear wave travel time versus
                pressure.

RESERVOIR SAMPLE 5B
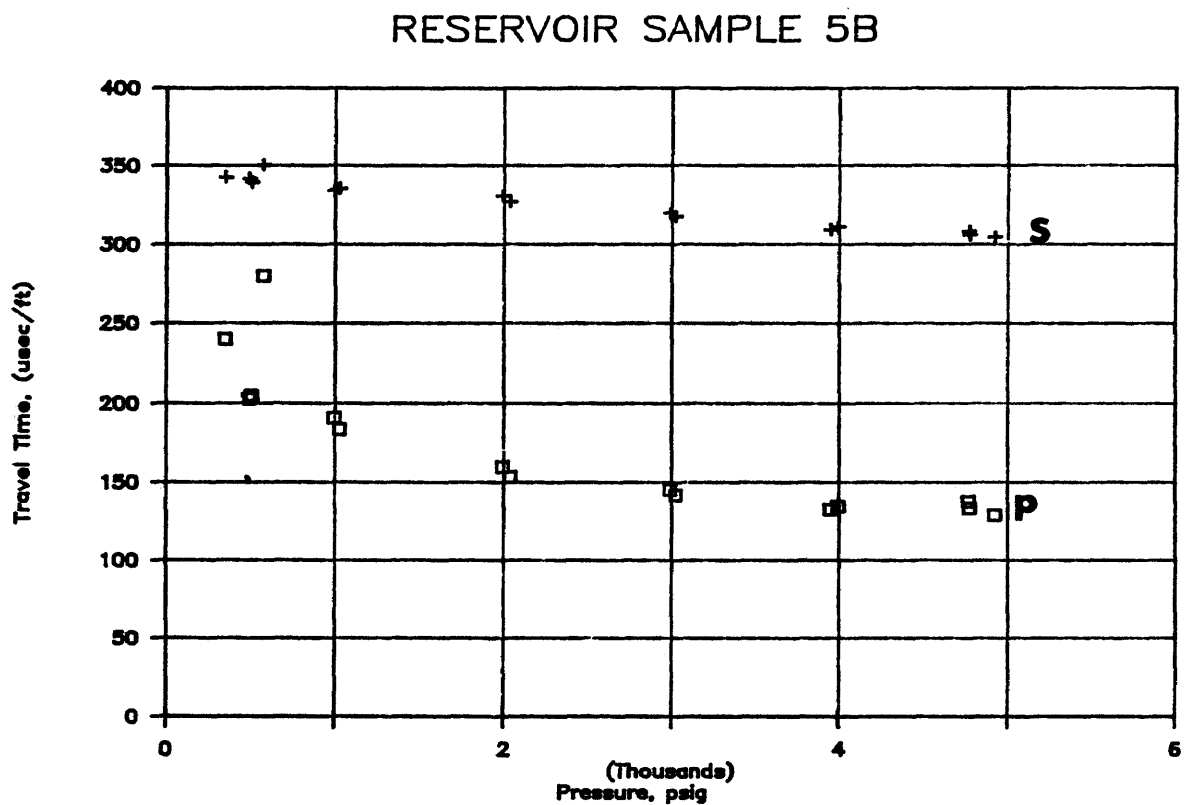
Figure B.19.   Longitudinal and shear wave travel time versus
              pressure.

RESERVOIR SAMPLE 6A
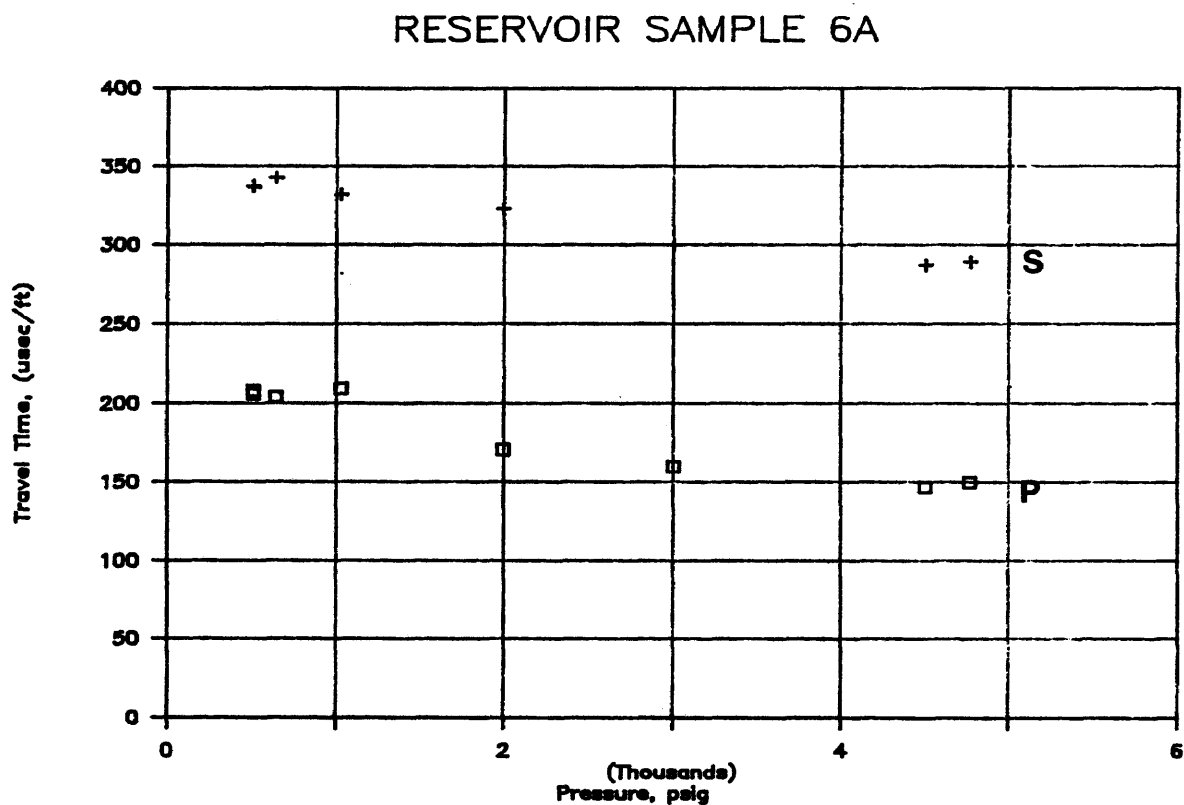
Figure B.20.   Longitudinal and shear wave travel time versus
                pressure.

RESERVOIR SAMPLE 7A
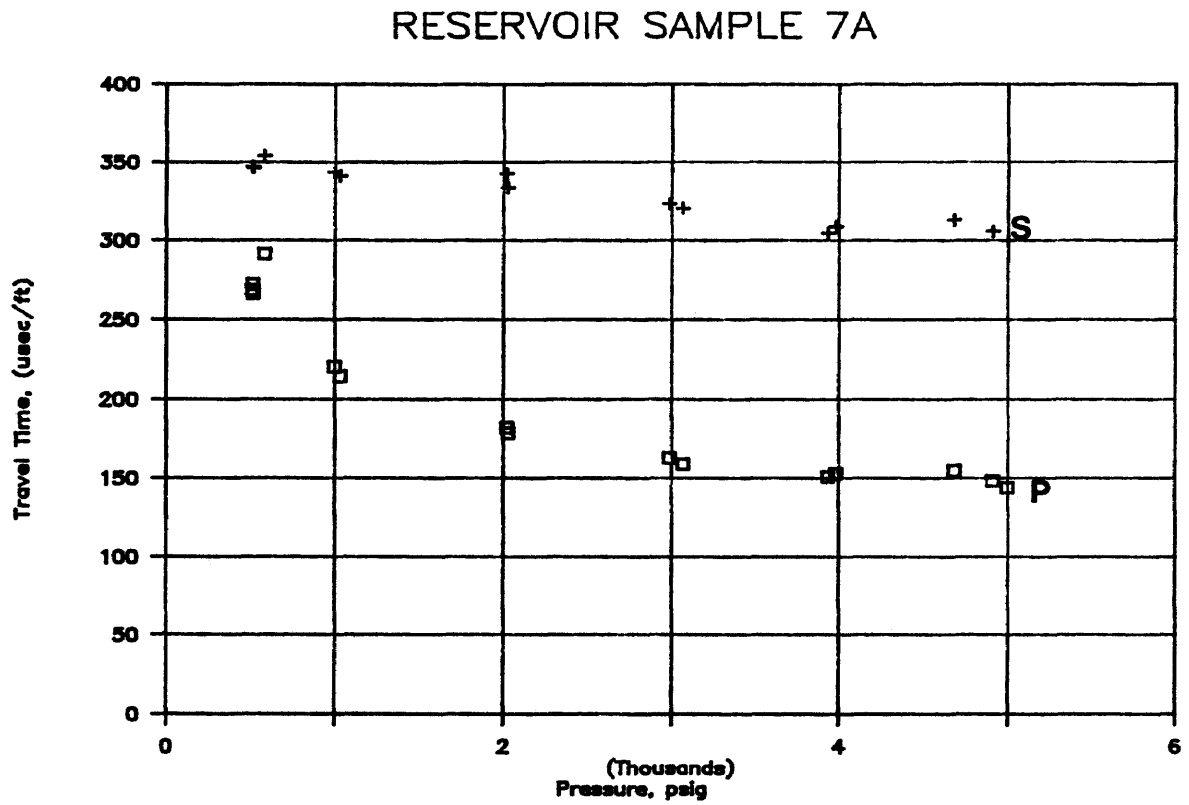
Figure B.21.   Longitudinal and shear wave travel time versus
               pressure.

RESERVOIR SAMPLE 8A
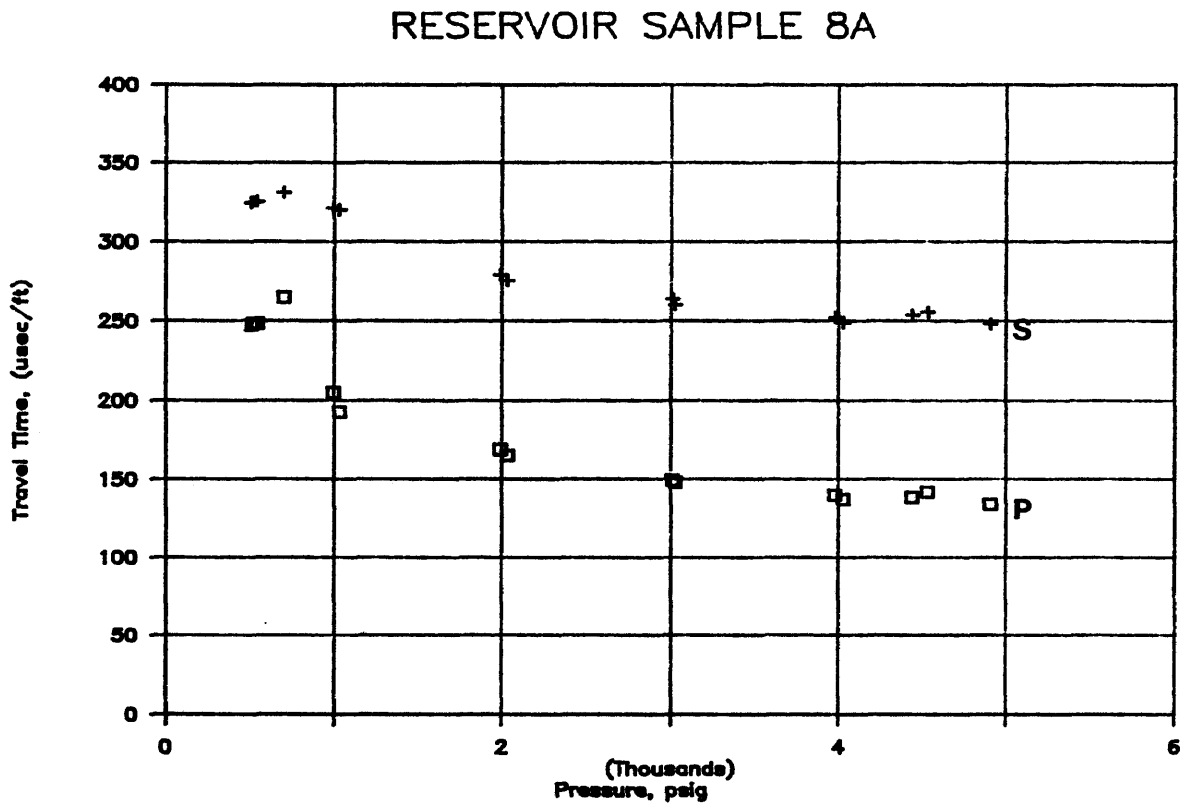
Figure B.22.   Longitudinal and shear wave travel time versus
              pressure.

MONTMAYEUR STD2
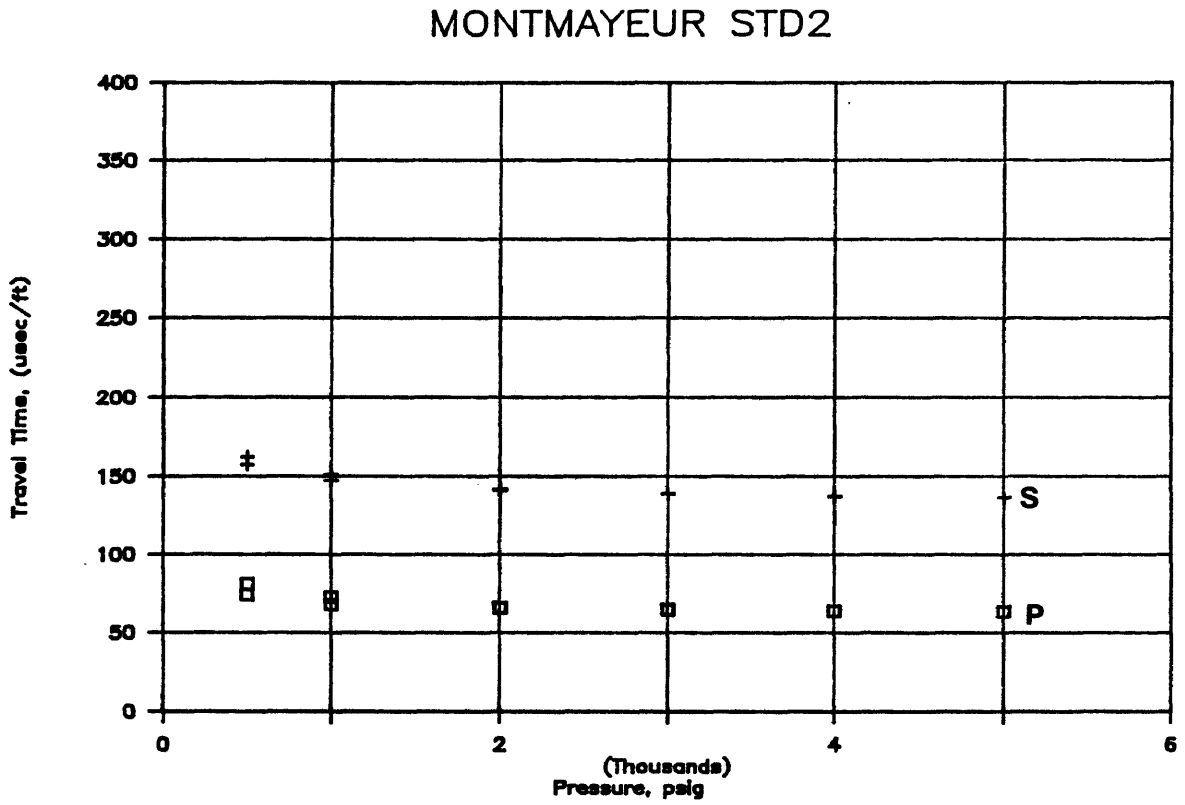
Figure B.23. Longitudinal and shear wave travel time versus
              pressure.

MONTMAYEUR STB5
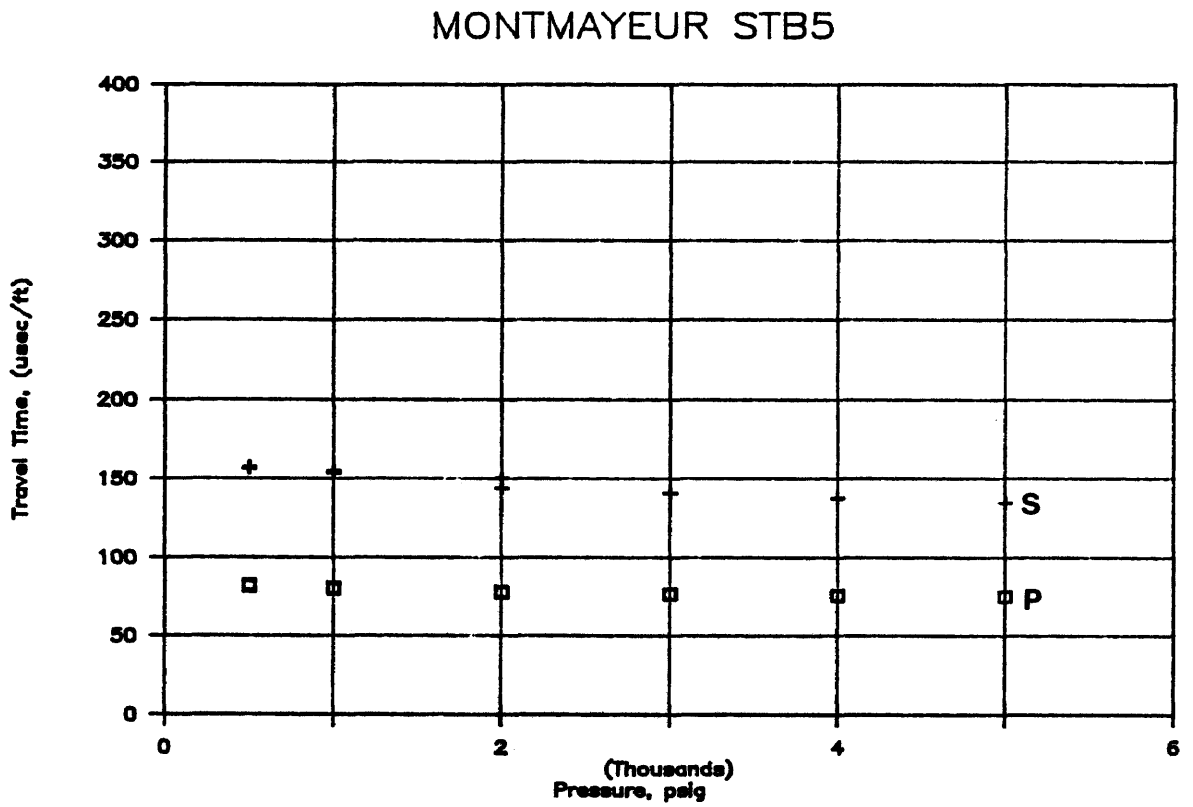
Figure B.24. Longitudinal and shear wave travel time versus pressure.
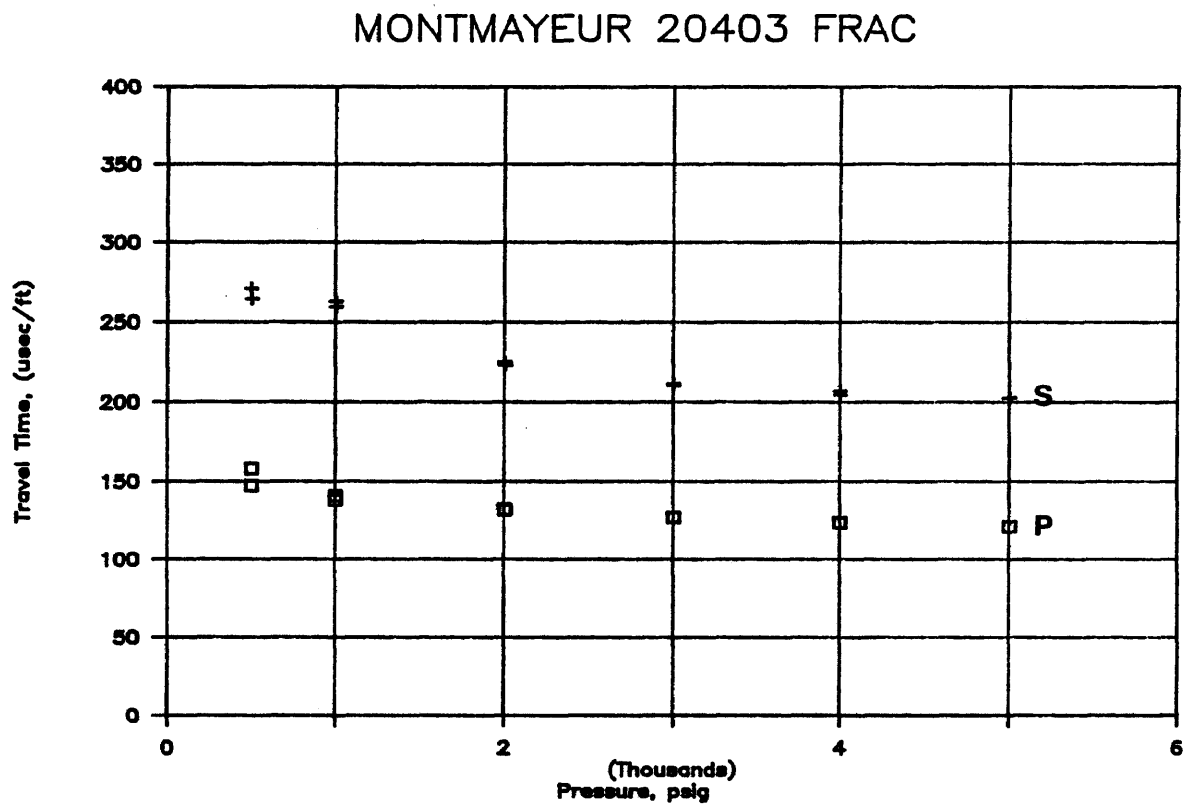
Figure B.25.   Longitudinal and shear wave travel time versus
                pressure.

MONTMAYEUR 20404 FRAC
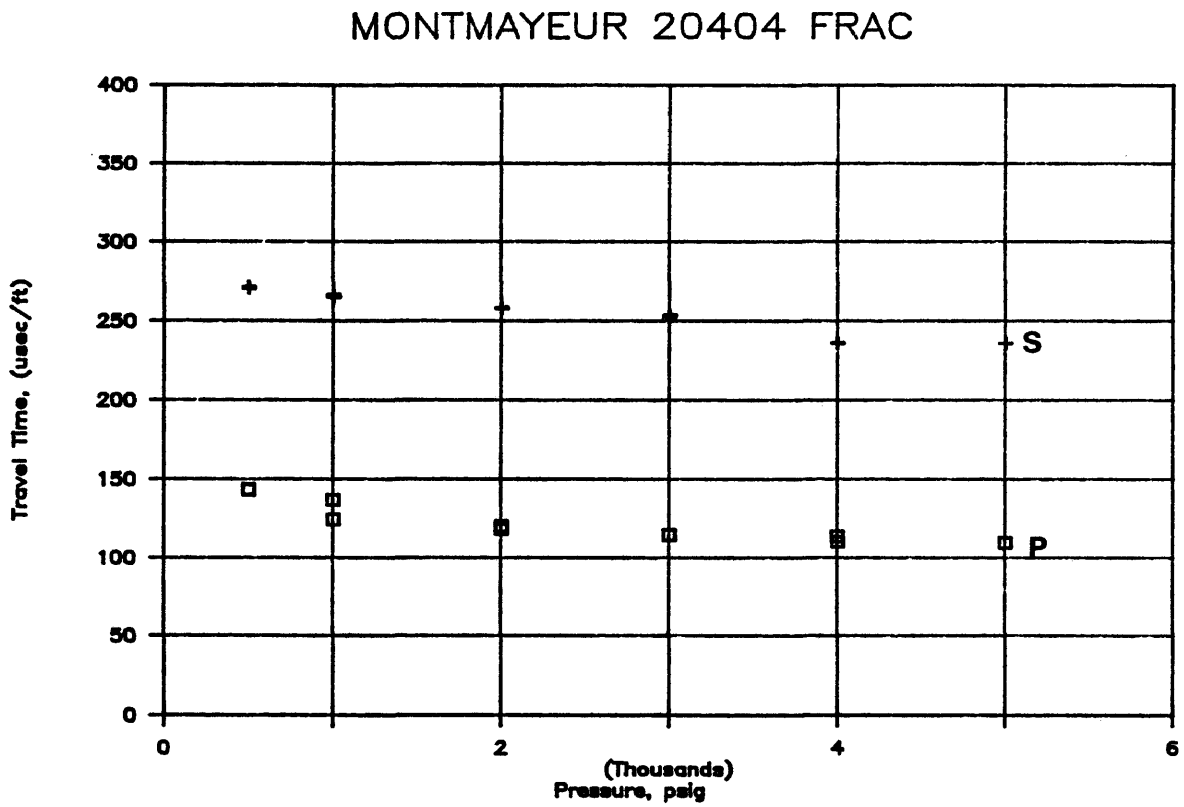
Figure B.26. Longitudinal and shear wave travel time versus pressure.

MONTMAYEUR 4060 FRAC
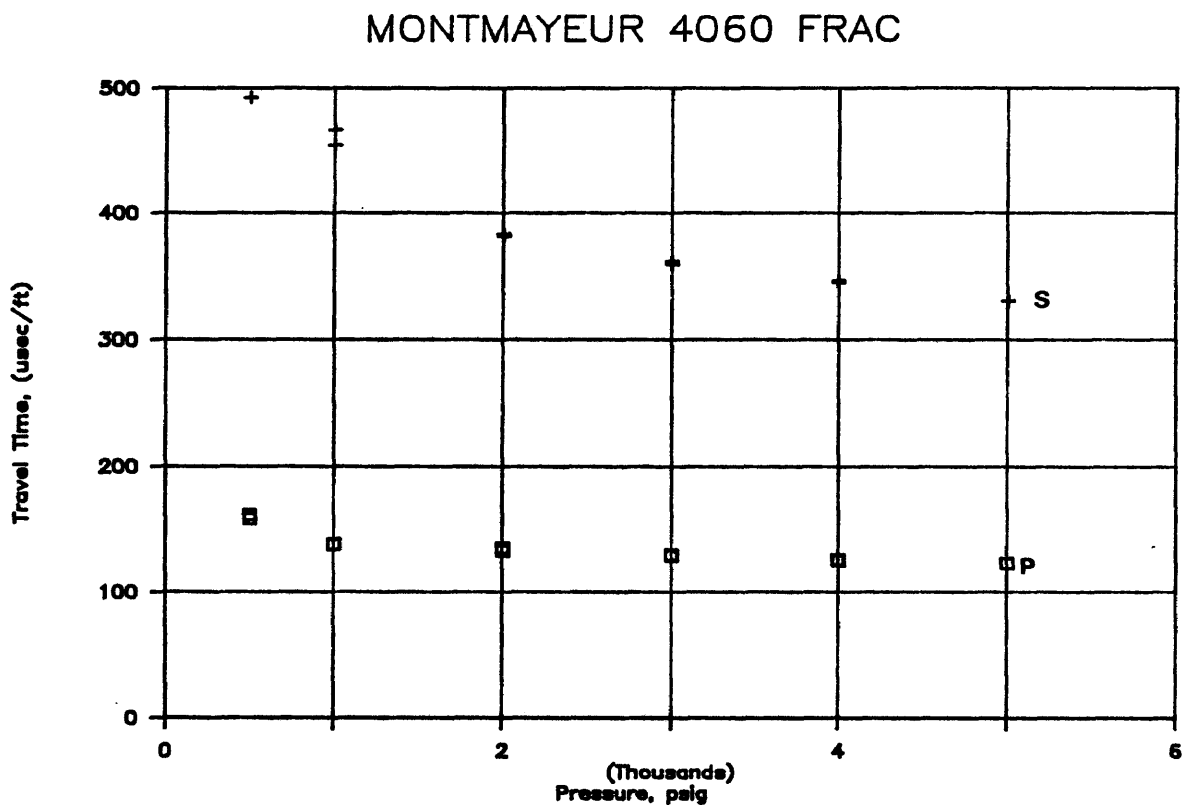
Figure B.27.   Longitudinal and shear wave travel time versus
               pressure.
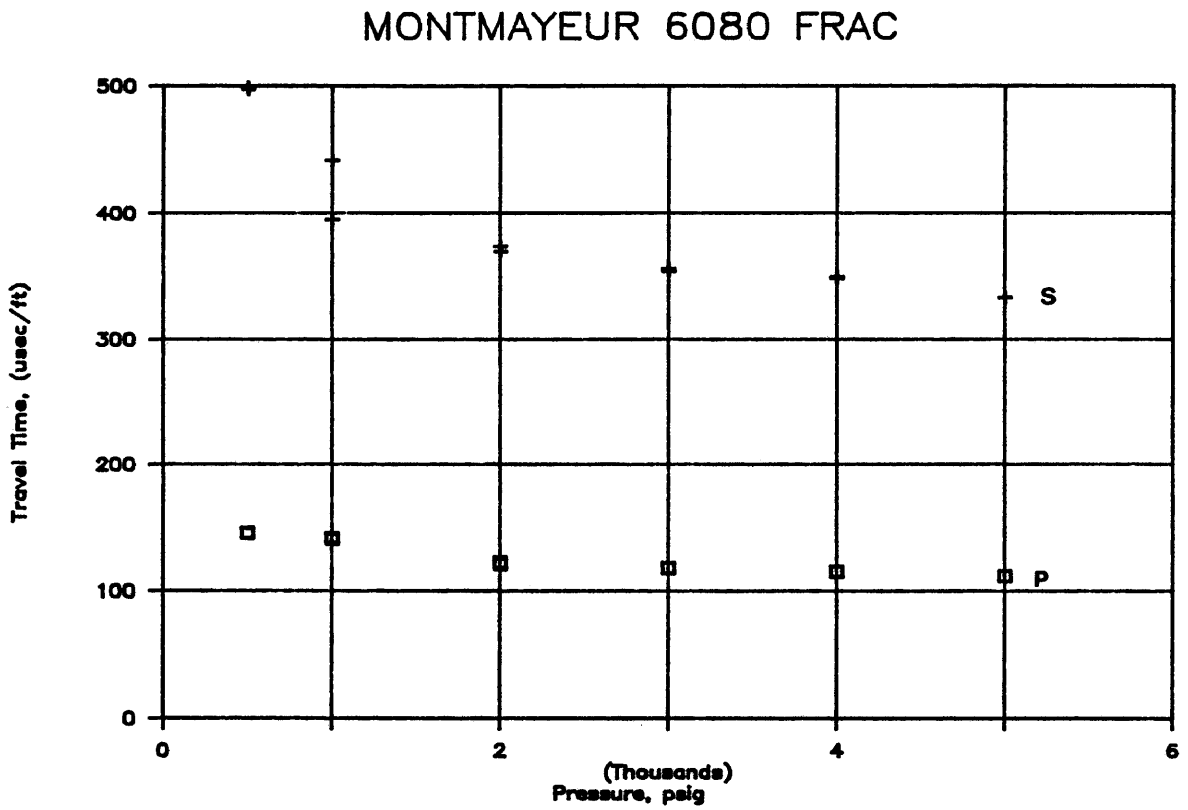
Figure B.28.   Longitudinal and shear wave travel time versus
               pressure.

MONTMAYEUR 8010 FRAC
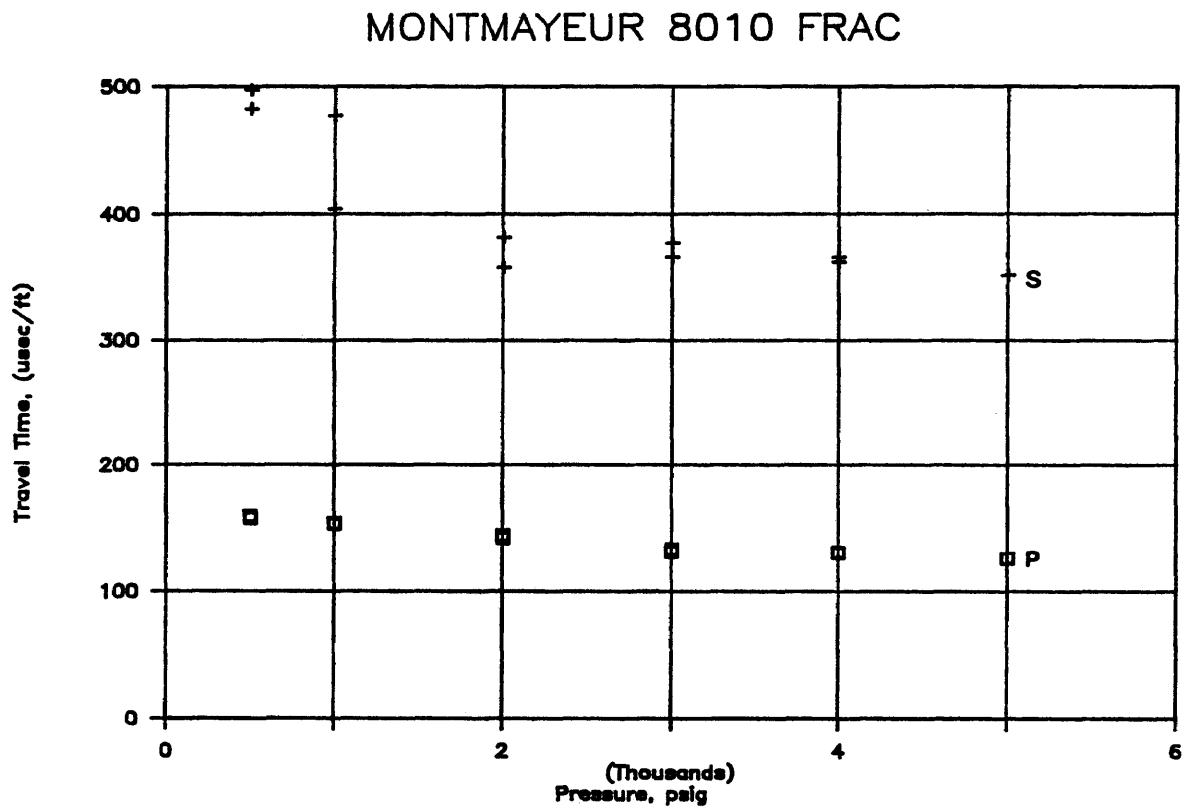
Figure B.29. Longitudinal and shear wave travel time versus
            pressure.

MONTMAYEUR 1012 FRAC
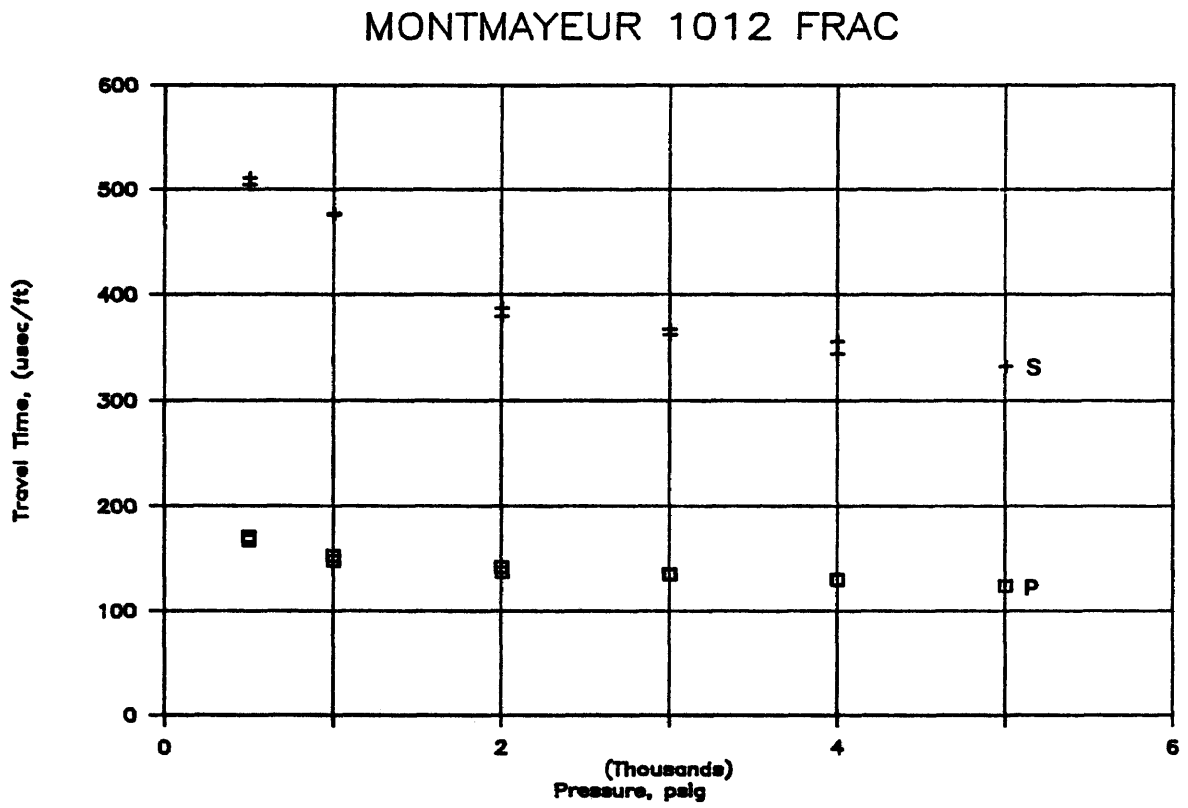
Figure B.30. Longitudinal and shear wave travel time versus
                pressure.

MONTMAYEUR 1217 FRAC
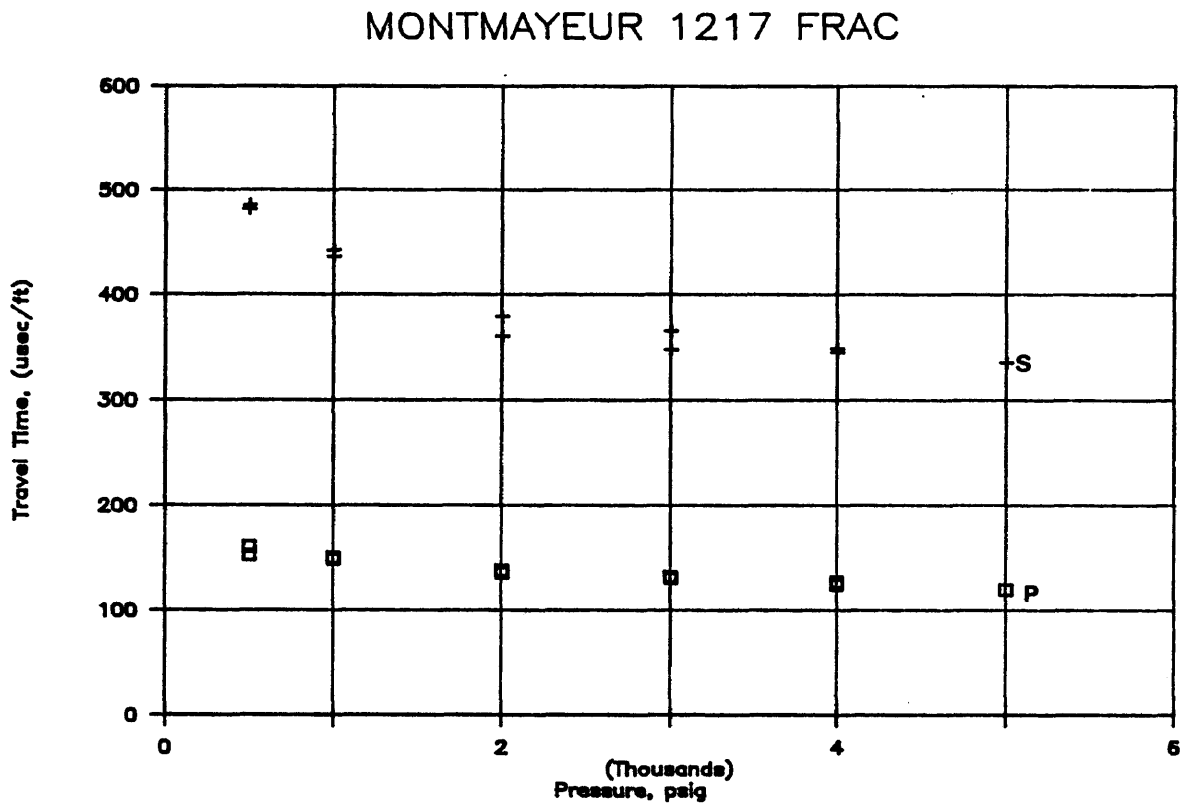
Figure B.31.   Longitudinal and shear wave travel time versus
                pressure.

MONTMAYEUR 1720 FRAC
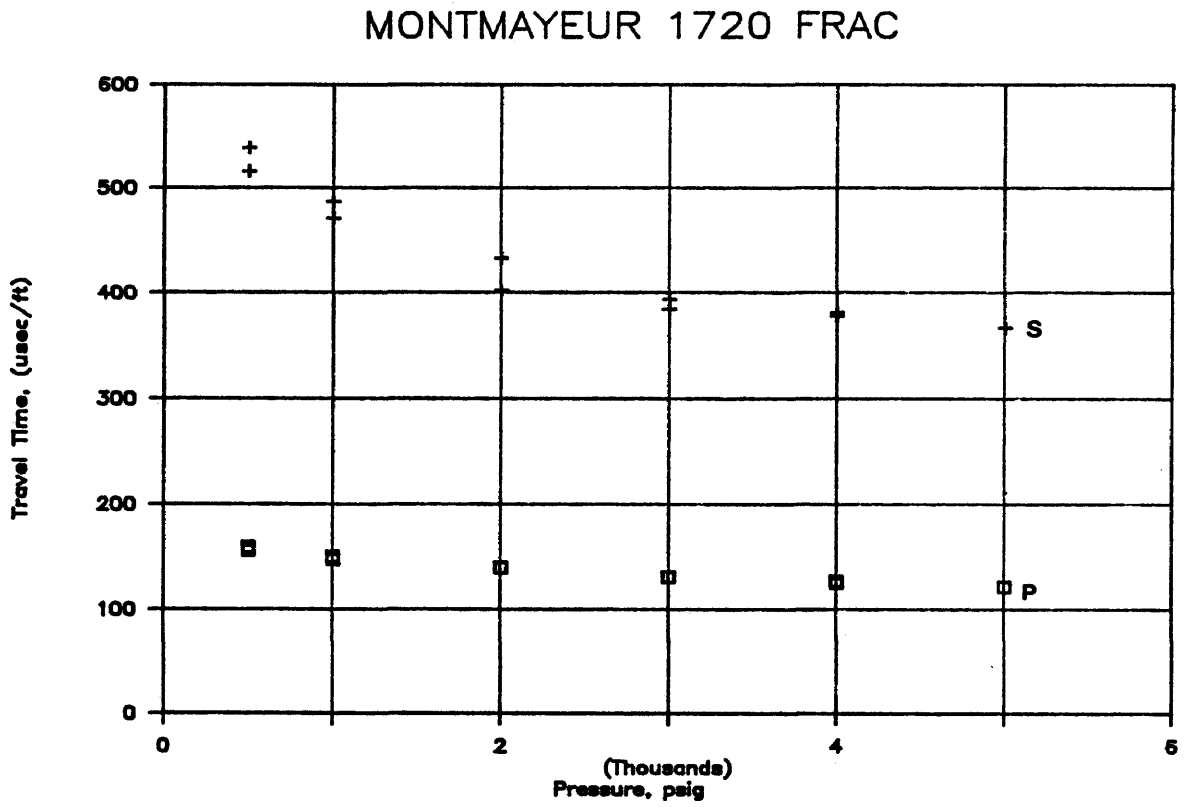
Figure B.32.   Longitudinal and shear wave travel time versus
               pressure.

STD2 — Howarth
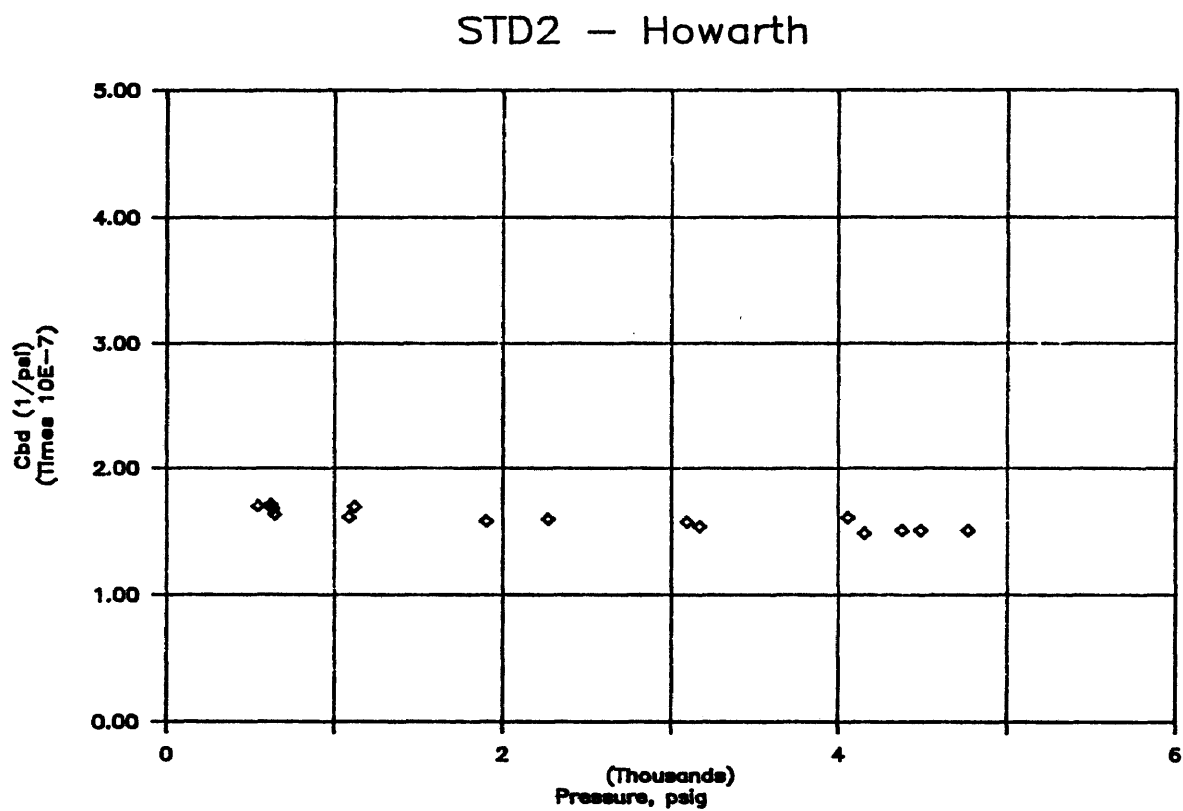
Figure B.33. Dynamic bulk compressibility versus pressure.
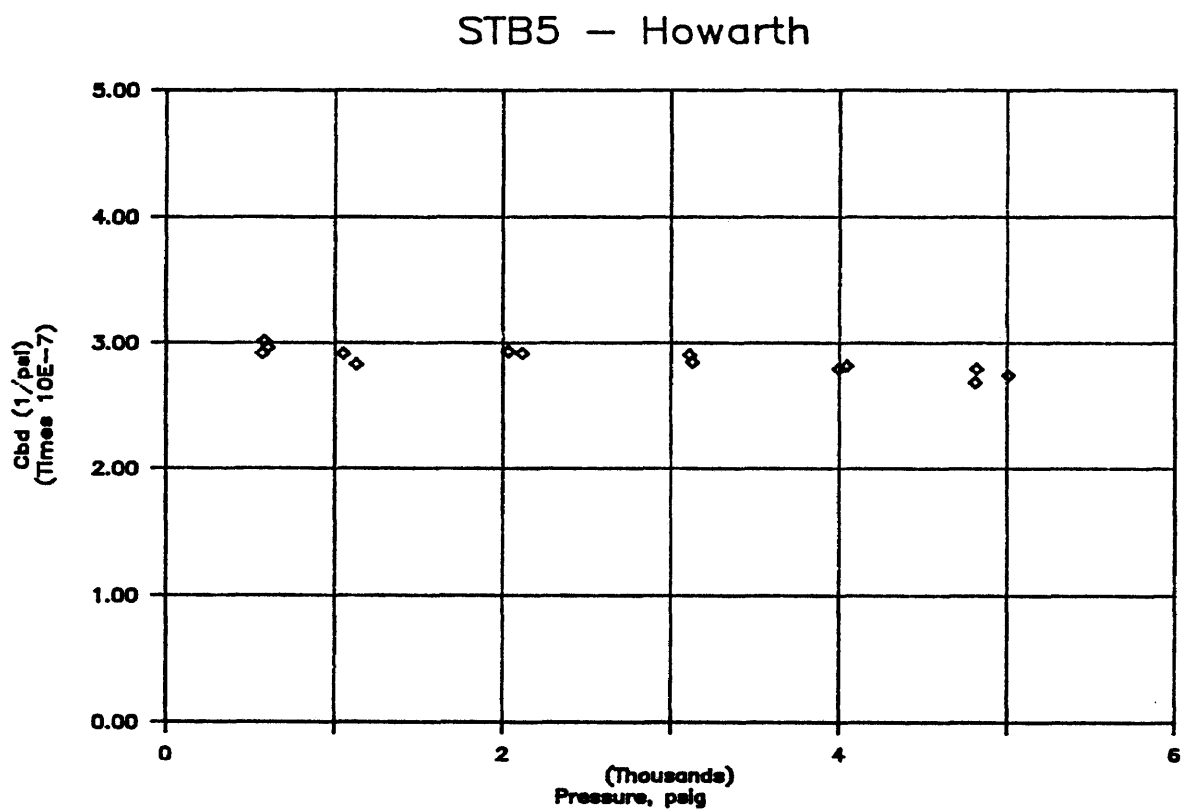
Figure B.34.   Dynamic bulk compressibility versus pressure.

HCB5
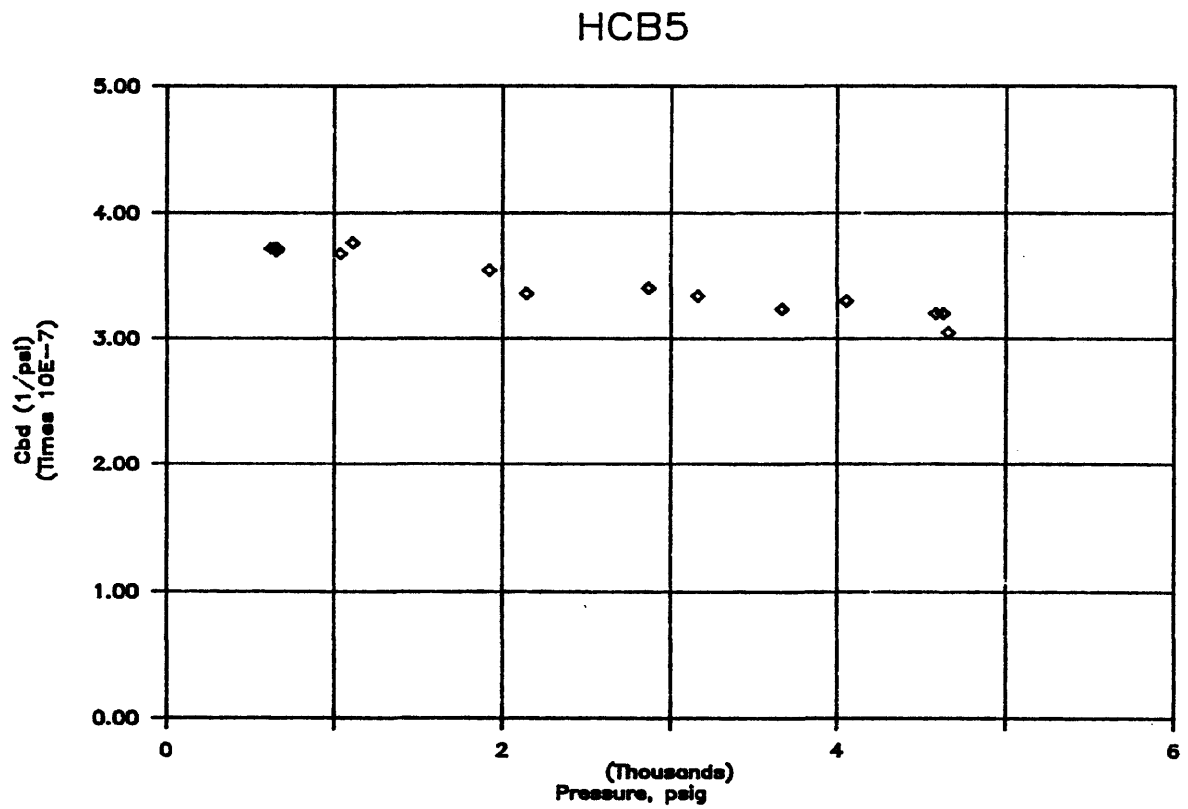
Figure B.35.   Dynamic bulk compressibility versus pressure.

HCB11
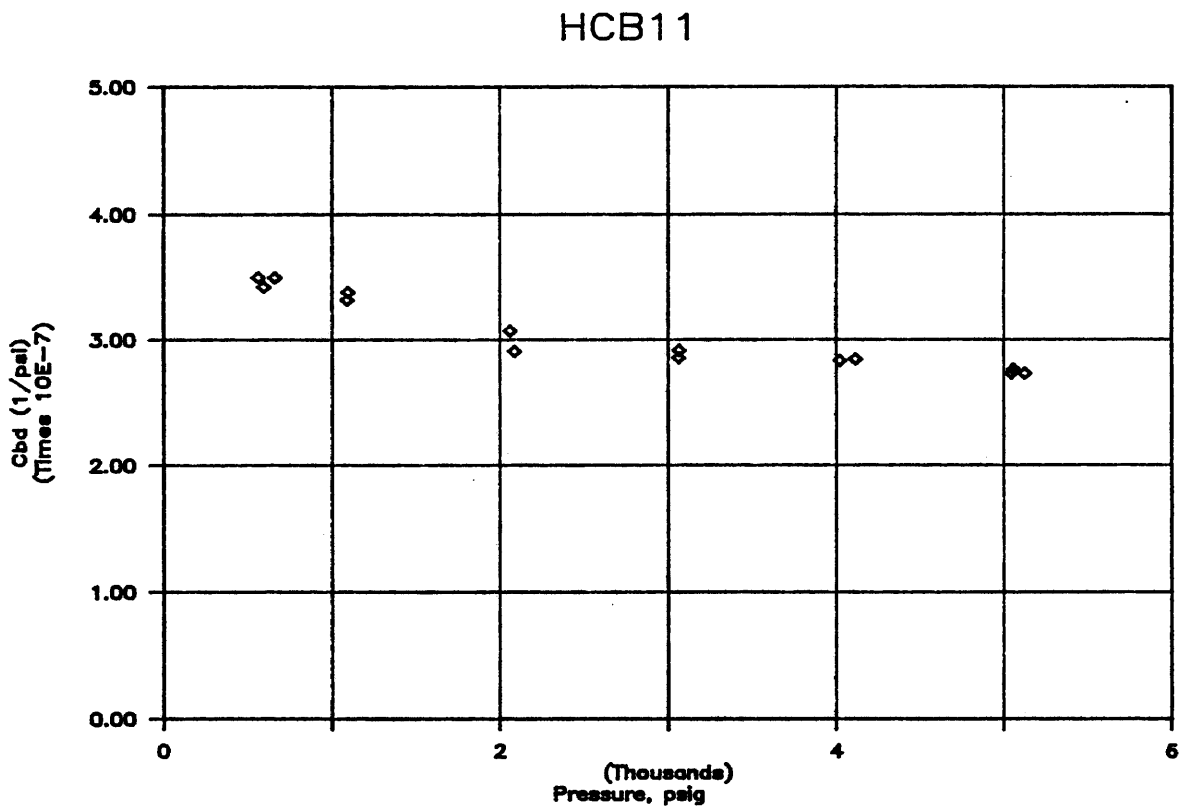
Figure B.36. Dynamic bulk compressibility versus pressure.

HCB13
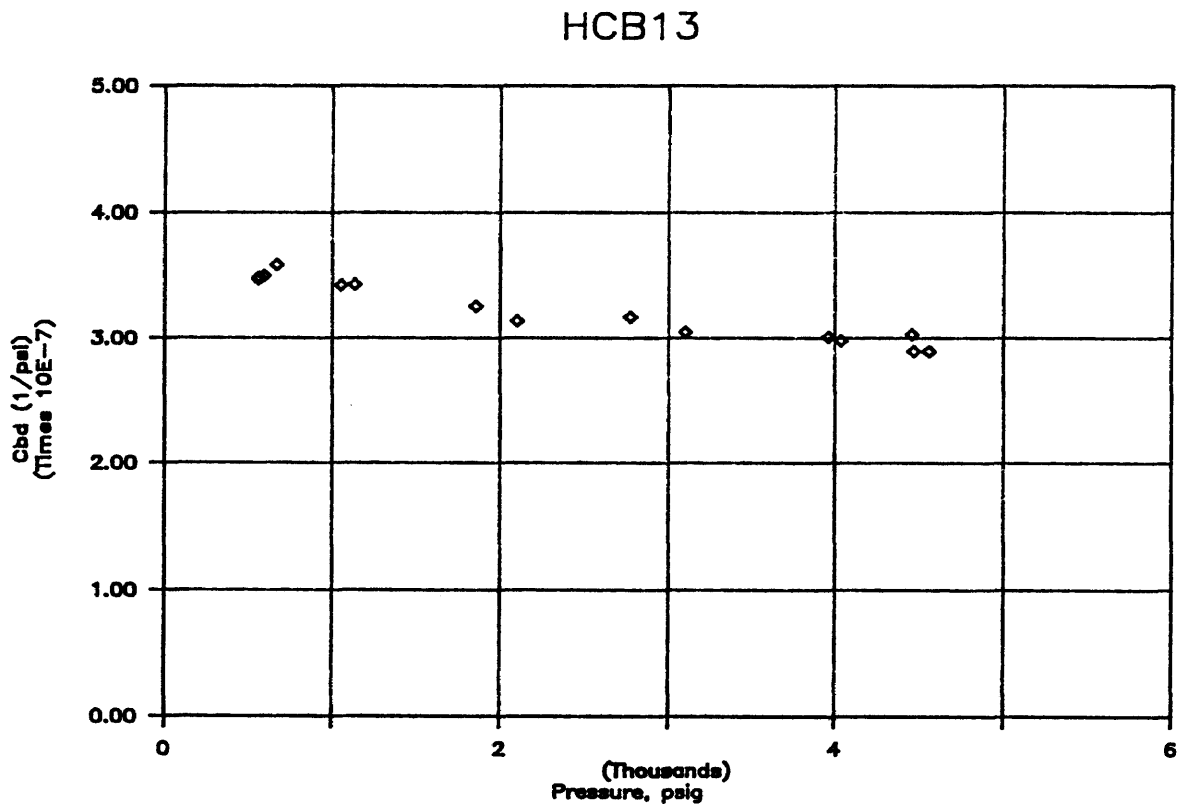
Figure B.37.   Dynamic bulk compressibility versus pressure.

G2040A
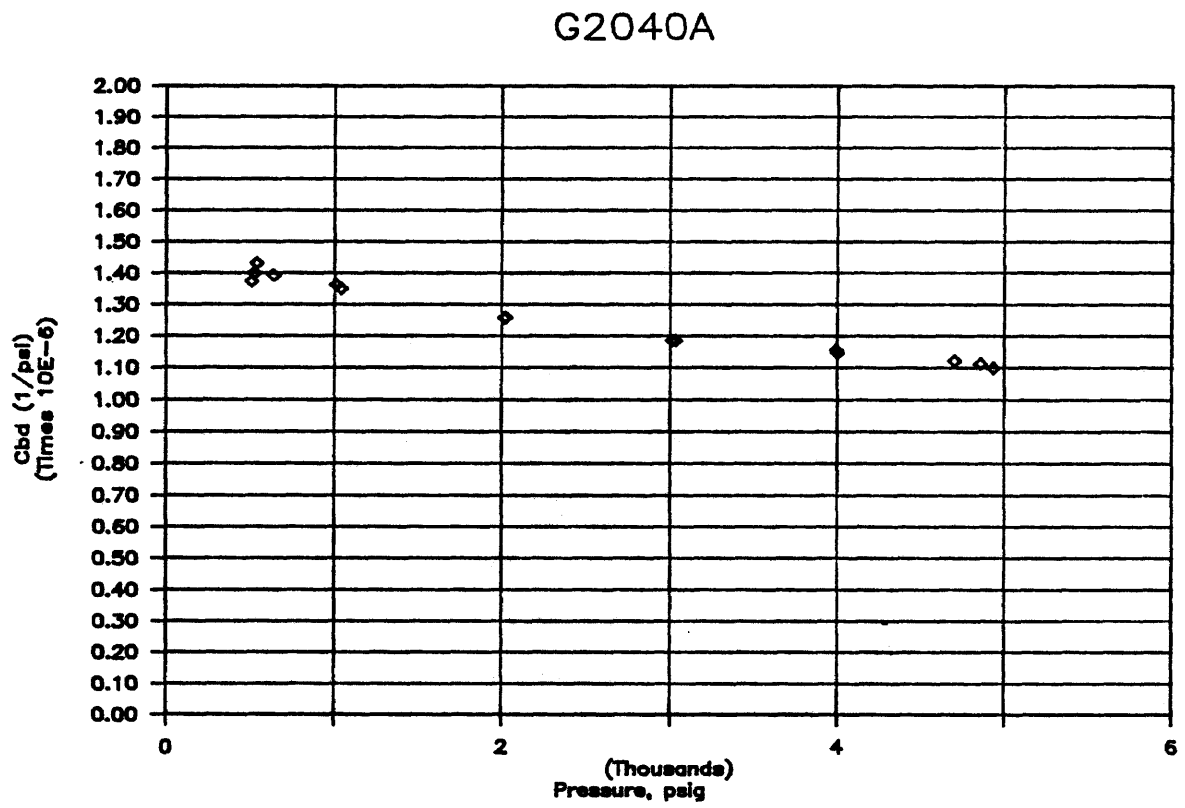
Figure B.38. Dynamic bulk compressibility versus pressure.

G1014A
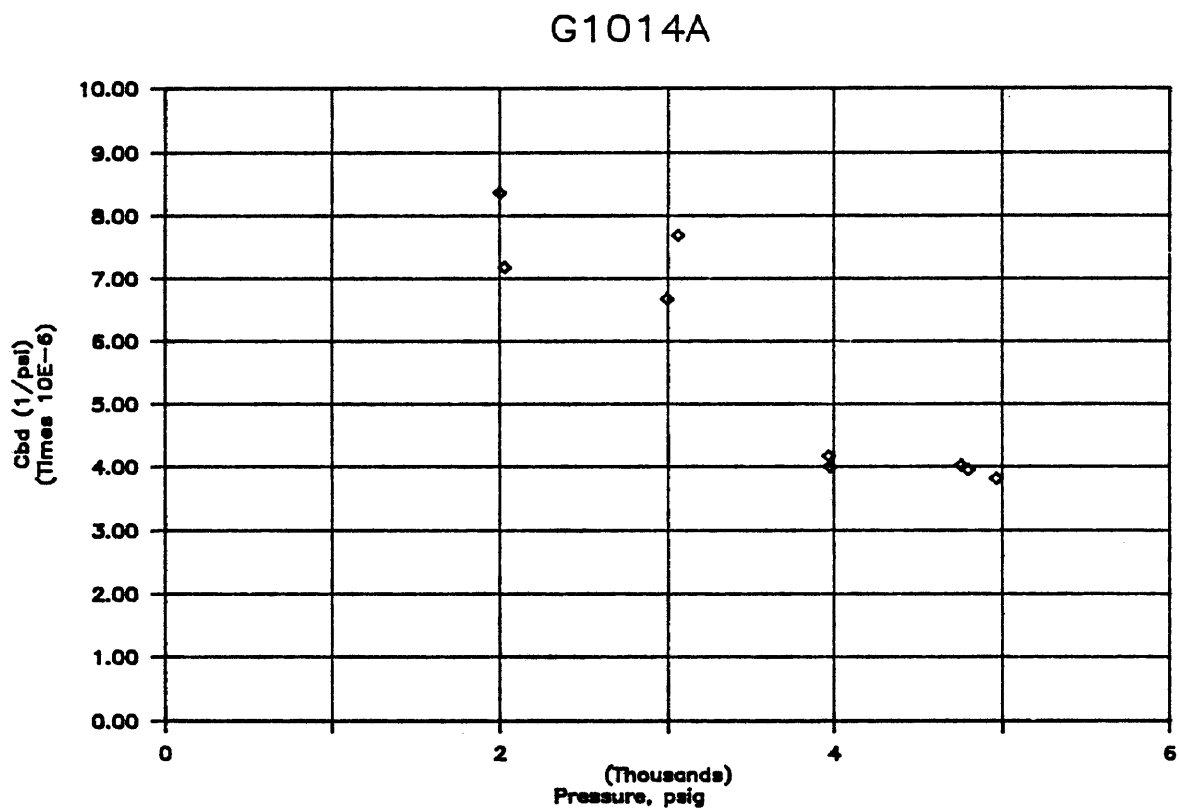
Figure B.39. Dynamic bulk compressibility versus pressure.

F2040C
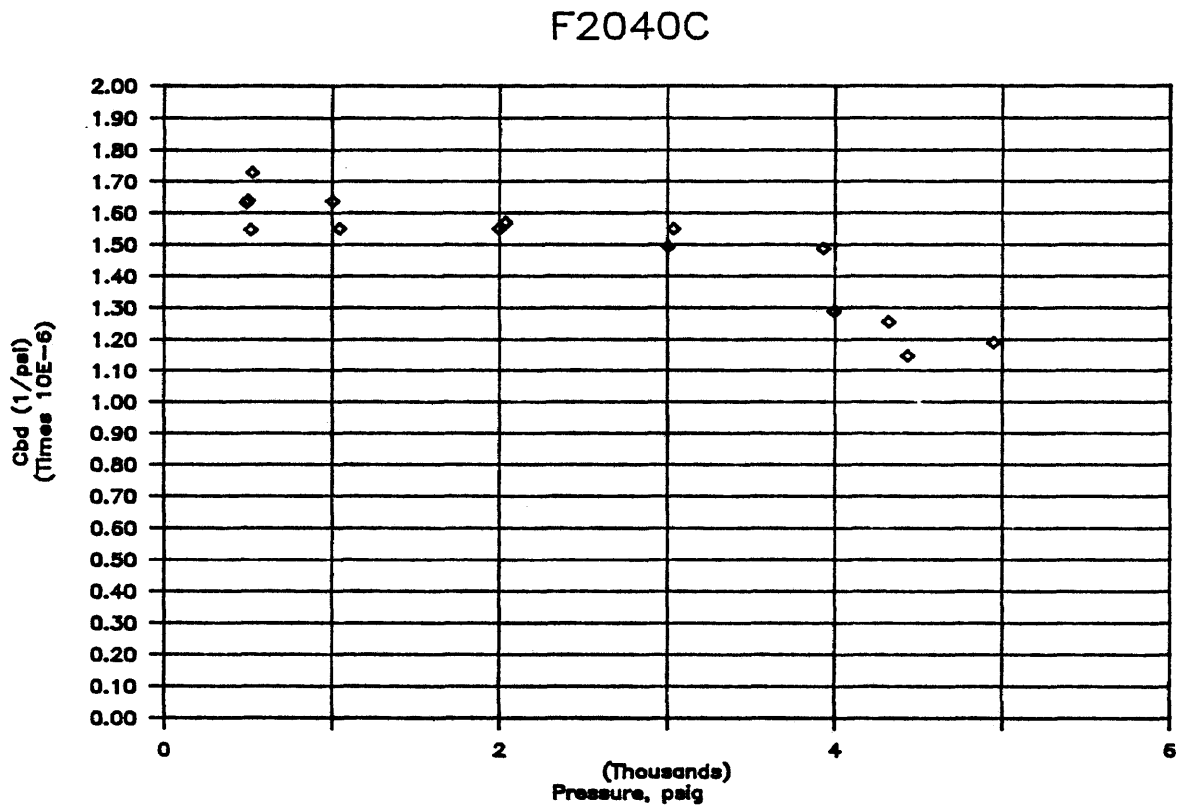
Figure B.40.   Dynamic bulk compressibility versus pressure.

F6080A
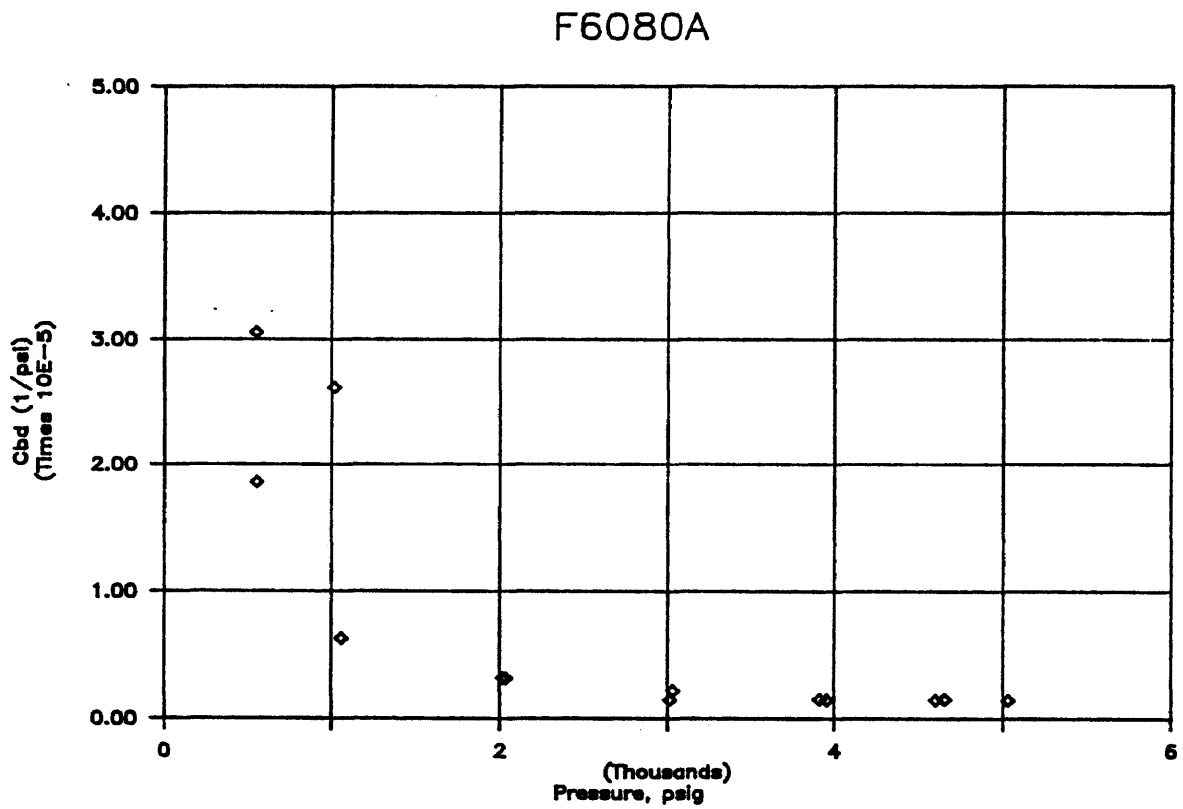
Figure B.41. Dynamic bulk compressibility versus pressure.

F6080B
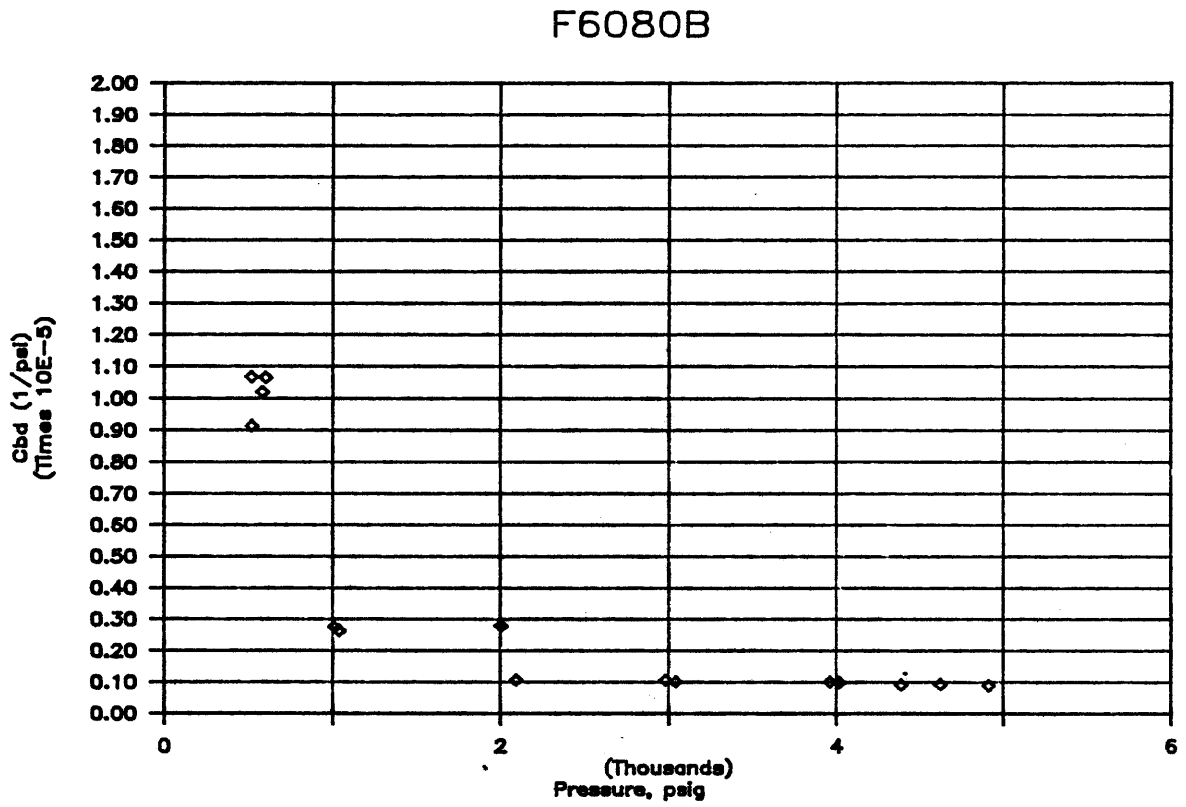
Figure B.42. Dynamic bulk compressibility versus pressure.

F6080D
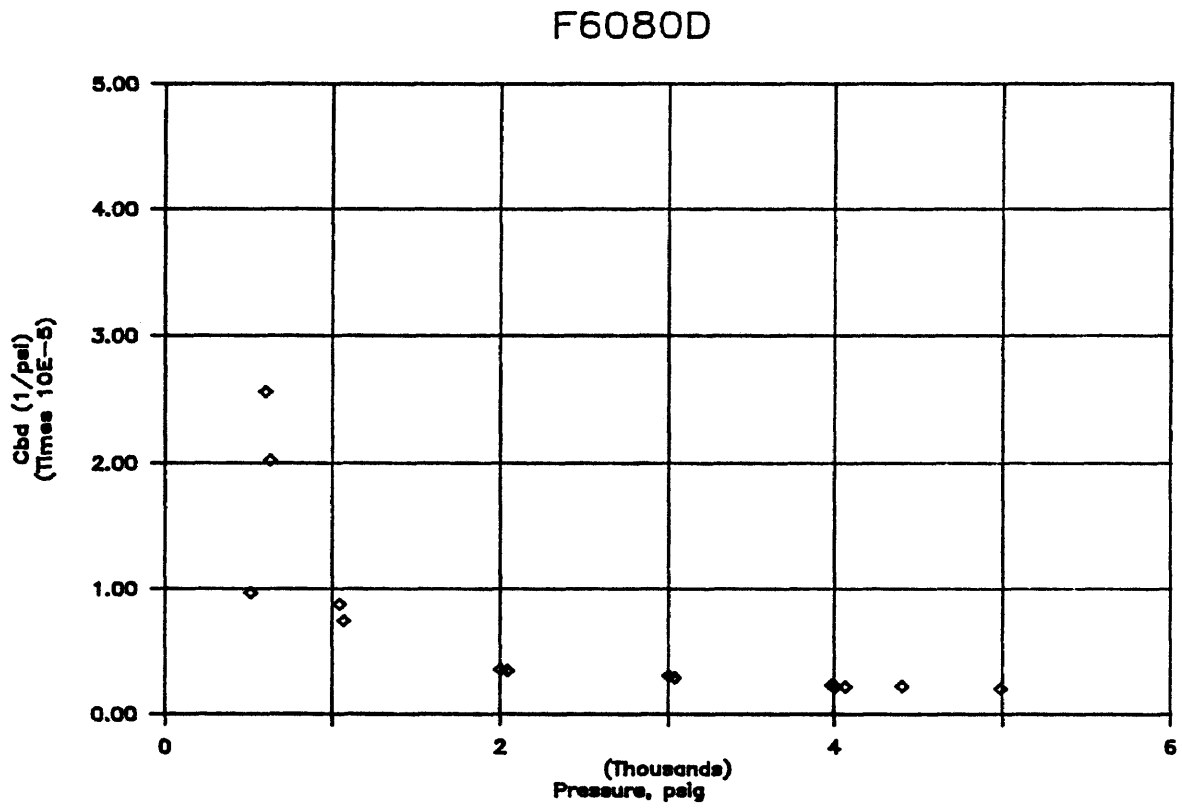
Figure B.43. Dynamic bulk compressibility versus pressure.

F1014A
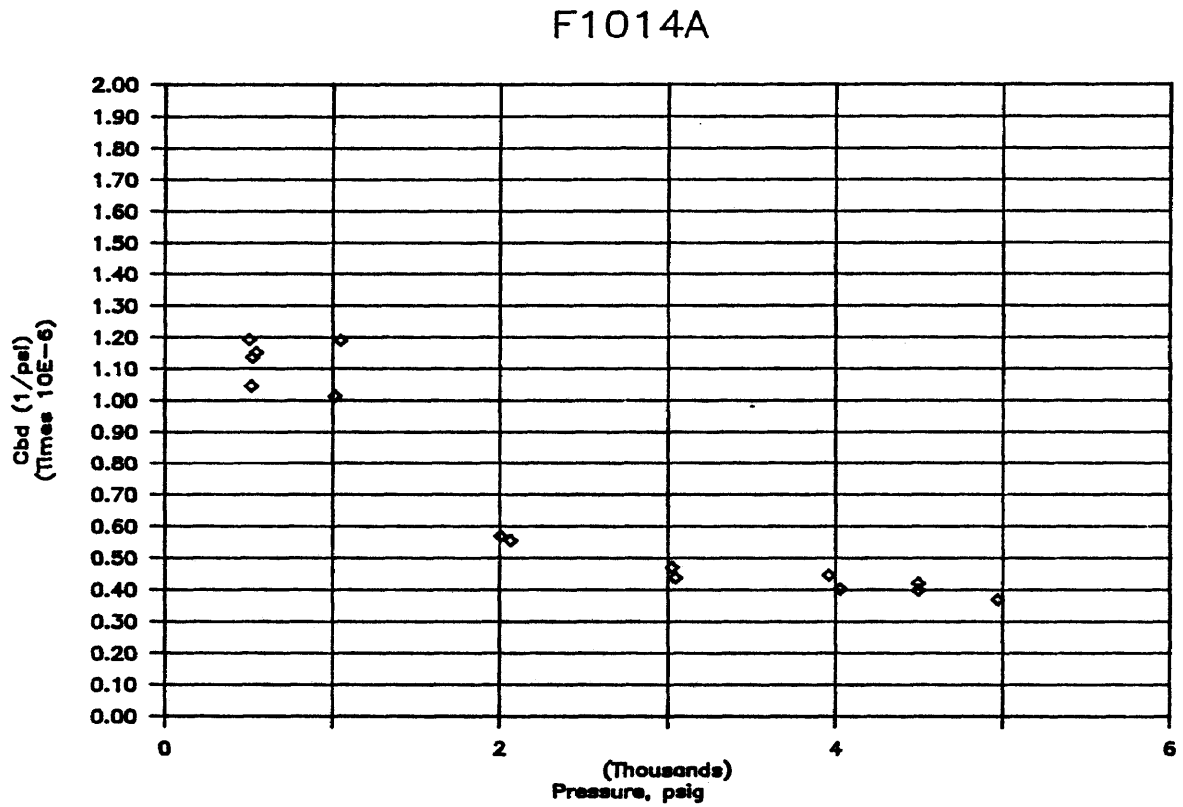
Figure B.44.   Dynamic bulk compressibility versus pressure.

F1014B
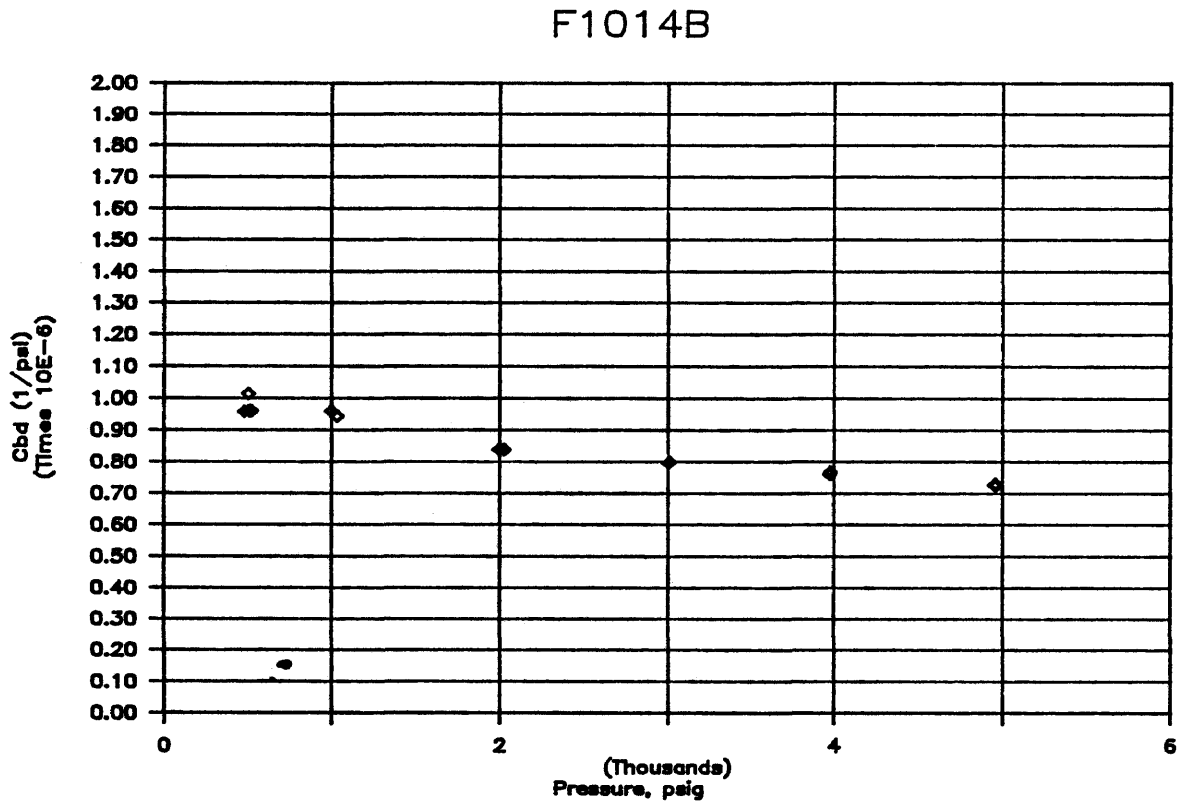
Figure B.45. Dynamic bulk compressibility versus pressure.

RESERVOIR SAMPLE 1A
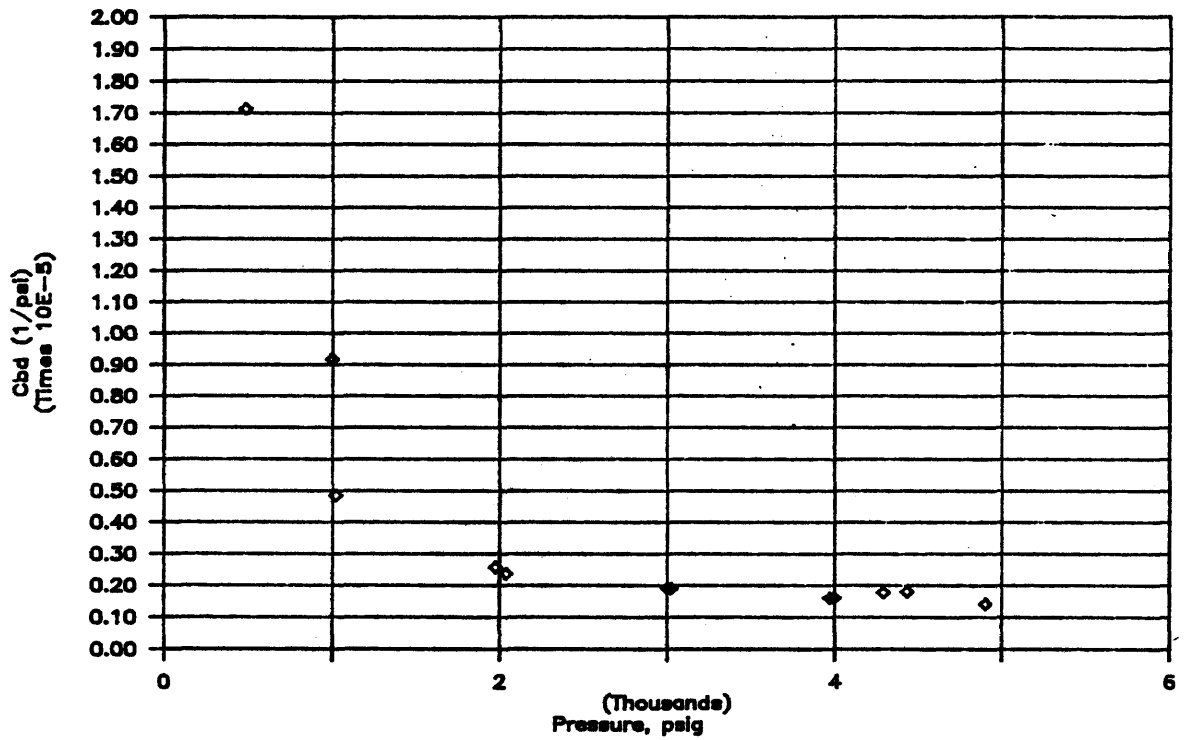
Figure B.46.   Dynamic bulk compressibility versus pressure.

RESERVOIR SAMPLE 2B
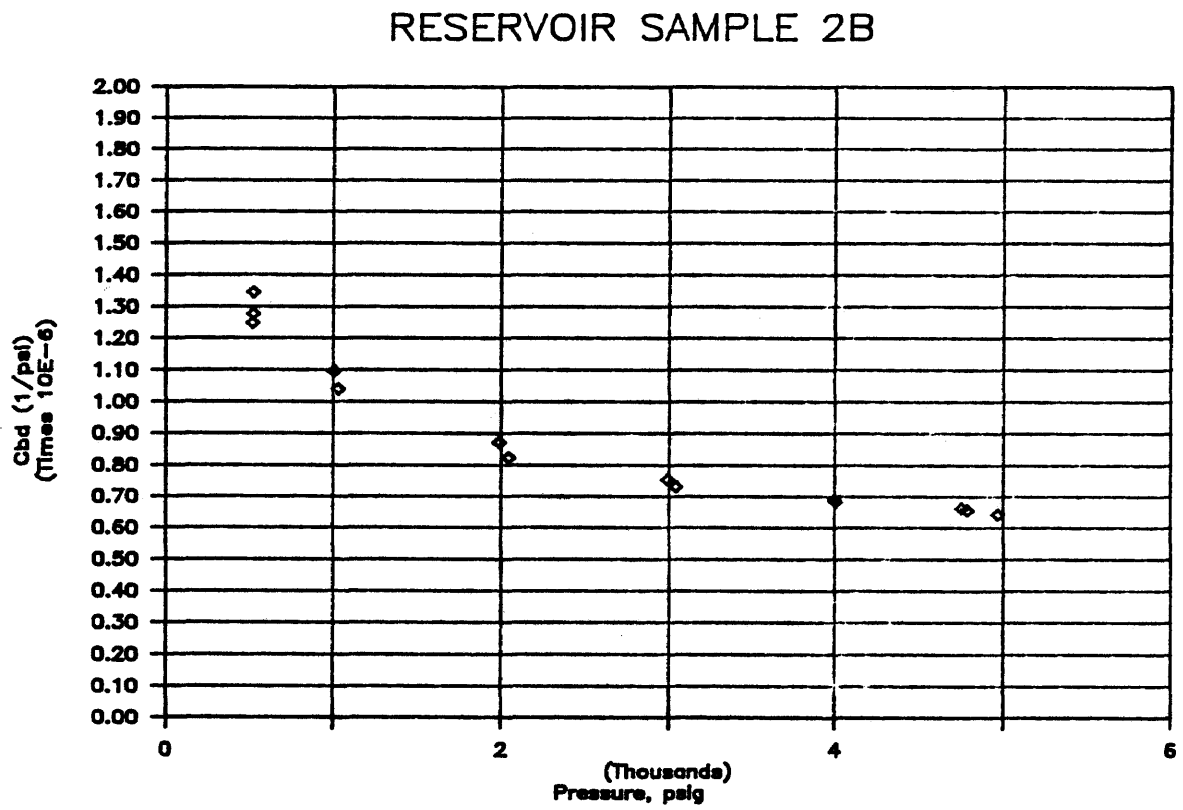
Figure B.47.   Dynamic bulk compressibility versus pressure.

RESERVOIR SAMPLE 3A
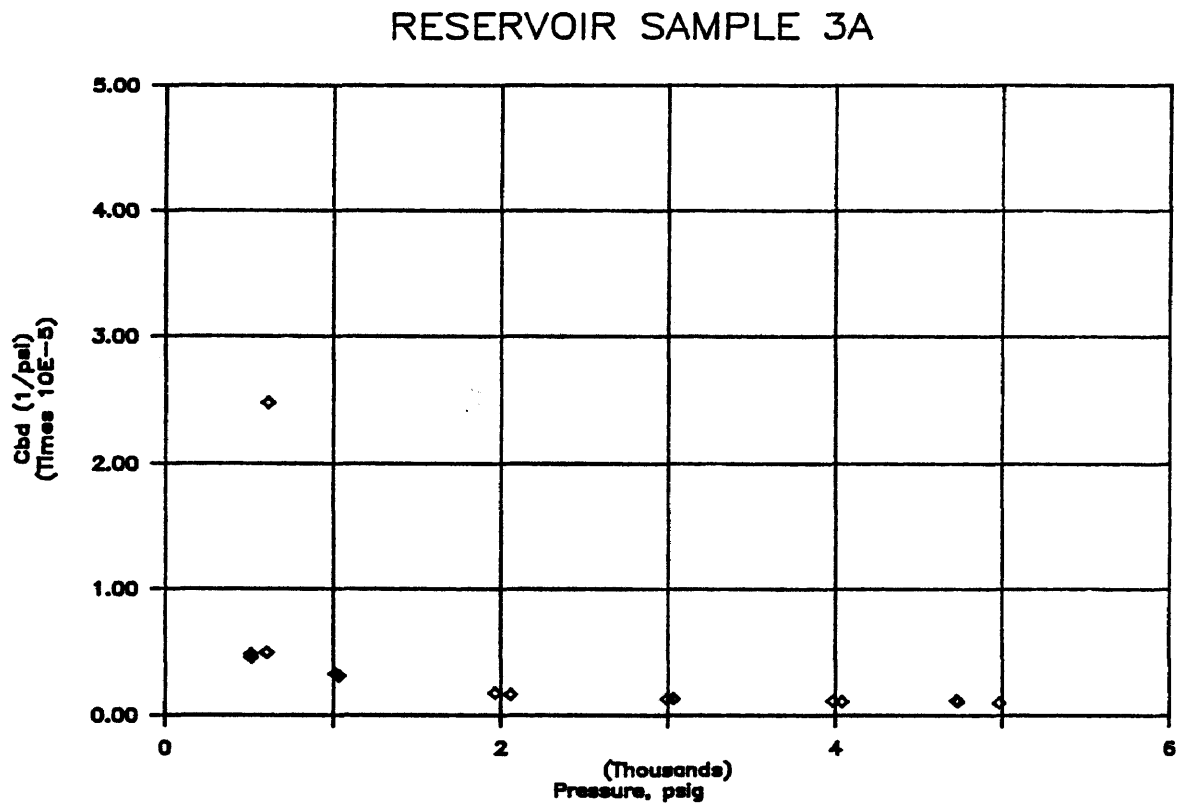
Figure B.48.   Dynamic bulk compressibility versus pressure.

RESERVOIR SAMPLE 4A
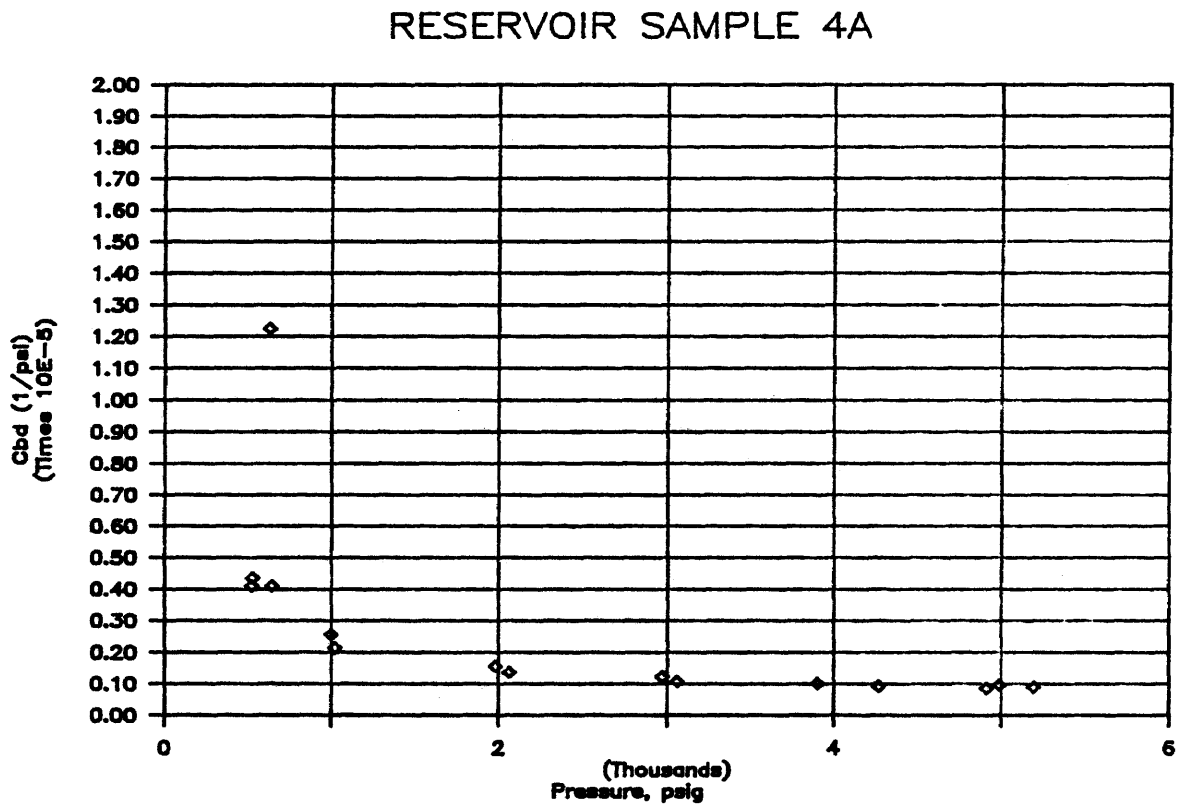
Figure B.49.   Dynamic bulk compressibility versus pressure.

RESERVOIR SAMPLE 5A
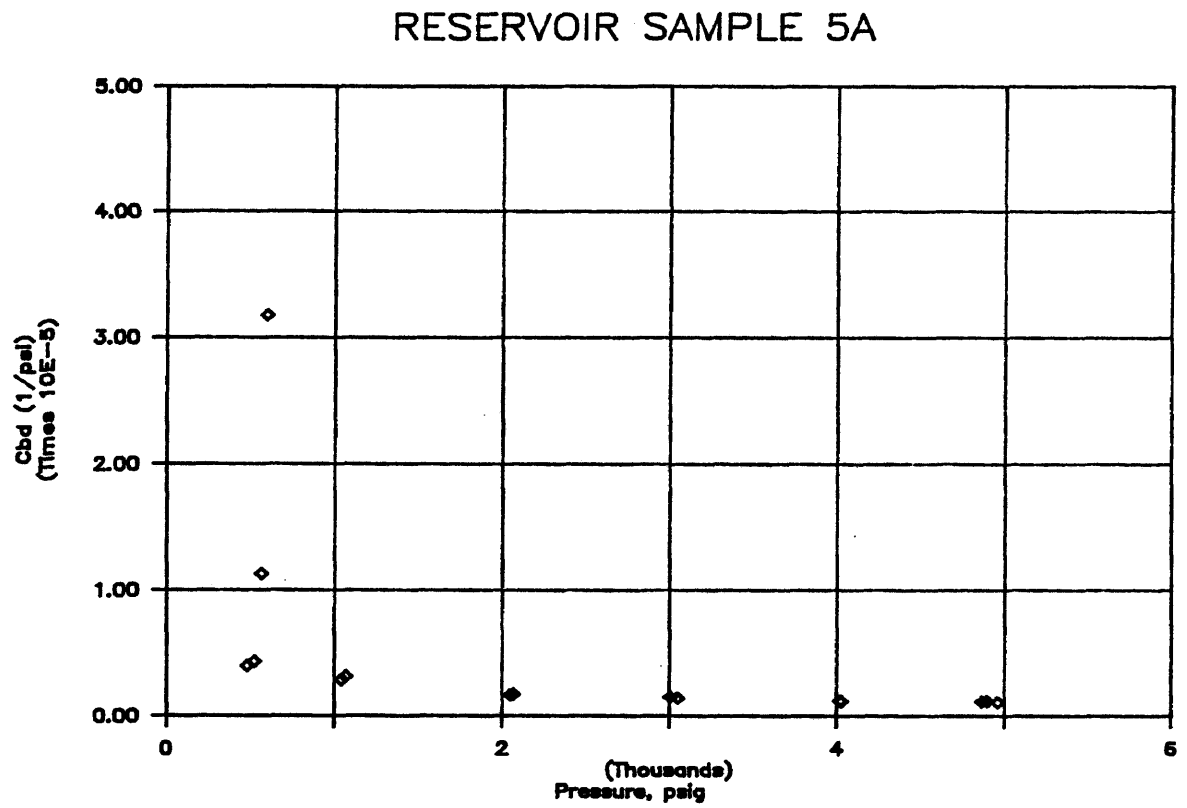
Figure B.50. Dynamic bulk compressibility versus pressure.

RESERVOIR SAMPLE 5B
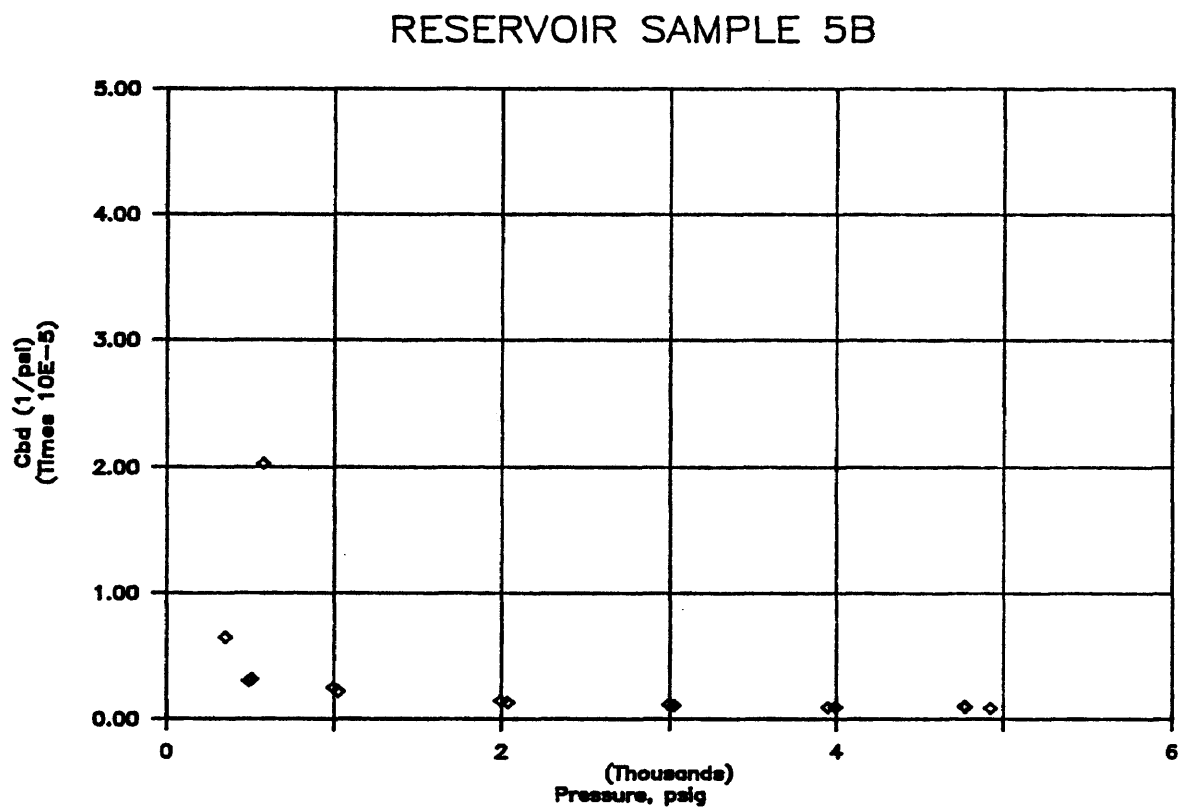
Figure B.51. Dynamic bulk compressibility versus pressure.

RESERVOIR SAMPLE 6A
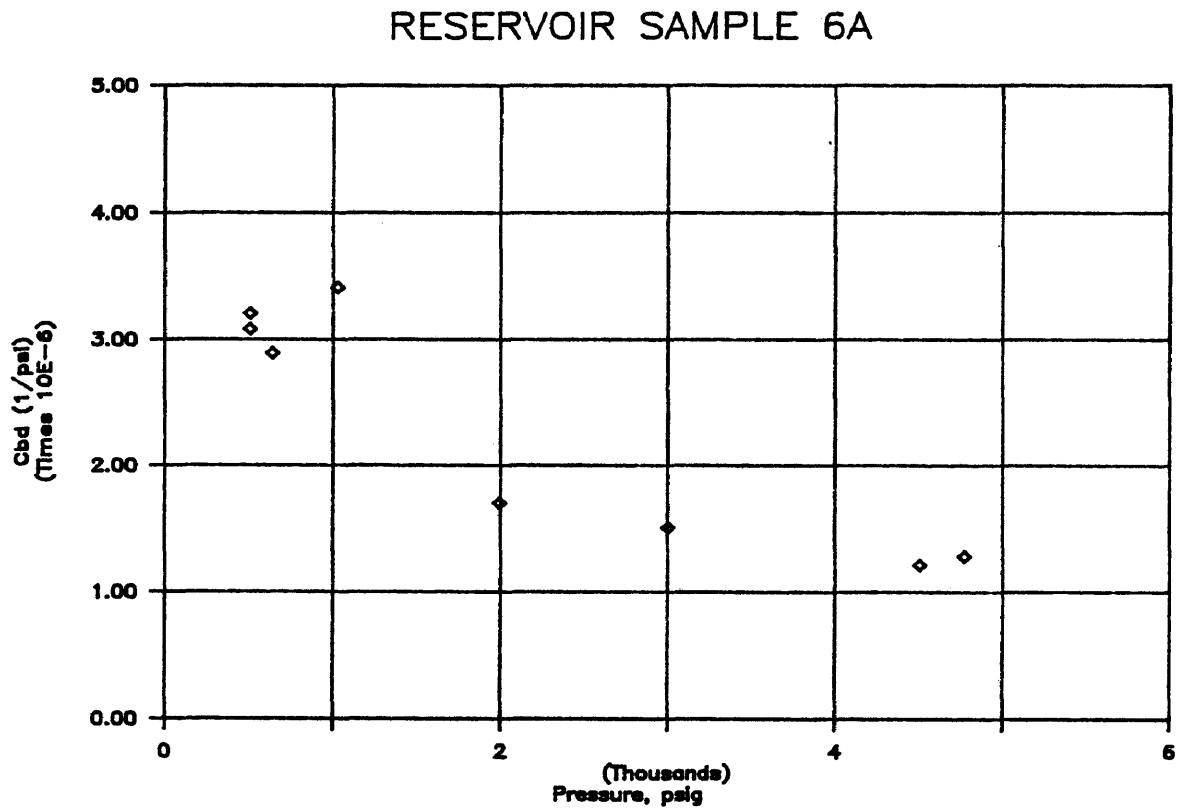
Figure B.52. Dynamic bulk compressibility versus pressure.

RESERVOIR SAMPLE 7A
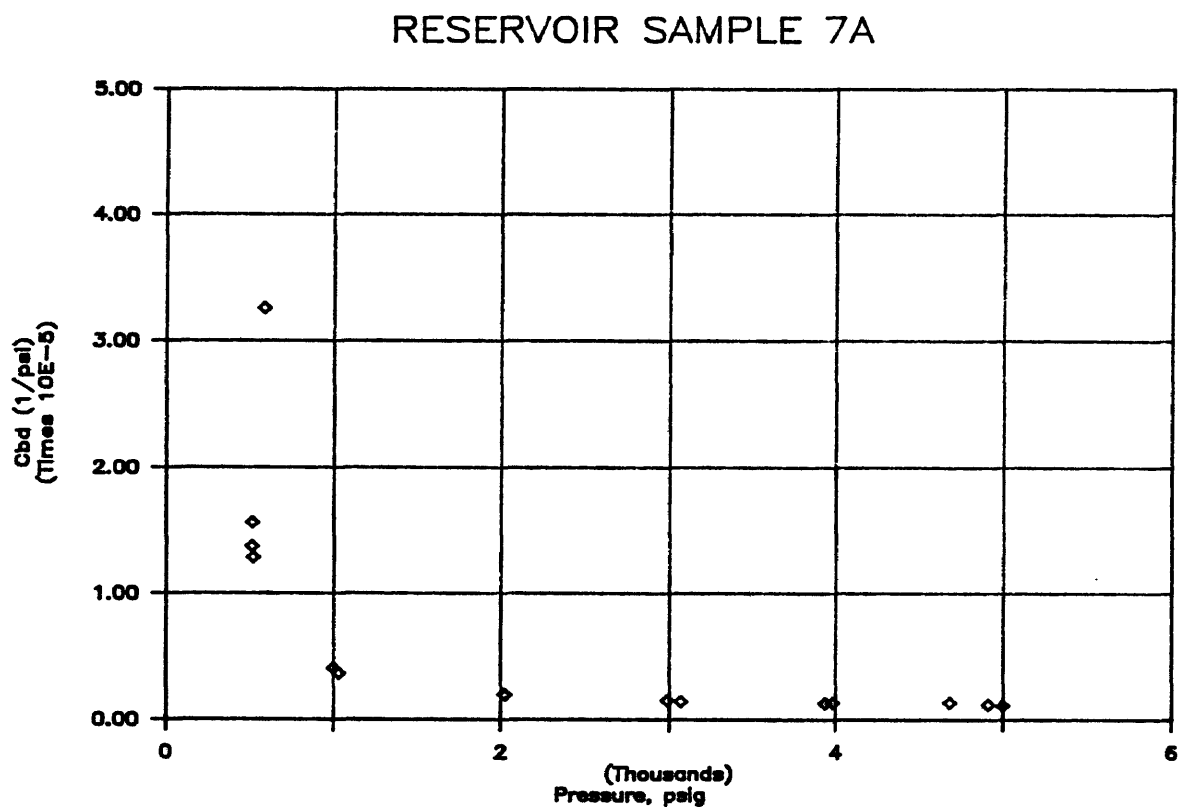
Figure B.53.   Dynamic bulk compressibility versus pressure.

RESERVOIR SAMPLE 8A
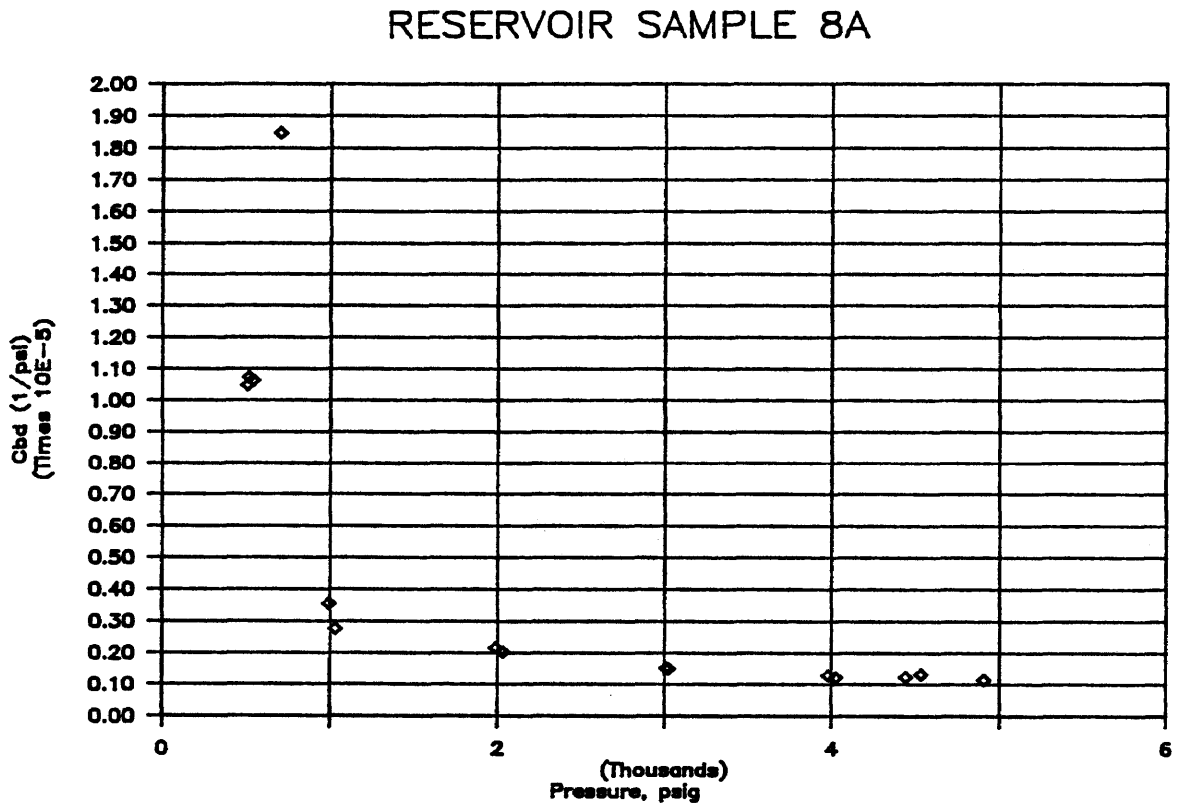
Figure B.54. Dynamic bulk compressibility versus pressure.

MONTMAYEUR STD2
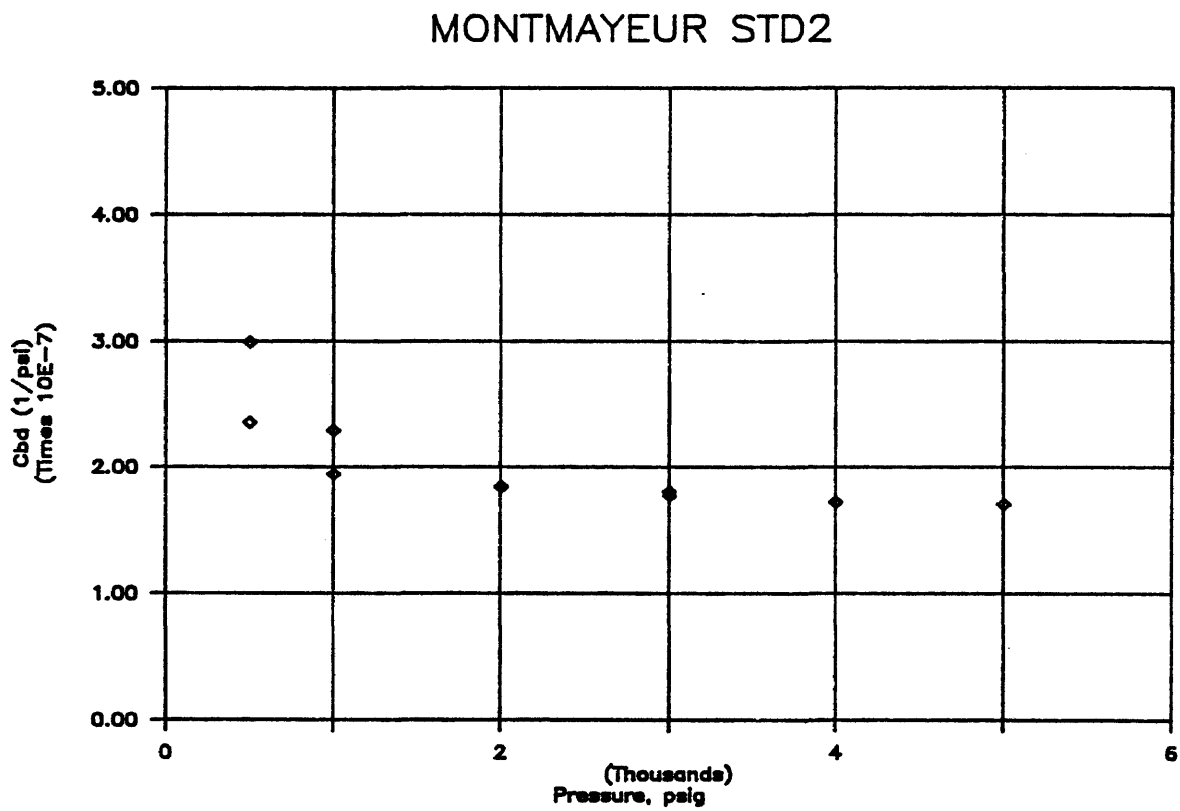
Figure B.55. Dynamic bulk compressibility versus pressure.

MONTMAYEUR STB5
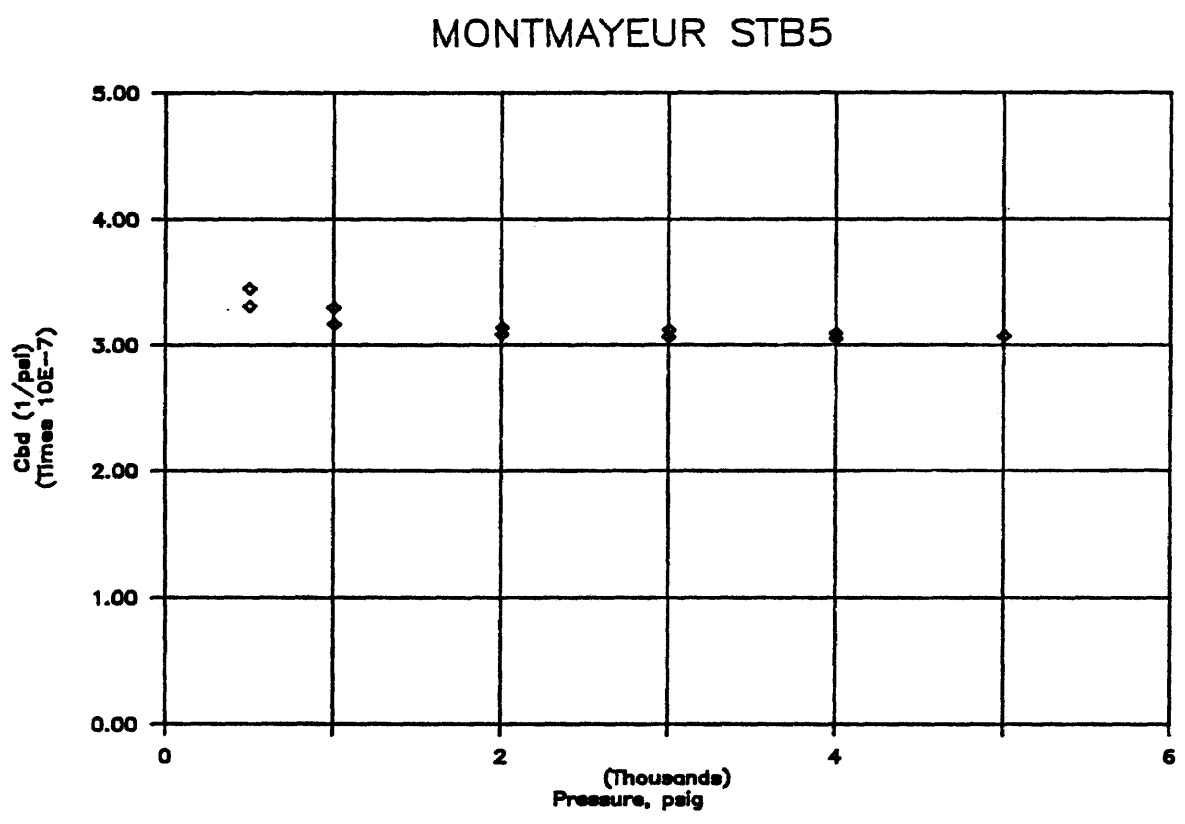
Figure B.56. Dynamic bulk compressibility versus pressure.
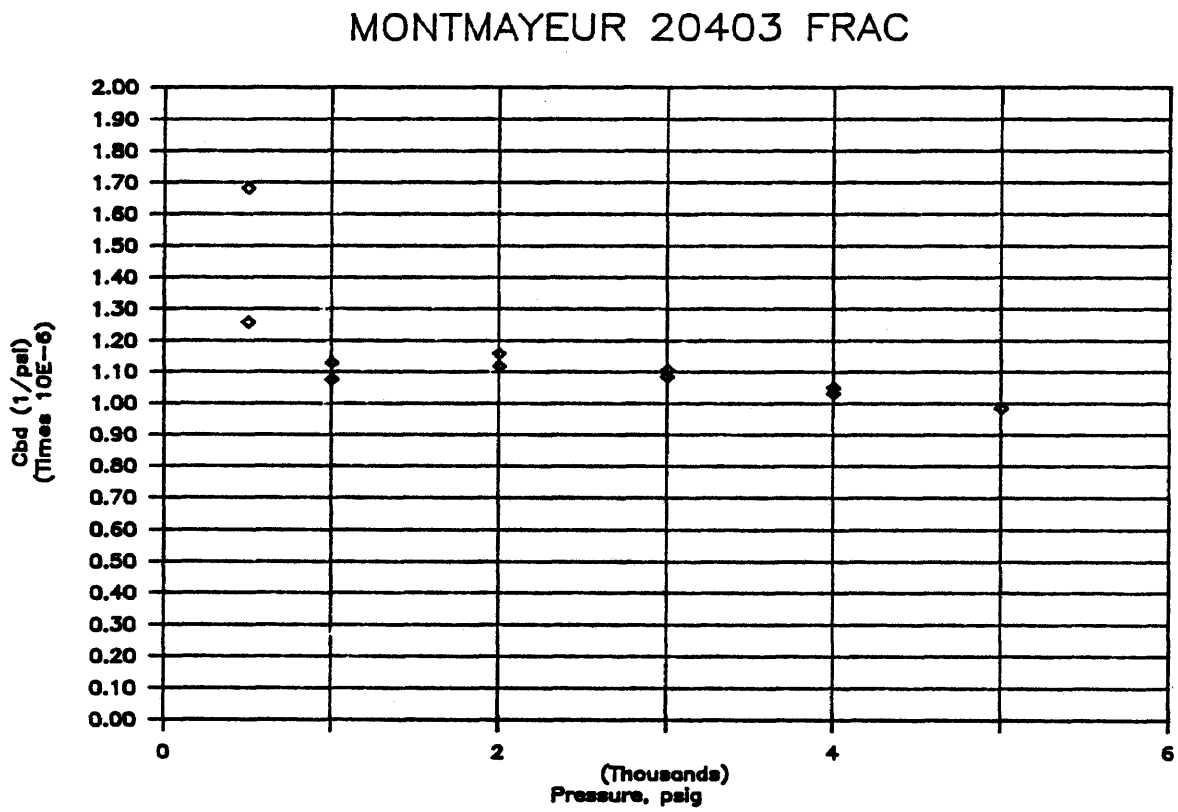
Figure B.57. Dynamic bulk compressibility versus pressure.
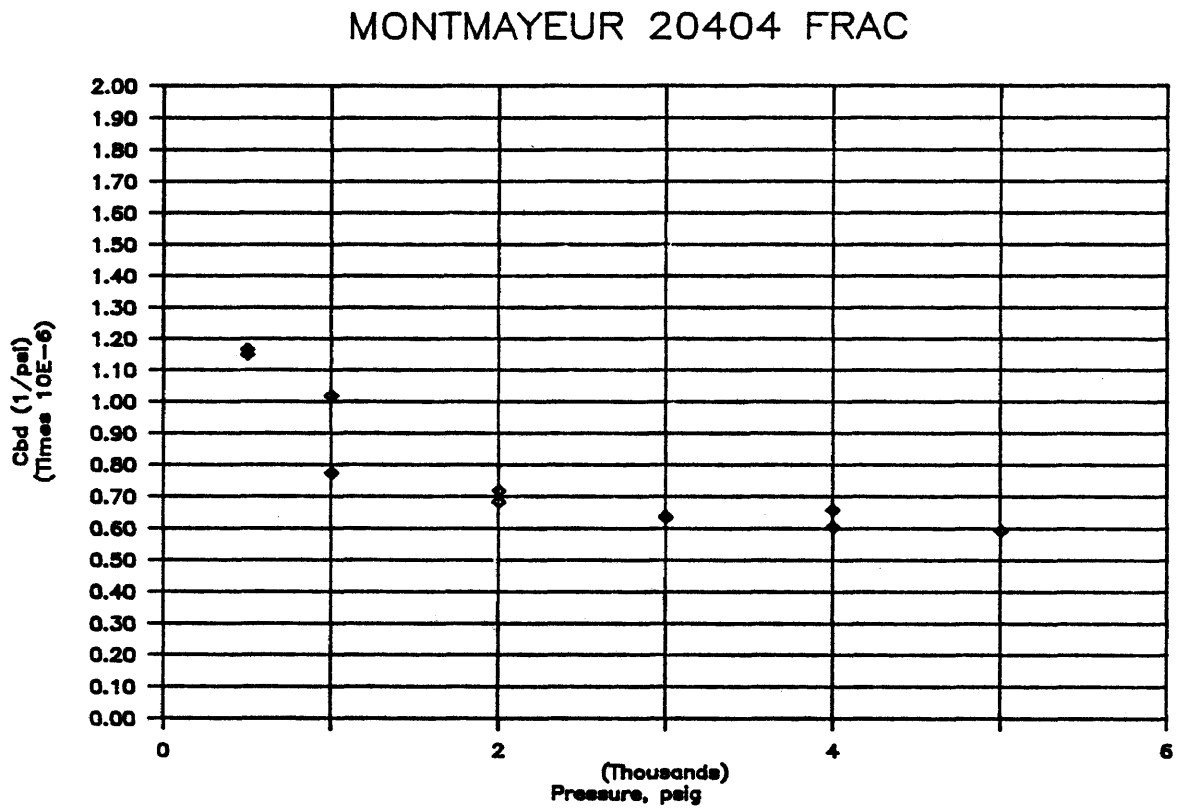
Figure B.58. Dynamic bulk compressibility versus pressure.

MONTMAYEUR 4060 FRAC
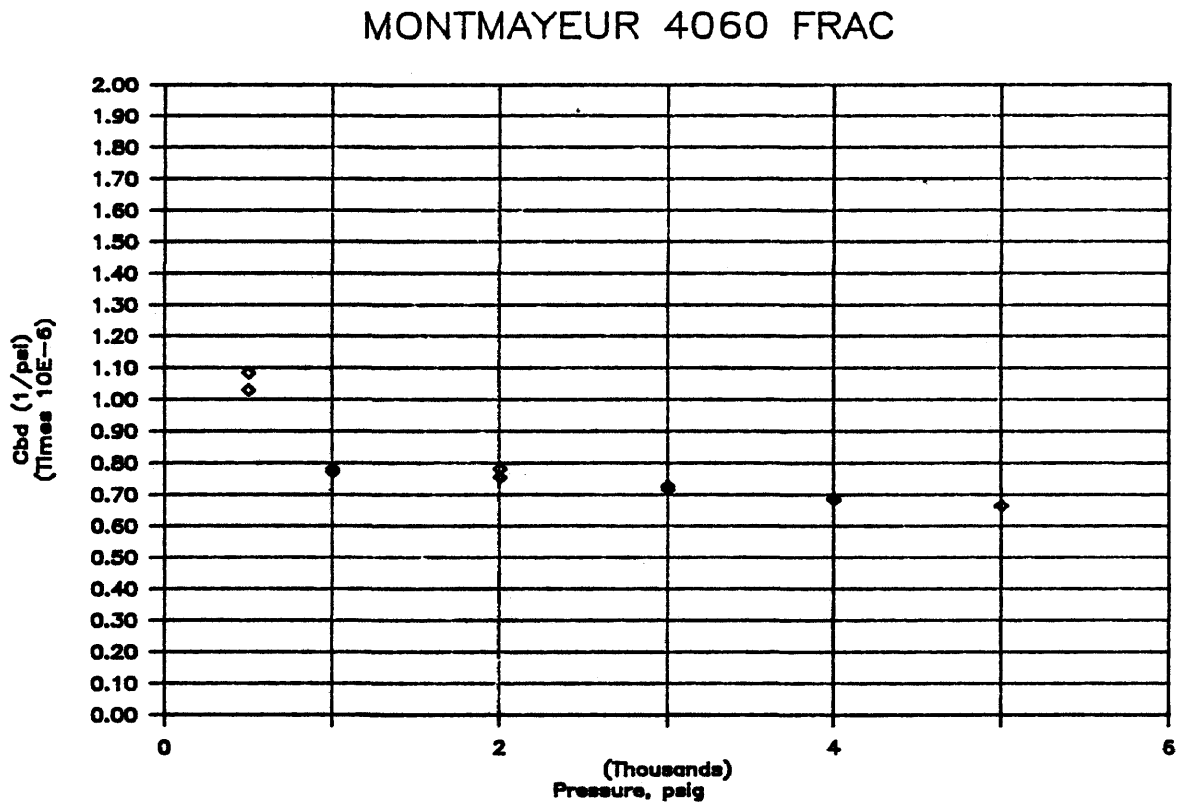
Figure B.59.   Dynamic bulk compressibility versus pressure.

MONTMAYEUR 6080 FRAC
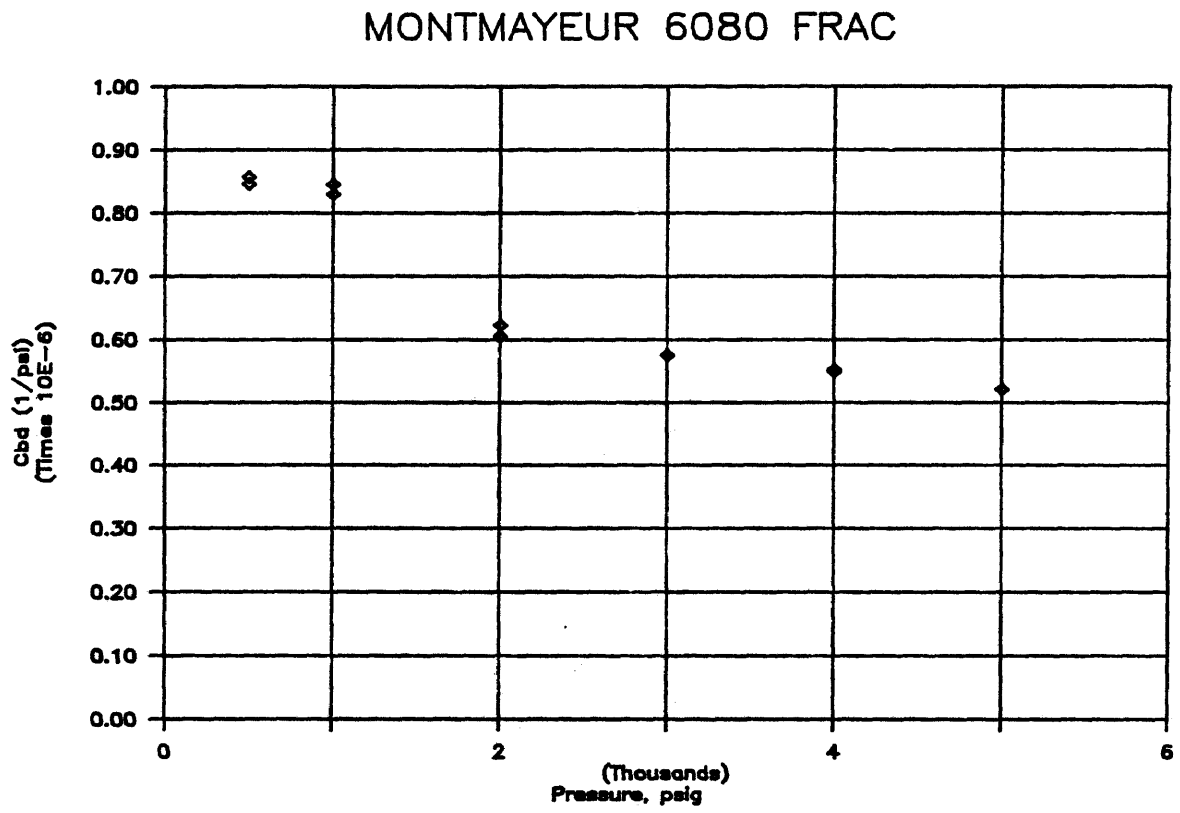
Figure B.60.   Dynamic bulk compressibility versus pressure.

MONTMAYEUR 8010 FRAC
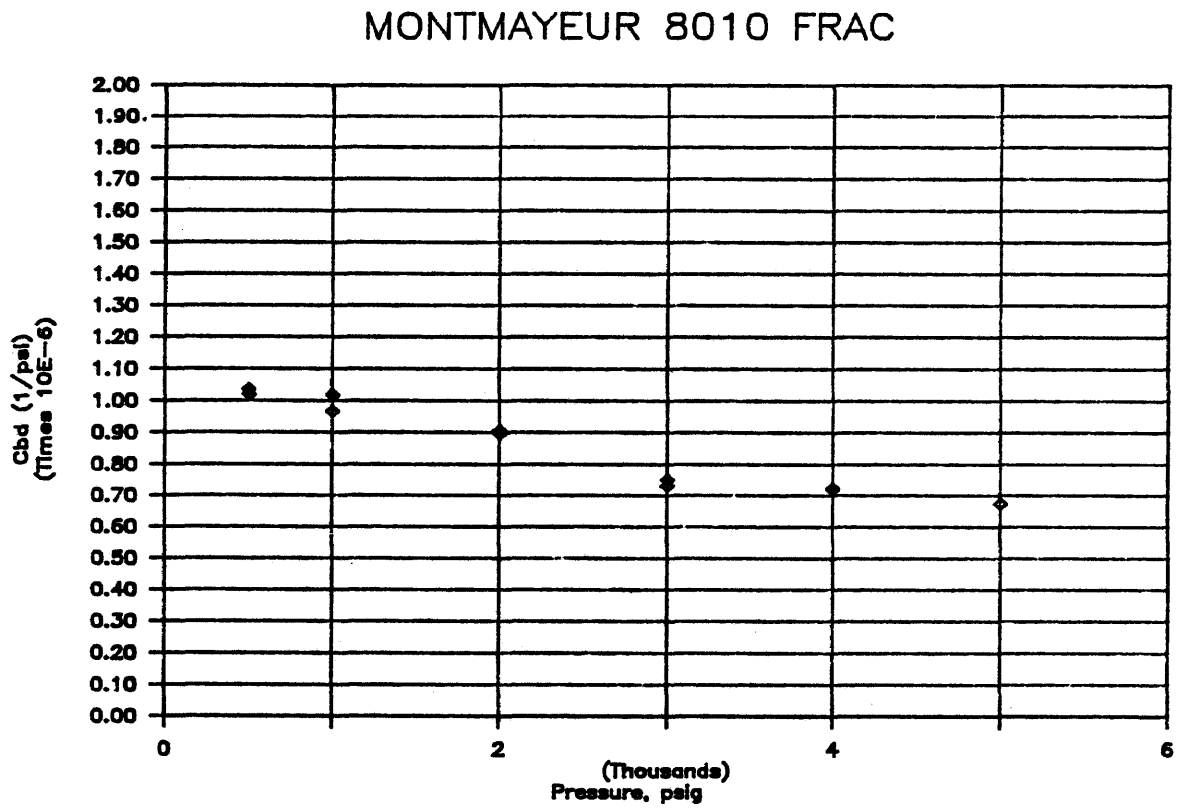
Figure B.61. Dynamic bulk compressibility versus pressure.

MONTMAYEUR 1012 FRAC
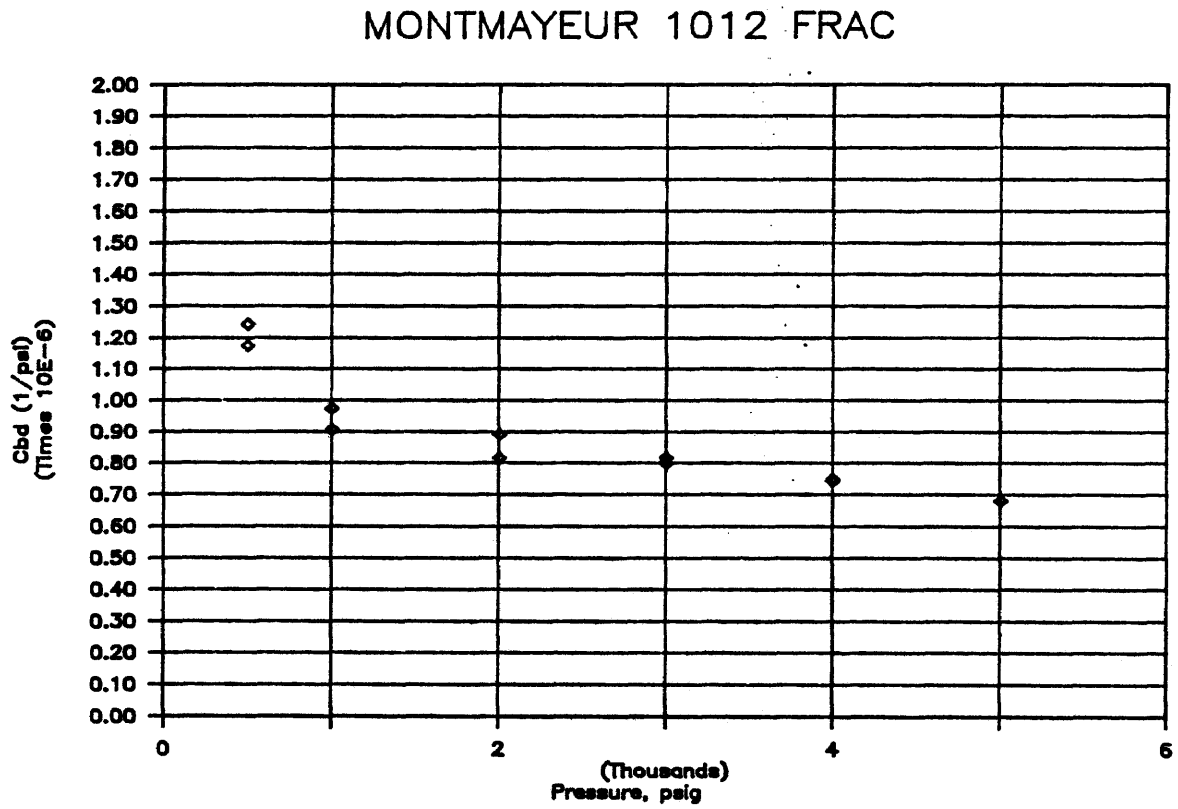
Figure B.62. Dynamic bulk compressibility versus pressure.

MONTMAYEUR 1217 FRAC
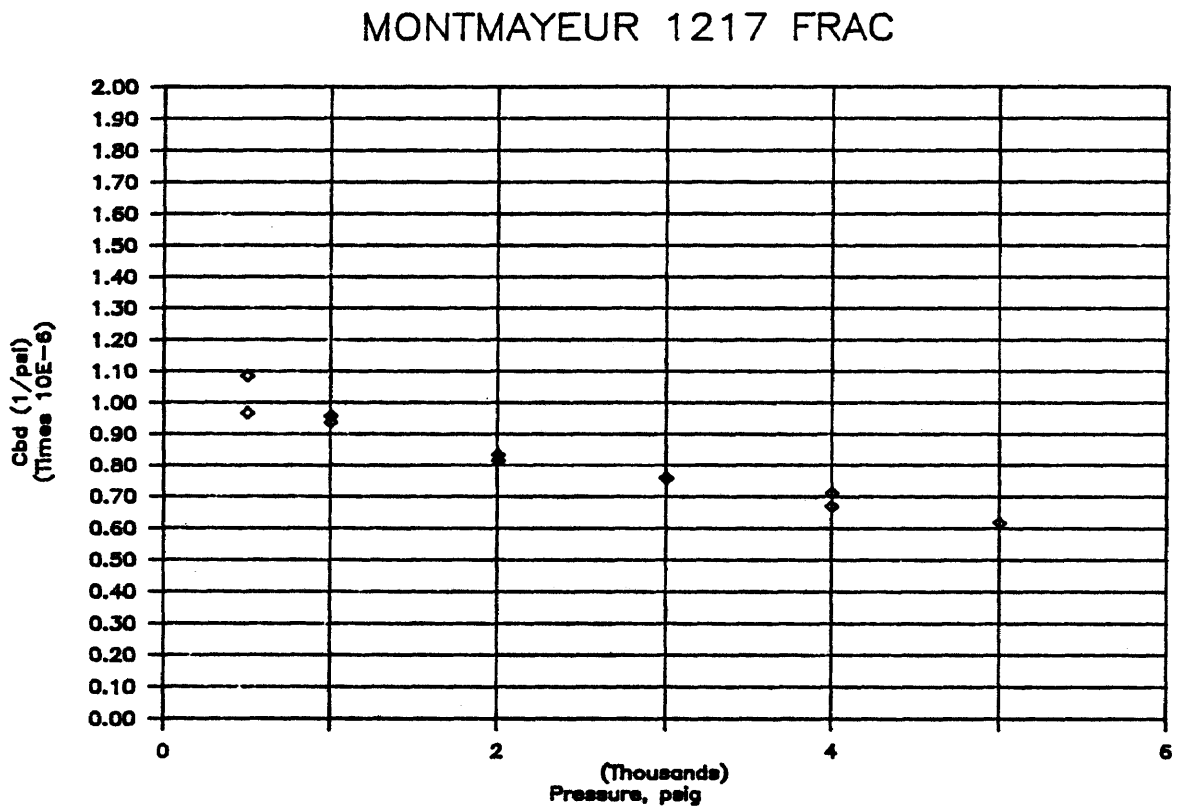
Figure B.63. Dynamic bulk compressibility versus pressure.

MONTMAYEUR 1720 FRAC
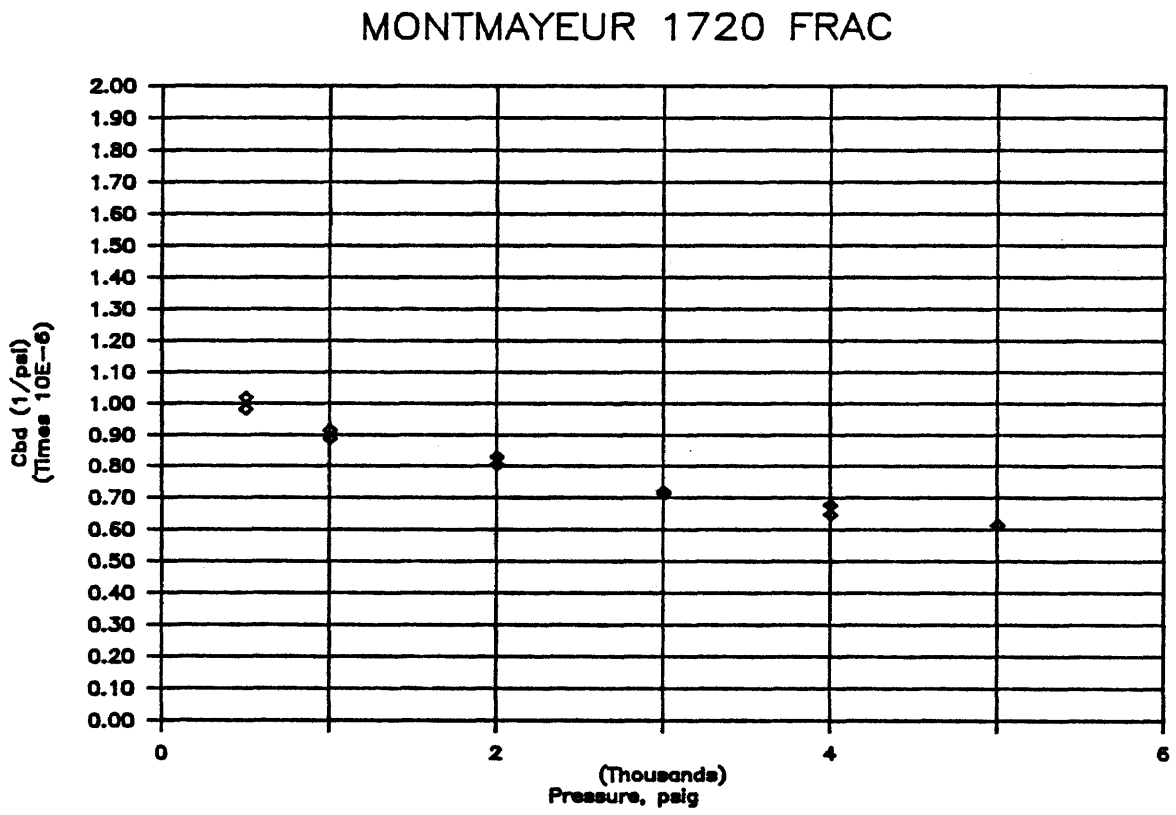
Figure B.64.   Dynamic bulk compressibility versus pressure.
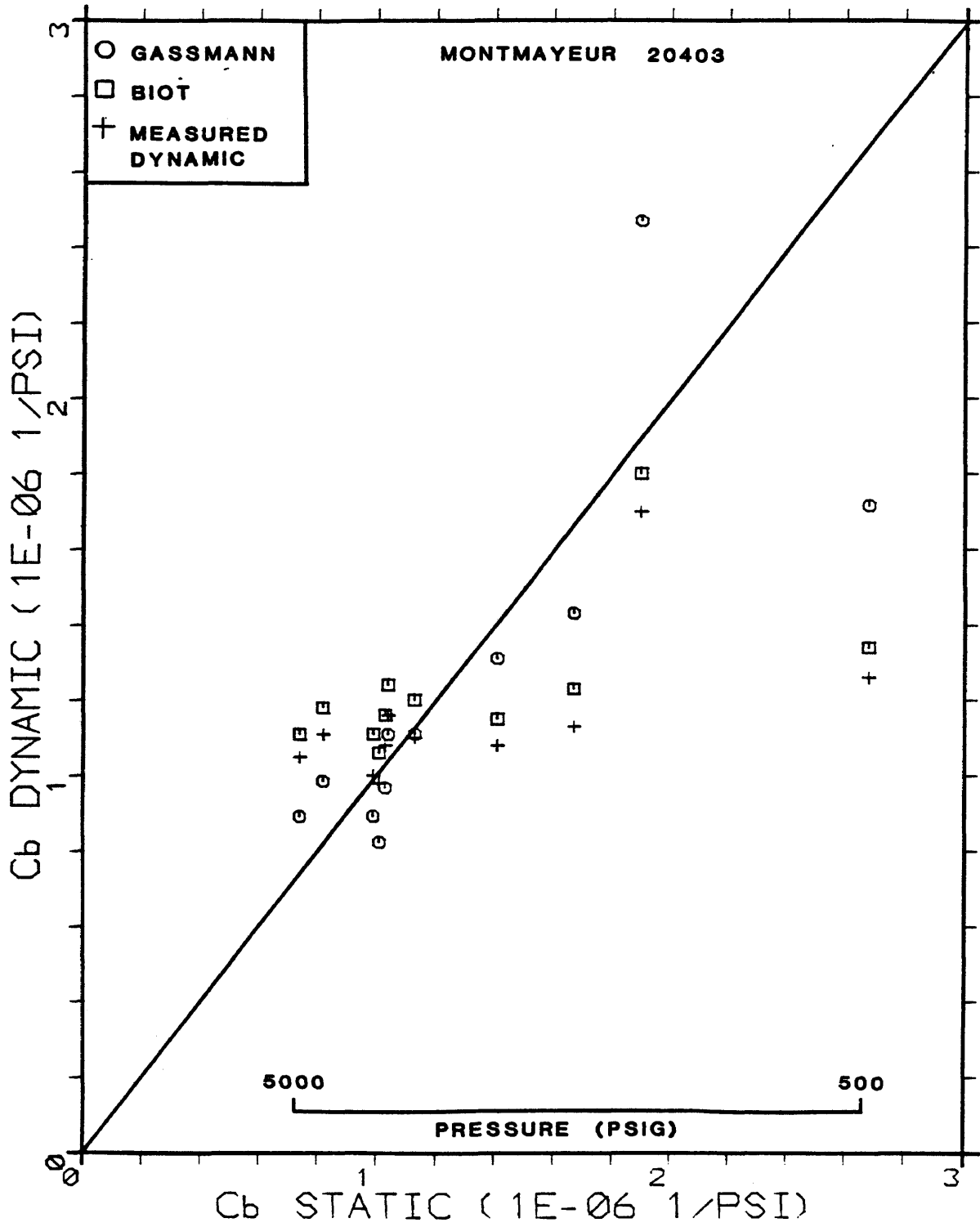
Figure B.65.   Bulk compressibility crossplot.
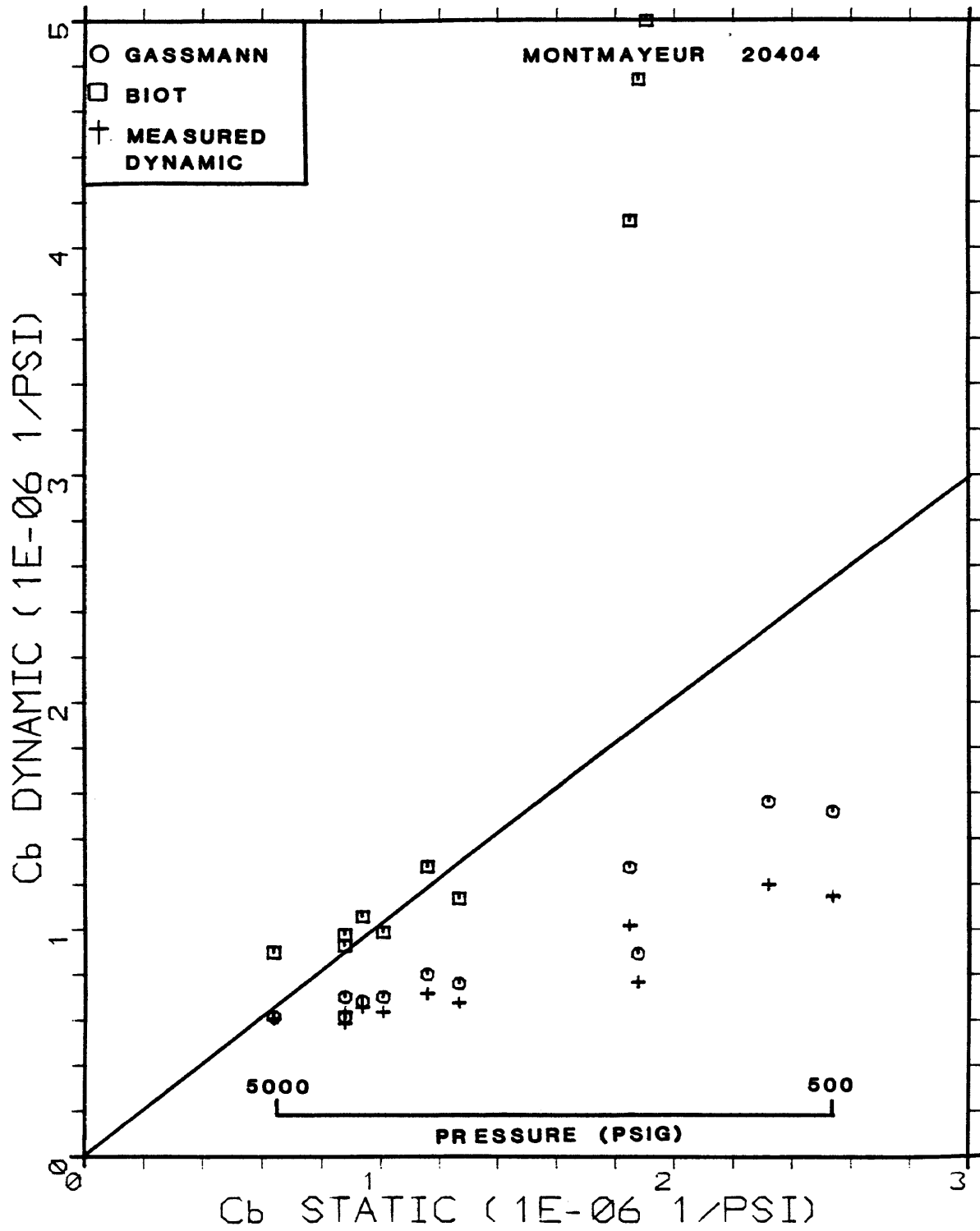
Figure B.66.   Bulk compressibility crossplot.
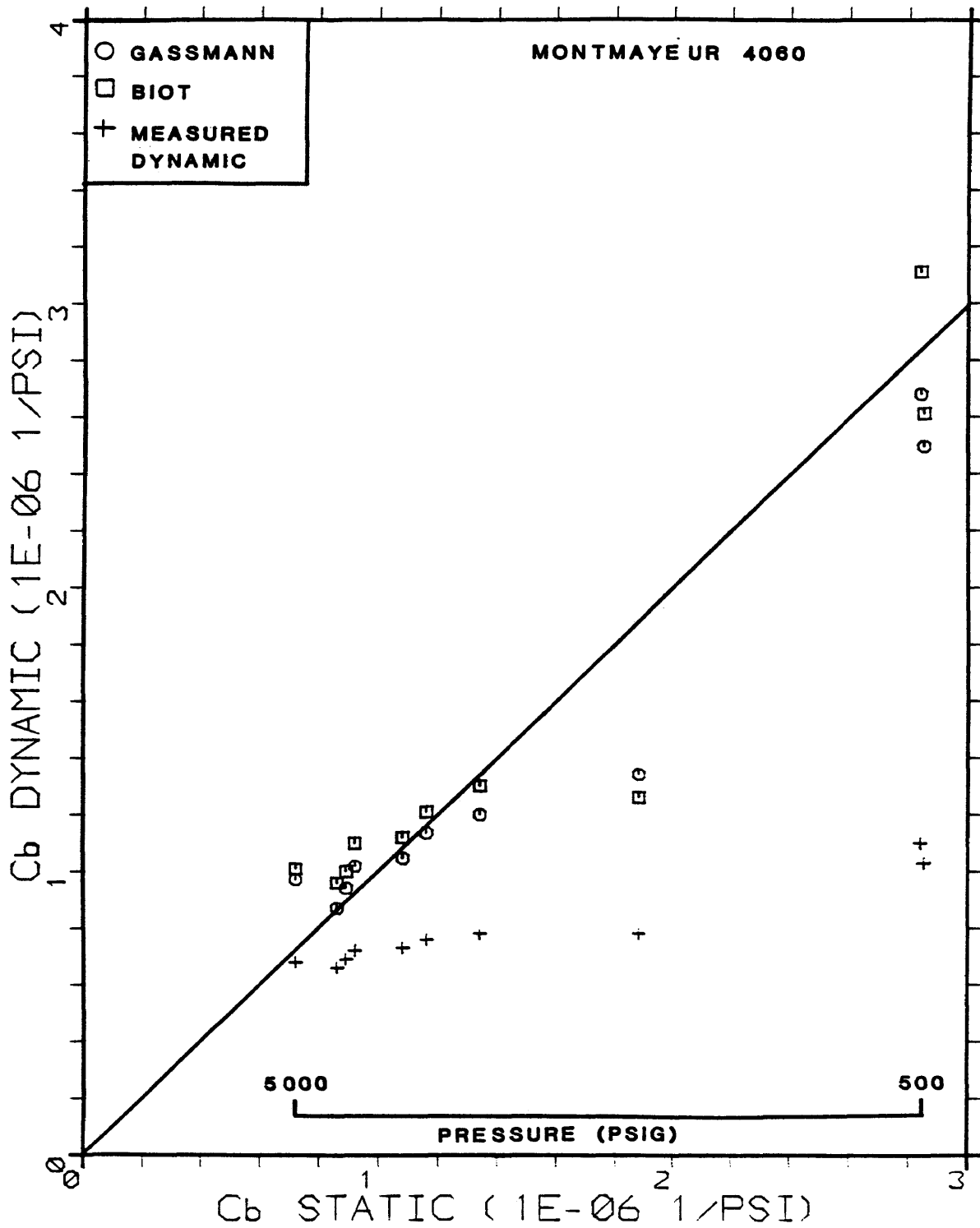
Figure B.67.   Bulk compressibility crossplot.
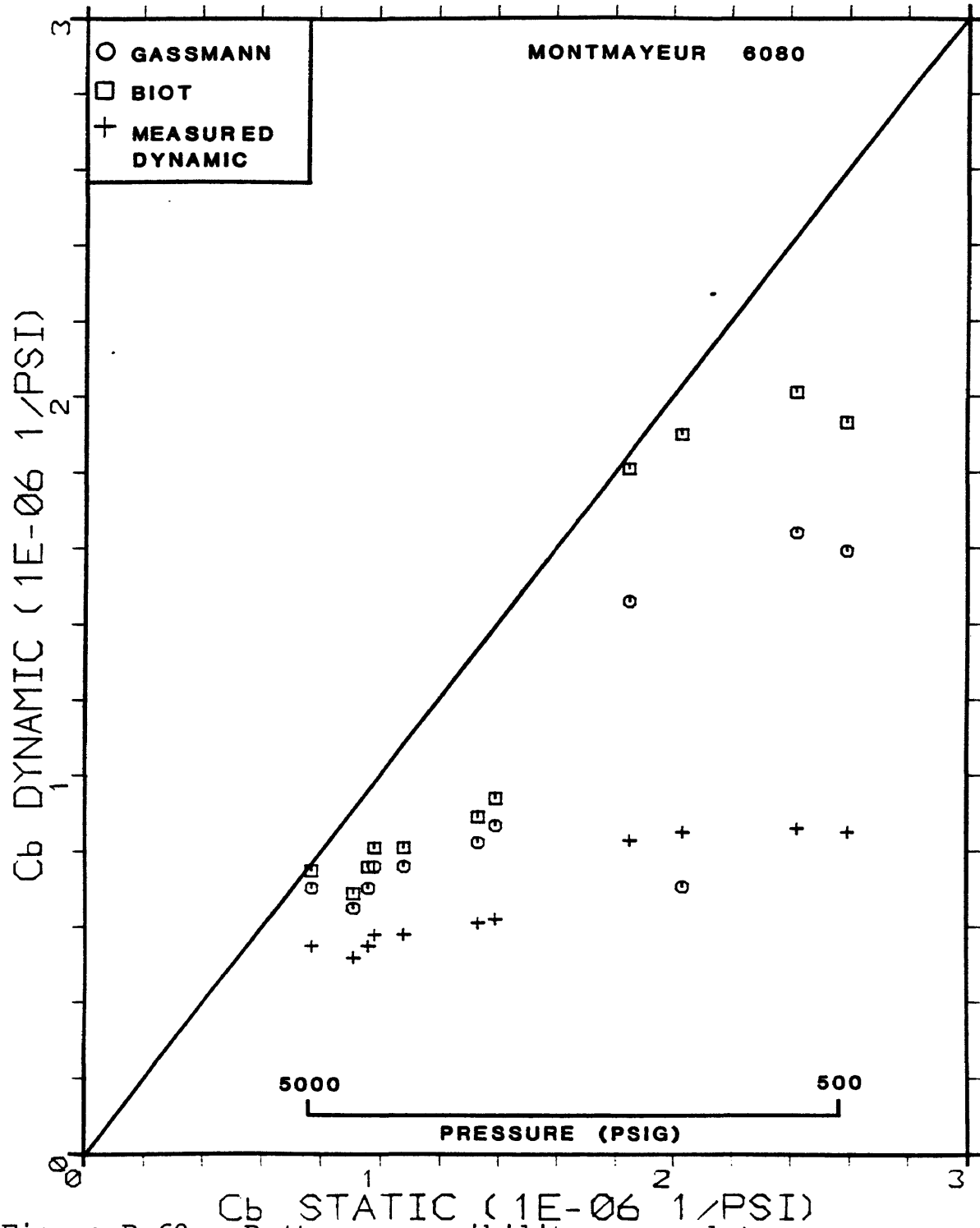
Figure B.68.   Bulk compressibility crossplot.
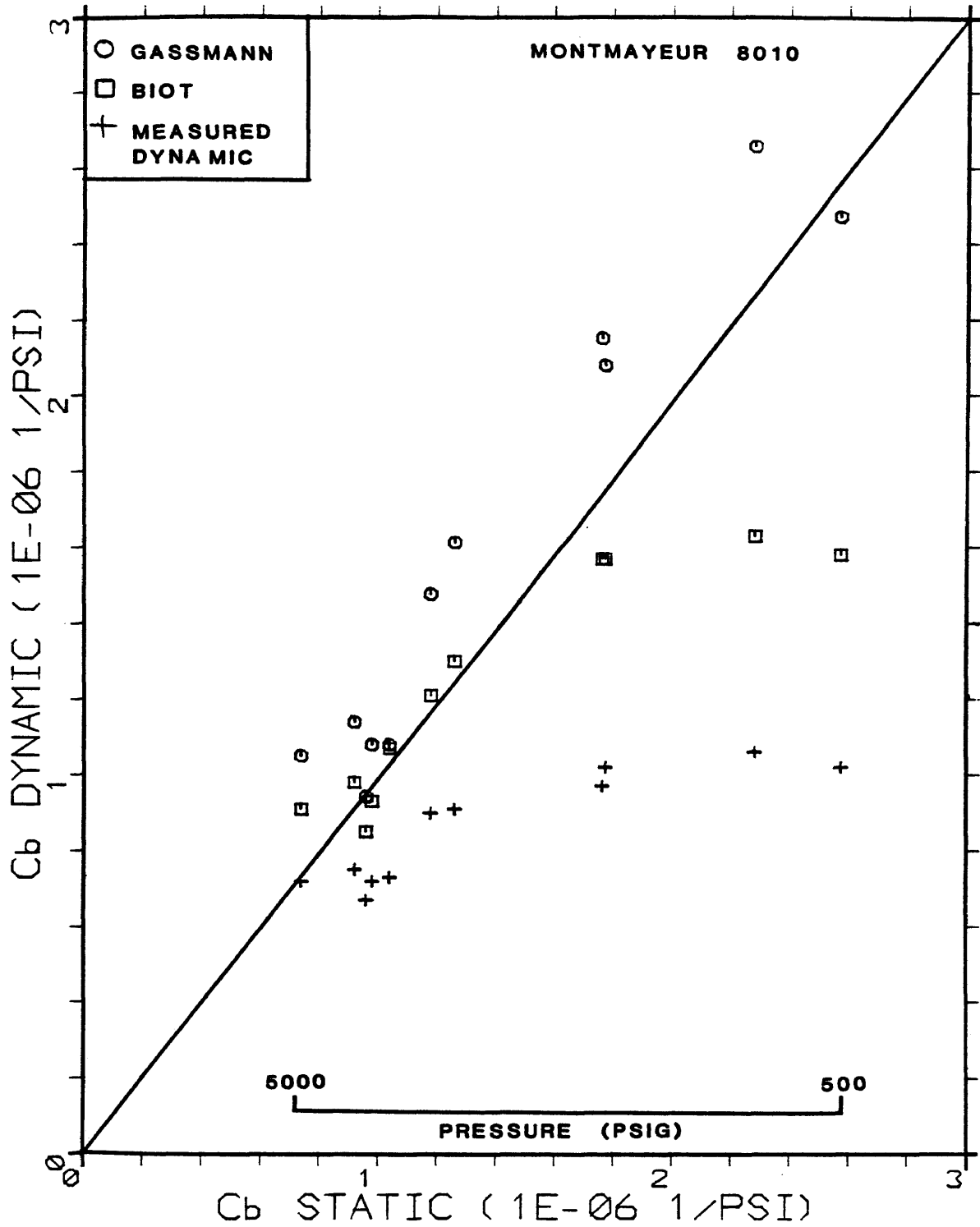
Figure B.69.   Bulk compressibility crossplot.
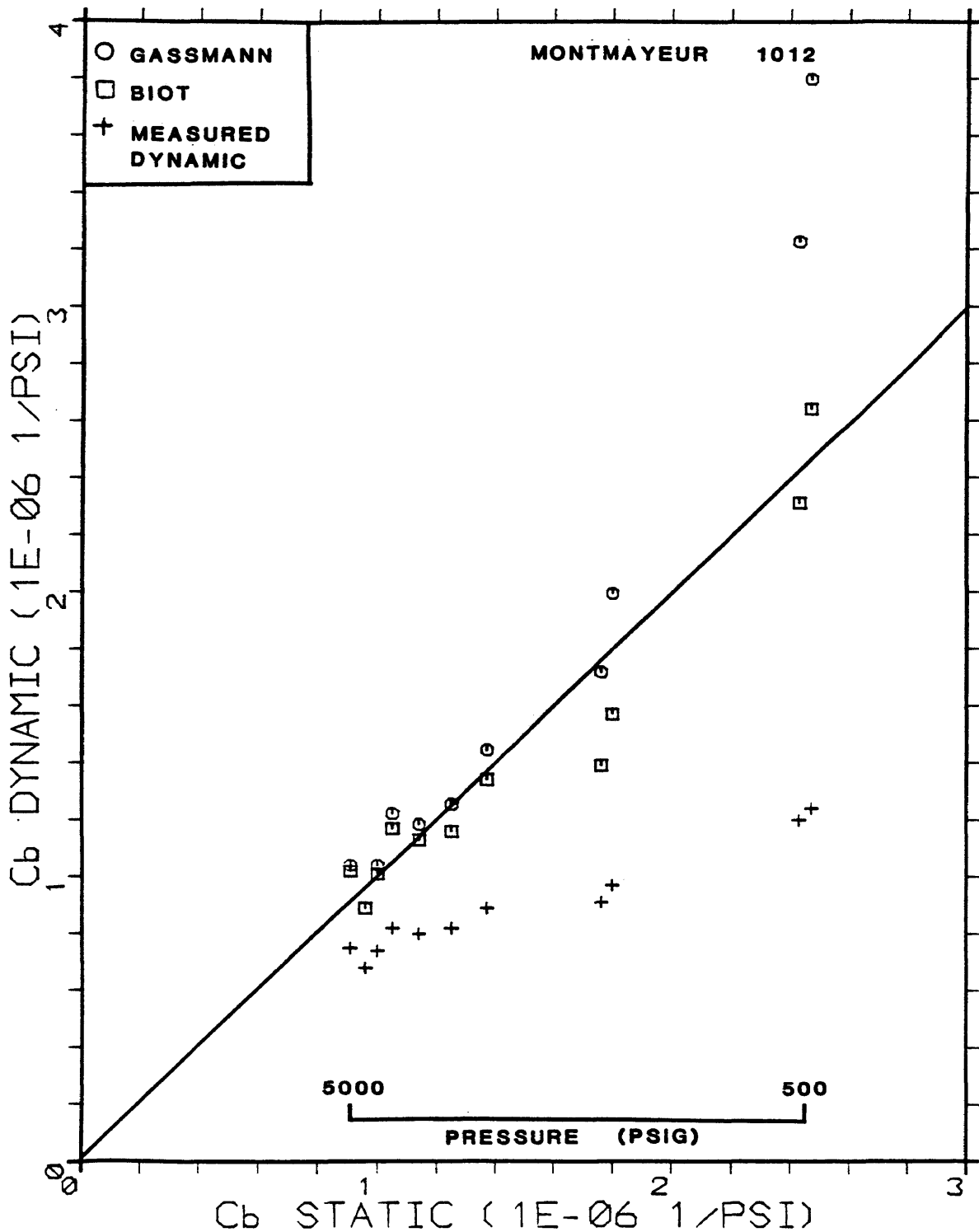
Figure B.70. Bulk compressibility crossplot.
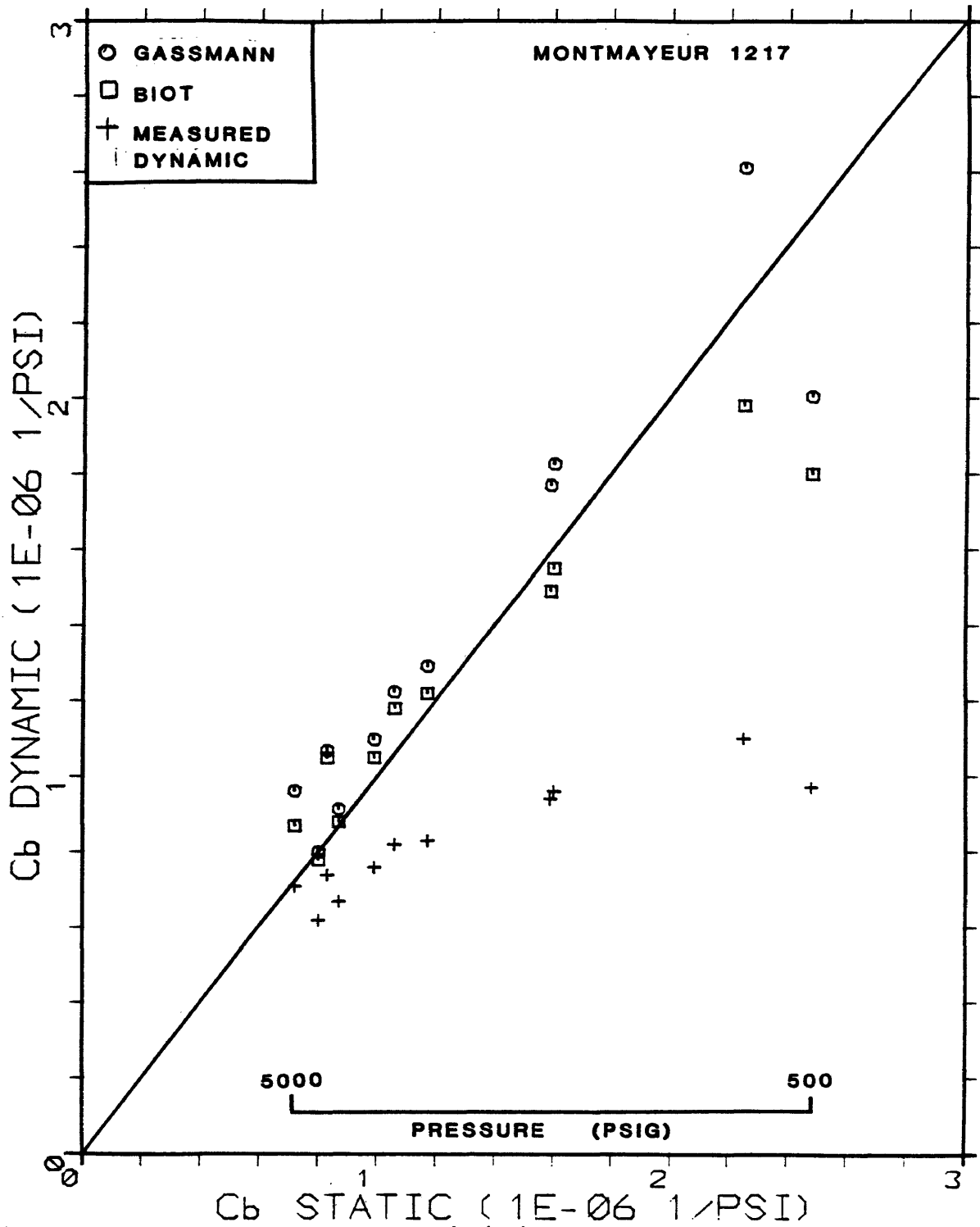
Figure B.71. Bulk compressibility crossplot.
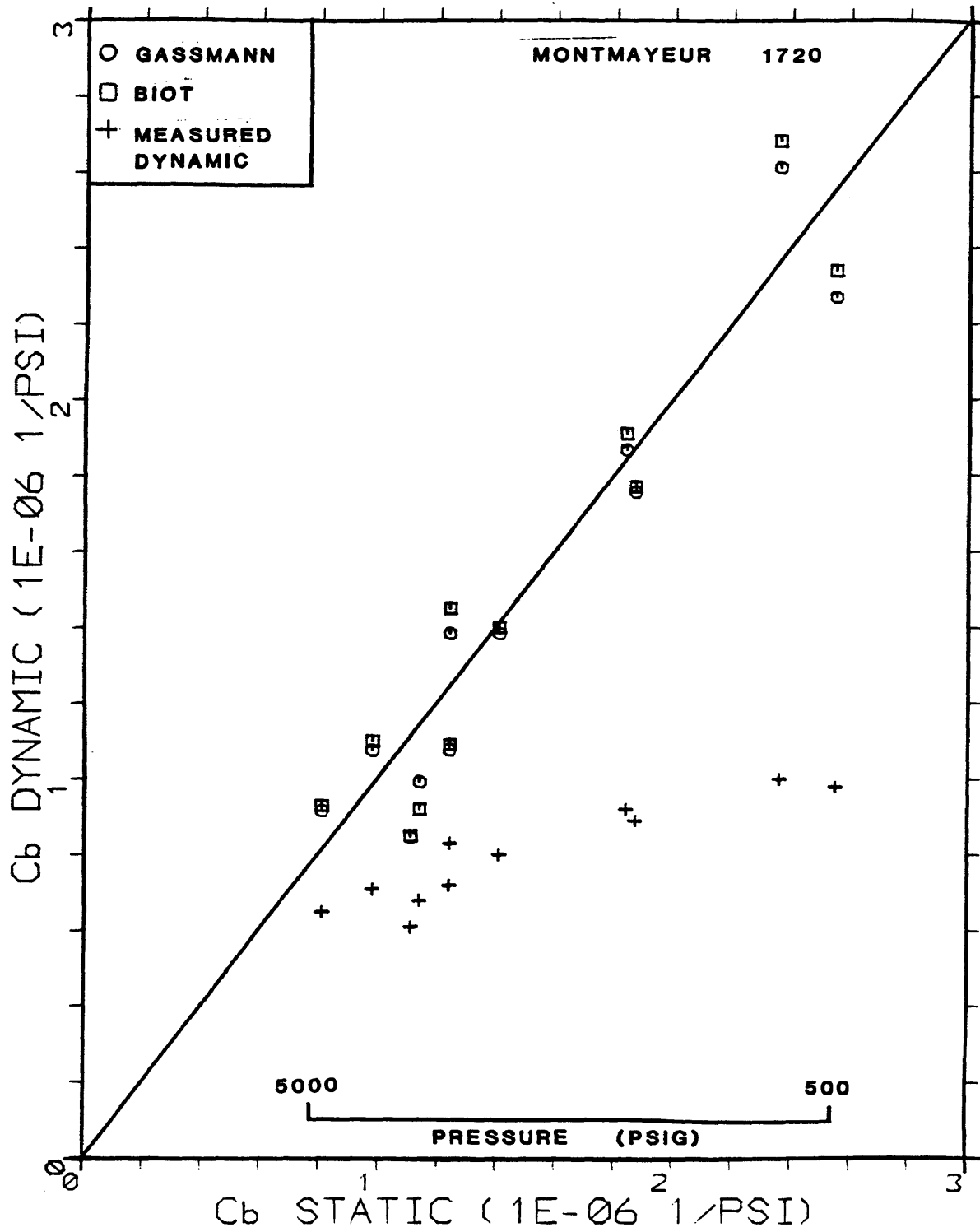
Figure B.72. Bulk compressibility crossplot.

Table B.1.
Raw Dynamic Core Data

Core Name   :Howarth STD2
Core Length   : 0.0861 ft
Core Density   : 2.4650 gm/cc

	Not Corrected*		Corrected								
Pressure	tp	ts	tpc	tsc	Vp	Vs	G	L+2G	L	Cb	G/Cb
psig	usec	usec	usec	usec	usec/ft	usec/ft	psi	psi	psi	psi^-1	psi^2
544	14.50	31.70	5.84	15.86	67.81	184.16	9.74E+05	7.18E+06	5.24E+06	1.70E-07	5.7E+12
4,487	14.10	29.90	5.44	14.06	63.17	163.26	1.24E+06	8.28E+06	5.80E+06	1.51E-07	8.2E+12
621	14.50	31.45	5.84	15.61	67.81	181.25	1.01E+06	7.18E+06	5.17E+06	1.71E-07	5.9E+12
4,376	14.10	29.90	5.44	14.06	63.17	163.26	1.24E+06	8.28E+06	5.80E+06	1.51E-07	8.2E+12
644	14.40	31.55	5.74	15.71	66.65	182.42	9.93E+05	7.44E+06	5.45E+06	1.64E-07	6.1E+12
1,088	14.35	31.30	5.69	15.46	66.07	179.51	1.03E+06	7.57E+06	5.52E+06	1.61E-07	6.4E+12
1,902	14.25	30.50	5.59	14.66	64.91	170.22	1.14E+06	7.84E+06	5.56E+06	1.58E-07	7.2E+12
3,092	14.20	29.95	5.54	14.11	64.33	163.84	1.23E+06	7.98E+06	5.52E+06	1.58E-07	7.8E+12
4,057	14.15	28.90	5.49	13.06	63.75	151.65	1.44E+06	8.13E+06	5.26E+06	1.61E-07	8.9E+12
4,766	14.10	29.90	5.44	14.06	63.17	163.26	1.24E+06	8.28E+06	5.80E+06	1.51E-07	8.2E+12
4,153	14.20	31.95	5.54	16.11	64.33	187.06	9.44E+05	7.98E+06	6.09E+06	1.49E-07	6.3E+12
3,169	14.30	32.30	5.64	16.46	65.49	191.12	9.04E+05	7.70E+06	5.89E+06	1.54E-07	5.9E+12
2,267	14.40	32.50	5.74	16.66	66.65	193.45	8.83E+05	7.44E+06	5.67E+06	1.60E-07	5.5E+12
1,120	14.55	32.60	5.89	16.76	68.39	194.61	8.72E+05	7.06E+06	5.32E+06	1.70E-07	5.1E+12
632	14.55	33.00	5.89	17.16	68.39	199.25	8.32E+05	7.06E+06	5.40E+06	1.68E-07	5.0E+12

* Not corrected for travel time through heads

Table B.2.
Raw Dynamic Core Data

Core Name   : Howarth STB5
Core Length   : 0.1052 ft
Core Density : 2.3335 gm/cc

	Not Corrected*		Corrected								
Pressure	tp	ts	tpc	tsc	Vp	Vs	G	L+2G	L	Cb	G/Cb
psig	usec	usec	usec	usec	usec/ft	usec/ft	psi	psi	psi	psi^-1	psi^2
603	17.25	34.60	8.59	18.76	81.69	178.41	9.82E+05	4.69E+06	2.72E+06	2.96E-07	3.3E+12
4,816	16.70	32.00	8.04	16.16	76.46	153.68	1.32E+06	5.35E+06	2.70E+06	2.79E-07	4.7E+12
569	17.15	34.20	8.49	18.36	80.74	174.61	1.03E+06	4.80E+06	2.75E+06	2.92E-07	3.5E+12
4,810	16.60	32.05	7.94	16.21	75.51	154.16	1.32E+06	5.48E+06	2.85E+06	2.68E-07	4.9E+12
579	17.25	34.20	8.59	18.36	81.69	174.61	1.03E+06	4.69E+06	2.63E+06	3.01E-07	3.4E+12
1,127	17.05	34.15	8.39	18.31	79.79	174.13	1.03E+06	4.91E+06	2.85E+06	2.83E-07	3.6E+12
2,031	17.00	33.05	8.34	17.21	79.31	163.67	1.17E+06	4.97E+06	2.64E+06	2.93E-07	4.0E+12
3,129	16.85	32.60	8.19	16.76	77.89	159.39	1.23E+06	5.15E+06	2.69E+06	2.85E-07	4.3E+12
3,996	16.75	32.30	8.09	16.46	76.94	156.54	1.28E+06	5.28E+06	2.73E+06	2.79E-07	4.6E+12
5,008	16.65	32.00	7.99	16.16	75.99	153.68	1.32E+06	5.42E+06	2.77E+06	2.74E-07	4.8E+12
4,044	16.75	32.15	8.09	16.31	76.94	155.11	1.30E+06	5.28E+06	2.68E+06	2.82E-07	4.6E+12
3,110	16.85	32.25	8.19	16.41	77.89	156.06	1.28E+06	5.15E+06	2.59E+06	2.90E-07	4.4E+12
2,114	16.95	32.80	8.29	16.96	78.84	161.29	1.20E+06	5.03E+06	2.63E+06	2.92E-07	4.1E+12
1,048	17.05	33.50	8.39	17.66	79.79	167.95	1.11E+06	4.91E+06	2.69E+06	2.91E-07	3.8E+12
582	17.20	33.85	8.54	18.01	81.22	171.28	1.07E+06	4.74E+06	2.61E+06	3.01E-07	3.5E+12

* Not corrected for travel time through heads

Table B.3.
Raw Dynamic Core Data

Core Name   : HCB5
Core Length   : 0.1195 ft
Core Density   : 2.2823 gm/cc

	Not Corrected*		Corrected								
Pressure	tp	ts	tpc	tsc	Vp	Vs	G	L+2G	L	Cb	G/Cb
psig	usec	usec	usec	usec	usec/ft	usec/ft	psi	psi	psi	psi^-1	psi^2
659	19.10	36.85	10.44	21.01	87.33	175.75	9.90E+05	4.01E+06	2.03E+06	3.72E-07	2.7E+12
4,656	18.00	34.20	9.34	18.36	78.13	153.58	1.30E+06	5.01E+06	2.42E+06	3.05E-07	4.3E+12
624	19.10	36.85	10.44	21.01	87.33	175.75	9.90E+05	4.01E+06	2.03E+06	3.72E-07	2.7E+12
4,584	18.15	34.20	9.49	18.36	79.38	153.58	1.30E+06	4.85E+06	2.26E+06	3.20E-07	4.1E+12
643	19.10	36.85	10.44	21.01	87.33	175.75	9.90E+05	4.01E+06	2.03E+06	3.72E-07	2.7E+12
1,037	19.00	36.50	10.34	20.66	86.49	172.82	1.02E+06	4.09E+06	2.04E+06	3.67E-07	2.8E+12
1,920	18.65	35.20	9.99	19.36	83.57	161.94	1.17E+06	4.38E+06	2.05E+06	3.54E-07	3.3E+12
2,865	18.40	34.55	9.74	18.71	81.47	156.51	1.25E+06	4.61E+06	2.11E+06	3.40E-07	3.7E+12
3,666	18.20	34.30	9.54	18.46	79.80	154.42	1.28E+06	4.80E+06	2.24E+06	3.23E-07	4.0E+12
4,626	18.15	34.20	9.49	18.36	79.38	153.58	1.30E+06	4.85E+06	2.26E+06	3.20E-07	4.1E+12
4,052	18.25	34.25	9.59	18.41	80.22	154.00	1.29E+06	4.75E+06	2.17E+06	3.30E-07	3.9E+12
3,160	18.45	35.15	9.79	19.31	81.89	161.53	1.17E+06	4.56E+06	2.22E+06	3.34E-07	3.5E+12
2,139	18.55	35.63	9.89	19.79	82.73	165.54	1.12E+06	4.47E+06	2.24E+06	3.36E-07	3.3E+12
1,109	19.05	36.30	10.39	20.46	86.91	171.15	1.04E+06	4.05E+06	1.96E+06	3.76E-07	2.8E+12
652	19.15	37.30	10.49	21.46	87.75	179.51	9.49E+05	3.97E+06	2.07E+06	3.69E-07	2.6E+12

* Not corrected for travel time through heads

Table B.4.
Raw Dynamic Core Data

Core Name   :HCB11
Core Length   : 0.1177 ft
Core Density   : 2.2816 gm/cc

| Pressure | Not Corrected* | | Corrected | | Vp | Vs | G | L+2G | L | Cb | G/Cb |
| | tp | ts | tpc | tsc | | | | | | | |
psig	usec	usec	usec	usec	usec/ft	usec/ft	psi	psi	psi	psi^-1	psi^2
5,057	18.10	38.15	9.44	22.31	80.22	189.58	8.51E+05	4.75E+06	3.05E+06	2.76E-07	3.1E+12
661	19.10	39.30	10.44	23.46	88.71	199.35	7.69E+05	3.88E+06	2.35E+06	3.50E-07	2.2E+12
5,126	18.05	38.15	9.39	22.31	79.79	189.58	8.51E+05	4.80E+06	3.10E+06	2.73E-07	3.1E+12
562	19.10	39.30	10.44	23.46	88.71	199.35	7.69E+05	3.88E+06	2.35E+06	3.50E-07	2.2E+12
1,094	18.95	39.15	10.29	23.31	87.44	198.08	7.79E+05	4.00E+06	2.44E+06	3.38E-07	2.3E+12
2,061	18.55	38.80	9.89	22.96	84.04	195.10	8.03E+05	4.33E+06	2.72E+06	3.07E-07	2.6E+12
3,067	18.30	38.25	9.64	22.41	81.92	190.43	8.43E+05	4.56E+06	2.87E+06	2.91E-07	2.9E+12
4,114	18.20	38.15	9.54	22.31	81.07	189.58	8.51E+05	4.65E+06	2.95E+06	2.84E-07	3.0E+12
5,048	18.05	38.15	9.39	22.31	79.79	189.58	8.51E+05	4.80E+06	3.10E+06	2.73E-07	3.1E+12
4,019	18.20	38.30	9.54	22.46	81.07	190.86	8.39E+05	4.65E+06	2.97E+06	2.83E-07	3.0E+12
3,063	18.25	38.50	9.59	22.66	81.49	192.56	8.25E+05	4.60E+06	2.95E+06	2.85E-07	2.9E+12
2,087	18.35	38.80	9.69	22.96	82.34	195.10	8.03E+05	4.51E+06	2.90E+06	2.91E-07	2.8E+12
1,086	18.85	38.90	10.19	23.06	86.59	195.95	7.96E+05	4.08E+06	2.49E+06	3.32E-07	2.4E+12
595	19.05	39.60	10.39	23.76	88.29	201.90	7.50E+05	3.92E+06	2.42E+06	3.42E-07	2.2E+12

* Not corrected for travel time through heads

Table B.5.
Raw Dynamic Core Data

Core Name   : HCB13
Core Length : 0.1241 ft
Core Density : 2.2739 gm/cc

Pressure psig	Not Corrected* tp usec	ts usec	Corrected tpc usec	tsc usec	Vp usec/ft	Vs usec/ft	G psi	L+2G psi	L psi	Cb psi^-1	G/Cb psi^2
666	19.45	38.35	10.79	22.51	86.98	181.45	9.25E+05	4.03E+06	2.18E+06	3.58E-07	2.6E+12
4,469	18.45	36.70	9.79	20.86	78.92	168.15	1.08E+06	4.89E+06	2.74E+06	2.89E-07	3.7E+12
558	19.25	37.85	10.59	22.01	85.37	177.42	9.68E+05	4.18E+06	2.25E+06	3.46E-07	2.8E+12
4,459	18.60	36.65	9.94	20.81	80.13	167.75	1.08E+06	4.75E+06	2.58E+06	3.03E-07	3.6E+12
594	19.30	37.95	10.64	22.11	85.77	178.23	9.59E+05	4.14E+06	2.22E+06	3.49E-07	2.7E+12
1,133	19.15	37.45	10.49	21.61	84.56	174.20	1.00E+06	4.26E+06	2.25E+06	3.42E-07	2.9E+12
1,855	18.95	37.35	10.29	21.51	82.95	173.39	1.01E+06	4.43E+06	2.40E+06	3.25E-07	3.1E+12
2,771	18.80	36.95	10.14	21.11	81.74	170.17	1.05E+06	4.56E+06	2.46E+06	3.17E-07	3.3E+12
3,962	18.60	36.80	9.94	20.96	80.13	168.96	1.07E+06	4.75E+06	2.61E+06	3.01E-07	3.5E+12
4,560	18.45	36.70	9.79	20.86	78.92	168.15	1.08E+06	4.89E+06	2.74E+06	2.89E-07	3.7E+12
4,039	18.55	36.70	9.89	20.86	79.72	168.15	1.08E+06	4.79E+06	2.64E+06	2.98E-07	3.6E+12
3,101	18.65	36.85	9.99	21.01	80.53	169.36	1.06E+06	4.70E+06	2.57E+06	3.05E-07	3.5E+12
2,100	18.80	37.20	10.14	21.36	81.74	172.18	1.03E+06	4.56E+06	2.51E+06	3.13E-07	3.3E+12
1,049	19.15	37.50	10.49	21.66	84.56	174.60	1.00E+06	4.26E+06	2.26E+06	3.41E-07	2.9E+12
560	19.30	38.05	10.64	22.21	85.77	179.03	9.51E+05	4.14E+06	2.24E+06	3.48E-07	2.7E+12

* Not corrected for travel time through heads

Table B.6.
Raw Dynamic Core Data

Core Name   :G2040A
Core Length   : 0.1143 ft
Core Density : 1.9187 gm/cc

| Pressure | Not Corrected* | | Corrected | | | | | | | | |
| | tp | ts | tpc | tsc | Vp | Vs | G | L+2G | L | Cb | G/Cb |
psig	usec	usec	usec	usec	usec/ft	usec/ft	psi	psi	psi	psi^-1	psi^2
637	27.35	58.70	18.69	42.86	163.46	374.86	1.83E+05	9.62E+05	5.96E+05	1.39E-06	1.3E+11
4,695	25.50	54.90	16.84	39.06	147.28	341.62	2.20E+05	1.19E+06	7.45E+05	1.12E-06	2.0E+11
537	27.55	58.75	18.89	42.91	165.21	375.29	1.83E+05	9.42E+05	5.77E+05	1.43E-06	1.3E+11
4,851	25.45	54.95	16.79	39.11	146.85	342.06	2.20E+05	1.19E+06	7.53E+05	1.11E-06	2.0E+11
524	27.40	58.80	18.74	42.96	163.90	375.73	1.82E+05	9.57E+05	5.93E+05	1.40E-06	1.3E+11
1,005	27.15	58.30	18.49	42.46	161.71	371.36	1.86E+05	9.83E+05	6.10E+05	1.36E-06	1.4E+11
2,013	26.50	57.35	17.84	41.51	156.03	363.05	1.95E+05	1.06E+06	6.66E+05	1.26E-06	1.6E+11
3,009	26.00	56.35	17.34	40.51	151.66	354.30	2.05E+05	1.12E+06	7.08E+05	1.18E-06	1.7E+11
3,997	25.70	55.50	17.04	39.66	149.03	346.87	2.14E+05	1.16E+06	7.30E+05	1.15E-06	1.9E+11
4,929	25.35	54.70	16.69	38.86	145.97	339.87	2.23E+05	1.21E+06	7.61E+05	1.10E-06	2.0E+11
3,991	25.75	55.50	17.09	39.66	149.47	346.87	2.14E+05	1.15E+06	7.23E+05	1.15E-06	1.9E+11
3,031	26.00	56.25	17.34	40.41	151.66	353.43	2.06E+05	1.12E+06	7.06E+05	1.19E-06	1.7E+11
2,020	26.50	57.25	17.84	41.41	156.03	362.17	1.96E+05	1.06E+06	6.64E+05	1.26E-06	1.6E+11
1,035	27.10	58.40	18.44	42.56	161.28	372.23	1.86E+05	9.88E+05	6.17E+05	1.35E-06	1.4E+11
506	27.35	59.60	18.69	43.76	163.46	382.73	1.76E+05	9.62E+05	6.11E+05	1.37E-06	1.3E+11

* Not corrected for travel time through heads

Table B.7.
Raw Dynamic Core Data

Core Name   :G1014A
Core Length   : 0.1143 ft
Core Density   : 1.8937 gm/cc

Pressure psig	Not Corrected* tp usec	ts usec	Corrected tpc usec	tsc usec	Vp usec/ft	Vs usec/ft	G psi	L+2G psi	L psi	Cb psi^-1	G/Cb psi^2
462	0.00	55.40	0.00	39.56	0.00	345.99	2.12E+05	ERR	ERR	ERR	ERR
4,792	32.25	51.75	23.59	35.91	206.32	314.07	2.57E+05	5.96E+05	8.16E+04	3.95E-06	6.5E+10
472	0.00	55.25	0.00	39.41	0.00	344.68	2.14E+05	ERR	ERR	ERR	ERR
4,752	32.30	51.65	23.64	35.81	206.76	313.20	2.59E+05	5.94E+05	7.62E+04	4.02E-06	6.4E+10
524	0.00	55.25	0.00	39.41	0.00	344.68	2.14E+05	ERR	ERR	ERR	ERR
998	44.45	54.75	35.79	38.91	313.02	340.31	2.19E+05	2.59E+05	-1.8E+05	-3.0E-05	-7.3E+09
1,996	36.55	53.80	27.89	37.96	243.93	332.00	2.30E+05	4.26E+05	-3.4E+04	8.37E-06	2.8E+10
2,993	35.20	52.95	26.54	37.11	232.12	324.57	2.41E+05	4.71E+05	-1.1E+04	6.68E-06	3.6E+10
3,977	32.50	52.25	23.84	36.41	208.51	318.44	2.50E+05	5.84E+05	8.32E+04	4.00E-06	6.3E+10
4,961	32.00	51.55	23.34	35.71	204.13	312.32	2.60E+05	6.09E+05	8.87E+04	3.82E-06	6.8E+10
3,966	32.70	52.20	24.04	36.36	210.26	318.01	2.51E+05	5.74E+05	7.22E+04	4.18E-06	6.0E+10
3,058	35.80	53.00	27.14	37.16	237.37	325.00	2.40E+05	4.50E+05	-3.0E+04	7.69E-06	3.1E+10
2,025	35.90	53.75	27.24	37.91	238.24	331.56	2.31E+05	4.47E+05	-1.5E+04	7.18E-06	3.2E+10
1,015	44.35	54.85	35.69	39.01	312.15	341.18	2.18E+05	2.60E+05	-1.8E+05	-3.3E-05	-6.6E+09
509	0.00	55.35	0.00	39.51	0.00	345.56	2.13E+05	ERR	ERR	ERR	ERR

* Not corrected for travel time through heads

Table B.8.
Raw Dynamic Core Data

Core Name   : F2040C
Core Length : 0.1099 ft
Core Density : 2.0410 gm/cc

	Not Corrected*		Corrected								
Pressure	tp	ts	tpc	tsc	Vp	Vs	G	L+2G	L	Cb	G/Cb
psig	usec	usec	usec	usec	usec/ft	usec/ft	psi	psi	psi	psi^-1	psi^2
488	27.85	55.20	19.19	39.36	174.60	358.12	2.13E+05	8.97E+05	4.71E+05	1.63E-06	1.3E+11
4,429	25.35	53.25	16.69	37.41	151.85	340.38	2.36E+05	1.19E+06	7.14E+05	1.15E-06	2.1E+11
496	27.85	55.05	19.19	39.21	174.60	356.75	2.15E+05	8.97E+05	4.67E+05	1.64E-06	1.3E+11
4,316	25.90	53.25	17.24	37.41	156.86	340.38	2.36E+05	1.11E+06	6.39E+05	1.26E-06	1.9E+11
522	28.20	55.05	19.54	39.21	177.78	356.75	2.15E+05	8.65E+05	4.36E+05	1.73E-06	1.2E+11
999	27.75	54.45	19.09	38.61	173.69	351.29	2.22E+05	9.07E+05	4.6E+05	1.6E-06	1.4E+11
1,992	27.25	53.50	18.59	37.66	169.14	342.65	2.33E+05	9.56E+05	4.9E+05	1.55E-06	1.5E+11
2,999	26.90	52.75	18.24	36.91	165.96	335.83	2.43E+05	9.93E+05	5.1E+05	1.49E-06	1.6E+11
3,928	26.75	52.00	18.09	36.16	164.59	329.00	2.53E+05	1.01E+06	5.04E+05	1.49E-06	1.7E+11
4,943	25.35	51.60	16.69	35.76	151.85	325.36	2.58E+05	1.19E+06	6.69E+05	1.19E-06	2.2E+11
3,992	25.85	51.75	17.19	35.91	156.40	326.73	2.56E+05	1.12E+06	6.06E+05	1.29E-06	2.0E+11
3,032	27.10	52.60	18.44	36.76	167.78	334.46	2.44E+05	9.72E+05	4.8E+05	1.55E-06	1.6E+11
2,032	27.30	53.30	18.64	37.46	169.60	340.83	2.35E+05	9.51E+05	4.8E+05	1.57E-06	1.5E+11
1,038	27.40	54.45	18.74	38.61	170.51	351.29	2.22E+05	9.41E+05	5.0E+05	1.5E-06	1.4E+11
512	27.45	54.90	18.79	39.06	170.96	355.39	2.17E+05	9.36E+05	5.03E+05	1.55E-06	1.4E+11

* Not corrected for travel time through heads

Table B.9.
Raw Dynamic Core Data

Core Name   :F6080A
Core Length   : 0.1161 ft
Core Density : 2.1059 gm/cc

Pressure psig	Not Corrected* tp usec	ts usec	Corrected tpc usec	tsc usec	Vp usec/ft	Vs usec/ft	G psi	L+2G psi	L psi	Cb psi^-1	G/Cb psi^2
624	0.00	53.05	0.00	37.21	0.00	320.38	2.75E+05	ERR	ERR	ERR	ERR
4,598	27.00	49.70	18.34	33.86	157.91	291.54	3.32E+05	1.13E+06	4.68E+05	1.45E-06	2.3E+11
638	0.00	53.00	0.00	37.16	0.00	319.95	2.76E+05	ERR	ERR	ERR	ERR
4,650	27.15	49.35	18.49	33.51	159.20	288.53	3.39E+05	1.11E+06	4.35E+05	1.51E-06	2.2E+11
549	39.65	53.20	30.99	37.36	266.83	321.68	2.73E+05	3.96E+05	-1.5E+05	3.06E-05	8.9E+09
1,016	39.10	52.75	30.44	36.91	262.09	317.80	2.79E+05	4.11E+05	-1.5E+05	2.6E-05	1.1E+10
2,014	31.90	51.95	23.24	36.11	200.10	310.91	2.92E+05	7.05E+05	1.2E+05	3.17E-06	9.2E+10
3,009	27.30	50.95	18.64	35.11	160.49	302.30	3.09E+05	1.10E+06	4.8E+05	1.46E-06	2.1E+11
3,955	27.15	50.00	18.49	34.16	159.20	294.12	3.26E+05	1.11E+06	4.61E+05	1.47E-06	2.2E+11
5,025	26.90	49.45	18.24	33.61	157.05	289.39	3.37E+05	1.14E+06	4.70E+05	1.44E-06	2.3E+11
3,910	27.40	50.45	18.74	34.61	161.35	298.00	3.18E+05	1.08E+06	4.48E+05	1.51E-06	2.1E+11
3,027	29.60	51.05	20.94	35.21	180.30	303.16	3.07E+05	8.68E+05	2.5E+05	2.18E-06	1.4E+11
2,033	31.80	51.75	23.14	35.91	199.24	309.19	2.95E+05	7.11E+05	1.2E+05	3.15E-06	9.4E+10
1,058	35.45	52.85	26.79	37.01	230.67	318.66	2.78E+05	5.30E+05	-2.5E+04	6.3E-06	4.4E+10
552	38.75	53.05	30.09	37.21	259.08	320.38	2.75E+05	4.20E+05	-1.3E+05	1.86E-05	1.5E+10

* Not corrected for travel time through heads

Table B.10.
Raw Dynamic Core Data

Core Name   : F60808
Core Length : 0.0974 ft
Core Density : 2.0833 gm/cc

Pressure psig	Not Corrected* tp usec	ts usec	Corrected tpc usec	tsc usec	Vp usec/ft	Vs usec/ft	G psi	L+2G psi	L psi	Cb psi^-1	G/Cb psi^2
582	32.00	46.00	23.34	30.16	239.53	309.52	2.91E+05	4.87E+05	-9.6E+04	1.02E-05	2.9E+10
4,384	21.65	43.40	12.99	27.56	133.31	282.84	3.49E+05	1.57E+06	8.73E+05	9.05E-07	3.9E+11
600	32.10	46.00	23.44	30.16	240.56	309.52	2.91E+05	4.82E+05	-1.0E+05	1.06E-05	2.7E+10
4,619	21.70	43.30	13.04	27.46	133.82	281.81	3.52E+05	1.56E+06	8.56E+05	9.17E-07	3.8E+11
517	32.20	46.15	23.54	30.31	241.58	311.06	2.89E+05	4.78E+05	-9.9E+04	1.07E-05	2.7E+10
1,007	27.35	45.75	18.69	29.91	191.81	306.96	2.96E+05	7.59E+05	1.7E+05	2.7E-06	1.1E+11
2,001	27.15	44.95	18.49	29.11	189.76	298.75	3.13E+05	7.75E+05	1.5E+05	2.79E-06	1.1E+11
2,982	22.50	44.25	13.84	28.41	142.03	291.56	3.28E+05	1.38E+06	7.3E+05	1.06E-06	3.1E+11
3,960	22.15	43.60	13.49	27.76	138.44	284.89	3.44E+05	1.46E+06	7.69E+05	1.00E-06	3.4E+11
4,909	21.60	43.60	12.94	27.76	132.80	284.89	3.44E+05	1.58E+06	8.95E+05	8.89E-07	3.9E+11
4,015	22.10	43.65	13.44	27.81	137.93	285.40	3.43E+05	1.47E+06	7.82E+05	9.90E-07	3.5E+11
3,039	22.30	44.20	13.64	28.36	139.98	291.05	3.30E+05	1.42E+06	7.7E+05	1.01E-06	3.2E+11
2,092	22.60	44.85	13.94	29.01	143.06	297.72	3.15E+05	1.36E+06	7.3E+05	1.06E-06	3.0E+11
1,034	27.15	45.75	18.49	29.91	189.76	306.96	2.96E+05	7.75E+05	1.8E+05	2.6E-06	1.1E+11
519	31.85	46.20	23.19	30.36	237.99	311.57	2.88E+05	4.93E+05	-8.2E+04	9.14E-06	3.1E+10

* Not corrected for travel time through heads

Table B.11.
Raw Dynamic Core Data

Core Name   :F6080D
Core Length   : 0.1106 ft
Core Density   : 2.0712 gm/cc

	Not Corrected*		Corrected								
Pressure	tp	ts	tpc	tsc	Vp	Vs	G	L+2G	L	Cb	G/Cb
psig	usec	usec	usec	usec	usec/ft	usec/ft	psi	psi	psi	psi^-1	psi^2
601	39.30	53.30	30.64	37.46	277.12	338.81	2.42E+05	3.61E+05	-1.2E+05	2.56E-05	9.4E+09
4,404	27.95	47.00	19.29	31.16	174.47	281.83	3.49E+05	9.17E+05	2.18E+05	2.22E-06	1.6E+11
627	38.85	53.15	30.19	37.31	273.05	337.45	2.44E+05	3.74E+05	-1.1E+05	2.02E-05	1.2E+10
4,067	28.10	47.60	19.44	31.76	175.83	287.25	3.36E+05	9.03E+05	2.30E+05	2.20E-06	1.5E+11
511	42.50	53.55	33.84	37.71	306.07	341.07	2.39E+05	2.98E+05	-1.8E+05	-5.0E-05	-4.8E+09
1,040	36.40	52.90	27.74	37.06	250.89	335.19	2.47E+05	4.43E+05	-5.1E+04	8.8E-06	2.8E+10
1,998	32.00	52.10	23.34	36.26	211.10	327.95	2.58E+05	6.26E+05	1.1E+05	3.54E-06	7.3E+10
3,001	30.10	49.00	21.44	33.16	193.91	299.92	3.09E+05	7.42E+05	1.3E+05	3.02E-06	1.0E+11
3,982	28.35	47.75	19.69	31.91	178.09	288.61	3.33E+05	8.80E+05	2.14E+05	2.29E-06	1.5E+11
4,986	27.45	46.90	18.79	31.06	169.95	280.92	3.52E+05	9.67E+05	2.63E+05	2.01E-06	1.8E+11
4,006	28.10	47.70	19.44	31.86	175.83	288.16	3.34E+05	9.03E+05	2.35E+05	2.19E-06	1.5E+11
3,034	29.85	48.90	21.19	33.06	191.65	299.01	3.10E+05	7.60E+05	1.4E+05	2.89E-06	1.1E+11
2,041	31.80	51.90	23.14	36.06	209.29	326.15	2.61E+05	6.37E+05	1.2E+05	3.46E-06	7.6E+10
1,065	35.70	52.75	27.04	36.91	244.56	333.83	2.49E+05	4.67E+05	-3.1E+04	7.4E-06	3.4E+10
513	37.05	53.45	28.39	37.61	256.77	340.16	2.40E+05	4.23E+05	-5.6E+04	9.65E-06	2.5E+10

* Not corrected for travel time through heads

Table B.12.
Raw Dynamic Core Data

Core Name   :F1014A
Core Length   : 0.0932 ft
Core Density   : 2.0086 gm/cc

| Pressure | Not Corrected* | | Corrected | | | | | | | | |
| | tp | ts | tpc | tsc | Vp | Vs | G | L+2G | L | Cb | G/Cb |
psig	usec	usec	usec	usec	usec/ft	usec/ft	psi	psi	psi	psi^-1	psi^2
524	22.65	47.40	13.99	31.56	150.15	338.71	2.35E+05	1.19E+06	7.2E+05	1.13E-06	2.1E+11
4,493	17.70	41.35	9.04	25.51	97.02	273.78	3.59E+05	2.86E+06	2.14E+06	4.20E-07	8.5E+11
547	22.75	47.60	14.09	31.76	151.22	340.86	2.32E+05	1.18E+06	7.1E+05	1.15E-06	2.0E+11
4,494	17.50	41.50	8.84	25.66	94.87	275.39	3.55E+05	2.99E+06	2.28E+06	3.97E-07	8.9E+11
503	23.05	48.65	14.39	32.81	154.44	352.13	2.17E+05	1.13E+06	6.9E+05	1.2E-06	1.8E+11
1,011	22.05	47.25	13.39	31.41	143.71	337.10	2.37E+05	1.30E+06	8.3E+05	1.0E-06	2.3E+11
2,002	19.10	44.20	10.44	28.36	112.05	304.37	2.91E+05	2.14E+06	1.6E+06	5.69E-07	5.1E+11
3,024	18.20	42.55	9.54	26.71	102.39	286.66	3.28E+05	2.57E+06	1.9E+06	4.69E-07	7.0E+11
3,958	17.95	41.80	9.29	25.96	99.70	278.61	3.47E+05	2.71E+06	2.01E+06	4.45E-07	7.8E+11
4,966	17.20	41.10	8.54	25.26	91.65	271.10	3.66E+05	3.20E+06	2.47E+06	3.68E-07	9.9E+11
4,026	17.55	41.55	8.89	25.71	95.41	275.93	3.54E+05	2.96E+06	2.25E+06	4.02E-07	8.8E+11
3,043	17.90	42.25	9.24	26.41	99.17	283.44	3.35E+05	2.74E+06	2.1E+06	4.37E-07	7.7E+11
2,064	18.95	43.60	10.29	27.76	110.44	297.93	3.03E+05	2.21E+06	1.6E+06	5.55E-07	5.5E+11
1,044	22.40	43.85	13.74	28.01	147.46	300.61	2.98E+05	1.24E+06	6.4E+05	1.2E-06	2.5E+11
517	22.25	47.70	13.59	31.86	145.85	341.93	2.30E+05	1.27E+06	8.0E+05	1.04E-06	2.2E+11

* Not corrected for travel time through heads

Table B.13.
Raw Dynamic Core Data

Core Name   :F10148
Core Length   : 0.1115 ft
Core Density   : 2.0803 gm/cc

	Not Corrected*		Corrected								
Pressure	tp	ts	tpc	tsc	Vp	Vs	G	L+2G	L	Cb	G/Cb
psig	usec	usec	usec	usec	usec/ft	usec/ft	psi	psi	psi	psi^-1	psi^2
478	24.55	53.30	15.89	37.46	142.45	335.82	2.47E+05	1.37E+06	8.8E+05	9.58E-07	2.6E+11
4,955	22.80	51.40	14.14	35.56	126.76	318.78	2.74E+05	1.73E+06	1.19E+06	7.30E-07	3.8E+11
506	24.55	53.20	15.89	37.36	142.45	334.92	2.49E+05	1.37E+06	8.8E+05	9.59E-07	2.6E+11
4,948	22.75	51.30	14.09	35.46	126.31	317.89	2.76E+05	1.75E+06	1.20E+06	7.25E-07	3.8E+11
519	24.55	53.20	15.89	37.36	142.45	334.92	2.49E+05	1.37E+06	8.8E+05	9.6E-07	2.6E+11
997	24.50	52.80	15.84	36.96	142.00	331.34	2.54E+05	1.38E+06	8.7E+05	9.6E-07	2.7E+11
1,992	23.70	52.70	15.04	36.86	134.83	330.44	2.55E+05	1.53E+06	1.0E+06	8.38E-07	3.0E+11
3,000	23.35	52.25	14.69	36.41	131.69	326.40	2.62E+05	1.61E+06	1.1E+06	7.95E-07	3.3E+11
3,971	23.05	51.80	14.39	35.96	129.00	322.37	2.68E+05	1.68E+06	1.14E+06	7.59E-07	3.5E+11
4,960	22.75	51.30	14.09	35.46	126.31	317.89	2.76E+05	1.75E+06	1.20E+06	7.25E-07	3.8E+11
3,977	23.10	51.65	14.44	35.81	129.45	321.03	2.70E+05	1.66E+06	1.12E+06	7.68E-07	3.5E+11
3,008	23.40	52.35	14.74	36.51	132.14	327.30	2.60E+05	1.60E+06	1.1E+06	8.00E-07	3.3E+11
2,021	23.70	52.70	15.04	36.86	134.83	330.44	2.55E+05	1.53E+06	1.0E+06	8.38E-07	3.0E+11
1,029	24.40	52.75	15.74	36.91	141.10	330.89	2.55E+05	1.40E+06	8.9E+05	9.4E-07	2.7E+11
500	24.90	53.35	16.24	37.51	145.59	336.27	2.47E+05	1.32E+06	8.2E+05	1.01E-06	2.4E+11

* Not corrected for travel time through heads

Table B.14.
Raw Dynamic Core Data

Core Name   :RESERVOIR SAMPLE 1A
Core Length   : 0.1127 ft
Core Density   : 1.9529 gm/cc

| Pressure | Not Corrected* | | Corrected | | | | | | | | |
| | tp | ts | tpc | tsc | Vp | Vs | G | L+2G | L | Cb | G/Cb |
psig	usec	usec	usec	usec	usec/ft	usec/ft	psi	psi	psi	psi^-1	psi^2
593	41.35	51.65	32.69	35.81	290.07	317.76	2.59E+05	3.11E+05	-2.1E+05	-2.9E-05	-9.0E+09
4,428	26.10	44.60	17.44	28.76	154.75	255.20	4.02E+05	1.09E+06	2.89E+05	1.80E-06	2.2E+11
528	40.55	51.15	31.89	35.31	282.97	313.32	2.67E+05	3.27E+05	-2.1E+05	-3.5E-05	-7.6E+09
4,288	25.95	44.30	17.29	28.46	153.42	252.54	4.10E+05	1.11E+06	2.91E+05	1.77E-06	2.3E+11
495	40.55	51.15	31.89	35.31	282.97	313.32	2.67E+05	3.27E+05	-2.1E+05	-3.5E-05	-7.6E+09
994	35.15	50.70	26.49	34.86	235.06	309.33	2.73E+05	4.74E+05	-7.3E+04	9.2E-06	3.0E+10
1,976	29.35	49.65	20.69	33.81	183.59	300.01	2.91E+05	7.76E+05	1.9E+05	2.57E-06	1.1E+11
3,024	26.85	46.30	18.19	30.46	161.41	270.28	3.58E+05	1.00E+06	2.9E+05	1.90E-06	1.9E+11
3,969	25.60	44.55	16.94	28.71	150.31	254.75	4.03E+05	1.16E+06	3.52E+05	1.61E-06	2.5E+11
4,899	24.85	43.95	16.19	28.11	143.66	249.43	4.21E+05	1.27E+06	4.27E+05	1.41E-06	3.0E+11
3,995	25.55	44.45	16.89	28.61	149.87	253.87	4.06E+05	1.17E+06	3.53E+05	1.60E-06	2.5E+11
2,997	26.80	45.90	18.14	30.06	160.96	266.73	3.68E+05	1.01E+06	2.7E+05	1.92E-06	1.9E+11
2,037	28.90	49.55	20.24	33.71	179.60	299.12	2.92E+05	8.11E+05	2.3E+05	2.37E-06	1.2E+11
1,016	32.75	50.60	24.09	34.76	213.76	308.44	2.75E+05	5.73E+05	2.3E+04	4.9E-06	5.7E+10
480	37.00	51.15	28.34	35.31	251.47	313.32	2.67E+05	4.14E+05	-1.2E+05	1.71E-05	1.6E+10

* Not corrected for travel time through heads

Table B.15.
Raw Dynamic Core Data

Core Name   :RESERVOIR SAMPLE 2B
Core Length   : 0.0955 ft
Core Density   : 2.0298 gm/cc

| Pressure | Not Corrected* | | Corrected | | Vp | Vs | G | L+2G | L | Cb | G/Cb |
| | tp | ts | tpc | tsc | | | | | | | |
psig	usec	usec	usec	usec	usec/ft	usec/ft	psi	psi	psi	psi^-1	psi^2
620	27.55	47.00	18.89	31.16	197.86	326.38	2.55E+05	6.95E+05	1.8E+05	2.8E-06	9.0E+10
4,751	19.95	43.35	11.29	27.51	118.25	288.15	3.28E+05	1.95E+06	1.29E+06	6.63E-07	4.9E+11
521	23.90	47.80	15.24	31.96	159.63	334.76	2.43E+05	1.07E+06	5.8E+05	1.3E-06	1.8E+11
4,787	19.85	42.80	11.19	26.96	117.21	282.39	3.41E+05	1.98E+06	1.30E+06	6.56E-07	5.2E+11
518	23.45	47.40	14.79	31.56	154.91	330.57	2.49E+05	1.13E+06	6.4E+05	1.2E-06	2.0E+11
1,003	22.65	46.40	13.99	30.56	146.53	320.09	2.65E+05	1.27E+06	7.4E+05	1.1E-06	2.4E+11
1,988	21.35	44.90	12.69	29.06	132.92	304.38	2.94E+05	1.54E+06	9.5E+05	8.71E-07	3.4E+11
2,991	20.60	44.15	11.94	28.31	125.06	296.53	3.09E+05	1.74E+06	1.1E+06	7.54E-07	4.1E+11
3,996	20.15	43.60	11.49	27.76	120.35	290.76	3.22E+05	1.88E+06	1.23E+06	6.90E-07	4.7E+11
4,966	19.75	42.65	11.09	26.81	116.16	280.81	3.45E+05	2.02E+06	1.33E+06	6.43E-07	5.4E+11
4,003	20.05	43.00	11.39	27.16	119.30	284.48	3.36E+05	1.91E+06	1.24E+06	6.84E-07	4.9E+11
3,040	20.45	44.05	11.79	28.21	123.49	295.48	3.12E+05	1.78E+06	1.2E+06	7.31E-07	4.3E+11
2,042	21.05	44.55	12.39	28.71	129.78	300.72	3.01E+05	1.61E+06	1.0E+06	8.24E-07	3.7E+11
1,029	22.35	46.05	13.69	30.21	143.39	316.43	2.72E+05	1.32E+06	7.8E+05	1.0E-06	2.6E+11
521	23.60	47.60	14.94	31.76	156.48	332.66	2.46E+05	1.11E+06	6.2E+05	1.28E-06	1.9E+11

* Not corrected for travel time through heads

Table B.16.
Raw Dynamic Core Data

Core Name   :RESERVOIR SAMPLE 3A
Core Length   : 0.1071 ft
Core Density   : 1.9699 gm/cc

Pressure	Not Corrected*		Corrected								
	tp	ts	tpc	tsc	Vp	Vs	G	L+2G	L	Cb	G/Cb
psig	usec	usec	usec	usec	usec/ft	usec/ft	psi	psi	psi	psi^-1	psi^2
610	38.65	52.75	29.99	36.91	279.97	344.57	2.22E+05	3.37E+05	-1.1E+05	2.5E-05	9.0E+09
4,721	24.25	48.05	15.59	32.21	145.54	300.69	2.92E+05	1.25E+06	6.62E+05	1.17E-06	2.5E+11
605	33.10	52.15	24.44	36.31	228.16	338.97	2.30E+05	5.07E+05	4.8E+04	5.0E-06	4.6E+10
4,730	23.80	47.25	15.14	31.41	141.34	293.22	3.07E+05	1.32E+06	7.07E+05	1.10E-06	2.8E+11
510	32.90	52.00	24.24	36.16	226.29	337.57	2.32E+05	5.15E+05	5.2E+04	4.8E-06	4.8E+10
1,009	30.75	51.55	22.09	35.71	206.22	333.37	2.38E+05	6.21E+05	1.5E+05	3.3E-06	7.2E+10
1,963	27.05	50.75	18.39	34.91	171.68	325.90	2.49E+05	8.96E+05	4.0E+05	1.77E-06	1.4E+11
2,994	25.05	49.40	16.39	33.56	153.01	313.30	2.69E+05	1.13E+06	5.9E+05	1.30E-06	2.1E+11
3,984	24.10	47.55	15.44	31.71	144.14	296.02	3.01E+05	1.27E+06	6.68E+05	1.15E-06	2.6E+11
4,981	23.20	46.75	14.54	30.91	135.74	288.56	3.17E+05	1.43E+06	7.99E+05	9.90E-07	3.2E+11
4,039	23.75	47.35	15.09	31.51	140.87	294.16	3.05E+05	1.33E+06	7.20E+05	1.08E-06	2.8E+11
3,031	25.00	48.65	16.34	32.81	152.54	306.29	2.81E+05	1.13E+06	5.7E+05	1.32E-06	2.1E+11
2,056	26.65	50.45	17.99	34.61	167.94	323.10	2.53E+05	9.36E+05	4.3E+05	1.67E-06	1.5E+11
1,029	30.40	51.40	21.74	35.56	202.95	331.97	2.40E+05	6.41E+05	1.6E+05	3.1E-06	7.7E+10
509	32.60	51.95	23.94	36.11	223.49	337.10	2.32E+05	5.28E+05	6.4E+04	4.57E-06	5.1E+10

* Not corrected for travel time through heads

Table B.17.
Raw Dynamic Core Data

Core Name   :RESERVOIR SAMPLE 4A
Core Length   : 0.1071 ft
Core Density   : 2.0265 gm/cc

| Pressure | Not Corrected* | | Corrected | | | | | | | | |
| | tp | ts | tpc | tsc | Vp | Vs | G | L+2G | L | Cb | G/Cb |
psig	usec	usec	usec	usec	usec/ft	usec/ft	psi	psi	psi	psi^-1	psi^2
627	37.05	52.75	28.39	36.91	265.03	344.57	2.29E+05	3.87E+05	-7.1E+04	1.2E-05	1.9E+10
4,987	23.10	46.40	14.44	30.56	134.80	285.29	3.34E+05	1.49E+06	8.27E+05	9.53E-07	3.5E+11
643	32.20	51.95	23.54	36.11	219.75	337.10	2.39E+05	5.62E+05	8.4E+04	4.1E-06	5.8E+10
5,194	22.70	45.95	14.04	30.11	131.07	281.09	3.44E+05	1.58E+06	8.93E+05	8.91E-07	3.9E+11
529	32.50	51.95	23.84	36.11	222.56	337.10	2.39E+05	5.48E+05	7.0E+04	4.4E-06	5.5E+10
996	29.55	51.70	20.89	35.86	195.02	334.77	2.42E+05	7.14E+05	2.3E+05	2.6E-06	9.5E+10
1,979	26.40	50.25	17.74	34.41	165.61	321.23	2.63E+05	9.90E+05	4.6E+05	1.56E-06	1.7E+11
2,971	24.60	47.80	15.94	31.96	148.81	298.36	3.05E+05	1.23E+06	6.2E+05	1.22E-06	2.5E+11
4,268	22.90	46.70	14.24	30.86	132.94	288.09	3.27E+05	1.54E+06	8.82E+05	9.09E-07	3.6E+11
4,911	22.50	45.85	13.84	30.01	129.20	280.15	3.46E+05	1.63E+06	9.35E+05	8.58E-07	4.0E+11
3,902	23.40	46.35	14.74	30.51	137.60	284.82	3.35E+05	1.43E+06	7.65E+05	1.01E-06	3.3E+11
3,057	23.80	47.25	15.14	31.41	141.34	293.22	3.16E+05	1.36E+06	7.3E+05	1.07E-06	3.0E+11
2,064	25.50	49.35	16.84	33.51	157.21	312.83	2.77E+05	1.10E+06	5.4E+05	1.37E-06	2.0E+11
1,017	28.50	51.55	19.84	35.71	185.21	333.37	2.44E+05	7.92E+05	3.0E+05	2.1E-06	1.1E+11
524	32.25	52.10	23.59	36.26	220.22	338.50	2.37E+05	5.60E+05	8.6E+04	4.10E-06	5.8E+10

* Not corrected for travel time through heads

Table B.18.
Raw Dynamic Core Data

Core Name   :RESERVOIR SAMPLE 5A
Core Length   : 0.1156 ft
Core Density   : 1.9090 gm/cc

Pressure psig	Not Corrected* tp usec	ts usec	Corrected tpc usec	tsc usec	Vp usec/ft	Vs usec/ft	G psi	L+2G psi	L psi	Cb psi^-1	G/Cb psi^2
597	40.35	54.25	31.69	38.41	274.02	332.12	2.32E+05	3.41E+05	-1.2E+05	3.2E-05	7.3E+09
4,894	25.25	49.40	16.59	33.56	143.45	290.19	3.04E+05	1.24E+06	6.36E+05	1.19E-06	2.5E+11
565	37.30	53.10	28.64	37.26	247.64	322.18	2.46E+05	4.17E+05	-7.6E+04	1.1E-05	2.2E+10
4,862	24.85	47.90	16.19	32.06	139.99	277.22	3.33E+05	1.31E+06	6.40E+05	1.16E-06	2.9E+11
526	33.35	53.00	24.69	37.16	213.49	321.32	2.48E+05	5.61E+05	6.6E+04	4.3E-06	5.7E+10
¡,068	31.60	52.85	22.94	37.01	198.36	320.02	2.50E+05	6.50E+05	1.5E+05	3.2E-06	7.9E+10
2,068	27.90	51.85	19.24	36.01	166.36	311.37	2.64E+05	9.24E+05	4.0E+05	1.75E-06	1.5E+11
3,004	26.80	50.70	18.14	34.86	156.85	301.43	2.82E+05	1.04E+06	4.8E+05	1.51E-06	1.9E+11
4,018	25.20	48.35	16.54	32.51	143.02	281.11	3.24E+05	1.25E+06	6.03E+05	1.22E-06	2.7E+11
4,956	24.40	47.46	15.74	31.62	136.10	273.39	3.42E+05	1.38E+06	6.97E+05	1.08E-06	3.2E+11
4,026	24.90	48.05	16.24	32.21	140.42	278.51	3.30E+05	1.30E+06	6.38E+05	1.17E-06	2.8E+11
3,048	26.50	50.50	17.84	34.66	154.26	299.70	2.85E+05	1.08E+06	5.1E+05	1.44E-06	2.0E+11
2,046	27.55	51.65	18.89	35.81	163.34	309.64	2.67E+05	9.59E+05	4.3E+05	1.66E-06	1.6E+11
1,040	31.00	52.65	22.34	36.81	193.17	318.29	2.53E+05	6.86E+05	1.8E+05	2.9E-06	8.8E+10
482	32.95	53.20	24.29	37.36	210.03	323.04	2.45E+05	5.80E+05	9.0E+04	3.95E-06	6.2E+10

* Not corrected for travel time through heads

Table B.19.
Raw Dynamic Core Data

Core Name   :RESERVOIR SAMPLE 5B
Core Length   : 0.0973 ft
Core Density   : 1.9270 gm/cc

| Pressure | Not Corrected* | | Corrected | | | | | | | | |
| | tp | ts | tpc | tsc | Vp | Vs | G | L+2G | L | Cb | G/Cb |
psig	usec	usec	usec	usec	usec/ft	usec/ft	psi	psi	psi	psi^-1	psi^2
576	35.90	49.95	27.24	34.11	280.03	350.65	2.10E+05	3.29E+05	-9.1E+04	2.0E-05	1.0E+10
4,765	22.05	45.80	13.39	29.96	137.65	307.99	2.72E+05	1.36E+06	8.18E+05	1.00E-06	2.7E+11
350	32.00	49.20	23.34	33.36	239.93	342.94	2.20E+05	4.49E+05	9.4E+03	6.4E-06	3.4E+10
4,769	21.65	45.60	12.99	29.76	133.54	305.93	2.76E+05	1.45E+06	8.96E+05	9.26E-07	3.0E+11
507	28.60	48.90	19.94	33.06	204.98	339.85	2.24E+05	6.15E+05	1.7E+05	3.2E-06	7.1E+10
994	27.20	48.35	18.54	32.51	190.59	334.20	2.31E+05	7.11E+05	2.5E+05	2.5E-06	9.3E+10
1,992	24.20	48.05	15.54	32.21	159.75	331.12	2.36E+05	1.01E+06	5.4E+05	1.43E-06	1.6E+11
2,990	22.80	46.95	14.14	31.11	145.36	319.81	2.52E+05	1.22E+06	7.2E+05	1.13E-06	2.2E+11
3,994	21.75	46.10	13.09	30.26	134.56	311.07	2.67E+05	1.43E+06	8.92E+05	9.34E-07	2.9E+11
4,921	21.20	45.45	12.54	29.61	128.91	304.39	2.79E+05	1.55E+06	9.96E+05	8.46E-07	3.3E+11
3,947	21.55	45.95	12.89	30.11	132.51	309.53	2.70E+05	1.47E+06	9.32E+05	9.00E-07	3.0E+11
3,022	22.45	46.75	13.79	30.91	141.76	317.75	2.56E+05	1.28E+06	7.7E+05	1.06E-06	2.4E+11
2,035	23.60	47.70	14.94	31.86	153.58	327.52	2.41E+05	1.09E+06	6.1E+05	1.29E-06	1.9E+11
1,024	26.50	48.50	17.84	32.66	183.39	335.74	2.29E+05	7.68E+05	3.1E+05	2.2E-06	1.1E+11
492	28.40	49.10	19.74	33.26	202.93	341.91	2.21E+05	6.27E+05	1.9E+05	3.01E-06	7.3E+10

* Not corrected for travel time through heads

Table B.20.
Raw Dynamic Core Data

Core Name   :RESERVOIR SAMPLE 6A
Core Length   : 0.1153 ft
Core Density   : 2.0433 gm/cc

Pressure psig	Not Corrected* tp usec	ts usec	Corrected tpc usec	tsc usec	Vp usec/ft	Vs usec/ft	G psi	L+2G psi	L psi	Cb psi^-1	G/Cb psi^2
641	32.20	55.35	23.54	39.51	204.12	342.61	2.33E+05	6.57E+05	1.9E+05	2.9E-06	8.1E+10
4,770	25.95	49.20	17.29	33.36	149.93	289.28	3.27E+05	1.22E+06	5.64E+05	1.28E-06	2.6E+11
511	32.65	54.75	23.99	38.91	208.03	337.40	2.41E+05	6.33E+05	1.5E+05	3.2E-06	7.5E+10
4,505	25.60	48.95	16.94	33.11	146.89	287.11	3.32E+05	1.27E+06	6.05E+05	1.21E-06	2.7E+11
509	32.40	54.70	23.74	38.86	205.86	336.97	2.41E+05	6.46E+05	1.6E+05	3.1E-06	7.8E+10
1,027	32.80	54.10	24.14	38.26	209.33	331.77	2.49E+05	6.25E+05	1.3E+05	3.4E-06	7.3E+10
1,993	28.35	53.05	19.69	37.21	170.74	322.66	2.63E+05	9.39E+05	4.1E+05	1.70E-06	1.5E+11
3,003	27.10	50.40	18.44	34.56	159.90	299.68	3.05E+05	1.07E+06	4.6E+05	1.51E-06	2.0E+11
4,007	25.85	49.05	17.19	33.21	149.06	287.98	3.30E+05	1.23E+06	5.72E+05	1.26E-06	2.6E+11
4,935	25.15	48.20	16.49	32.36	142.99	280.61	3.48E+05	1.34E+06	6.44E+05	1.14E-06	3.0E+11
4,033	25.70	48.95	17.04	33.11	147.76	287.11	3.32E+05	1.25E+06	5.90E+05	1.23E-06	2.7E+11
3,023	27.05	50.25	18.39	34.41	159.47	298.38	3.08E+05	1.08E+06	4.6E+05	1.50E-06	2.1E+11
2,049	28.25	52.85	19.59	37.01	169.87	320.93	2.66E+05	9.49E+05	4.2E+05	1.68E-06	1.6E+11
1,046	32.00	53.85	23.34	38.01	202.39	329.60	2.52E+05	6.68E+05	1.6E+05	3.0E-06	8.4E+10
523	34.50	54.50	25.84	38.66	224.07	335.24	2.44E+05	5.45E+05	5.8E+04	4.54E-06	5.4E+10

* Not corrected for travel time through heads

Table B.21.
Raw Dynamic Core Data

Core Name   :RESERVOIR SAMPLE 7A
Core Length   : 0.1052 ft
Core Density   : 1.9770 gm/cc

	Not Corrected*		Corrected								
Pressure	tp	ts	tpc	tsc	Vp	Vs	G	L+2G	L	Cb	G/Cb
psig	usec	usec	usec	usec	usec/ft	usec/ft	psi	psi	psi	psi^-1	psi^2
582	39.30	53.10	30.64	37.26	291.39	354.35	2.11E+05	3.12E+05	-1.1E+05	3.3E-05	6.5E+09
4,679	24.95	48.75	16.29	32.91	154.92	312.98	2.70E+05	1.10E+06	5.63E+05	1.35E-06	2.0E+11
514	37.30	52.35	28.64	36.51	272.37	347.22	2.20E+05	3.57E+05	-8.2E+04	1.6E-05	1.4E+10
4,908	24.25	48.00	15.59	32.16	148.26	305.85	2.83E+05	1.21E+06	6.39E+05	1.21E-06	2.3E+11
511	36.95	52.35	28.29	36.51	269.04	347.22	2.20E+05	3.66E+05	-7.3E+04	1.4E-05	1.6E+10
996	31.85	51.95	23.19	36.11	220.54	343.41	2.25E+05	5.45E+05	9.5E+04	4.1E-06	5.5E+10
2,018	27.80	51.85	19.14	36.01	182.02	342.46	2.26E+05	8.00E+05	3.5E+05	2.01E-06	1.1E+11
2,986	25.80	49.85	17.14	34.01	163.00	323.44	2.53E+05	9.97E+05	4.9E+05	1.52E-06	1.7E+11
3,984	24.75	48.30	16.09	32.46	153.02	308.70	2.78E+05	1.13E+06	5.75E+05	1.31E-06	2.1E+11
4,997	23.80	47.35	15.14	31.51	143.98	299.66	2.95E+05	1.28E+06	6.88E+05	1.13E-06	2.6E+11
3,935	24.55	47.90	15.89	32.06	151.12	304.90	2.85E+05	1.16E+06	5.90E+05	1.28E-06	2.2E+11
3,066	25.40	49.55	16.74	33.71	159.20	320.59	2.58E+05	1.05E+06	5.3E+05	1.43E-06	1.8E+11
2,024	27.45	50.95	18.79	35.11	178.70	333.90	2.38E+05	8.30E+05	3.5E+05	1.95E-06	1.2E+11
1,030	31.20	51.70	22.54	35.86	214.36	341.03	2.28E+05	5.77E+05	1.2E+05	3.7E-06	6.2E+10
518	36.70	52.25	28.04	36.41	266.66	346.26	2.21E+05	3.73E+05	-6.9E+04	1.28E-05	1.7E+10

* Not corrected for travel time through heads

Table B.22.
Raw Dynamic Core Data

Core Name   :RESERVOIR SAMPLE 8A
Core Length   : 0.1083 ft
Core Density   : 1.9310 gm/cc

Pressure psig	Not Corrected* tp usec	ts usec	Corrected tpc usec	tsc usec	Vp usec/ft	Vs usec/ft	G psi	L+2G psi	L psi	Cb psi^-1	G/Cb psi^2
699	37.35	51.71	28.69	35.87	264.99	331.31	2.36E+05	3.68E+05	-1.0E+05	1.8E-05	1.3E+10
4,532	24.00	43.50	15.34	27.66	141.69	255.48	3.96E+05	1.29E+06	4.96E+05	1.32E-06	3.0E+11
542	35.55	51.10	26.89	35.26	248.37	325.67	2.44E+05	4.19E+05	-6.8E+04	1.1E-05	2.3E+10
4,439	23.65	43.30	14.99	27.46	138.45	253.63	4.02E+05	1.35E+06	5.45E+05	1.23E-06	3.3E+11
517	35.55	51.05	26.89	35.21	248.37	325.21	2.45E+05	4.19E+05	-7.0E+04	1.1E-05	2.3E+10
994	30.85	50.60	22.19	34.76	204.95	321.06	2.51E+05	6.16E+05	1.1E+05	3.6E-06	7.1E+10
1,989	26.95	46.05	18.29	30.21	168.93	279.03	3.32E+05	9.07E+05	2.4E+05	2.16E-06	1.5E+11
3,009	24.85	44.40	16.19	28.56	149.54	263.79	3.72E+05	1.16E+06	4.1E+05	1.51E-06	2.5E+11
3,980	23.80	43.15	15.14	27.31	139.84	252.25	4.07E+05	1.32E+06	5.10E+05	1.28E-06	3.2E+11
4,905	23.15	42.70	14.49	26.86	133.83	248.09	4.20E+05	1.44E+06	6.04E+05	1.13E-06	3.7E+11
4,026	23.50	42.80	14.84	26.96	137.07	249.01	4.17E+05	1.38E+06	5.43E+05	1.22E-06	3.4E+11
3,022	24.70	44.05	16.04	28.21	148.15	260.56	3.81E+05	1.18E+06	4.2E+05	1.49E-06	2.6E+11
2,031	26.55	45.70	17.89	29.86	165.24	275.80	3.40E+05	9.48E+05	2.7E+05	2.02E-06	1.7E+11
1,030	29.50	50.50	20.84	34.66	192.49	320.13	2.52E+05	6.98E+05	1.9E+05	2.8E-06	9.1E+10
508	35.45	51.00	26.79	35.16	247.44	324.75	2.45E+05	4.23E+05	-6.8E+04	1.05E-05	2.3E+10

* Not corrected for travel time through heads

Table B.23.
Raw Dynamic Core Data

Core Name   :Montmayeur STB5
Core Length   : 0.1187 ft
Core Density   : 2.3360 gm/cc

Pressure psig	Not Corrected* tp usec	ts usec	Corrected tpc usec	tsc usec	Vp usec/ft	Vs usec/ft	G psi	L+2G psi	L psi	Cb psi^-1	G/Cb psi^2
500	15.70	22.35	9.81	18.71	82.68	157.68	1.26E+06	4.58E+06	2.1E+06	3.4E-07	3.7E+12
1,000	15.50	22.05	9.61	18.41	81.00	155.16	1.30E+06	4.77E+06	2.17E+06	3.29E-07	3.9E+12
2,000	15.20	21.50	9.31	17.86	78.47	150.52	1.38E+06	5.08E+06	2.3E+06	3.1E-07	4.5E+12
3,000	14.95	20.35	9.06	16.71	76.36	140.83	1.58E+06	5.37E+06	2.21E+06	3.06E-07	5.2E+12
4,000	14.90	20.00	9.01	16.36	75.94	137.88	1.65E+06	5.43E+06	2.1E+06	3.1E-07	5.3E+12
5,000	14.80	19.65	8.91	16.01	75.10	134.93	1.72E+06	5.55E+06	2.1E+06	3.1E-07	5.6E+12
4,000	14.85	19.95	8.96	16.31	75.52	137.46	1.66E+06	5.49E+06	2.2E+06	3.05E-07	5.4E+12
3,000	15.00	20.35	9.11	16.71	76.79	140.83	1.58E+06	5.31E+06	2.2E+06	3.12E-07	5.1E+12
2,000	15.10	20.75	9.21	17.11	77.63	144.20	1.51E+06	5.19E+06	2.18E+06	3.14E-07	4.8E+12
1,000	15.35	21.90	9.46	18.26	79.74	153.89	1.32E+06	4.92E+06	2.28E+06	3.16E-07	4.2E+12
500	15.55	22.25	9.66	18.61	81.42	156.84	1.27E+06	4.72E+06	2.18E+06	3.31E-07	3.8E+12

* Not corrected for travel time through heads

Table B.24.
Raw Dynamic Core Data

Core Name   :Montmayeur STD2
Core Length   : 0.1202 ft
Core Density   : 2.4685 gm/cc

	Not Corrected*		Corrected								
Pressure	tp	ts	tpc	tsc	Vp	Vs	G	L+2G	L	Cb	G/Cb
psig	usec	usec	usec	usec	usec/ft	usec/ft	psi	psi	psi	psi^-1	psi^2
500	15.65	23.15	9.76	19.51	81.24	162.37	1.25E+06	5.01E+06	2.5E+06	3.0E-07	4.2E+12
1,000	14.60	21.80	8.71	18.16	72.50	151.14	1.45E+06	6.29E+06	3.40E+06	2.29E-07	6.3E+12
2,000	13.80	20.70	7.91	17.06	65.84	141.99	1.64E+06	7.63E+06	4.3E+06	1.8E-07	8.9E+12
3,000	13.70	20.35	7.81	16.71	65.01	139.07	1.71E+06	7.83E+06	4.41E+06	1.80E-07	9.5E+12
4,000	13.55	20.20	7.66	16.56	63.76	137.82	1.74E+06	8.14E+06	4.7E+06	1.7E-07	1.0E+13
5,000	13.50	20.05	7.61	16.41	63.35	136.58	1.77E+06	8.24E+06	4.7E+06	1.7E-07	1.0E+13
4,000	13.55	20.20	7.66	16.56	63.76	137.82	1.74E+06	8.14E+06	4.7E+06	1.72E-07	1.0E+13
3,000	13.65	20.35	7.76	16.71	64.59	139.07	1.71E+06	7.93E+06	4.5E+06	1.77E-07	9.7E+12
2,000	13.80	20.65	7.91	17.01	65.84	141.57	1.65E+06	7.63E+06	4.33E+06	1.84E-07	9.0E+12
1,000	14.05	21.40	8.16	17.76	67.92	147.81	1.51E+06	7.17E+06	4.14E+06	1.94E-07	7.8E+12
500	14.80	22.60	8.91	18.96	74.16	157.80	1.33E+06	6.01E+06	3.36E+06	2.36E-07	5.6E+12

* Not corrected for travel time through heads

Table B.25.
Raw Dynamic Core Data

Core Name   :Montmayeur 20403 FRAC
Core Length   : 0.1238 ft
Core Density   : 2.1244 gm/cc

Pressure	Not Corrected*		Corrected								
	tp	ts	tpc	tsc	Vp	Vs	G	L+2G	L	Cb	G/Cb
psig	usec	usec	usec	usec	usec/ft	usec/ft	psi	psi	psi	psi^-1	psi^2
500	30.15	41.40	19.60	32.79	158.28	264.79	4.06E+05	1.14E+06	3.2E+05	1.7E-06	2.4E+11
1,000	27.50	40.70	17.10	32.15	138.09	259.63	4.22E+05	1.49E+06	6.48E+05	1.08E-06	3.9E+11
2,000	26.56	36.35	16.30	27.88	131.63	225.14	5.62E+05	1.64E+06	5.2E+05	1.1E-06	5.0E+11
3,000	25.80	34.65	15.71	26.22	126.87	211.74	6.35E+05	1.77E+06	4.99E+05	1.08E-06	5.9E+11
4,000	25.40	34.05	15.34	25.64	123.88	207.05	6.64E+05	1.86E+06	5.3E+05	1.0E-06	6.4E+11
5,000	25.05	33.50	15.00	25.09	121.13	202.61	6.93E+05	1.94E+06	5.5E+05	9.8E-07	7.0E+11
4,000	25.40	34.00	15.34	25.39	123.88	205.04	6.77E+05	1.86E+06	5.0E+05	1.05E-06	6.4E+11
3,000	25.85	34.55	15.76	26.12	127.27	210.93	6.40E+05	1.76E+06	4.8E+05	1.11E-06	5.8E+11
2,000	26.60	36.15	16.40	27.68	132.44	223.53	5.70E+05	1.62E+06	4.84E+05	1.16E-06	4.9E+11
1,000	27.85	40.60	17.45	32.60	140.92	263.26	4.11E+05	1.43E+06	6.12E+05	1.13E-06	3.6E+11
500	28.80	42.20	18.25	33.59	147.38	271.25	3.87E+05	1.31E+06	5.37E+05	1.26E-06	3.1E+11

* Not corrected for travel time through heads

Table B.26.
Raw Dynamic Core Data

Core Name   :Montmayeur 20404 FRAC
Core Length   : 0.1209 ft
Core Density   : 2.1162 gm/cc

Pressure psig	Not Corrected* tp usec	ts usec	Corrected tpc usec	tsc usec	Vp usec/ft	Vs usec/ft	G psi	L+2G psi	L psi	Cb psi^-1	G/Cb psi^2
500	27.95	41.50	17.40	32.89	143.89	271.99	3.83E+05	1.37E+06	6.0E+05	1.2E-06	3.3E+11
1,000	26.95	40.80	16.55	32.25	136.87	266.70	3.99E+05	1.51E+06	7.16E+05	1.02E-06	3.9E+11
2,000	24.50	39.75	14.30	31.28	118.26	258.68	4.24E+05	2.03E+06	1.2E+06	6.8E-07	6.2E+11
3,000	23.95	39.00	13.86	30.57	114.62	252.81	4.44E+05	2.16E+06	1.27E+06	6.38E-07	7.0E+11
4,000	23.80	37.00	13.74	28.59	113.63	236.43	5.07E+05	2.20E+06	1.2E+06	6.6E-07	7.7E+11
5,000	23.30	37.00	13.25	28.59	109.57	236.43	5.07E+05	2.36E+06	1.3E+06	5.9E-07	8.5E+11
4,000	23.40	37.00	13.34	28.59	110.32	236.43	5.07E+05	2.33E+06	1.3E+06	6.05E-07	8.4E+11
3,000	23.95	39.20	13.86	30.77	114.62	254.46	4.38E+05	2.16E+06	1.3E+06	6.35E-07	6.9E+11
2,000	24.75	39.70	14.55	31.23	120.33	258.27	4.25E+05	1.96E+06	1.11E+06	7.19E-07	5.9E+11
1,000	25.45	40.65	15.05	32.10	124.46	265.46	4.02E+05	1.83E+06	1.03E+06	7.73E-07	5.2E+11
500	27.85	41.35	17.30	32.74	143.07	270.75	3.87E+05	1.39E+06	6.12E+05	1.15E-06	3.4E+11

* Not corrected for travel time through heads

Table B.27.
Raw Dynamic Core Data

Core Name   :Montmayeur 4060 FRAC
Core Length : 0.1205 ft
Core Density : 2.0949 gm/cc

	Not Corrected*		Corrected								
Pressure	tp	ts	tpc	tsc	Vp	Vs	G	L+2G	L	Cb	G/Cb
psig	usec	usec	usec	usec	usec/ft	usec/ft	psi	psi	psi	psi^-1	psi^2
500	30.00	67.95	19.45	59.34	161.41	492.45	1.16E+05	1.08E+06	8.5E+05	1.1E-06	1.1E+11
1,000	27.05	64.75	16.65	56.20	138.18	466.40	1.29E+05	1.47E+06	1.21E+06	7.70E-07	1.7E+11
2,000	26.50	54.60	16.30	46.13	135.27	382.83	1.92E+05	1.53E+06	1.2E+06	7.8E-07	2.4E+11
3,000	25.75	52.00	15.66	43.57	129.96	361.58	2.15E+05	1.66E+06	1.23E+06	7.27E-07	3.0E+11
4,000	25.25	50.15	15.19	41.74	126.06	346.39	2.34E+05	1.77E+06	1.3E+06	6.9E-07	3.4E+11
5,000	24.90	48.25	14.85	39.84	123.24	330.63	2.57E+05	1.85E+06	1.3E+06	6.6E-07	3.9E+11
4,000	25.20	50.05	15.14	41.64	125.64	345.56	2.35E+05	1.78E+06	1.3E+06	6.83E-07	3.4E+11
3,000	25.65	51.75	15.56	43.32	129.13	359.51	2.17E+05	1.68E+06	1.2E+06	7.17E-07	3.0E+11
2,000	26.25	54.45	16.05	45.98	133.20	381.58	1.93E+05	1.58E+06	1.20E+06	7.55E-07	2.6E+11
1,000	27.10	63.30	16.70	54.75	138.59	454.36	1.36E+05	1.46E+06	1.19E+06	7.81E-07	1.7E+11
500	29.65	69.60	19.10	60.99	158.51	506.15	1.10E+05	1.12E+06	8.98E+05	1.03E-06	1.1E+11

* Not corrected for travel time through heads

Table B.28.
Raw Dynamic Core Data

Core Name   :Montmayeur 6080 FRAC
Core Length   : 0.1192 ft
Core Density   : 2.0985 gm/cc

	Not Corrected*		Corrected								
Pressure	tp	ts	tpc	tsc	Vp	Vs	G	L+2G	L	Cb	G/Cb
psig	usec	usec	usec	usec	usec/ft	usec/ft	psi	psi	psi	psi^-1	psi^2
500	27.95	68.05	17.40	59.44	146.01	498.80	1.13E+05	1.32E+06	1.1E+06	8.6E-07	1.3E+11
1,000	27.30	61.20	16.90	52.65	141.82	441.82	1.44E+05	1.40E+06	1.11E+06	8.29E-07	1.7E+11
2,000	24.80	52.99	14.60	44.52	122.52	373.59	2.01E+05	1.87E+06	1.5E+06	6.2E-07	3.2E+11
3,000	24.10	50.85	14.01	42.42	117.57	355.97	2.22E+05	2.03E+06	1.59E+06	5.75E-07	3.9E+11
4,000	23.80	50.05	13.74	41.64	115.30	349.43	2.30E+05	2.12E+06	1.7E+06	5.5E-07	4.2E+11
5,000	23.35	48.10	13.30	39.69	111.61	333.06	2.53E+05	2.26E+06	1.8E+06	5.2E-07	4.9E+11
4,000	23.75	49.95	13.69	41.54	114.88	348.59	2.31E+05	2.13E+06	1.7E+06	5.49E-07	4.2E+11
3,000	24.10	50.65	14.01	42.22	117.57	354.29	2.24E+05	2.03E+06	1.6E+06	5.76E-07	3.9E+11
2,000	24.60	52.55	14.40	44.08	120.84	369.90	2.06E+05	1.93E+06	1.51E+06	6.05E-07	3.4E+11
1,000	27.15	55.65	16.75	47.10	140.56	395.24	1.80E+05	1.42E+06	1.06E+06	8.45E-07	2.1E+11
500	27.85	67.85	17.30	59.24	145.17	497.12	1.14E+05	1.33E+06	1.11E+06	8.46E-07	1.3E+11

* Not corrected for travel time through heads

Table B.29.
Raw Dynamic Core Data

Core Name   :Montmayeur 8010 FRAC
Core Length   : 0.1162 ft
Core Density   : 2.1260 gm/cc

	Not Corrected*		Corrected								
Pressure	tp	ts	tpc	tsc	Vp	Vs	G	L+2G	L	Cb	G/Cb
psig	usec	usec	usec	usec	usec/ft	usec/ft	psi	psi	psi	psi^-1	psi^2
500	29.10	66.45	18.55	57.84	159.57	497.55	1.15E+05	1.12E+06	8.9E+05	1.0E-06	1.1E+11
1,000	28.30	64.00	17.90	55.45	153.98	476.99	1.25E+05	1.20E+06	9.51E+05	9.67E-07	1.3E+11
2,000	27.00	52.80	16.80	44.33	144.52	381.33	1.96E+05	1.36E+06	9.7E+05	9.1E-07	2.2E+11
3,000	25.35	50.95	15.26	42.52	131.27	365.76	2.13E+05	1.65E+06	1.23E+06	7.30E-07	2.9E+11
4,000	25.25	50.95	15.19	42.54	130.67	365.94	2.13E+05	1.67E+06	1.2E+06	7.2E-07	2.9E+11
5,000	24.70	49.25	14.65	40.84	126.02	351.31	2.31E+05	1.79E+06	1.3E+06	6.7E-07	3.4E+11
4,000	25.20	50.50	15.14	42.09	130.24	362.06	2.17E+05	1.68E+06	1.2E+06	7.20E-07	3.0E+11
3,000	25.60	52.30	15.51	43.87	133.42	377.38	2.00E+05	1.60E+06	1.2E+06	7.50E-07	2.7E+11
2,000	26.70	53.05	16.50	41.58	141.94	357.68	2.23E+05	1.41E+06	9.69E+05	8.95E-07	2.5E+11
1,000	28.20	55.55	17.80	47.00	153.12	404.30	1.74E+05	1.22E+06	8.67E+05	1.02E-06	1.7E+11
500	28.90	64.70	18.35	56.09	157.85	482.49	1.22E+05	1.14E+06	8.99E+05	1.02E-06	1.2E+11

* Not corrected for travel time through heads

Table B.30.
Raw Dynamic Core Data

Core Name   :Montmayeur 1012 FRAC
Core Length   : 0.1206 ft
Core Density   : 2.0668 gm/cc

Pressure psig	Not Corrected* tp usec	ts usec	Corrected tpc usec	tsc usec	Vp usec/ft	Vs usec/ft	G psi	L+2G psi	L psi	Cb psi^-1	G/Cb psi^2
500	30.70	70.25	20.15	61.64	167.10	511.18	1.06E+05	9.92E+05	7.8E+05	1.2E-06	9.0E+10
1,000	28.80	66.05	18.40	57.50	152.59	476.85	1.22E+05	1.19E+06	9.46E+05	9.74E-07	1.3E+11
2,000	27.30	54.20	17.10	45.73	141.81	379.24	1.93E+05	1.38E+06	9.9E+05	8.9E-07	2.2E+11
3,000	26.35	52.70	16.26	44.27	134.84	367.13	2.05E+05	1.52E+06	1.11E+06	8.01E-07	2.6E+11
4,000	25.75	51.30	15.69	42.89	130.12	355.69	2.19E+05	1.64E+06	1.2E+06	7.4E-07	2.9E+11
5,000	25.00	48.45	14.95	40.04	123.98	332.05	2.51E+05	1.80E+06	1.3E+06	6.8E-07	3.7E+11
4,000	25.70	49.90	15.64	41.49	129.70	344.08	2.34E+05	1.65E+06	1.2E+06	7.49E-07	3.1E+11
3,000	26.45	52.10	16.36	43.67	135.67	362.15	2.11E+05	1.50E+06	1.1E+06	8.18E-07	2.6E+11
2,000	26.75	55.20	16.55	46.73	137.25	387.53	1.84E+05	1.47E+06	1.10E+06	8.17E-07	2.3E+11
1,000	28.25	65.95	17.85	57.40	148.03	476.02	1.22E+05	1.26E+06	1.02E+06	9.08E-07	1.3E+11
500	31.15	69.50	20.60	60.89	170.84	504.96	1.09E+05	9.49E+05	7.32E+05	1.24E-06	8.7E+10

* Not corrected for travel time through heads

Table B.31.
Raw Dynamic Core Data

Core Name   :Montmayeur 1217 FRAC
Core Length   : 0.1204 ft
Core Density   : 2.0810 gm/cc

| | Not Corrected* | | Corrected | | | | | | | | |
| Pressure | tp | ts | tpc | tsc | Vp | Vs | G | L+2G | L | Cb | G/Cb |
psig	usec	usec	usec	usec	usec/ft	usec/ft	psi	psi	psi	psi^-1	psi^2
500	29.90	67.15	19.35	58.54	160.69	486.15	1.18E+05	1.08E+06	8.4E+05	1.1E-06	1.1E+11
1,000	28.50	61.85	18.10	53.30	150.31	442.63	1.42E+05	1.23E+06	9.50E+05	9.57E-07	1.5E+11
2,000	26.85	54.10	16.65	45.63	138.27	378.93	1.94E+05	1.46E+06	1.1E+06	8.3E-07	2.3E+11
3,000	26.00	52.40	15.91	43.97	132.12	365.15	2.09E+05	1.60E+06	1.18E+06	7.58E-07	2.8E+11
4,000	25.05	50.40	14.99	41.99	124.48	348.71	2.29E+05	1.80E+06	1.3E+06	6.7E-07	3.4E+11
5,000	24.45	48.80	14.40	40.39	119.58	335.42	2.48E+05	1.95E+06	1.5E+06	6.2E-07	4.0E+11
4,000	25.40	50.00	15.34	41.59	127.39	345.38	2.34E+05	1.72E+06	1.3E+06	7.11E-07	3.3E+11
3,000	25.85	50.30	15.76	41.87	130.88	347.71	2.31E+05	1.63E+06	1.2E+06	7.57E-07	3.0E+11
2,000	26.55	51.90	16.35	43.43	135.78	360.66	2.14E+05	1.51E+06	1.08E+06	8.15E-07	2.6E+11
1,000	28.30	61.15	17.90	52.60	148.65	436.82	1.46E+05	1.26E+06	9.70E+05	9.37E-07	1.6E+11
500	28.95	66.70	18.40	58.09	152.80	482.41	1.20E+05	1.19E+06	9.55E+05	9.67E-07	1.2E+11

* Not corrected for travel time through heads

Table B.32.
Raw Dynamic Core Data

Core Name   :Montmayeur 1720 FRAC
Core Length   : 0.1191 ft
Core Density   : 2.1110 gm/cc

Pressure psig	Not Corrected* tp usec	ts usec	Corrected tpc usec	tsc usec	Vp usec/ft	Vs usec/ft	G psi	L+2G psi	L psi	Cb psi^-1	G/Cb psi^2
500	29.55	72.20	19.00	64.09	159.55	538.19	9.77E+04	1.11E+06	9.2E+05	1.0E-06	9.6E+10
1,000	28.30	66.50	17.90	57.95	150.31	486.63	1.19E+05	1.25E+06	1.01E+06	9.15E-07	1.3E+11
2,000	26.85	60.00	16.65	51.53	139.82	432.72	1.51E+05	1.45E+06	1.1E+06	8.0E-07	1.9E+11
3,000	25.70	54.15	15.61	45.72	131.08	383.93	1.92E+05	1.65E+06	1.26E+06	7.19E-07	2.7E+11
4,000	25.25	53.80	15.19	45.39	127.56	381.16	1.95E+05	1.74E+06	1.3E+06	6.8E-07	2.9E+11
5,000	24.55	52.05	14.50	43.64	121.76	366.46	2.11E+05	1.91E+06	1.5E+06	6.1E-07	3.4E+11
4,000	24.95	53.45	14.89	45.04	125.04	378.22	1.98E+05	1.81E+06	1.4E+06	6.47E-07	3.1E+11
3,000	25.70	55.35	15.61	46.92	131.08	394.01	1.82E+05	1.65E+06	1.3E+06	7.13E-07	2.6E+11
2,000	26.90	56.40	16.70	47.93	140.24	402.49	1.75E+05	1.44E+06	1.09E+06	8.30E-07	2.1E+11
1,000	28.00	64.65	17.60	56.10	147.79	471.09	1.27E+05	1.30E+06	1.04E+06	8.89E-07	1.4E+11
500	29.15	70.05	18.60	61.44	156.19	515.94	1.06E+05	1.16E+06	9.47E+05	9.82E-07	1.1E+11

* Not corrected for travel time through heads

Table B.33.
Calculations of Bulk Compressibility

Core Name   : Montmayeur 20403 FRAC

Pressure psig	Static Measured Cb E-06/psi	Dynamic Measured Cb E-06/psi	Biot Corrected Cb E-06/psi	Gassmann Corrected Cb E-06/psi
500	1.90	1.70	1.80	2.470
1,000	1.41	1.08	1.15	1.310
2,000	1.13	1.10	1.20	1.110
3,000	1.03	1.08	1.16	0.968
4,000	0.99	1.00	1.11	0.893
5,000	1.01	0.98	1.06	0.824
4,000	0.74	1.05	1.11	0.893
3,000	0.82	1.11	1.18	0.986
2,000	1.04	1.16	1.24	1.109
1,000	1.67	1.13	1.23	1.431
500	2.68	1.26	1.34	1.716

Table B.34.
Calculations of Bulk Compressibility

Core Name   : Montmayeur 20404 FRAC

Pressure psig	Static Measured Cb E-06/psi	Dynamic Measured Cb E-06/psi	Biot Corrected Cb E-06/psi	Gassmann Corrected Cb E-06/psi
500	2.32	1.20	15.05	1.561
1,000	1.85	1.02	4.12	1.275
2,000	1.27	0.68	1.14	0.762
3,000	1.01	0.64	0.99	0.704
4,000	0.94	0.66	1.06	0.685
5,000	0.88	0.59	0.93	0.617
4,000	0.64	0.61	0.90	0.617
3,000	0.88	0.64	0.98	0.704
2,000	1.16	0.72	1.28	0.803
1,000	1.88	0.77	4.74	0.893
500	2.54	1.15	11.41	1.518

Table B.35.
Calculations of Bulk Compressibility

Core Name   : Montmayeur 4060 FRAC

Pressure psig	Static Measured Cb E-06/psi	Dynamic Measured Cb E-06/psi	Biot Corrected Cb E-06/psi	Gassmann Corrected Cb E-06/psi
500	2.84	1.10	3.11	2.680
1,000	1.92	0.77	1.26	1.304
2,000	1.34	0.78	1.30	1.200
3,000	1.08	0.73	1.12	1.047
4,000	0.89	0.69	1.00	0.941
5,000	0.86	0.66	0.96	0.870
4,000	0.72	0.68	1.01	0.972
3,000	0.92	0.72	1.10	1.019
2,000	1.16	0.76	1.21	1.136
1,000	1.88	0.78	1.26	1.341
500	2.85	1.03	2.61	2.495

Table B.36.
Calculations of Bulk Compressibility

Core Name : **Montmayeur 6080 FRAC**

Pressure psig	Static Measured Cb E-06/psi	Dynamic Measured Cb E-06/psi	Biot Corrected Cb E-06/psi	Gassmann Corrected Cb E-06/psi
500	2.42	0.86	2.01	1.640
1,000	1.85	0.83	1.81	1.460
2,000	1.39	0.62	0.94	0.868
3,000	1.08	0.58	0.81	0.761
4,000	0.96	0.55	0.76	0.704
5,000	0.91	0.52	0.69	0.651
4,000	0.77	0.55	0.75	0.704
3,000	0.98	0.58	0.81	0.761
2,000	1.33	0.61	0.89	0.823
1,000	2.03	0.85	1.90	0.706
500	2.59	0.85	1.93	1.591

Table B.37.
Calculations of Bulk Compressibility

Core Name   : Montmayeur 8010 FRAC

Pressure psig	Static Measured Cb E-06/psi	Dynamic Measured Cb E-06/psi	Biot Corrected Cb E-06/psi	Gassmann Corrected Cb E-06/psi
500	2.28	1.06	1.63	2.659
1,000	1.76	0.97	1.57	2.152
2,000	1.26	0.91	1.30	1.614
3,000	1.04	0.73	1.07	1.079
4,000	0.98	0.72	0.93	1.079
5,000	0.96	0.67	0.85	0.942
4,000	0.74	0.72	0.91	1.050
3,000	0.92	0.75	0.98	1.140
2,000	1.18	0.90	1.12	1.470
1,000	1.77	1.02	1.57	2.080
500	2.57	1.02	1.58	2.470

Table B.38.
Calculations of Bulk Compressibility

Core Name   : Montmayeur 1012 FRAC

Pressure psig	Static Measured Cb E-06/psi	Dynamic Measured Cb E-06/psi	Biot Corrected Cb E-06/psi	Gassmann Corrected Cb E-06/psi
500	2.43	1.20	2.31	3.225
1,000	1.80	0.97	1.57	1.994
2,000	1.37	0.89	1.34	1.444
3,000	1.14	0.80	1.13	1.189
4,000	1.00	0.74	1.01	1.040
5,000	0.96	0.68	0.89	0.889
4,000	0.91	0.75	1.02	1.040
3,000	1.05	0.82	1.17	1.223
2,000	1.25	0.82	1.16	1.255
1,000	1.76	0.91	1.39	1.716
500	2.47	1.24	2.64	3.795

Table B.39.
Calculations of Bulk Compressibility

Core Name   : Montmayeur 1217 FRAC

Pressure psig	Static Measured Cb E-06/psi	Dynamic Measured Cb E-06/psi	Biot Corrected Cb E-06/psi	Gassmann Corrected Cb E-06/psi
500	2.25	1.10	1.98	2.610
1,000	1.60	0.96	1.55	1.827
2,000	1.17	0.83	1.22	1.292
3,000	0.99	0.76	1.05	1.098
4,000	0.87	0.67	0.88	0.913
5,000	0.80	0.62	0.78	0.801
4,000	0.72	0.71	0.87	0.962
3,000	0.83	0.74	1.05	1.069
2,000	1.06	0.82	1.18	1.224
1,000	1.59	0.94	1.49	1.771
500	2.48	0.97	1.80	2.004

Table B.40.
Calculations of Bulk Compressibility

Core Name   : Montmayeur 1720 FRAC

Pressure psig	Static Measured Cb E-06/psi	Dynamic Measured Cb E-06/psi	Biot Corrected Cb E-06/psi	Gassmann Corrected Cb E-06/psi
500	2.36	1.00	2.68	2.610
1,000	1.84	0.92	1.91	1.867
2,000	1.41	0.80	1.40	1.384
3,000	1.24	0.72	1.09	1.076
4,000	1.14	0.68	0.92	0.992
5,000	1.11	0.61	0.85	0.840
4,000	0.81	0.65	0.93	0.916
3,000	0.98	0.71	1.10	1.076
2,000	1.24	0.83	1.45	1.384
1,000	1.87	0.89	1.77	1.756
500	2.55	0.98	2.34	2.270

APPENDIX C: Montmayeur's (1985)
                        Formulation of the Biot Model

This appendix is a reproduction of Montmayeur's (1985) derivation and formulation of the Biot model. It was used by Montmayeur to predict static bulk compressibilities from dynamic wave measurements and can be found in his Ph.D dissertation, T-3099, at the Colorado School of Mines.

Appendix A

Derivation of longitudinal and shear wave velocities using Biot's formulation.

Derivations are based on papers of Biot (1956a,b), Geertsma and Smit (1961), Domenico (1977), and White (1983). First, expressions using complex variables are given. Second, a derivation neglecting any energy loss effect is given, and finally expressions to compute rock elastic properties are derived.

A.1. Full equation using complex variables

- Compressional waves

The differential equations governing the propagation of waves are given by Biot (1956,b). The study of the propagation of plane waves yields a compatibility equation (Geertsma and Smit 1961).

$$(\sigma_L - \sigma_K^2)Z^2 + (2\gamma_f \sigma_K - \sigma_L - \gamma_c + \frac{i\omega_G F(W)}{\omega})Z$$

$$-(\gamma_f^2 - \gamma_c + \frac{i\omega_G F(W)}{\omega}) = 0$$

$$\text{where} \quad Z = \frac{V_c^2}{V_p^2} \; ; \quad V_c^2 = \frac{H}{\rho_B} \tag{A1}$$

$$V_p = \text{longitudinal velocity}$$

$$V_c = \text{reference velocity};$$

and $\quad \gamma_f = \dfrac{\rho_f}{\rho_B} \; ; \quad \gamma_c = \dfrac{\rho_c}{\rho_B} \; ; \quad \rho_c = \dfrac{k_c \rho_f}{\phi} \; ;$

and

$$\sigma_L = \frac{L}{H} \; ; \quad \sigma_K = \frac{K}{H}$$

$$L = \frac{1}{(1-\phi-\beta)C_R + \phi C_f}$$

$$K = (1-\beta)L$$

$$H = \frac{1}{C_B} + \frac{4}{3} G + (1-\beta) K$$

$$\beta = \frac{C_R}{C_B}$$

$$\omega_c = \frac{\mu_f \phi}{k \rho_f} = \frac{\phi \rho_B}{\rho_f} \omega_G \quad \text{or} \quad \omega_G = \frac{\mu_f}{k \rho_B}$$

$$F(W) = \frac{W T(W)}{4 \left[1 - \dfrac{2T(W)}{iW} \right]}$$

$$T(W) = \frac{\text{ber}'W + i\,\text{bei}'W}{\text{ber}\,W + i\,\text{bei}\,W}$$

$$W = \left(S \frac{\omega}{\omega_c} \right)^{1/2} \qquad\qquad (A2)$$

k   = rock permeability

μ_f = fluid viscosity

ω = propagation wave frequence

S   = structural factor

ber,bei = zero order Kelvin functions (Abramovitz
            and Stegun 1970). The primes indicate
            differentiation.

Different expressions have been presented in the
literature for ω_c.
Biot derived:

$$\omega_c = \frac{4\mu}{\pi a^2 \rho_f} \tag{A3}$$

where a = pore radius.

Using Darcy's law and Poiseuille's law, we can derive
that:

$$\frac{k}{\phi} = \frac{a^2}{8} \tag{A4}$$

Replacing (A4) in (A3) yields (A2). This formulation
is also given by White (1983).

Equation (A1) is of the form:

$$a^2 Z^2 - bZ + 1 = 0 \tag{A5}$$

whose solution is:

$$Z = \frac{1}{a} \left(\frac{b}{2a} - \sqrt{\frac{b^2}{4a^2} - 1} \right)$$

for the fast compressional wave. The solution can also be
written as:

$$Z = \frac{2b}{1 + \sqrt{1 - \frac{4a^2}{b^2}}}$$

and V_p = Real $(Z^{1/2} V_c)$ (A6)

In this form rock elastic properties (C_B), (G) can be
used as complex variables.

- Shear waves

The differential equations governing the propagation of
wave are given by Biot (1956,b). The study of the
propagation of shear wave yields the equation:

$$V_s = \text{Real} \left\{ \frac{G}{\rho_B} \; \frac{1 - \frac{i\,\omega_G F(W)}{\omega}}{1 - \frac{\phi \rho_f}{k_c \rho_B} - \frac{i\omega_G F(W)}{\omega}} \right\}^{1/2}$$ (A7)

In this form, the rock elastic property (G) can be used
as a complex variable.

A.2 Equations for the velocities neglecting the viscous
drag of the fluid

This approximation is valid for high frequency.
- Compressional velocity

Equation (A1) reduces to:

$$(\sigma_L - \sigma_K^2)\ Z^2 + (2\gamma_f \sigma_K - \sigma_L - \gamma_c)\ Z - (\gamma_f^2 - \gamma_c) = 0 \qquad (A8)$$

Velocity can be expressed directly as a function of the skeleton and fluid properties. After lengthy manipulations, it can be shown that:

$$V_P^2 = (U+V)\left[\ \frac{1}{2} + \sqrt{\frac{1}{4} - \frac{U}{(U+V)^2}\ \frac{\phi}{k_c \rho_f[(1-\phi-\beta)C_R + \phi C_f]}}\ \right] \qquad (A9)$$

where:
$$U = \frac{\dfrac{1}{c_B} + \dfrac{4}{3}\,G}{\rho_B\left(1 - \dfrac{\phi}{k_c}\,\dfrac{\rho_f}{\rho_B}\right)}$$

$$V = \frac{\dfrac{\phi \rho_B}{k_c \rho_f} - (1-\beta)\left(1-\beta - \dfrac{2\phi}{k_c}\right)}{(1-\phi-\beta)C_R + \phi\,C_f} \times \frac{1}{\rho_B\left(1 - \dfrac{\phi}{k_c}\,\dfrac{\rho_f}{\rho_B}\right)}$$

- Shear velocity

Equation (A7) reduces to:

$$V_s^2 = \frac{G}{\rho_B\left(1 - \dfrac{\phi \rho_f}{k_c \rho_B}\right)} \qquad (A10)$$

The different approximations given in the literature can be derived from relation (A9) and (A10).

- Neglecting the second term in the square root of equation (A9) compressional velocity becomes:

$$V_P{}^2 = U+V \tag{A11}$$

This relation is given by Geertsma (1961) and has been used by Domenico (1977). As shown in a discussion following Domenico's paper, the assumption is not always valid. Also making the assumption that the coupling coefficient (k_c) is infinite is only valid when the fluid and the skeleton are perfectly coupled. This is only true at low frequencies.

Relation (A9) reduces to:

$$V_P{}^2 = \left(\frac{1}{C_B} + \frac{4}{3} G + \frac{(1-\beta)^2}{(1-\phi-\beta)C_R+\phi C_f}\right) \frac{1}{\rho_B} \tag{A12}$$

Relation (A10) reduces to:

$$V_s{}^2 = \frac{G}{\rho_B} \tag{A13}$$

These relations were shown to be identical to the formulation of Gassmann (Geertsma, 1961).

A.3. Computation of the static rock properties from compressional and shear wave velocities.

Equations (A9) and (A10) can be written as:

$$V_P{}^2 = f(K_B, G_B) = (U+V)\left(\frac{1}{2} + FAC1\right)$$

$$V_s{}^2 = g(G_B).$$

The Raphson-Newton iteration technique yields:

$$K_{Bnew} = K_{Bo} + \frac{g^1_G[V_p^2 - f(K_{Bo}, G_{Bo})] - f^1_G[V_s^2 - g(G_{Bo})]}{f^1_K \, g^1_G} \Big|_{K_{Bo}}$$

$$G_{new} = G_o - \frac{[V_s^2 - g(G_{Bo})]}{g^1_G} \Big|_{B_{Bo}} \qquad (A14)$$

where:

$$f^1_G = [\tfrac{1}{2} + FAC1 - \frac{(V-U)}{2} FAC2] \frac{dU}{dG}$$

$$f^1_K = [\tfrac{1}{2} + FAC1 - (\frac{V-U}{2}) FAC2] \frac{dU}{dK_B}$$

$$- \frac{U \, C_R^2 \, \phi}{2k_c \rho_f[(1-\phi-\beta)C_R + \phi C_f]^2 (U+V) FAC1}$$

$$+ [\tfrac{1}{2} + FAC1 + U \, FAC2] \frac{dV}{dK_B}$$

$$g^1_G = \frac{1}{\rho_B \, (1 - \frac{\phi \rho_f}{k_c \rho_B})}$$

$$FAC1 = (\tfrac{1}{4} - \frac{U\phi}{(U+V)^2 k_c \rho_f[(1-\phi-\beta)C_R + \phi C_f]})^{1/2}$$

$$FAC2 = \frac{\phi}{(U+V)^2 k_c \rho_f[(1-\phi-\beta)C_R + \phi C_f] \, FAC1}$$

$$\frac{dU}{dG} = \frac{4}{3\rho_B \, (1 - \frac{\phi \rho_f}{k_c \rho_B})}$$

$$\frac{dU}{dK_B} = \frac{1}{\rho_B \, (1 - \frac{\phi \rho_f}{k_c \rho_B})}$$

$$\frac{dV}{dK_B} = \frac{C_R}{\rho_B\left(1 - \frac{\phi\rho_f}{k_c\rho_B}\right)} \quad X$$

$$\frac{C_R\left[(1-\beta)(1-\beta-\frac{2\phi}{k_c}) + \frac{\phi\rho_B}{k_c\rho_f}\right] - 2(1-\beta-\frac{\phi}{k_c})\left[(1-\phi-\beta)C_R+\phi C_f\right]}{\left[(1-\phi-\beta)C_R+\phi C_f\right]^2}$$

These equations may appear complicated but they are very simple to implement on a computer.

APPENDIX D: Core Sample Nomenclature and Cross-Reference

Table D.1
Core Sample Nomenclature and Cross Reference

Core Name	Other Names Used in Text, Figures and Tables	Description of Core
Consolidated Rocks:		
STB1	–	Montmayeur's standard Berea core number 1
STB2	–	Montmayeur's standard Berea core number 2
STB5	MSTB5	Montmayeur's standard Berea core number 5
K5C2	–	Montmayeur's sandstone core
STD2	MSTD2	Montmayeur's standard dolomite core number 2
HCB1	–	Howarth's Berea core number 1
HCB2	–	Howarth's Berea core number 2
HCB3	–	Howarth's Berea core number 3
HCB4	–	Howarth's Berea core number 4
HCB5	–	Howarth's Berea core number 5
HCB6	–	Howarth's Berea core number 6
HCB7	–	Howarth's Berea core number 7
HCB8	–	Howarth's Berea core number 8
HCB9	–	Howarth's Berea core number 9
HCB10	–	Howarth's Berea core number 10
HCB11	–	Howarth's Berea core number 11
HCB12	–	Howarth's Berea core number 12
HCB13	–	Howarth's Berea core number 13
HCB14	–	Howarth's Berea core number 14
HCB15	–	Howarth's Berea core number 15
HCB16	–	Howarth's Berea core number 16
HSTB5	STB5	Montmayeur's STB5 re-prepared and tested by Howarth
HSTD2	STD2	Montmayeur's STB5 re-prepared and tested by Howarth
Unconolidated Samples:		
20403	–	Montmayeur's 20/40 mesh frac sand, sample 3
20404	–	Montmayeur's 20/40 mesh frac sand, sample 4
4060	–	Montmayeur's 40/60 mesh frac sand
6080	–	Montmayeur's 60/80 mesh frac sand
8010	–	Montmayeur's 80/100 mesh frac sand
1012	–	Montmayeur's 100/120 mesh frac sand
1217	–	Montmayeur's 120/170 mesh frac sand
1720	–	Montmayeur's 170/200 mesh frac sand

Table D.1
Core Sample Nomenclature and Cross Reference
(Continued)

Core Name	Other Names Used in Text, Figures and Tables	Description of Core
G2040A	-	Howarth's 20/40 mesh glass beads, sample A
G1014A	-	Howarth's 100/140 mesh glass beads, sample A
F2040C	-	Howarth's 20/40 mesh frac sand, sample C
F6080A	-	Howarth's 60/80 mesh frac sand, sample A
F6080B	-	Howarth's 60/80 mesh frac sand, sample B
F6080D	-	Howarth's 60/80 mesh frac sand, sample D
F1014A	-	Howarth's 100/140 mesh frac sand, sample A
F1014B	-	Howarth's 100/140 mesh frac sand, sample B
Reservoir Sample 1A	RS1A	Howarth's Reservoir Sand 1, sample A
Reservoir Sample 2B	RS2B	Howarth's Reservoir Sand 2, sample B
Reservoir Sample 3A	RS3A	Howarth's Reservoir Sand 3, sample A
Reservoir Sample 4A	RS4A	Howarth's Reservoir Sand 4, sample A
Reservoir Sample 5A	RS5A	Howarth's Reservoir Sand 5, sample A
Reservoir Sample 5B	RS5B	Howarth's Reservoir Sand 5, sample B
Reservoir Sample 6A	RS6A	Howarth's Reservoir Sand 6, sample A
Reservoir Sample 7A	RS7A	Howarth's Reservoir Sand 7, sample A
Reservoir Sample 8A	RS8A	Howarth's Reservoir Sand 8, sample A